SIMULATED AUTOMOBILE AND ROTARY-WING AIRCRAFT IMPACTS: DYNAMIC NECK RESPONSE AFTER SURGICAL TREATMENT FOR CERVICAL SPONDYLOSIS

NICHOLAS ALAN WHITE

Dissertation submitted to the faculty of the Virginia Polytechnic Institute and State University in partial fulfillment of the requirements for the degree of

Doctor of Philosophy
In
Biomedical Engineering

Joel D. Stitzel
Kerry A. Danelson
F. Scott Gayzik
Wesley Hsu
Alexander K. Powers
Stefan M. Duma

December 9, 2013
Blacksburg, VA

Keywords: Cervical Spine, Arthroplasty, Arthrodesis, Finite Element Analysis, GHBMC

SIMULATED AUTOMOBILE AND ROTARY-WING AIRCRAFT IMPACTS: DYNAMIC NECK RESPONSE AFTER SURGICAL TREATMENT FOR CERVICAL SPONDYLOSIS

NICHOLAS ALAN WHITE

Abstract

Degeneration of the cervical spine is part of the normal aging process, usually occurring without clinical symptoms. Symptomatic degeneration most often occurs in the lower cervical spine, presenting as axial neck pain, radiculopathy, myelopathy, or any combination of the three. When conservative treatment does not adequately manage these symptoms, surgical intervention may be required. The longstanding surgical treatment for cervical degeneration is arthrodesis achieved through anterior cervical discectomy and fusion (ACDF). A relatively newer treatment is arthroplasty with a cervical total disc replacement (CTDR), a motion-sparing procedure designed to maintain adjacent-level loading. While literature exists comparing the effects of cervical arthrodesis and cervical arthroplasty on neck kinematics and loading, the vast majority of these studies applied only quasi-static, non-injurious loading conditions. This dissertation research used a state-of-the-art, full body human finite element (FE) model to investigate the effects of these surgical procedures on neck response during simulated dynamic impacts.

A method was developed to measure cross-sectional forces and moments at each level of the neck in the FE model. Neck loading was captured during three automobile impact simulations: a frontal impact of a belted driver with airbag deployment, a frontal impact of a belted passenger without airbag deployment, and an unbelted side impact. The measured neck forces and moments were compared to existing injury threshold values and used to calculate injury criteria values. Four additional simulations of the frontal impact with the belted driver were conducted with neck modifications representative of either a fusion or arthroplasty of C5-6.

While cross-sectional loading above and below the implants did not vary appreciably, key differences were noted in both the interbody and facet response. However, no neck injury thresholds were exceeded in any of the simulations.

With cervical radiculopathy diagnosed in 24,742 active-duty U.S. military personnel between 2000 and 2009, interest in cervical arthroplasty as treatment for symptomatic cervical degeneration in this population has increased. This motion-sparing procedure has the potential to expedite post-operative recovery time, allowing for these highly trained individuals to return to active-duty sooner than with a fusion. Due to the physically demanding nature of the military environment, it is important to ensure that this surgical procedure does not increase the likelihood of a neck injury.

An FE simulation environment was developed to investigate aviator head and neck response during a survivable, rotary-wing aircraft impact with the ground using both an anthropomorphic test device (ATD) and a human body model. The head and neck response of the ATD FE simulation was successfully validated against the results of a previously conducted experimental sled test. A more biofidelic head and neck response was produced with the human body model, including realistic changes in neck curvature. Additional simulations were conducted with the human body model to investigate the neck response after cervical arthroplasty of C5-6. While the adjacent-level, cross-sectional loading for the C5-6 segment was not appreciably altered by the CTDRs, the interbody range-of-motion was increased; subsequently altering both the interbody and cervical facet loading. Again, no neck injury thresholds were exceeded in these simulations. Overall, cervical arthroplasty did not appear to have a deleterious effect on the dynamic neck response during a simulated rotary-wing aircraft impact.

Dedication

This dissertation is dedicated to my Grandma and my Great Aunt Mary – two stubborn Italian women without filters, but with hearts of gold.

Acknowledgments

This tremendous journey called graduate school has finally come to an end. I would never have seen this day without the constant love and support from my family, friends, and colleagues.

I would like to express gratitude to my doctoral committee chair, Dr. Joel Stitzel. His constant encouragement and positive attitude were instrumental to my success. I would also like to thank Dr. Stefan Duma, Dr. Scott Gayzik, Dr. Kerry Danelson, Dr. Wesley Hsu, and Dr. Alexander Powers for serving on my doctoral committee.

I would like to thank Dan Moreno for offering his expert technical advice, Glenn Paskoff for assisting with experimental inquires, Dr. David Chin and Dr. Timothy Miller for maintaining the WFU DEAC cluster, and the VT ILLiad staff for finding every article I requested, no matter how obscure.

I would be remiss if I did not thank all of my fellow lab mates, though too numerous to mention all by name. I thank Adam Golman for the hours of intellectual conversations and for his friendship. I thank Philip Brown for his mechanical prowess, and I truly look forward to the day when he runs his own orthopedic biomechanics lab. I thank Nick Vavalle for his modeling expertise and competitive spirit for working latest in the lab.

Of course I cannot forget to thank Stan Gregory, one of my best friends. To all of the sleepless hours we spent working in the sled lab, the late-night gas station runs, and the countless slices of pizza we consumed. At the end of the day, we both made it – with one heck of a story to tell.

A wise man once shared this proverb with me: “Give a man a fish and you feed him for a day. Teach a man to fish and you feed him for a lifetime.” Thank you KHY for teaching me to fish.

And lastly, I cannot thank my family enough, especially my parents Barbara and John, for their unyielding love and support. I could always count on them to have by back, through thick and thin.

Table of Contents

List of Figures

List of Tables

Attributions

Several colleagues aided in the writing and research behind several of the chapters of this dissertation. A brief description of their contributions is included here.

Philip J. Brow, M.S. is currently a Ph.D. student at Wake Forest University and part of the Virginia Tech - Wake Forest Center for Injury Biomechanics. Mr. Brown was a co-author on Chapter 5. Mr. Brown assisted in the reverse engineering of the cervical disc replacements and was responsible for the 3D replicas.

Kerry A. Danelson, Ph.D. is currently an Assistant Professor at the Virginia Tech - Wake Forest Center for Injury Biomechanics. Dr. Danelson was a co-author on Chapters 6 and 7. Dr. Danelson also provided invaluable advice on the military-related aspects of this research.

F. Scott Gayzik, Ph.D. is currently an Assistant Professor at the Virginia Tech - Wake Forest Center for Injury Biomechanics and Program Leader for the Integration Center of the Global Human Body Models Consortium project. Dr. Gayzik was a co-author on Chapters 3, 5, 6, and 7.

Wesley Hsu, M.D. is currently an Assistant Professor of Neurosurgery at Wake Forest Baptist Medical Center. Dr. Hsu was a co-author on Chapters 5 and 7. Dr. Hsu provided his expertise on cervical disc replacements, as well as his assistance during the development of solid and finite element models of the Prestige ST and ProDisc-C implants.

Daniel P. Moreno, M.S. is currently a Senior Research Engineer for the Virginia Tech – Wake Forest University Center for Injury Biomechanics. Mr. Moreno was a co-author on Chapters 3 and 5. Mr. Moreno developed the original simulations used in these chapters. He also provided technical support for the GHBMC model during the course of this research.

Alexander Powers, M.D. is currently an Assistant Professor of Neurosurgery at Wake Forest Baptist Medical Center. Dr. Powers was a co-author on Chapters 5 and 7. Dr. Powers provided his expertise on cervical disc replacements. He also provided me with the opportunity to shadow him during several cervical spine surgeries.

Joel D. Stitzel, Ph.D. is currently the Chair of the Biomedical Engineering Department at Wake Forest University, Associate Head of the Virginia Tech – Wake Forest University School of Biomedical Engineering and Sciences, and Program Leader for the Virginia Tech – Wake Forest University Center for Injury Biomechanics. Dr. Stitzel was a co-author on Chapters 3, 5, 6, and 7. Dr. Stitzel has played an integral role in all parts of this research, including the initial conception of the cross-sectional method to measure neck loading.

Chapter 1: Introduction and Research Objectives

Introduction

Cervical spondylosis is defined as a "degenerative joint disease affecting the cervical vertebrae, intervertebral disks, and surrounding ligaments and connective tissue" [1]. Degeneration of the cervical spine is part of the normal aging process, usually occurring in the absence of clinical symptoms [2-5]. When symptoms present, they manifest as axial neck pain, radiculopathy, myelopathy, or any combination of the three [6, 7]. Symptomatic degeneration most often occurs in the lower cervical spine between C5 and C6 and may require surgical intervention [2-5, 8]. Anterior cervical discectomy and fusion (ACDF) is the primary surgical treatment for cervical degenerative disc disease (CDDD) [9-13]. Cervical arthrodesis of the affected level typically involves replacing the disc with an autograft, allograft, or synthetic graft, and securing the adjacent vertebrae with anterior plating [14, 15]. An alternative to fusion is cervical arthroplasty, which involves replacing the intervertebral disc (IVD) with a cervical total disc replacement (CTDR). Unlike ACDF, cervical arthroplasty maintains the range-of-motion (ROM) and adjacent-level loading [16-22], potentially decreasing the incidence of adjacent segment degeneration (ASD) [12, 23, 24]. Additionally, shorter post-operative recovery times have been reported for cervical arthroplasty as compared to ACDF [23, 25-28]. While experimental and computational studies have supported the functional equivalence between a CTDR and an IVD under quasi-static loading conditions [17, 20-22, 29], little is known about the response of the surgically altered neck under dynamic, higher energy, loading conditions [30, 31].

Between 2001 and 2010, 131,986 active-duty U.S. military personnel were diagnosed with degenerative disc disease (DDD), with pilot and aircrew personnel composing 5,505 of these individuals [32]. A total of 90,855 lost duty days were attributed to DDD-specific and DDD-related medical encounters. Cervical radiculopathy was diagnosed in 24,742 active-duty U.S. military personnel between 2000 and 2009 [33]. Interest in cervical arthroplasty as treatment for CDDD in members of the armed forces has recently increased due to the potential for expedited post-operative recovery [28, 34]. However, it is important to ensure that this surgical procedure does not place these individuals at a greater risk of injury, especially due to the physically demanding nature of their jobs [35-38]. While preliminary studies have reported positive findings on cervical arthroplasty in the military population [28, 34], more research is required to evaluate dynamic neck response post-arthroplasty; particularly for military helicopter pilots [39, 40].

Research Objectives

The purpose of this dissertation was to investigate the effects of CTDRs on neck response during dynamic impact events through finite element (FE) analysis. The dissertation research was broken down into 5 research objectives:

Objective #1: Develop a method to capture cross-sectional forces and moments in the neck of a human body FE model.

A series of cross sections was defined in the neck to capture force and moment contributions from bones, ligaments, active muscles, passive muscles, and soft tissue at each level of the cervical spine. These forces and moments were reported in local coordinate systems specific to the cervical level. To evaluate dynamic neck loading in the model using these cross sections, three automobile impact simulations were conducted: a frontal impact of a belted driver with airbag deployment, a frontal impact of a belted passenger without airbag deployment, and an unbelted side impact. The measured neck forces and moments were compared to existing injury threshold values and used to calculate injury criteria values.

Objective #2: Model cervical arthrodesis and cervical arthroplasty at the C5-6 level of the human body FE model.

Cervical arthrodesis was modeled both as a series of constrained nodal rigid bodies between the inferior C5 and superior C6 vertebral bodies and as a generic cage, core, and anterior plate implant. Cervical arthroplasty was modeled using two different CTDRs: a Prestige ST and ProDisc-C. The geometries were reverse engineered from physical implants to create solid models, which were subsequently used to produce physical 3D replicas using a direct metal laser sintering process. These replicas were compared to the original implants for geometric accuracy. Once satisfied with the geometry, the solid models were converted to FE models and assigned appropriate material properties. The IVD and anterior longitudinal ligament were removed at the C5-6 level of the neck model and the adjacent vertebral bodies modified to accept the FE models of the generic interbody fusion implant and the CTDRs.

Objective #3: Investigate the effects of cervical arthrodesis and arthroplasty on dynamic neck response during a simulated frontal automobile crash.

The frontal impact simulation of a belted driver with airbag deployment completed in Objective #1 was repeated with the implants developed in Objective #2. Adjacent-level loading, interbody loading, and facet loading were evaluated in each simulation.

Objective #4: Simulate a rotary-wing aircraft impact using an FE ATD and human body model.

A rotary-wing aircraft impact was simulated with an FE anthropomorphic test device (ATD) and validated against a previously conducted experimental sled test. Effects of initial positioning of the ATD on head and neck response were evaluated. An additional simulation was conducted with a human body model to produce a more biofidelic head and neck response than the ATD simulations. Changes in neck curvature and cross-sectional loading were examined.

Objective #5: Investigate the effects of cervical arthroplasty on dynamic neck response during a simulated rotary-wing aircraft impact.

The rotary-wing aircraft impact simulation conducted in Objective #4 was repeated to evaluate the neck response of the human body model with the CTDRs developed in Objective #2. Cross-sectional loading, interbody loading, and facet loading and strain were examined for the C5-6 segment. Neck curvature and interbody kinematics were also reported.

Dissertation Structure

Chapter 1 provides a brief introduction and the research objectives of this dissertation. Chapter 2 provides background information on relevant anatomy, cervical degenerative disc disease, injury biomechanics, and rotary-wing aircraft crashworthiness. Chapter 3 addresses Objective #1 and is based on a paper published by White et al. [41] in Computer Methods in Biomechanics and Biomedical Engineering. Chapters 4-7 address Objectives #2-5, respectively. Chapter 8 provides a summary of the dissertation results and conclusions, along with a list of expected publications and potential future work.

Chapter 1 References

[1] Saunders. Dorland's Illustrated Medical Dictionary. 26th ed. Philadelphia, 1985.

[2] Gore DR, Sepic SB, Gardner GM. Roentgenographic Findings of the Cervical Spine in Asymptomatic People. Spine. 1986;11:521-4.

[3] Gore DR. Roentgenographic Findings in the Cervical Spine in Asymptomatic Persons: A Ten-Year Follow-Up. Spine. 2001;26:2463-6.

[4] Boden SD, McCowin PR, Davis DO, Dina TS, Mark AS, Wiesel S. Abnormal Magnetic-Resonance Scans of the Cervical Spine in Asymptomatic Subjects. A Prospective Investigation. The Journal of bone and joint surgery American volume. 1990;72:1178-84.

[5] Roh JS, Teng AL, Yoo JU, Davis J, Furey C, Bohlman HH. Degenerative Disorders of the Lumbar and Cervical Spine. The Orthopedic clinics of North America. 2005;36:255-62.

[6] Habela NM, McAfee PC. Indications and Contraindications for Cervical Nonfusion Surgery: Patient Selection. In: Yue JJ, Bertagnoli R, McAfee PC, An HS, editors. Motion Preservation Surgery of the Spine: Advanced Techniques and Controversies. Philadelphia: Saunders; 2008. p. 80-4.

[7] Matan AJ, Connolly PJ. Concepts of Cervical Decompression. In: Herkowitz HN, editor. The Cervical Spine Surgery Atlas. 2 ed. Philadelphia: Lippincott Williams & Wilkins; 2004. p. 123-38.

[8] Montgomery DM, Brower RS. Cervical Spondylotic Myelopathy. Clinical Syndrome and Natural History. The Orthopedic clinics of North America. 1992;23:487-93.

[9] Bailey RW, Badgley CE. Stabilization of the Cervical Spine by Anterior Fusion. The Journal of bone and joint surgery American volume. 1960;42-A:565-94.

[10] Cloward RB. The Anterior Approach for Removal of Ruptured Cervical Disks. Journal of neurosurgery. 1958;15:602-17.

[11] Fallah A, Akl EA, Ebrahim S, Ibrahim GM, Mansouri A, Foote CJ, et al. Anterior Cervical Discectomy with Arthroplasty Versus Arthrodesis for Single-Level Cervical Spondylosis: A Systematic Review and Meta-Analysis. PloS one. 2012;7:e43407.

[12] Mummaneni PV, Amin BY, Wu JC, Brodt ED, Dettori JR, Sasso RC. Cervical Artificial Disc Replacement Versus Fusion in the Cervical Spine: A Systematic Review Comparing Long-Term Follow-up Results from Two FDA Trials. Evidence-based spine-care journal. 2012;3:59-66.

[13] Smith GW, Robinson RA. The Treatment of Certain Cervical-Spine Disorders by Anterior Removal of the Intervertebral Disc and Interbody Fusion. The Journal of bone and joint surgery American volume. 1958;40-A:607-24.

[14] Majid K, Fischgrund JS. Anterior Cervical Discectomy and Fusion (ACDF). In: Benzel EC, editor. The Cervical Spine. 5th ed. Philadelphia, PA: Lippincott Williams & Wilkins; 2012. p. 956-63.

[15] Zdeblick T. Anterior Cervical Plating. In: Herkowitz HN, editor. The Cervical Spine Surgery Atlas. 2nd ed. Philadelphia, PA: Lippincott Williams & Wilkins; 2004. p. 353-9.

[16] Bauman JA, Jaumard NV, Guarino BB, Weisshaar CL, Lipschutz DE, Welch WC, et al. Facet Joint Contact Pressure Is Not Significantly Affected by Prodisc Cervical Disc Arthroplasty in Sagittal Bending: A Single-Level Cadaveric Study. The spine journal : official journal of the North American Spine Society. 2012;12:949-59.

[17] DiAngelo DJ, Foley KT, Morrow BR, Schwab JS, Song J, German JW, et al. In Vitro Biomechanics of Cervical Disc Arthroplasty with the Prodisc-C Total Disc Implant. Neurosurgical focus. 2004;17:E7.

[18] Eck JC, Humphreys SC, Lim TH, Jeong ST, Kim JG, Hodges SD, et al. Biomechanical Study on the Effect of Cervical Spine Fusion on Adjacent-Level Intradiscal Pressure and Segmental Motion. Spine. 2002;27:2431-4.

[19] Jaumard NV, Bauman JA, Guarino BB, Gokhale AJ, Lipschutz DE, Weisshaar CL, et al. Prodisc Cervical Arthroplasty Does Not Alter Facet Joint Contact Pressure During Lateral Bending or Axial Torsion. Spine. 2013;38:E84-93.

[20] Liu F, Cheng J, Komistek RD, Mahfouz MR, Sharma A. In Vivo Evaluation of Dynamic Characteristics of the Normal, Fused, and Disc Replacement Cervical Spines. Spine. 2007;32:2578-84.

[21] Puttlitz CM, Rousseau MA, Xu Z, Hu S, Tay BK, Lotz JC. Intervertebral Disc Replacement Maintains Cervical Spine Kinetics. Spine. 2004;29:2809-14.

[22] Womack W, Leahy PD, Patel VV, Puttlitz CM. Finite Element Modeling of Kinematic and Load Transmission Alterations Due to Cervical Intervertebral Disc Replacement. Spine. 2011;36:E1126-33.

[23] Mummaneni PV, Burkus JK, Haid RW, Traynelis VC, Zdeblick TA. Clinical and Radiographic Analysis of Cervical Disc Arthroplasty Compared with Allograft Fusion: A Randomized Controlled Clinical Trial. Journal of neurosurgery Spine. 2007;6:198-209.

[24] Upadhyaya CD, Wu JC, Trost G, Haid RW, Traynelis VC, Tay B, et al. Analysis of the Three United States Food and Drug Administration Investigational Device Exemption Cervical Arthroplasty Trials. Journal of neurosurgery Spine. 2012;16:216-28.

[25] Heller JG, Sasso RC, Papadopoulos SM, Anderson PA, Fessler RG, Hacker RJ, et al. Comparison of Bryan Cervical Disc Arthroplasty with Anterior Cervical Decompression and Fusion: Clinical and Radiographic Results of a Randomized, Controlled, Clinical Trial. Spine. 2009;34:101-7.

[26] Park JH, Roh KH, Cho JY, Ra YS, Rhim SC, Noh SW. Comparative Analysis of Cervical Arthroplasty Using Mobi-C(R) and Anterior Cervical Discectomy and Fusion Using the Solis(R) -Cage. Journal of Korean Neurosurgical Society. 2008;44:217-21.

[27] Steinmetz MP, Patel R, Traynelis V, Resnick DK, Anderson PA. Cervical Disc Arthroplasty Compared with Fusion in a Workers' Compensation Population. Neurosurgery. 2008;63:741-7; discussion 7.

[28] Tumialan LM, Ponton RP, Garvin A, Gluf WM. Arthroplasty in the Military: A Preliminary Experience with Prodisc-C and Prodisc-L. Neurosurgical focus. 2010;28:E18.

[29] Galbusera F, Bellini CM, Raimondi MT, Fornari M, Assietti R. Cervical Spine Biomechanics Following Implantation of a Disc Prosthesis. Medical engineering & physics. 2008;30:1127-33.

[30] Dang AB, Hu SS, Tay BK. Biomechanics of the Anterior Longitudinal Ligament During 8 G Whiplash Simulation Following Single- and Contiguous Two-Level Fusion: A Finite Element Study. Spine. 2008;33:607-11.

[31] Duggal N, Rabin D, Chamberlain RH, Baek S, Crawford NR. Traumatic Loading of the Bryan Cervical Disc Prosthesis: An in Vitro Study. Neurosurgery. 2007;60:388-92; discussion 92-3.

[32] Mydlarz D. Degenerative Disc Disease, Active Component, U.S. Armed Forces, 2001-2011. Msmr. 2012;19:6-9.

[33] Schoenfeld AJ, George AA, Bader JO, Caram PM, Jr. Incidence and Epidemiology of Cervical Radiculopathy in the United States Military: 2000 to 2009. Journal of spinal disorders & techniques. 2012;25:17-22.

[34] Kang DG, Lehman RA, Tracey RW, Cody JP, Rosner MK, Bevevino AJ. Outcomes Following Cervical Disc Arthroplasty in an Active Duty Military Population. Journal of surgical orthopaedic advances. 2013;22:10-5.

[35] Bass CR, Salzar R, Ash J, Ziemba A, Lucas S, Peterson R, et al. Dynamic Models for the Assessment of Spinal Injury from Repeated Impact in High Speed Planing Boats. International Research Council on Biomechanics of Injury. The Netherlands. 2007.

[36] Hendriksen IJ, Holewijn M. Degenerative Changes of the Spine of Fighter Pilots of the Royal Netherlands Air Force (RNLAF). Aviation, space, and environmental medicine. 1999;70:1057-63.

[37] Knapp SC. Medical and Physiological Effects of Ejection and Parachuting an Overview. Fort Rucker, AL: US Army Aeromedical Research Laboratory. USAARL Report No. 71-9. 1970.

[38] Petren-Mallmin M, Linder J. Cervical Spine Degeneration in Fighter Pilots and Controls: A 5-Yr Follow-up Study. Aviation, space, and environmental medicine. 2001;72:443-6.

[39] Reaume J. Cervical Total Disc Replacement in a Military Helicopter and General Aviation Pilot. The Federal Air Surgeon's Medical Bulletin. 2012;50:11-2.

[40] Reaume J. You're the Flight Surgeon: Cervical Degenerative Joint Disease and Total Disc Arthroplasty. Aviation, space, and environmental medicine. 2013;84:169-71.

[41] White NA, Moreno DP, Gayzik FS, Stitzel JD. Cross-Sectional Neck Response of a Total Human Body Fe Model During Simulated Frontal and Side Automobile Impacts. Computer methods in biomechanics and biomedical engineering. 2013.

Chapter 2: Background and Literature Review

Brief Overview of Relevant Anatomy

Skeleton

The cervical spine is composed of seven vertebrae (C1-C7) with lordotic curvature maintained by the wedge-shaped intervertebral discs (IVDs) (Figure 2-1) [1]. The first two cervical vertebrae, C1 (atlas) and C2 (axis), are geometrically atypical (Figure 2-2). Anterior and posterior arches connect two lateral masses, creating the ring-like structure of C1 [2]. Its superior articular surfaces couple with the occipital condyles on the base of skull, carrying the cranium. This vertebra lacks a body and spinous process. C1 rotates about the odontoid process of C2, articulating about its large superior articular facets. This process, also referred to as the dens, is a bony pivot point that protrudes cranially from the body of C2. No IVD exists between these two vertebrae. The remaining cervical vertebrae (C3-C7) are similar to one another in structure and contain IVDs between each adjacent vertebral body (VB) Figure 2-3.

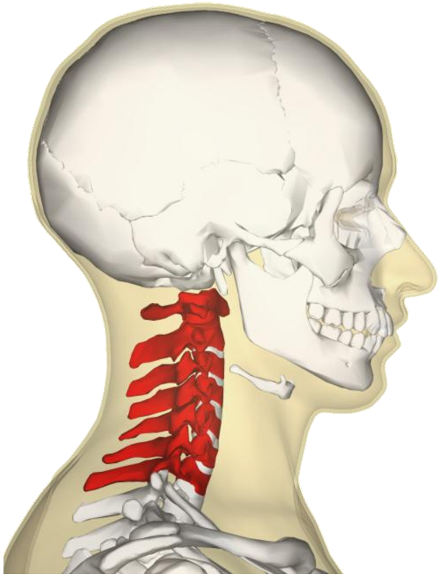

Figure 2-1: Lateral view of the head and cervical spine [3].

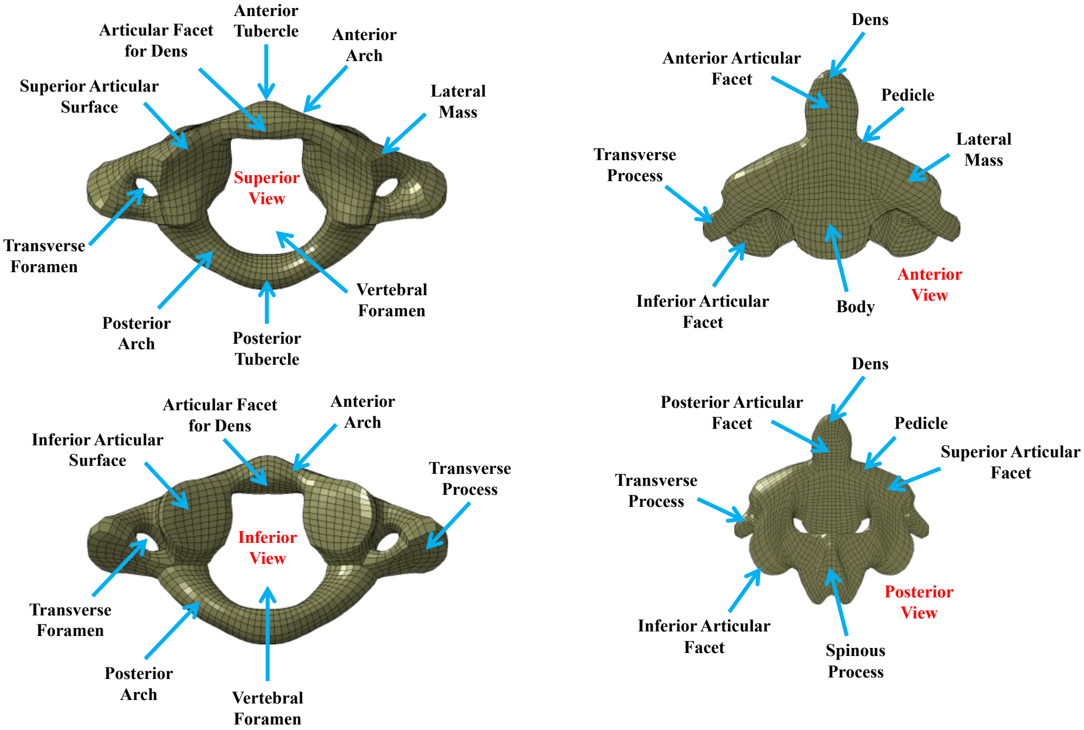

(a) (b)

Figure 2-2: The atypical (a) C1 and (b) C2 cervical vertebrae.

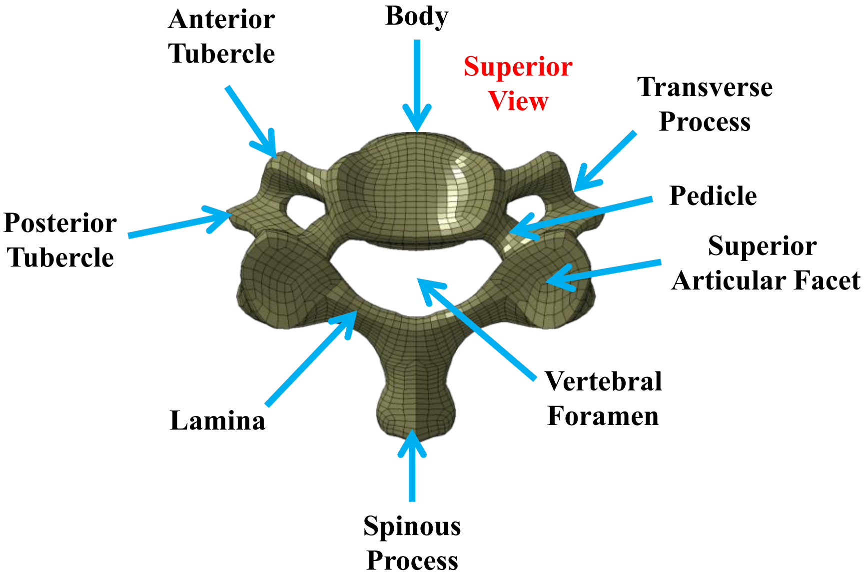

Figure 2-3: Superior view of a typical cervical vertebra.

Intervertebral Disc

The IVDs provide a strong, shock-absorbing attachment between adjacent VBs, and account for up to 1/3 the height of the vertebral column [1, 2]. The IVD can be broken down into three distinct parts: the nucleus pulposus (NP), annulus fibrosus (AF), and cartilaginous end-plates [4]. The gelatinous NP located in the center of the disc is composed of 90% water in the young adult, with a reduction to 70% in the older population. The remainder of the NP is made up of type II collagen and proteoglycans. As with the water content, the total amount of proteoglycan decreases with age. The outer layer of the IVD is composed of approximately 90 concentric lamellar bands of collagen collectively referred to as the AF. The water content is 78% in younger adults, decreasing to 70% with age. Both type I and type II collagen fibers run at 30° angles to the disc. The NP and AF are separated from the VB by a hyaline cartilaginous end-plate.

Ligaments

The biomechanically-relevant ligaments of the cervical spine include the anterior longitudinal ligament (ALL), posterior longitudinal ligament (PLL), capsular ligaments, ligamenta flava, interspinous ligaments, and supraspinous ligaments (Figure 2-4) [4]. The ALL runs over the anterior aspect of the vertebral bodies, narrowing in width as it passes over the IVDs. The IVD portion of the ALL is excised at the level of cervical arthrodesis or arthroplasty prior to discectomy. The PLL runs along the posterior aspect of VBs, widening as it passes over the IVDs. Unlike the ALL, the PLL is interwoven with the IVD AF. The capsular ligaments run along the margins of articulating processes of the facet and uncovertebral joints, and contain synovial fluid [2]. The LF connects the anterior laminae borders of adjacent vertebrae and is considered the most elastic tissue in the body. The interspinous ligaments connect adjacent spinous processes and are minimally developed in the cervical spine. The supraspinous ligament, referred to as the ligamentum nuchae in the neck, connects the tips of each spinous process.

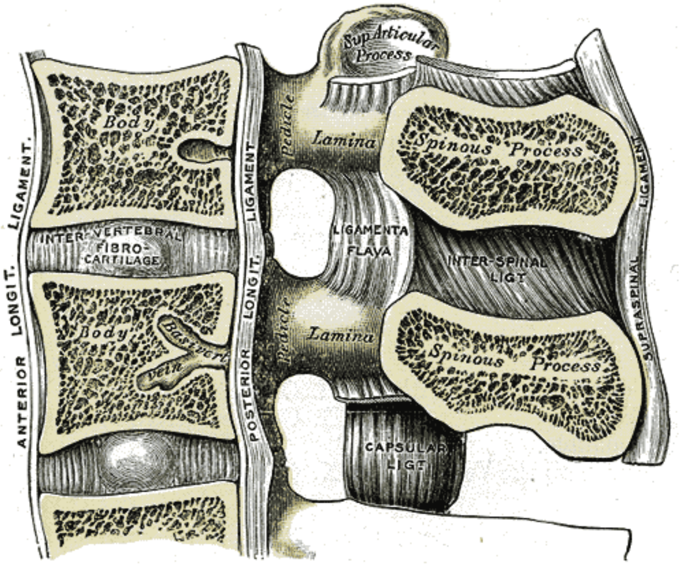

Figure 2-4: Major ligaments of the cervical spine [5].

Fascial Layers and Musculature

Several layers of deep cervical fascia compartmentalize structures within the neck (Figure 2-5) [2]. These layers create avascular cleavage planes utilized during surgery to separate tissue without disrupting the neck vasculature. The major muscles of the neck (Figure 2-6) are grouped into five categories: superficial, lateral prevertebral, anterior prevertebral, suprahyoid, and infrahyoid.

The superficial neck muscles include the platysma, sternocleidomastoid, and trapezius. The platysma is a very thin muscle responsible for certain facial expressions and is the only neck muscle not contained within the deep cervical fascia. The sternocleidomastoids are responsible for lateral bending and rotation of the head when acting independently, and flexion and extension of the head when acting in unison. The trapezius is responsible for elevation, retraction, and rotation of the scapula, as well as lateral bending, axial rotation and extension of the head and neck. The lateral prevertebral muscles include the splenius capitis, levator scapulae, and the posterior, middle, and anterior scalene. The splenius capitis muscles laterally flex and rotate the head and neck when acting independently and extend the head and neck when acting in unison. The levator scapulae elevate and inferiorly rotate the scapula. The posterior and middle scalene laterally flex the neck, while the anterior scalene both laterally flexes and rotates the neck. The anterior prevertebral muscles include the longus colli, longus capitis, rectus capitis anterior, and rectus capitus lateralis. The longus colli flexes the neck; with lateral rotation if acting unilaterally. The longus capitis and rectus capitis muscles flex the head. The suprahyoid muscles include the mylohyoid, geniohyoid, stylohyoid, and digastric. The infrahyoid muscles include the sternohyoid, omohyoid, sternothyroid, and thyrohyoid. The hyoid muscles elevate and depress the hyoid bone, aiding in swallowing and speaking.

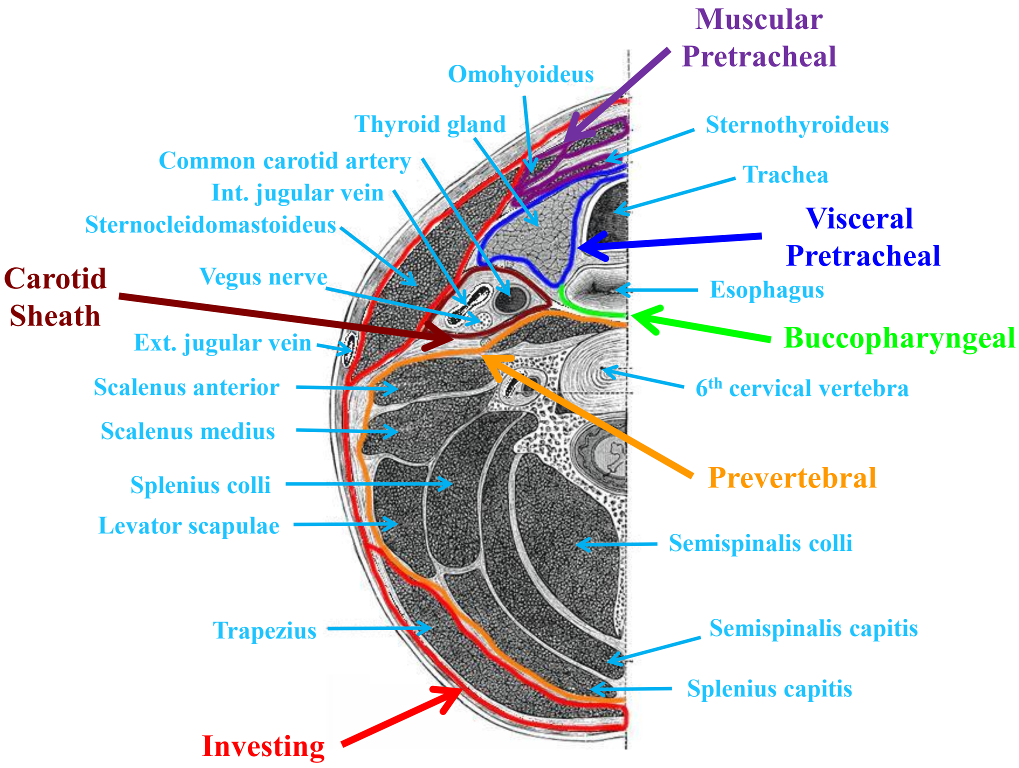

Figure 2-5: Cross-sectional view of the neck musculature including the fascial layers [5].

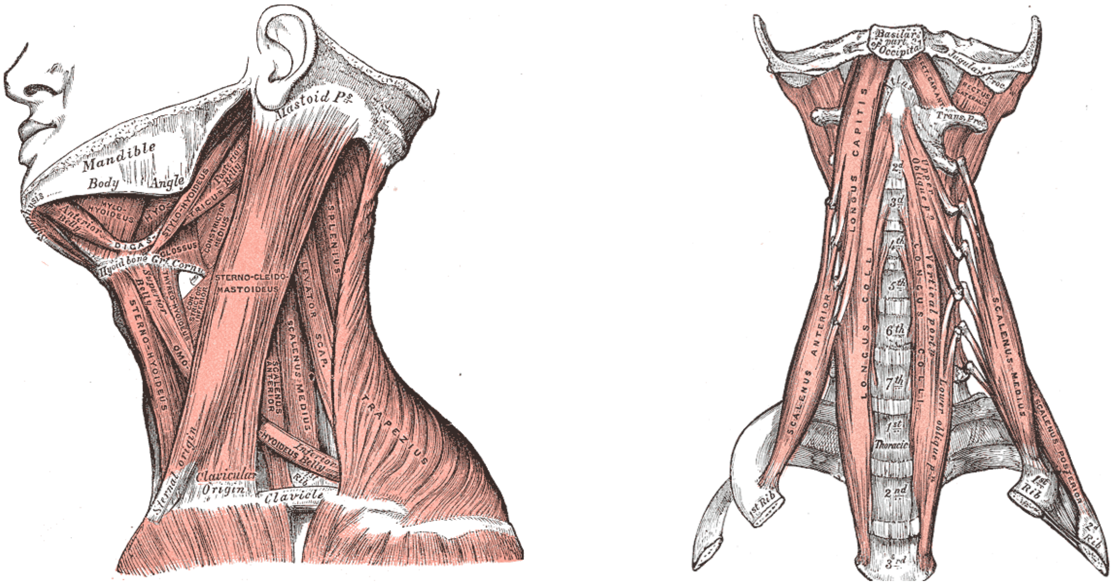

(a)

(b)

Figure 2-6: Muscles of the neck: (a) superficial, lateral prevertebral, suprahyoid, and infrahyoid, and (b) anterior prevertebral [5].

Surgical Treatment for Cervical Spondylosis

Overview

Reduction in disc height, disc bulging or herniation (Figure 2-7), osteophyte formation, spinal stenosis, and facet arthrosis are all forms of cervical spondylosis which may lead to axial neck pain, radiculopathy and/or myelopathy [6]. When nonoperative treatment fails to adequately relieve these symptoms, surgical decompression may be required. Using an anterior surgical approach to access the cervical spine allows cervical decompression of both the spinal cord and nerve roots [7]. A lateral, transverse incision is made at the affected level of the neck and platysma muscle is divided [8]. The deep fascial planes are carefully dissected, separating the carotid sheath laterally and trachea medially (Figure 2-8). The anterior vertebral column is then located through blunt finger dissection. The prevertebral fascia is dissected and longus colli muscles separated from the anterolateral aspect of the VBs. A discectomy is then performed which includes removal of the IVD, ALL, and any osteophytes. The void between the adjacent VBs is filled with either a fusion graft or CTDR.

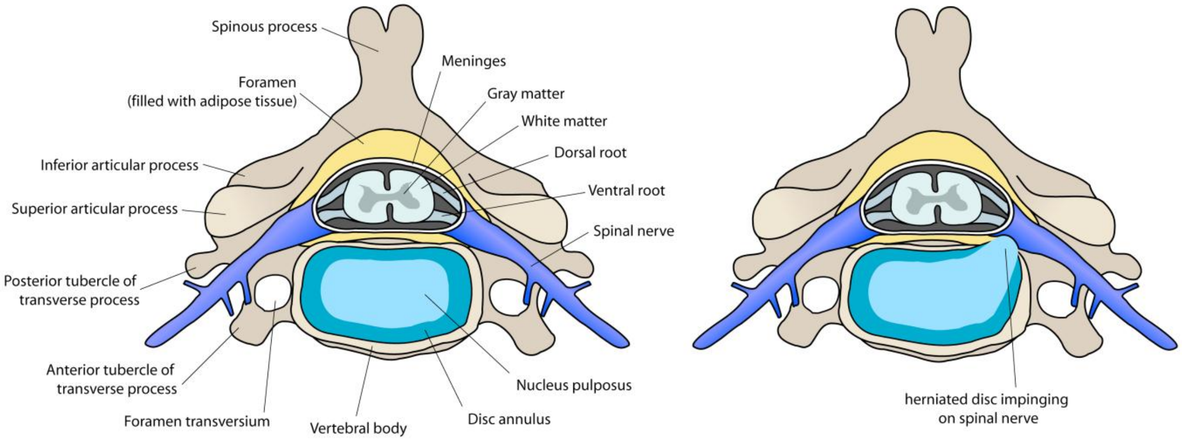

Figure 2-7: Herniated IVD impinging on a spinal nerve [9].

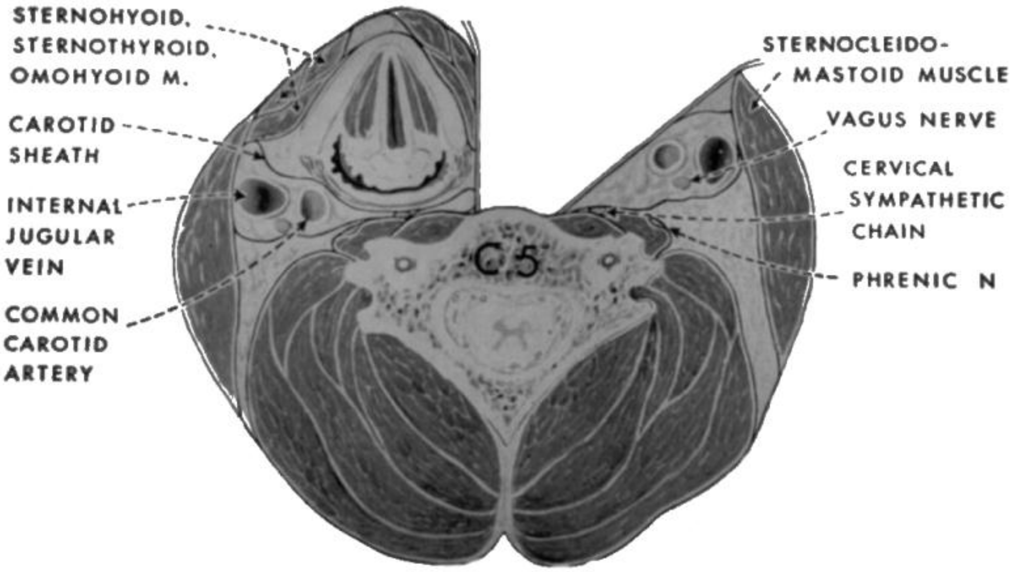

Figure 2-8: Cross section of the anterior surgical approach to the cervical spine (used with permission [10]).

Cervical Arthrodesis

Cervical arthrodesis is the primary surgical intervention for cervical degenerative disc disease [10-14]. After cervical decompression is completed, an autograft, allograft, or synthetic graft is implanted into the disc space. An anterior cervical plate provides rigid fixation between adjacent vertebra, increasing both cervical stability and fusion rate [8]. Patients are typically allowed to begin physical therapy, including range-of-motion (ROM) and strength exercises, 6-weeks postop. While most patients are allowed to return to full activity 3-months postop, complete fusion takes from 6-months to a year [8, 15].

Cervical Arthroplasty

The first artificial discs, metal balls, were introduced the second half of the 19th century. While Fenstrom is typically credited with being the first to attempt arthroplasty of the spine, there were similar attempts made by other surgeons [16-18]. Only four CTDRs are currently approved for use by the FDA. Both the Prestige ST (Medtronic, Memphis, TN) and the ProDisc-C (Synthes Spine, Paoli, PA) were approved in 2007, the BRYAN (Medtronic, Memphis, TN) in 2009, and the Mobi-C (LDR Médical, Troyes, France) in 2013. The characteristics of these CTDRs, along with others currently in clinical trials, are described in Table 2-1 in terms of design, material construct, degrees-of-freedom (DOF), center of rotation (COR), mobility, and fixation technique. The design is described as the number of pieces, joint type, and articulation type. The material description covers both the endplates and any insert or nucleus. Degrees-of-freedom are described as rotational and direction-dependent translational, and the COR as either mobile or fixed. Fixation technique includes press-fit methods and any additional hardware used to secure the CTDR to the adjacent vertebrae. Typically a titanium (Ti) coating is applied to the endplate of the CTDR to promote bone ingrowth.

Only the Prestige ST and ProDisc-C were evaluated in this dissertation research. The Prestige ST is a 2-piece, ball-and-trough design with one point of articulation (Figure 2-9). This stainless steel, metal-on-metal implant is capable of three-axis rotation and pure anteroposterior (AP) translation, allowing for a mobile, instantaneous COR. Vertebral body screws are used to secure the implant to the adjacent VBs. The ProDisc-C is a 3-piece, ball-and-socket design with one point of articulation (Figure 2-10). The endplates are constructed of cobalt-Chromium-molybdenum (CoCrMo) and the polymer insert of ultra-high-molecular-weight polyethylene (UHMWPE), creating a metal-on-polymer joint. Only three-axis rotation is preserved, creating a fixed COR. The CTDR is press-fit between adjoining vertebrae, with central keels implanted into the adjacent VBs.

Table 2-1: Currently available CTDRs. Only the BRYAN, Mobi-C, Prestige ST, and ProDisc-C CTDRs are FDA approved devices.

Implant	Company	Design	Material	DOF	COR	Fixation
BRYAN	Medtronic (Memphis, TN)	3-Piece, Biarticular Core	Ti-alloy, Polyurethane, Metal-on-Polymer	Rotation, AP/Lat Translation	Mobile	Press-fit
Mobi-C	LDR Médical (Troyes, France)	3-Piece, Biarticular	CoCrMo, UHMWPE, Metal-on-Polymer	Rotation, AP/Lat Translation	Mobile	Teeth
Prestige ST	Medtronic (Memphis, TN)	2-Piece, Ball-and-Trough, Uniarticular	Stainless-Steel, Metal-on-Metal	Rotation, AP Translation	Mobile	VB Screws
ProDisc-C	Synthes Spine (Paoli, PA)	3-Piece, Ball-and-Socket, Uniarticular	CoCrMo, UHMWPE, Metal-on-Polymer	Rotation	Fixed	Central Keel
Cerpass	NuVasive (San Diego, CA)	2-Piece, Ball-and-Socket, Uniarticular	Ti-alloy, Ceramic, Metal-on-Ceramic	Rotation	Fixed	Press-fit
CerviCore	Stryker Spine (Allendale, NJ)	2-Piece, Saddle-Shaped-Ball-and-Socket, Uniarticular	CoCrMo, Metal-on-Metal	Rotation	Semi-Mobile	Fins
Discovery	DePuy Spine (Raynham, MA)	2-Piece, Ball-and-Socket, Uniarticular	CoCrMo, UHMWPE, Metal-on-Polymer	Rotation	Fixed	Teeth
Kineflex|c	Spinal Motion (Mountainview, CA)	3-piece, Biarticular Core	CoCrMo, Metal-on-Metal	Rotation AP/Lat Translation	Mobile	Central Keel
M6	Spinal Kinetics (Sunnyvale, CA)	3-Piece, Compressible Core, Biarticular	Ti, Polymer Nucleus, Metal-on-Polymer	Rotation AP/Lat Translation	Mobile	Keels
PCM	NuVasive (San Diego, CA)	Ball-and-Socket, Uniarticular, (several types)	CoCrMo, UHMWPE, Metal-on-Polymer	Rotation	Fixed	Press-fit, Surface Ridges, VB Screws
Prestige LP	Medtronic (Memphis, TN)	2-Piece, Ball-and-Trough, Uniarticular	Ti-ceramic composite, Metal-on-Metal	Rotation, AP Translation	Mobile	Rails
SECURE-C	Globus Medical (Audubon, PA)	3-Piece, Biarticular, Spherical Superior Surface, Cylindrical Inferior Surface	CoCrMo, UHMWPE, Metal-on-Polymer	Rotation, AP Translation	Mobile	Central Keel


(a) (b) (c)

Figure 2-9: Prestige ST: (a) anterior view, (b) lateral cross-sectional view, and (c) implanted at the C5-6 level.

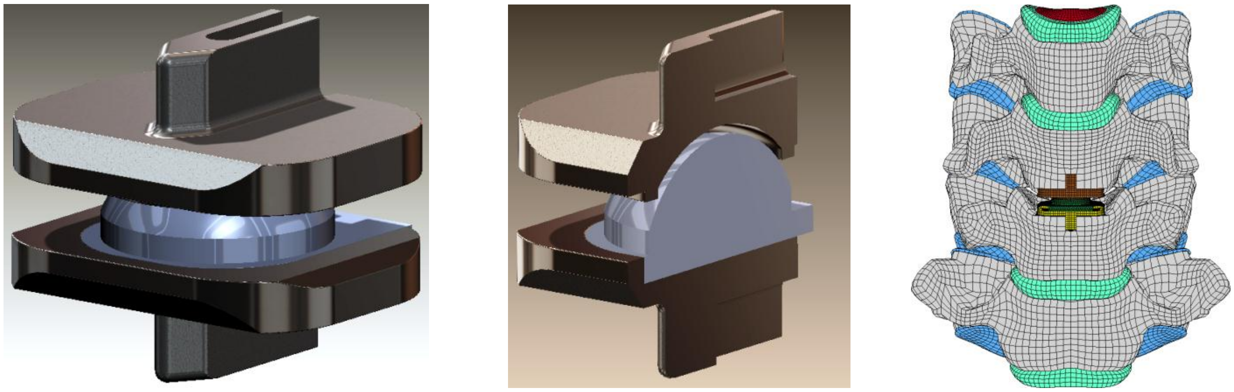
(a) (b) (c)

Figure 2-10: ProDisc-C: (a) anterior view, (b) lateral cross-sectional view, and (c) implanted at the C5-6 level.

Neck Injury Biomechanics

Overview

In order to discuss neck injury biomechanics, a common lexicon must be established with regards to neck loading relative to head and chest motion. Relative motion corresponding to positive polarity for neck force and moment is illustrated in Figure 2-11, Figure 2-12, and Figure 2-13. Neck loading modes are further illustrated on the skeletal level in Figure 2-14. This loading convention is based on SAE J211 standards used in the automobile safety industry [19].

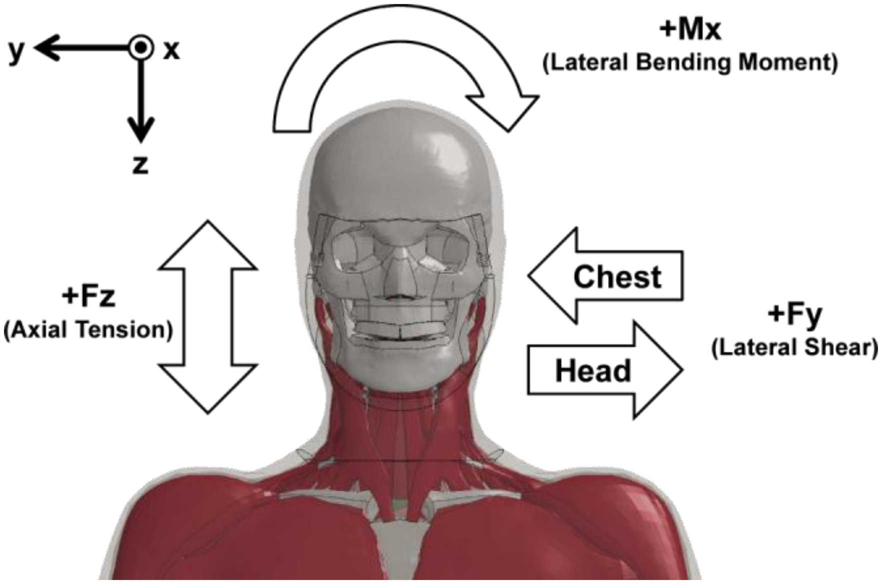

Figure 2-11: Relative head and chest motion corresponding to positive neck lateral shear force, axial force, and lateral bending moment.

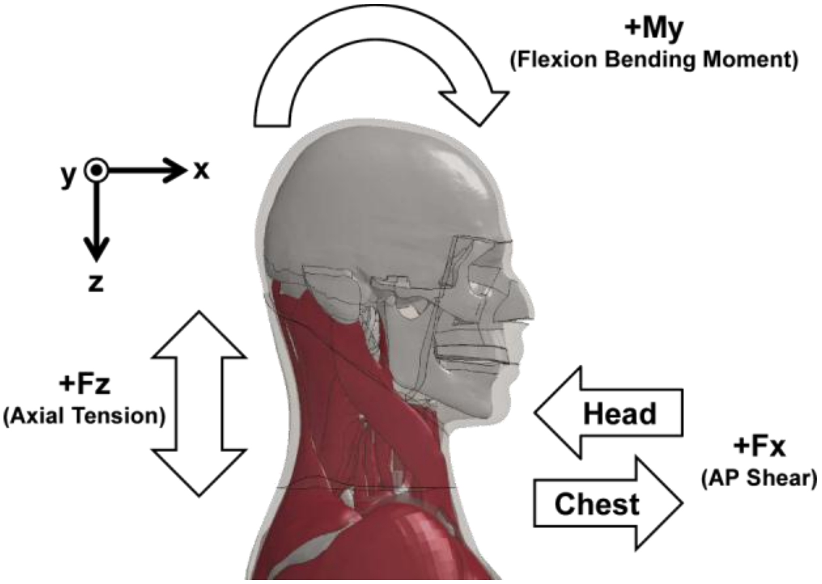

Figure 2-12: Relative head and chest motion corresponding to positive neck AP shear force, axial force, and lateral flexion bending moment.

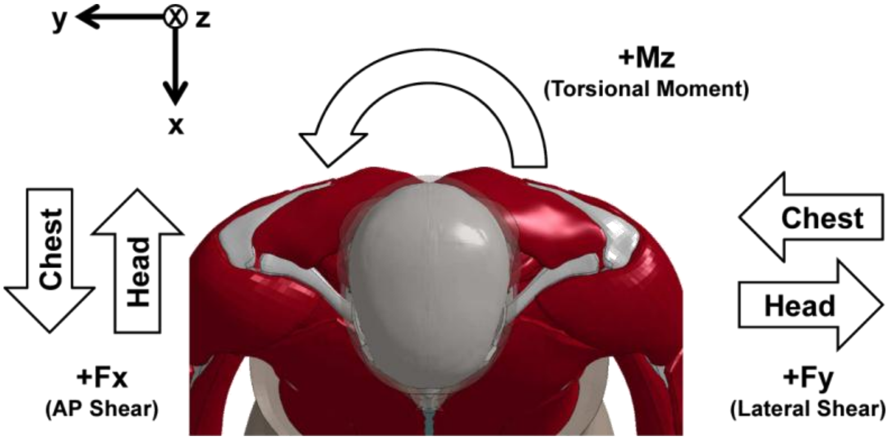

Figure 2-13: Relative head and chest motion corresponding to positive neck AP shear force, lateral shear force, and torsional bending moment.

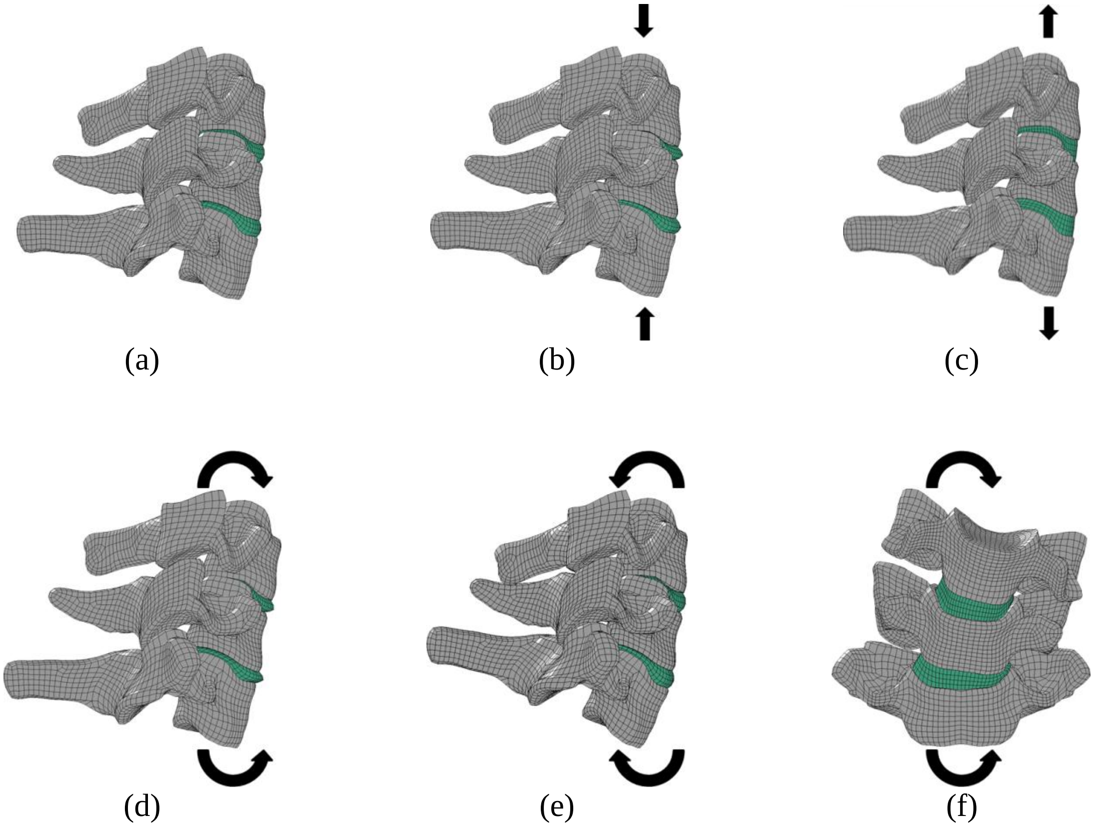

Figure 2-14: Neck loading modes for (a) no loading, (b) compression, (c) tension, (d) flexion, (e) extension, and (f) lateral bending. AP shear and torsion are not shown.

Both volunteer and cadaver testing have been previously conducted to determine injury threshold for a variety of quasi-static and dynamic neck loading modes [20, 21]. Injury assessment reference values (IARVs) have also been defined for different loading modes and are incorporated into government crash safety standards [22-25]. A variety of neck injury criteria have also been established to understand the risk of neck injury during different loading modes and are concisely described by Schmitt et al. [21] . These criteria include the NIC, N_{ij}, N_{km}, LNL, as well as time-dependent duration criteria. The majority of these neck injury thresholds and criteria were developed specifically for the automotive community. However, other thresholds and criteria have been developed for military use, in which vertical loading is much more prominent [26-28].

Anthropomorphic Test Devices

The Hybrid III 50th percentile male Anthropomorphic Test Device (ATD) was developed as a biofidelic surrogate to study occupant protection in frontal and rear motor vehicle collisions [29]. The Hybrid III ATD neck, while designed to produce a biofidelic mechanical response during frontal impacts, does not include the anatomical complexity of the human neck, nor does it try to incorporate the effects of muscle response. The natural lordotic curvature of the human cervical spine is not replicated in the ATD neck. Another difference in spinal curvature exists in the lumbar spine, which is curved in the Hybrid III ATD. Other ATDs with more accurate lumbar spine orientation exist for aviation crash testing, such as the Hybrid II and FAA Hybrid III ATDs [30].

The neck of the ATD is a single-piece elastomer component with three interleaving aluminum disc elements and two aluminum end plates [31]. Rotation of the head occurs about a pin-joint, representing the approximate location of the OC-C1 interface, on the cephalic endplate. A pair of nodding blocks on this endplate limits the head flexion and extension. Axial tension of the neck is augmented through a central steel cable while compression is predominantly the product of the compressive properties of the elastomer. The different flexion and extension response of the neck are due to the asymmetrical cross-sectional geometry and three anterior slits built into the geometry of the elastomer. Both the upper neck and lower neck are instrumented with a single six-degree-of-freedom load cell, allowing for forces and moments to be calculated at the occipital condyle and the base of the neck.

Global Human Body Models Consortium 50th Percentile Male Model

This dissertation research used the Global Human Body Models Consortium 50th percentile male model (v3.5), a high fidelity human body model specifically designed for crash simulation. Composed of 1.3 million nodes, 1.95 million elements, and 847 parts, this FE model is the product of a team of research universities from around the world [32]. The neck is comprised of over 25,000 deformable elements composing the seven cervical vertebrae, IVDs, ligaments, musculature, and soft tissue. The geometry of the neck was developed at Wake Forest University (WFU) School of Medicine [33] and further developed into an FE model at the University of Waterloo in Ontario, Canada. The biofidelity of the neck has been rigorously validated both at individual cervical segment levels and for the full cervical spine Table 2-2 [34-37]. Additionally, whole body validation has been conducted for a number a different impact scenarios [38-41]. Simulations were run with LS-DYNA (R4.2.1, LSTC, Livermore, CA) on the Wake Forest University DEAC Cluster, a high performance computing (HPC) environment. The

DEAC Cluster is a heterogeneous collection of 238 64-bit Intel Xeon based computational nodes, containing over 11.4TB of RAM and 100TB of disk storage.

Table 2-2: Validation of the GHBMC neck model per the manual [32].

Validation Level	Type of Loading	Specific Load Case	Evaluation Criteria	Primary Literature Reference	Supplemental Literature Reference
Cervical Segment	Physiological ROM (non-injurious loading)	Axial Rotation	Vertebral Angular Rotation	[42-44]	
		Lateral Bending	Vertebral Angular Rotation	[43, 44]	[45]
		AP Shear	Stiffness Response	[46, 47]	
		Flexion/Extension	Flexion/Extension Angular Rotation	[43, 44, 48-51]	[4, 45, 52]
		Compression	Force/Displacement	[46, 47]	[53, 54]
		Tension	Force/Displacement	[46, 47, 55]	[56, 57]
	Traumatic Loading	Tension	Force/Displacement Vertebral Fracture, Disc Injury, Ligament Injury	[55]	
		Compression	Force/Displacement Vertebral Fracture, Disc Injury, Ligament Injury	[58]	[45]
		Flexion/Extension	Flexion/Extension Angular Rotation Disc Injury, Ligament Injury	[49, 50]	
Full Cervical Spine	Lateral	7g Kinematics	Head CG	[59]	
	Frontal Crash	8g Kinematics	Head CG	[60]	[59, 61]
		15g Kinematics	Head CG	[60]	[59, 61]
		Injury Prediction	Ligament Strain	[62]	
			IVD Shear Strain	[63]	
	Rear Impact	4g Kinematics	Head Response	[64, 65]	
		7g Kinematics	Head Response	[66]	[67, 68]
		Injury Prediction	IVD	[69]	
			Ligament Strain	[70, 71]	[72]
		Rotated Head Kinematics	Intervertebral Rotation	[73]	
	Tension	Tension		[55]	

Rotary-Wing Aircraft Crashworthiness

Experimental Crash Testing

Since the 1970s, full-scale crash tests of rotary-wing aircraft have been conducted at the Impact Dynamics Research Facility (IDRF) located at the NASA Langley Research Center (Hampton, VA) [74]. Many of these full-scale helicopter tests evaluated the effectiveness of energy absorption systems, crew restraint systems, and occupant response [74-82]. While these full-scale experiments are extremely valuable in evaluating the crashworthiness of a rotary-wing aircraft, they are costly and complex. When seat and occupant response are of primary interest, an alternative experimental approach is to mount the fuselage or seat directly to a crash sled and apply an acceleration or deceleration pulse comparable to an actual crash pulse. Several sled test experiments have been previously conducted, with cadavers or ATDs, in an effort to study seat response and occupant protection during a simulated rotary-wing aircraft crash [26, 27, 83-88].

Between 1979 and 1985, a series of 15 cadaver sled tests were conducted at the Wayne State University Bioengineering Center (Detroit, MI) to determine the load threshold of spinal injury during simulated helicopter crashes [84, 85]. The majority of the tests used a production UH-60A Black Hawk crew seat with energy absorber limit-load factor between 8.6 and 14.5 g. These non-helmeted cadavers were secured to the seat with the five-point restraint system pre-tensioned to approximately 133.4 N. The seat was pitched forward either 17° or 34° with respect to the velocity vector and subjected to a triangular deceleration sled pulse with 12.8 m/s delta-V. Upon test completion, the vertebral column was excised for each cadaver and compression tests were conducted to determine the ultimate compression strengths of the various vertebrae. As direct loading of the spine could not be obtained from the cadavers, complimentary ATD sled tests were conducted to estimate cadaveric lumbar spine loading. The spinal load to strength ratio

(SLSR) was then calculated from complimentary cadaver and ATD tests as the quotient of applied axial spinal load measured from the ATD lumbar spine to the ultimate compressive strength of the cadaver L5 vertebra. The magnitude of the SLSR was found to correlate with the rate of spinal injury. A method to correlate spinal injury rate and energy absorber limit-load was developed from this relationship. It was recommended that the 14.5 g energy absorber load-limit on existing U.S. Army aircraft seats be retained since this limit correlated to a 20% spinal injury rate.

Under the direction of the U.S. Army Aeromedical Research Laboratory (USAARL), the Federal Aviation Administration's (FAA) Civil Aeromedical Institute (Oklahoma City, OK) conducted a series of 8 deceleration sled tests in 1988 using an OH-58 helicopter fuselage [83, 86]. The sled pulse delta-V ranged between 7.2 and 10.9 m/s and the fuselage orientation varied between 0° and 90° pitch-down. A helmeted 50th and 95th percentile ATD were positioned in the right and left cockpit seats, respectively, and belted with the inertia reels set to the unlocked condition. In two test conditions, the larger ATD was removed and the fuselage was oriented with a 15° right yaw. The purpose of these tests was two-fold: to evaluate the effectiveness of a new energy absorption seat in mitigating back injury, and to study potential head impact with a new pilot display unit (PDU). It was concluded that the new seat design absorbed more energy than the existing seat, decreasing vertical loading to the lumbar spine. Additionally, helmeted head to PDU impact did not produce injurious levels of head acceleration or neck loading.

Four series of head-supported mass (HSM) tests were performed between 2002 and 2004 at the University of Virginia Center for Applied Biomechanics (Charlottesville, VA), also under the auspices of USAARL [26, 27]. The purpose of these tests was to investigate the effects of HSM on cervical spine injury during experimentally simulated rotary-wing aircraft crashes and to subsequently develop a new injury criterion for the lower neck. Head-neck component and whole-body experiments were conducted with cadavers and two types of ATDs: the Hybrid III 50th percentile male and the THOR-alpha. A halo device was attached to the head of each surrogate, allowing for HSM to be added in the form of weights at varying distances from the head center of gravity (CG). For the component tests, the head-neck complexes were suspended from the underside of a mini-sled with the neck angled -45°, 0°, 15°, 30° or 45° from the horizontal. The HSM varied between 0.0 and 4.0 kg and was located between 0 and 118 mm superior to the head CG. The mini-sled was accelerated with a pneumatic impactor, producing a maximum velocity between 1.70 and 6.96 m/s. The whole-body sled tests were conducted with surrogates secured with a five-point restraint system to a seat fixture angled 30° from the horizontal. The HSM varied between 0.0 and 2.0 kg and was located at the head CG. A triangular deceleration profile representative of a rotary-wing aircraft crash was imparted to the sled, producing a delta-V between 9.3 and 13.3 m/s. The kinematic responses of the head and neck during these sled tests were reported to be noticeably different between the cadaver, Hybrid III, and THOR. The most prominent visual difference in kinematics was noted in the shear motion of the head relative to the torso between the cadaver and Hybrid III. Post-test necropsies were conducted for all cadaver tests with neck injuries assigned a Maximum Abbreviated Injury Score (MAIS) [89]. The majority of both component and whole-body injuries were to the posterior ligaments of the cervical spine, predominantly occurring between C5 and T2. A new lower neck injury criterion, the Beam Criterion, was subsequently developed predicting a 50% risk of at least a moderate injury at unity.

In 2004, an extensive series of sled tests was performed at the Naval Air Warfare Center (NAWC) Aircraft Division Horizontal Accelerator facility (Patuxent River, MD) to study neck kinematics resulting from rotary-wing aircraft crashes [87, 88]. The aviator size, helmet mass properties, and impact severity were varied for each of the 43 sled tests. A Hybrid III ATD 50th percentile male, 95th percentile male, and 5th percentile female were used as aviator surrogates, each with a custom head fixture. The mass properties, representing different helmet configurations, were simulated by directly bolting weights to different holes in these fixtures. Each test was run using a low, medium, or high-severity sled pulse corresponding to a delta-V of 7.6, 9.6 or 15.2 m/s, respectively. These crash pulses were based on existing 30° pitch-down seat qualification crash corridors and were representative of the seat pan acceleration of an energy-absorbing seat. A generic five-point restraint system, pre-tensioned between 160 and 195 N, secured the ATD to a rigid seat. Neck loading, head acceleration, and chest acceleration were reported for each test. The likelihood of injury to the upper and lower cervical spine was evaluated using both a modified version of the Neck Injury Criteria (N_{ij}) [90-92] and load duration limits for neck tension, compression, and AP shear [23]. Statistical analysis revealed that the additional head mass did not have a significant effect on the neck response. However, sled pulse severity and ATD size for a given sled pulse severity were found to have a significant effect on most neck parameters.

Crash Modeling and Simulation

Computational modeling has been used to evaluate aircraft crashworthiness, particularly helicopter crashworthiness, for close to four decades [74, 93-96]. In the early 1970s, the Lockheed-California Company released KRASH, a kinematic lumped parameter computer program developed to simulate helicopter structural response during simulated crashes [95, 97-100]. Initially sponsored by the U.S. Army, further development of the program was sponsored by the FAA [101]. During the same time period, the Grumman Aerospace Corporation developed the program DYCAST (DYnamic Crash Analysis of STructures) with the support of NASA and the FAA [102]. This nonlinear structural finite element program was capable of both implicit and explicit time integration [103]. DYCAST has been used to study the structural crashworthiness of both rotary and fixed-wing aircrafts [104-106].

With support from the FAA, the computer program SOM-LA (Seat/Occupant Model – Light Aircraft) was developed by Simula Inc. in the late 1970s to study aircraft seat and occupant response in a crash environment [107, 108]. This program consisted of a 12-segment lumped parameter occupant with an implicit finite element model seat structure. It was used extensively to evaluate occupant response in an energy-absorbing helicopter seat during a simulated impact [107-110]. A modified version of the program, SOM-TA (Seat/Occupant Model – Transport Aircraft) was later developed with more complex seat structure capable of seating 2-3 passengers of different sizes [108, 111].

The Articulated Total Body (ATB) model, a dynamic-linkage system supported in part by the Air Force Research Laboratory (AFRL), was developed to predict gross body motion during simulated dynamic impacts [112]. While primarily used to model automobile collisions and aircraft ejection with windblast exposure, the ATB model has been used by USAARL to study occupant response during simulated helicopter crashes. In particular, several studies have investigated the effects of HSM and multi-airbag restraints on head and neck response during these simulations [113-118]. A more advanced multi-body model program, MADYMO (MAthematical DYnamic Models, TNO, Netherlands), has also been used to predict neck injuries from HSM during simulated helicopter crashes [119]. Preliminary MADYMO simulations were also used in the development of a series of experimental sled tests conducted by the NAWC to evaluate risk of neck injury from HSM in helicopter crashes [87, 88].

Most of the more recent helicopter crash simulation studies used explicit time integration FE programs, including MSC.Dytran (MSC Software Corporation, Santa Ana, CA) and LS-DYNA (LSTC, Livermore, CA) [95]. These codes allow for analysis of high-speed, dynamic impacts involving large deformations. The U.S. Army Research Laboratory (ARL) converted an MSC.Nastran modal-vibrations model of an Advanced Composite Airframe Program (ACAP) helicopter into an MSC.Dytran model for use in full-scale helicopter crash simulations [120]. The predicted responses of the overall aircraft structure, landing gear, floor, and occupant seats were compared to the experimental results of a full-scale helicopter crash [121-124]. The majority of the FE occupant response studies utilized LS-DYNA. The Polytechnic University of Milan simulated a previously reported experimental sled test of an energy absorbing helicopter seat using both a generic and an FAA Hybrid III ATD FE model [125]. The difference in lumbar curvature between the two models appeared to greatly affect both lumbar loading and upper seat stroke. Vertical drop testing of a WASP helicopter skid gear was experimentally conducted and modeled by NASA using two Hybrid III 95th percentile ATDs seated on different foam padding [126, 127]. The occupant response validation included both pelvic and chest accelerations. NASA also conducted two full-scale MD-500 helicopter crash tests, with and without a composite deployable energy absorber located on the underbody of the aircraft [128-130]. Both of these tests were simulated in LS-DYNA with the four occupants modeled as Hybrid III 50th percentile males, one with a modified human torso. While structural response took priority in these studies, experimental and predicted lumbar loading of the pilot and passenger were compared [128]. Vertical seat drop tests have also been conducted with the THOR-NT advanced crash test dummy and subsequently simulated with both a THOR-NT and THUMS (Toyota Human Model for Safety) FE model [131]. While neck loading was comparable between both the ATD and human models, a greater degree of bending in the mid-sagittal plane was observed for the THUMS model, attributed to flexibility of the spinal column.

Due to the time and cost associated with experimental aircraft crashworthiness testing, the concept of certification by computational analysis has become more appealing to both the FAA and aircraft manufactures. In 2003, the FAA released Advisory Circular 20-146, which provides guidance on aircraft seat compliance demonstration through computation modeling [132]. A baseline seat model must first be validated against dynamic experimental tests, meeting a set of general and application-specific validation criteria. As this process is subjective in nature, the FAA stressed the importance of “good engineering judgment” when interpreting the validation results. This validated seat model may then be used in support of dynamic testing to determine critical loading scenarios or in lieu of dynamic testing when incremental changes have been made to the seat design. Application of the certification by analysis approach, including the details behind initial validation of a baseline aircraft seat model, has been previously reported [133, 134]. Jackson et al. [95] discussed the potential of crash certification by analysis as it applies to military helicopter design. The authors recommend, at minimum, one full-scale experimental crash test for crashworthiness qualification purposes, with the results used to validate an FE model. This validated model is to then be used merely as a tool to further evaluate the crashworthiness of the aircraft design.

Conclusions

The use of FE modeling to evaluate rotary-wing aircraft crashworthiness is becoming more prevalent. This valuable tool can also be used to evaluate occupant response, particularly neck response, during a rotary-wing aircraft impact. Military pilots suffering from cervical degeneration may require surgical intervention that can potentially alter neck biomechanics during such an impact. It is important to understand how the surgically altered neck would respond and to assure that these military personnel are not placed at a higher risk of neck injury. The purpose of this dissertation is to evaluate the effects of surgical treatment for cervical spondylosis on neck response during a simulated frontal automobile impact and survivable rotary-wing aircraft impact.

Chapter 2 References

[1] Moskovich R. Biomechanics of the Cervical Spine. In: Nordin M, Frankel VH, Leger D, editors. Basic Biomechanics of the Musculoskeletal System. 4 ed. Philadelphia: Lippincott Williams & Wilkins; 2012. p. 286-321.

[2] Moore KL, Agur AMR. Essential Clinical Anatomy. Second ed. Philadelphia: Lippincott Williams & Wilkins; 2002.

[3] Okubo K, Anatomography, Database Center for Life Science,
Web. <http://en.wikipedia.org/wiki/File:Cervical_vertebrae_lateral2.png>.

[4] White AA, Panjabi MM. Clinical Biomechanics of the Spine. 2 ed. Philadelphia: Lippincott Williams & Wilkins; 1990.

[5] Gray, H, Anatomy of the Human Body. Philadelphia: Lea & Febiger, 1918; Bartleby.com, 2000. Web <www.bartleby.com/107/>.

[6] Schoenfeld AJ, Bobo CM. Degenerative Disease. In: Benzel EC, editor. The Cervical Spine. 5th ed. Philadelphia, PA: Lippincott Williams & Wilkins; 2012. p. 885-96.

[7] Matan AJ, Connolly PJ. Concepts of Cervical Decompression. In: Herkowitz HN, editor. The Cervical Spine Surgery Atlas. 2nd ed. Philadelphia, PA: Lippincott Williams & Wilkins; 2004. p. 123-38.

[8] Majid K, Fischgrund JS. Anterior Cervical Discectomy and Fusion (ACDF). In: Benzel EC, editor. The Cervical Spine. 5th ed. Philadelphia, PA: Lippincott Williams & Wilkins; 2012. p. 956-63.

[9] Debivort. Annotated Diagram of Preconditions for Anterior Cervical Discectomy and Fusion. Web. <http://en.wikipedia.org/wiki/File:ACDF_coronal_english.png>.

[10] Bailey RW, Badgley CE. Stabilization of the Cervical Spine by Anterior Fusion. The Journal of bone and joint surgery American volume. 1960;42-A:565-94.

[11] Cloward RB. The Anterior Approach for Removal of Ruptured Cervical Disks. Journal of neurosurgery. 1958;15:602-17.

[12] Fallah A, Akl EA, Ebrahim S, Ibrahim GM, Mansouri A, Foote CJ, et al. Anterior Cervical Discectomy with Arthroplasty Versus Arthrodesis for Single-Level Cervical Spondylosis: A Systematic Review and Meta-Analysis. PloS one. 2012;7:e43407.

[13] Mummaneni PV, Amin BY, Wu JC, Brodt ED, Dettori JR, Sasso RC. Cervical Artificial Disc Replacement Versus Fusion in the Cervical Spine: A Systematic Review Comparing Long-Term Follow-up Results from Two FDA Trials. Evidence-based spine-care journal. 2012;3:59-66.

[14] Smith GW, Robinson RA. The Treatment of Certain Cervical-Spine Disorders by Anterior Removal of the Intervertebral Disc and Interbody Fusion. The Journal of bone and joint surgery American volume. 1958;40-A:607-24.

[15] Hsu W. Personal Communication: Cervical Arthrodesis. In: White NA, 2013.

[16] Fernstrom U. Arthroplasty with Intercorporal Endoprothesis in Herniated Disc and in Painful Disc. Acta chirurgica Scandinavica Supplementum. 1966;357:154-9.

[17] Reitz H, Joubert MJ. Intractable Headache and Cervico-Brachialgia Treated by Complete Replacement of Cervical Intervertebral Discs with a Metal Prosthesis. South African medical journal = Suid-Afrikaanse tydskrif vir geneeskunde. 1964;38:881-4.

[18] McKenzie AH. The Basis for Motion Preservation Surgery: Lessons Learned from the Past. In: Yue JJ, Bertagnoli R, McAfee P, An HS, editors. Motion Preservation Surgery of the Spine: Advanced Techniques and Controversies. Philadelphia: Saunders; 2008.

[19] Society of Automotive Engineers. SAE J211/1 - Instrumentation for Impact Test-Part 1-Electronic Instrumentation. 2007.

[20] McElhaney J, Nightingale R, Winkelstein B, Chancey V, Myers B. Biomechanical Aspects of Cervical Trauma. In: Nahum A, Melvin J, editors. Accidental Injury: Biomechanics and Prevention. New York: Springer; 2002. p. 324-73.

[21] Schmitt K-U, Niederer P, Muser M, Walz F. Trauma Biomechanics: Accidental Injury in Traffic and Sports. 3rd ed. New York: Springer; 2010.

[22] Eppinger R, Sun E, Kuppa S, Saul R. Development of Improved Injury Criteria for the Assessment of Advanced Automobile Restraint Systems - II. NHTSA Docket No. 2010-03-19. 2000.

[23] Mertz HJ, Irwin AL, Prasad P. Biomechanical and Scaling Bases for Frontal and Side Impact Injury Assessment Reference Values. Stapp car crash journal. 2003;47:155-88.

[24] NHTSA. Title 49 Code of Federal Regulations (CFR) Part 571 Section 208, Occupant Crash Protection. Washington, DC: Office of the Federal Register, National Archives and Records Administration; 2008.

[25] NHTSA. Title 49 Code of Federal Regulations (CFR) Part 571 Section 214, Side Impact Protection. Washington, DC: Office of the Federal Register, National Archives and Records Administration; 2008.

[26] Bass CR, Donnellan L, Salzar R, Lucas S, Folk B, Davis M, et al. A New Neck Injury Criterion in Combined Vertical/Frontal Crashes with Head Supported Mass. International Research Council on Biomechanics of Injury. Madrid, Spain. 2006.

[27] Bass CR, Salzar R, Donnellan L, Lucas H. Injury Risk from HSM Loading (HM 2,3,4,5 Series). Charlottesville, VA.: University of Virginia Center for Applied Biomechanics. Report HEADMASS2. 2004.

[28] Nichols JP. Overview of Ejection Neck Injury Criteria. Forty Fourth Annual SAFE Association Symposium. Reno, NV. 2006.

[29] Mertz HJ. Anthropomorphic Test Device. In: Nahum A, Melvin J, editors. Accidental Injury: Biomechanics and Prevention. New York: Springer; 2002.

[30] Pellettiere J, Moorcroft D, Olivares G. Anthropomorphic Test Dummy Lumbar Load Variation. 22nd Enhanced Safety of Vehicles Conference. Washington, DC. 2011.

[31] Foster J, Kortge J, Wolanin M. Hybrid III-a Biomechanically-Based Crash Test Dummy. SAE Technical Paper 770938. 1977.

[32] Stitzel JD. Global Human Body Models Consortium (GHBMC) Male 50th Percentile (M50) Occupant Model Manual. Virginia Tech – Wake Forest University Center for Injury Biomechanics; 2011.

[33] Gayzik FS, Moreno DP, Geer CP, Wuertzer SD, Martin RS, Stitzel JD. Development of a Full Body CAD Dataset for Computational Modeling: A Multi-Modality Approach. Annals of biomedical engineering. 2011;39:2568-83.

[34] DeWit JA, Cronin DS. Cervical Spine Segment Finite Element Model for Traumatic Injury Prediction. Journal of the mechanical behavior of biomedical materials. 2012;10:138-50.

[35] Fice JB, Cronin DS. Investigation of Whiplash Injuries in the Upper Cervical Spine Using a Detailed Neck Model. Journal of biomechanics. 2012;45:1098-102.

[36] Fice JB, Cronin DS, Panzer MB. Cervical Spine Model to Predict Capsular Ligament Response in Rear Impact. Annals of biomedical engineering. 2011;39:2152-62.

[37] Mattucci SF, Moulton JA, Chandrashekar N, Cronin DS. Strain Rate Dependent Properties of Younger Human Cervical Spine Ligaments. Journal of the mechanical behavior of biomedical materials. 2012;10:216-26.

[38] Gayzik FS, Moreno DP, Vavalle NA, Rhyne AC, Stitzel JD. Development of a Full Human Body Finite Element Model for Blunt Injury Prediction Utilizing a Multi-Modality Medical Imaging Protocol. 12th Int'l LS-DYNA User Conf Dearborn, MI. 2012.

[39] Rhyne AC, Moreno DP, Vavalle NA, Stitzel JD, Galbusera F. Validation of Simulated Chestband Data in Frontal and Lateral Loading Using a Human Body Finite Element Model. Traffic Injury Prevention. 2013; IN PRESS.

[40] Vavalle NA, Jelen BC, Moreno DP, Stitzel JD, Gayzik FS. An Evaluation of Objective Rating Methods for Full-Body Finite Element Model Comparison to PMHS Tests. Traffic Inj Prev. 2013;14 Suppl:S87-94.

[41] Vavalle NA, Moreno DP, Rhyne AC, Stitzel JD, Gayzik FS. Lateral Impact Validation of a Geometrically Accurate Full Body Finite Element Model for Blunt Injury Prediction. Annals of biomedical engineering. 2013;41:497-512.

[42] Chang H, Gilbertson LG, Goel VK, Winterbottom JM, Clark CR, Patwardhan A. Dynamic Response of the Occipito-Atlanto-Axial (C0-C1-C2) Complex in Right Axial Rotation. Journal of orthopaedic research : official publication of the Orthopaedic Research Society. 1992;10:446-53.

[43] Goel VK, Clark CR, Gallaes K, Liu YK. Moment-Rotation Relationships of the Ligamentous Occipito-Atlanto-Axial Complex. Journal of biomechanics. 1988;21:673-80.

[44] Goel VK, Clark CR, Harris KG, Schulte KR. Kinematics of the Cervical Spine: Effects of Multiple Total Laminectomy and Facet Wiring. Journal of orthopaedic research : official publication of the Orthopaedic Research Society. 1988;6:611-9.

[45] Moroney SP, Schultz AB, Miller JA, Andersson GB. Load-Displacement Properties of Lower Cervical Spine Motion Segments. Journal of biomechanics. 1988;21:769-79.

[46] Panjabi MM, Summers DJ, Pelker RR, Videman T, Friedlaender GE, Southwick WO. Three-Dimensional Load-Displacement Curves Due to Forces on the Cervical Spine. Journal of orthopaedic research : official publication of the Orthopaedic Research Society. 1986;4:152-61.

[47] Shea M, Edwards WT, White AA, Hayes WC. Variations of Stiffness and Strength Along the Human Cervical Spine. Journal of biomechanics. 1991;24:95-107.

[48] Camacho DLA, Nightingale RW, Robinette JJ, Vanguri SK, Coates DJ, Myers BS. Experimental Flexibility Measurements for the Development of a Computational Head-Neck Model Validated for near-Vertex Head Impact. 41st Stapp Car Crash Conference. 1997.

[49] Nightingale RW, Carol Chancey V, Ottaviano D, Luck JF, Tran L, Prange M, et al. Flexion and Extension Structural Properties and Strengths for Male Cervical Spine Segments. Journal of biomechanics. 2007;40:535-42.

[50] Nightingale RW, Winkelstein BA, Knaub KE, Richardson WJ, Luck JF, Myers BS. Comparative Strengths and Structural Properties of the Upper and Lower Cervical Spine in Flexion and Extension. Journal of biomechanics. 2002;35:725-32.

[51] Wheeldon JA, Pintar FA, Knowles S, Yoganandan N. Experimental Flexion/Extension Data Corridors for Validation of Finite Element Models of the Young, Normal Cervical Spine. Journal of biomechanics. 2006;39:375-80.

[52] Panjabi MM, Crisco JJ, Vasavada A, Oda T, Cholewicki J, Nibu K, et al. Mechanical Properties of the Human Cervical Spine as Shown by Three-Dimensional Load-Displacement Curves. Spine. 2001;26:2692-700.

[53] Kopperdahl DL, Keaveny TM. Yield Strain Behavior of Trabecular Bone. Journal of biomechanics. 1998;31:601-8.

[54] Nightingale RW, McElhaney JH, Richardson WJ, Myers BS. Dynamic Responses of the Head and Cervical Spine to Axial Impact Loading. Journal of biomechanics. 1996;29:307-18.

[55] Dibb AT, Nightingale RW, Luck JF, Chancey VC, Fronheiser LE, Myers BS. Tension and Combined Tension-Extension Structural Response and Tolerance Properties of the Human Male Ligamentous Cervical Spine. Journal of biomechanical engineering. 2009;131:081008.

[56] Pintar FA, Yoganandan N, Sances Jr. A, Reinartz J, Harris G, Larson S. Kinematic and Anatomical Analysis of the Human Cervical Spine Column under Axial Loading. 33rd Stapp Car Crash Conference. 1989.

[57] Van Ee CA, Chasse AL, Myers BS. Quantifying Skeletal Muscle Properties in Cadaveric Test Specimens: Effects of Mechanical Loading, Postmortem Time, and Freezer Storage. Journal of biomechanical engineering. 2000;122:9-14.

[58] Carter DR, Hayes WC. The Compressive Behavior of Bone as a Two-Phase Porous Structure. The Journal of bone and joint surgery American volume. 1977;59:954-62.

[59] Wismans J, van Oorashot H, Woltring HJ. Omni-Directional Human Head-Neck Response. 30th Stapp Car Crash Conference 1986.

[60] Ewing CL, Thomas DJ. Human Head and Neck Response to Impact Acceleration, Monograph 21. Naval Aerospace Medical Research Laboratory; 1972.

[61] Thunnissen J, Wismans J, Ewing CL, Thomas DJ. Human Volunteer Head-Neck Response in Frontal Flexion: A New Analysis. 39th Stapp Car Crash Conference 1995.

[62] Panjabi MM, Ito S, Pearson AM, Ivancic PC. Injury Mechanisms of the Cervical Intervertebral Disc During Simulated Whiplash. Spine. 2004;29:1217-25.

[63] Ito S, Ivancic PC, Pearson AM, Tominaga Y, Gimenez SE, Rubin W, et al. Cervical Intervertebral Disc Injury During Simulated Frontal Impact. European spine journal : official publication of the European Spine Society, the European Spinal Deformity Society, and the European Section of the Cervical Spine Research Society. 2005;14:356-65.

[64] Davidsson J, Deutscher C, Hell W, Linder A, Lövsun P, Svensson M. Human Volunteer Kineamtics in Rear-End Sled Collisions. IRCOBI. Göteborg. 1998.

[65] Davidsson J, Deutscher C, Hell W, Lövsun P, Svensson M. Human Volunteer Kinematics in Rear-End Sled Collisions. Journal of Crash Prevention and Injury Control 2001;2:319-33.

[66] Deng B. Kinematics of Human Cadaver Cervical Spine During Low Speed Rear End Impacts: Wayne State University; 1999.

[67] Deng B, Begeman PC, Yang KH, Tashman S, King AI. Kinematics of Human Cadaver Cervical Spine During Low Speed Rear-End Impacts. Stapp car crash journal. 2000;44:171-88.

[68] Luan F, Yang KH, Deng B, Begeman PC, Tashman S, King AI. Qualitative Analysis of Neck Kinematics During Low-Speed Rear-End Impact. Clinical biomechanics. 2000;15:649-57.

[69] Panjabi MM, Pearson AM, Ito S, Ivancic PC, Gimenez SE, Tominaga Y. Cervical Spine Ligament Injury During Simulated Frontal Impact. Spine. 2004;29:2395-403.

[70] Ivancic PC, Pearson AM, Panjabi MM, Ito S. Injury of the Anterior Longitudinal Ligament During Whiplash Simulation. European spine journal : official publication of the European Spine Society, the European Spinal Deformity Society, and the European Section of the Cervical Spine Research Society. 2004;13:61-8.

[71] Pearson AM, Ivancic PC, Ito S, Panjabi MM. Facet Joint Kinematics and Injury Mechanisms During Simulated Whiplash. Spine. 2004;29:390-7.

[72] Stemper BD, Yoganandan N, Pintar FA. Gender Dependent Cervical Spine Segmental Kinematics During Whiplash. Journal of biomechanics. 2003;36:1281-9.

[73] Ivancic PC, Panjabi MM, Tominaga Y, Malcolmson GF. Predicting Multiplanar Cervical Spine Injury Due to Head-Turned Rear Impacts Using Iv-Nic. Traffic injury prevention. 2006;7:264-75.

[74] Jackson KE, Boitnott RL, Fasanella EL, Jones LE, Lyle KH. A History of Full-Scale Aircraft and Rotorcraft Crash Testing and Simulation at NASA Langley Research Center. Fourth Triennial International Fire and Cabin Safety Research Conference. Lisbon, Portugal. 2004.

[75] Boitnott RL, Jackson KE, Fasanella EL, Kellas S. Full-Scale Crash Test of the Sikorsky Advanced Composite Airframe Program Helicopter. Proceedings of the American Helicopter Society Forum 56. Virginia Beach, VA. 2000.

[76] Burrows L, Lane R, McElhenney J. Ch-47 Crash Test (T-40) Structural, Cargo Restraint, and Aircrew Inflatable Restraint Experiments. USARTL-TR-78-22. 1978.

[77] Cronkhite JD, Mazza LT. Bell ACAP Full-Scale Aircraft Crash Test and Krash Correlation. Proceedings of the 44th Annual Forum of the American Helicopter Society. Washington, D.C. 1988.

[78] Perschbacher JP, Clarke C, Furnes K, Carnell B. Advanced Composite Airframe Program (ACAP) Militarization Test and Evaluation (MT&E) Volume V- Airframe Drop Test. USAATCOM TR 88-D-22E. 1996.

[79] Singley GT, III. Full-Scale Crash Testing of a CH-47C Helicopter. Proceedings of the 32nd V/STOL Forum of the American Helicopter Society. Washington, D.C. 1976.

[80] Smith KF. Full-Scale Crash Test (T-41) of the YAH-63 Attack Helicopter. USAAVSCOM TR-86-D-2. 1986.

[81] Thomson DT, Clarke CW. Advanced Composite Airframe Program (ACAP) Militarization Test and Evaluation (MT&E) Volume I- Landing Gear Drop Test. USAAVSCOM TR-88-D-22A. 1989.

[82] Jackson KE, Fasanella EL, Boitnott RL, McEntire BJ, Lewis A. Occupant Responses in a Full-Scale Crash Test of the Sikorsky ACAP Helicopter. NASA/TM-2002-211733 (ARL-TR-2735). 2002.

[83] Haley Jr. JL, Palmer RW. Evaluation of a Retrofit OH-58 Pilot's Seat to Prevent Back Injury. Fort Rucker, AL: US Army Aeromedical Research Laboratory. USAARL Report No. 95-9. 1994.

[84] Coltman JW, Van Ingen C, Selker F. Crash-Resistant Crewseat Limit-Load Optimization through Dynamic Testing with Cadavers. Fort Eustis, VA: US Army Aviation Systems Command. USAAVSCOM TR-85-D-11. 1986.

[85] Coltman JW. Design and Test Criteria for Increased Energy-Absorbing Seat Effectiveness. USAAVRADCOM-TR-82-D-42. 1983.

[86] Haley JL, Jr., McEntire BJ. OH-58 Pilot Display Unit (PDU) Simulated Crash Tests. Fort Rucker, AL: United States Army Aeromedical Research Laboratory. USAARL Report No. 95-10. 1994.

[87] Paskoff GR. Cervical Injury Risk Resulting from Rotary Wing Impact: Assessment of Injury Based Upon Aviator Size, Helmet Mass Properties and Impact Severity. Patuxent River, Maryland. . NAWCADPAX/RTR-2004/86. 2004.

[88] Paskoff GR, Sieveka E. Influence of Added Head Mass Properties on Head/Neck Loads During Standard Helicopter Impact Conditions. Forty Second Annual SAFE Association Symposium. Salt Lake City, Utah. 2004.

[89] Association for the Advancement of Automotive Medicine. The Abbreviated Injury Scale, 1998 Update. 1998.

[90] Kleinberger M, Sun E, Eppinger R, Kuppa S, Saul R. Development of Improved Injury Criteria for the Assessment of Advanced Automobile Restraint Systems. NHTSA Docket No. 1998-4405-9. 1998.

[91] Eppinger R, Sun E, Bandak F, Haffner M, Khaewpong N, Maltese M, et al. Development of Improved Injury Criteria for the Assessment of Advanced Automobile Restraint Systems - II. NHTSA Docket No. 1999-6407-5. 1999.

[92] Eppinger R, Sun E, Kuppa S, Saul R. Development of Improved Injury Criteria for the Assessment of Advanced Automobile Restraint Systems - II. NHTSA Docket No. 2010-03-19. 2000.

[93] Fasanella EL, Carden HC, Boitnott RL, Hayduk RJ. A Review of the Analytical Simulation of Aircraft Crash Dynamics. NASA Technical Memorandum (TM) 102595. 1990.

[94] Fasanella EL, Jackson KE. Best Practices for Crash Modeling and Simulation. U.S. Army Research Laboratory. ARL-TR-2849. 2002.

[95] Jackson KE, Fasanella EL, Lyle KH. Crash Certification by Analysis – Are We There Yet? American Helicopter Society 62nd Annual Forum. Phoenix, AZ. 2006.

[96] Jackson KE, Fuchs YT, Kellas S. Overview of the National Aeronautics and Space Administration Subsonic Rotary Wing Aeronautics Research Program in Rotorcraft Crashworthiness. Journal of Aerospace Engineering. 2009;22:229-39.

[97] Gamon MA. General Aviation Airplane Structural Crashworthiness User's Manual: Volume I Program "Krash" Theory. Washington, DC: U.S. Department of Transportation. FAA-RD-77-I89. 1978.

[98] Wittlin G. Analysis of Aircraft Dynamic Behavior in a Crash Environment. Journal of Aircraft. 1983;20:762-9.

[99] Wittlin G, Gamon MA. Experimental Program for the Development of Improved Helicopter Structural Crashworthiness Analytical and Design Techniques: Volume II. Test Data and Description of an Unsymmetrical Crash Analysis Computer Program, Including a User's Guide and Sample Case. USAAMRDL Technical Report 72-72B. 1973.

[100] Wittlin G, Gamon MA. Experimental Program for the Development of Improved Helicopter Structural Crashworthiness Analytical and Design Techniques: Volume I. Computerized Unsymmetrical Mathematical Simulation and Experimental Verification for Helicopter Crashworthiness in Which Multidirectional Impact Forces Are Present. USAAMRDL Technical Report 72-72A. 1973.

[101] Gamon MA. Krash 85 User's Guide: Input/Output Format. Atlantic City Airport: FAA Technical Center. DOT/FAA/CT-85/10. 1985.

[102] Armen H, Pifko AB, Levine H. Nonlinear Finite Element Techniques for Aircraft Crash Analysis. Aircraft Crashworthiness. 1975:517-48.

[103] Pifko AB, Winter R, Ogilvie PL. Dycast, a Finite Element Program for the Crash Analysis of Structures. Washington, D.C. NASA Contractor Report 4040. 1987.

[104] Winter R, Pifko AB, Armen H. Crash Simulation of Skin-Frame Structures Using a Finite Element Code. SAE Paper 770484. 1977.

[105] Winter R, Cronkhite J. Crash Simulation of Composite and Aluminum Helicopter Fuselages Using a Finite-Element Program. 20th Structures, Structural Dynamics, and Materials Conference. St. Louis, MO. 1979.

[106] Fasanella EL, Widmayer E, Robinson MP. Structural-Analysis of the Controlled Impact Demonstration of a Jet Transport Airplane. Journal of Aircraft. 1987;24:274-80.

[107] Laananen DH. Mathematical Simulation for Crashworthy Aircraft Seat Design. Journal of Aircraft. 1978;15:567-73.

[108] Laananen DH. Computer Simulation of an Aircraft Seat and Occupants in a Crash Environment - Program Som-La/Som-Ta User Manual. Atlantic CIty Airport, NJ: FAA Technical Center. DOT/FAA/CT-90/4. 1991.

[109] Laananen DH, Bolukbasi AO, Coltman JW. Computer Simulation of an Aircraft Seat and Occupant Environment, Volume I - Technical Report. Atlantic City Airport, NJ: US Department of Transportation Federal Aviation Administration. DOT/FAA/CT-82/33-I. 1983.

[110] Bolukbasi AO, Laananen DH. Nonlinear Finite-Element Method in Crashworthiness Analysis of Aircraft Seats. Journal of Aircraft. 1984;21:512-9.

[111] Bolukbasi AO, Laananen DH. Computer Simulation of a Transport Aircraft Seat and Occupant(S) in a Crash Environment: Volume I - Technical Report. Atlantic City Airport: FAA Technical Center. DOT/FAA/CT-86/25-I. 1986.

[112] Cheng H, Rizer AL, Obergefell LA. Articulated Total Body Model Version V User's Manual. Wright-Patterson AFB, OH: United States Air Force Research Laboratory. AFRL-HE-WP-TR-1998-0015. 1998.

[113] Beale DG, Alem NM, Butler BP. A Correlative Investigation of Simulated Occupant Motion and Accident Report in a Helicopter Crash. Fort Ruckers, AL: United States Army Aeromedical Research Laboratory. USAARL Report No. 94-42. 1994.

[114] Strawn G, Alem NM. Biodynamic Simulation of Pilot Interaction with a Helicopter Multiairbag Restraint System. Fort Rucker, AL: US Army Aeromedical Research Laboratory. USAARL Report No. 95-3. 1994.

[115] Ashrafiuon H, Alem NM, McEntire BJ. Effects of Weight and Center of Gravity Location of Head-Supported Devices on Neck Loading. Aviation, space, and environmental medicine. 1997;68:915-22.

[116] Alem NM, Mobasher AA, Brozoski FT, Beale DG. Simulations of Head Strikes in Helicopters and the Roles of Restraints, Seat Stroke and Airbags on Their Reduction. Fort Rucker, AL: US Army Aeromedical Research Laboratory. USAARL Report No. 98-11. 1998.

[117] Brozoski FT, Mobasher AA, McEntire BJ, Alem NM. Mass and Location Criteria of Head-Supported Devices Using Articulated Total Body Simulations. RTO HFM Symposium on "Current Aeromedical Issues in Rotary Wing Operations". San Diego, CA. 1998.

[118] Mobasher AA, Brozoski FT, McEntire B, Alem NM. Effects of Seat Stroke Distance on the Allowable Mass of Head Supported Devices. Fort Rucker, AL: US Army Aeromedical Research Laboratory. USAARL Report No. 98-26. 1998.

[119] Manoogian SJ, Kennedy EA, Wilson KA, Duma SM, Alem NM. Predicting Neck Injuries Due to Head-Supported Mass. Aviation, space, and environmental medicine. 2006;77:509-14.

[120] Lyle KH, Jackson KE, Fasanella EL. Development of an ACAP Helicopter Finite Element Impact Model. Journal of the American Helicopter Society. 2000;45:137-42.

[121] Fasanella EL, Jackson KE, Lyle KH. Finite Element Simulation of a Full-Scale Crash Test of a Composite Helicopter. American Helicopter Society 56th Annual Forum. Virginia Beach, VA. 2000.

[122] Fasanella EL, Boitnott RL, Lyle KH, Jackson KE. Full-Scale Crash Test and Simulation of a Composite Helicopter. International Journal of Crashworthiness. 2001;6:485-98.

[123] Lyle KH, Jackson KE, Fasanella EL. Simulation of Aircraft Landing Gears with a Nonlinear Dynamic Finite Element Code. Journal of Aircraft. 2002;39:142-7.

[124] Jackson K, Fasanella EL, Boitnott RL, Lyle KH. Full-Scale Crash Test and Finite Element Simulation of a Composite Prototype Helicopter. Hampton, VA: Langley Research Center. NASA/TP-2003-212641, ARL-TR-2824. 2003.

[125] Anghileri M, Castelletti LML, Fracasso E. Hybrid III Numerical Model for Aircraft Seat Crash Performance Assessment. Journal of Aircraft. 2007;44:1691-700.

[126] Jackson K, Fuchs Y. Vertical Drop Testing and Analysis of the Wasp Helicopter Skid Gear. Washington, D.C. NASA TM-2007-214901. 2007.

[127] Fuchs YT, Jackson KE. Vertical Drop Testing and Analysis of the Wasp Helicopter Skid Gear. American Helicopter Society 64th Annual Forum. Montréal, Canada. 2008.

[128] Annett MS. LS-DYNA Analysis of a Full-Scale Helicopter Crash Test. 11th International LS-DYNA Users Conference. Detroit, MI. 2010.

[129] Annett MS, Horta LG. Comparison of Test and Finite Element Analysis for Two Full-Scale Helicopter Crash Tests. Hampton, VA: NASA Langley Research Center. NF1676L-11145. 2011.

[130] Annett MS, Lucas H. Comparison of Test and Finite Element Analysis for Two Full-Scale Helicopter Crash Tests. 52nd Aiaa/ASME/ASCE/AHS/ASC Structures, Structural Dynamics and Materials Conference: American Institute of Aeronautics and Astronautics; 2011.

[131] Putnam JB, Untaroiu CD. Investigation of Human Kinematics and Risk of Injury During a Vertical Impact Using Dummy and Human Finite Element Models. The Ohio State University's 9th Annual Injury Biomechanics Symposium. Columbus, OH. 2013.

[132] Federal Aviation Administration. Methodology for Dynamic Seat Certification by Analysis for Use in Parts 23, 25, 27, and 29 Airplanes and Rotorcraft. AC No: 20-146. 2003.

[133] Olivares G, Acosta JF, Yadav V. Certification by Analysis I and II. JAMS Annual Meeting. Seattle, Washington. 2010.

[134] Dhole N, Yadav V, Olivares G. Certification of a Typical Aircraft Seat. 12th International LS-DYNA Users Conference. Dearborn, MI. 2012.

Chapter 3: Cross-Sectional Neck Response of a Total Human Body FE Model during Simulated Frontal and Side Automobile Impacts

Nicholas A. White, Daniel P. Moreno, F. Scott Gayzik, and Joel D. Stitzel

Published in: *Computer Methods in Biomechanics and Biomedical Engineering*, 2013, Aug 9 [Epub].

Abstract

Human body finite element models are beginning to play a more prevalent role in the advancement of automotive safety. A methodology has been developed to evaluate neck response at multiple levels in a human body finite element model during simulated automotive impacts. Three different impact scenarios were simulated: a frontal impact of a belted driver with airbag deployment, a frontal impact of a belted passenger without airbag deployment, and an unbelted side impact sled test. Cross sections were created at each vertebral level of the cervical spine to calculate the force and moment contributions of different anatomical components of the neck. Adjacent level axial force ratios varied between 0.74 and 1.11 and adjacent level bending moment ratios between 0.55 and 1.15. The present technique is ideal for comparing neck forces and moments to existing injury threshold values, calculating injury criteria, and for better understanding the biomechanical mechanisms of neck injury and load-sharing during sub-injurious and injurious loading.

Keywords: Finite Element Methods, Cross Section, Cervical Spine, Neck, Biomechanics, Injury

Introduction and Background

Neck Injury Biomechanics and Tolerances

Motor vehicle collisions (MVCs) are the most common cause of cervical spine fracture and dislocation [1]. According to the National Spinal Cord Injury Statistical Center, MVCs were responsible for 39.2% of all reported spinal cord injuries between 2005 and 2011 [2]. A previous review of epidemiological data from clinical and accident database files found MVC-related cervical spine injuries tended to manifest between the occipital condyle (OC) and C2 of the upper region and C5-C6 in the lower region [3]. Upper cervical spine injuries were commonly associated with fatalities and lower cervical spine injuries with survivors. Of the serious injuries reported, 20% were to the spinal cord and 65% to the bone. Still, the majority of MVC-related injuries to the cervical spine are minor soft tissue injuries usually resulting from low-speed, rear-end impacts [4]. While not life-threatening, these injuries are associated with high socioeconomic costs on a global level [5].

In 1976, General Motors introduced the Hybrid III 50th percentile male Anthropomorphic Test Device (ATD) as a biofidelic surrogate to study occupant protection in simulated frontal and rear MVCs [6]. In the following years, scaled versions of the ATD were developed, representing the small 5th percentile female, large 95th percentile male, 3- and 6-year old child, and a 6-, 12- and 18-month infant. Each of these ATDs is instrumented with a single six degree of freedom load cell in both the upper and lower neck. These load cells allow for forces and moments to be calculated at the levels of the OC-C1 junction and at T1, and compared with defined Injury Assessment Reference Values (IARVs) [6, 7]. These IARVs were selected so that the risk of associated injuries would be minimized for a particularly sized occupant, as long as the IARVs are not exceeded. To account for the viscoelastic properties of tissue, time-dependent loading criteria for the neck in tension, compression, and shear have also been developed in the form of exceedence plots [8].

The N_{ij} neck injury criterion is the primary method to evaluate the risk of neck injury from a frontal MVC, including any airbag interaction [9-12]. The criterion is based on matched 3-year old ATD and animal airbag interaction tests which linearly combine normalized axial and sagittal bending moments from the upper neck load cell [13-15]. Four possible loading scenarios are evaluated: tension-extension, tension-flexion, compression-extension, and compression-flexion. Rear-end impact criterion include the Neck Injury Criterion (NIC), Neck Protection Criterion (N_{km}) and Lower Neck Load Index (LNL). The NIC value is calculated from the relative acceleration and velocity between the upper and lower neck in the anterior-posterior (AP) direction [16]. It is based on the hypothesis that transient pressure changes in the cervical spinal canal, caused by a quick extension-flexion motion of the neck, lead to ganglion injuries. The N_{km} value is based on the summation of normalized shear loads in the AP direction and flexion/extension moments, similar to the N_{ij} [17]. The critical intercepts used to normalize the load and moment were based on non-injurious volunteer studies [18, 19]. The LNL value takes into account three force components and two bending moments of the lower neck load cell, normalized by critical intercept values [20].

Government-mandated occupant crash protection regulations differ from region to region around the world. In the USA, Federal Motor Vehicle Safety Standards (FMVSS) 208 sets peak reaction forces and moments, and N_{ij} critical intercept values for the upper neck during frontal crash tests for different ATD sizes [21]. In Europe, the Economic Commission for Europe (ECE) R94 sets thresholds for maximum neck extension moment, as well as time-dependent loading criteria for neck tension and shear for frontal impact test [22].

Brief Review of Finite Element Neck Models

While physical crash testing with ATDs is the standard for evaluating the safety of new vehicles, computer simulations have become more and more prevalent in studying the potential for MVC-induced injury. Mathematical modeling of occupant kinematics during a vehicle crash was born close to 50 years ago with the advent of computers [23, 24]. Extensive reviews of human body computational models used to study impact biomechanics exist in the literature [24-26]. One of the first finite element (FE) neck models developed was a simplified geometry 2-D model to study laminectomy deformity [27]. As technology has progressed, more complex 3D FE neck models, with detailed geometries based on CT and MRI scans, were developed with numerous injury biomechanics applications including frontal, lateral, and rear impacts [26, 28-41].

The current study utilized the Global Human Body Models Consortium 50^{th} percentile male model (GHBMC M50, v3-5), a state-of-the-art FE model of a seated average-sized male built for LS-DYNA, R4.2.1 (LSTC, Livermore, CA) (Figure 3-1) [42-44]. The model was developed by a team of research university centers of excellence (COEs) around the world with the Full Body Model COE model integration center located at Wake Forest University School of Medicine and the Virginia Tech – Wake Forest Center for Injury Biomechanics. The GHBMC neck model was developed at the Neck COE, the University of Waterloo, in Ontario, Canada [45-48]. It is composed of seven cervical vertebrae with detailed facet joints and accompanying intervertebral discs, as well as non-linear rate dependent ligaments, 3D passive muscles and 1D active muscles (Figure 3-2). Element types include hexahedral solids, shells, 1D beam and discrete springs with a 1.5 mm representative mesh size for the vertebrae and neck muscles and 1.0 mm size for the intervertebral discs. The neck model has been rigorously validated both at individual cervical segment levels and for the full cervical spine [44, 49]. At the segmental level, non-injurious axial, lateral, shear, flexion, extension, compression, and tension loading mode validations were performed. Traumatic flexion, extension, compression, and tension-loading mode validations have also been completed. The full cervical spine has been validated against lateral, frontal and rear end car crash events, as well as in tension.

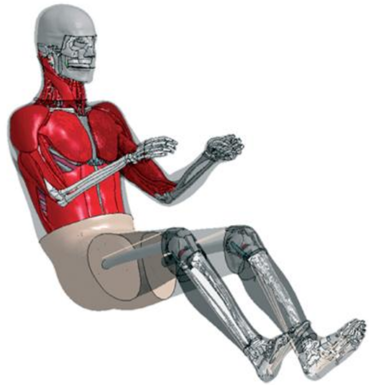

Figure 3-1: The GHBMC 50th percentile seated male model.

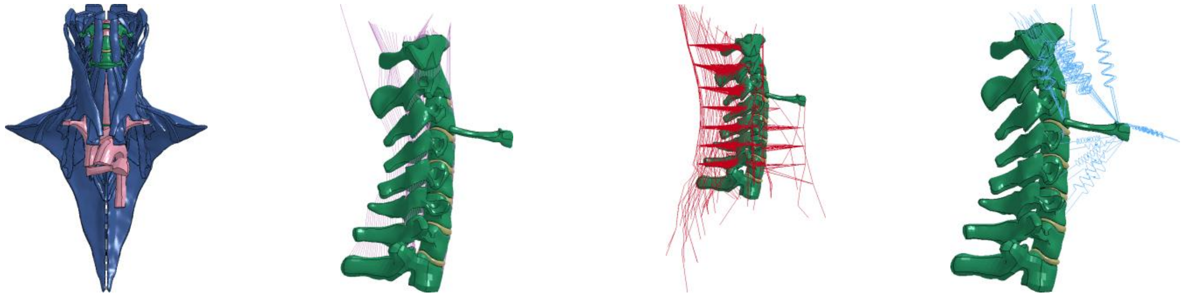

(a) (b) (c) (d)

Figure 3-2: Breakdown of the GHBMC neck model including (a) passive muscles and vasculature, (b) ligaments, (c) active muscles, and (d) supportive discrete elements.

Cross Sections

The purpose of the current study is to describe a methodology to evaluate neck forces and moments at multiple levels of a human body FE model during simulated MVCs. Cross sections were implemented in the neck to capture loading contributions of different anatomical components. For each cervical level, transverse cutting planes were created according to a locally defined coordinate system. Cross-sectional interfaces were then automatically calculated using LS-DYNA. Each of these interfaces contained a node set defining the cutting surface and one or more element sets. Only deformable elements to one side of the interface were selected. Forces and moments for each anatomical component, at every cervical level, were reported in the corresponding local coordinate system (LCSYS) and compared with current IARVs and injury criteria.

Methodology

Simulations

The GHBMC whole body model was validated against various regional impacts and full-body cadaver sled tests [44, 49]. Three of these validation simulations, two frontal and one side impact, have been repeated in the current study to examine the neck response at each cervical level using cross sections. The first simulation was of a force-limited, 3-point belted driver subjected to a 13.3 m/s ΔV, frontal impact with airbag deployment [50]. The second simulation was of a 3-point belted (no retractor) passenger subjected to an 11.1 m/s ΔV frontal impact without airbag deployment [51]. The third simulation was a 6.7 m/s ΔV lateral impact using a Heidelberg-type seat fixture with no side wall padding [52-54]. The simulations were run under LS-DYNA, (R4.2.1) on the WFU DEAC Cluster, a high performance computing environment with 238 computational nodes containing 1904 processors, 11.4TB of total memory, and 100TB of disk storage.

Local Coordinate System

A LCSYS (Figure 3-3) was defined for vertebral bodies C1-T1 in accordance with SAE J211 sign convention [55]. The center of gravity (CG) for each vertebra, including both shell and solid elements, was computed with the Mass Trimming interface in LS-PrePost (LSTC, Livermore, CA). The local origin of the vertebra was defined by a node placed at this CG. A second node was defined at the midpoint of the superior and inferior portion of the anterior vertebral body, in the same sagittal plane as the CG, indicating the positive x-direction. A third node was then defined in the local xy-plane, with the positive y-direction to the right, orthogonal to the sagittal plane. Constrained Nodal Rigid Bodies (*CNRBs) were used to rigidly attach the LCSYS to a node on its corresponding vertebra, allowing local axes to rotate with the vertebra. The global coordinates of these nodes were output at 0.1-ms increments.

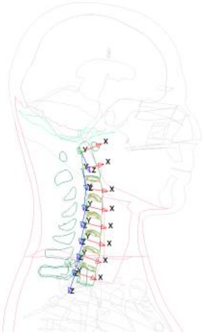

Figure 3-3: Local coordinate system for each vertebral level with the origin at the centers of gravity for each vertebrae and axes oriented according to SAE J211 convention [55].

Cross Sections

Six parts sets were created, separating the neck into anatomical components including: bones, intervertebral discs (IVDs), ligaments, soft tissue, active muscles, and passive muscles. Database Cross Section Planes (*DCSPs), parallel with the local xy-plane, were defined at each cervical level (Figure 3-4). These cross sections were centered at the vertebral local origin and extended radially, just past the outer surface of the neck skin. The same plane was defined six times for each vertebra, allowing capture of the six part sets individually. The model was run for a single time step, allowing for LS-DYNA to automatically capture all elements and nodes associated with each cross-sectional interface, reporting them in the D3HSP (high speed printer) ASCII output file under the heading "interface definition". The captured elements and nodes for each interface were extracted and placed into individual sets. Database Cross Section Sets (*DCSSs) were then created based on these element sets and incorporated into the model (Figure 3-5). Projected views of the cross-sectional cuts are presented in Appendix A. It is important to note that only deformable bodies are included in cross sections, not rigid bodies.

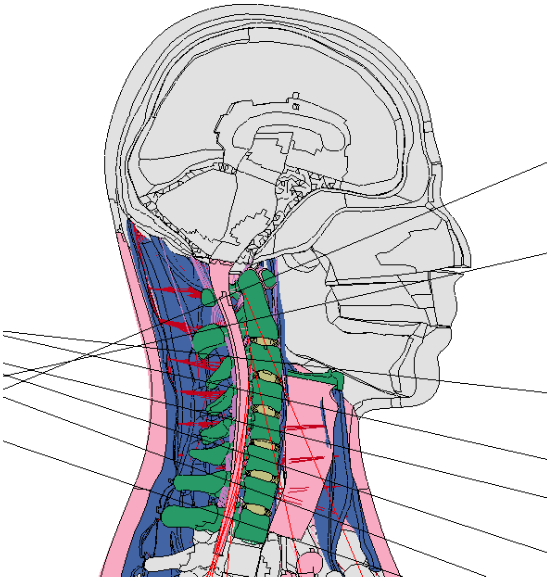

Figure 3-4: View of the GHBMC head and neck along the mid-sagittal plane. Cross-sectional planes were defined coplanar with each local coordinate system xy-plane, capturing only elements and nodes within the neck, and trying to avoid redundant measurement (overlapping section planes).

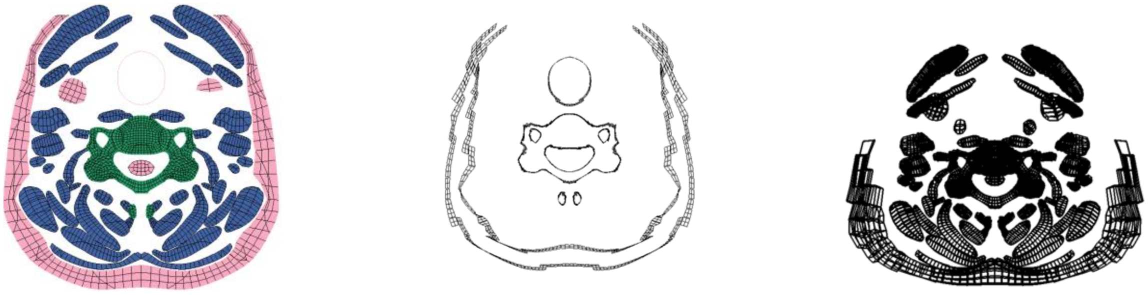
(a) (b) (c)

Figure 3-5: Projected cross-sectional view of the (a) bone, passive muscles and soft tissue, (b) *SET_SHELL and (c) *SET_SOLID captured at the level of C6.

Cross-Section-Force (CSF), Cross-Section-Moment (CSM) and Cross-Section-Centroid (CSC) data was output at 0.1-ms increments for each *DCSS. The CSF is the summation of the internal node forces defined at the cross-sectional interface. The moment contribution from each node defined in the cross-sectional interface is calculated as the cross product of the internal nodal force and the vector from the CSC to the location of this force. The CSM is the summation of these cross products, representing the total moment about the CSC, not the local origin. Since the CSC varies throughout time and is dependent on which part set is defined in the *DCSS, the reported moments require transformation to the local origins. Using the concept of equivalent force systems, the moments about the local origins were calculated by adding the CSM to the cross product of the CSF and vector from the local origin to the CSC.

While the CSF and CSM can be directly reported in the specified LCSYS, a problem lies with the CSC which is only reported in global coordinates, regardless of how the *DCSS is defined. Even though this issue may be resolved in newer versions of LS-DYNA, currently the GHBMC model is stable only in R4.2.1. To properly transform the CSMs to the local origin, a 3x3 direction cosine rotation matrix was constructed from the global coordinate time histories of the nodes used to define the vertebral LCSYSs. The CSC data was transformed into the LCSYS using this matrix prior to moment correction. For consistency, this rotation matrix was used to rotate both the CSF and CSM global results into LCSYSs.

Discrete Elements

Since version R4.2.1 of LS-DYNA does not capture discrete elements using either *DCSP or *DCSS, the force and moment contributions of these elements must be added to the CSF and CSM results for each cervical level. The global forces and nodal coordinates of each discrete element were output at 0.1-ms increments. Analytical geometry was used to calculate the intersection points of the discrete elements with the cross-sectional interfaces. The coordinates of any point, l_n, along a discrete element can be calculated using Eq. 1, where l_a and l_b correspond to the coordinates of the two nodes defining the element. While the value of t may be any real number, it must remain between 0 and 1 for l_n to lie within the physical boundaries of the discrete element. The coordinates of any point, p_n, on the plane defined by three, non-collinear points p_0, p_1, and p_2, can be calculated using Eq. 2. These three points correspond to the coordinates of the three nodes defining the xy-plane of a vertebral LCSYS. A parametric equation can be created by equating Eq. 1 and Eq. 2, where t can be solved and then plugged back into Eq. 1 to calculate the point of intersection. For each cervical level, the cross product of the vector from the local origin to the point of intersection and discrete element force was used to calculate the moment contribution from each discrete element. These individual moments were summed and rotated into the LCSYS using the rotation matrix.

$$l_n = la + (lb - la)t \quad \text{(Eq. 1)}$$

$$p_n = p_0 + (p_1 - p_0)u + (p_2 - p_0)v \quad \text{(Eq. 2)}$$

Data Processing

The binary output files were post-processed using Oasys T/HIS 10.2-64 bit (Arup, London, UK). The CSF results were filtered at CFC 1000 and CSM results at CFC 600 according to SAE J211 specifications for neck load cells in the Hybrid III ATD [55]. For purposes of N_{ij} calculation, both the CFC and CSM results were filtered at CFC 600 according to FMVSS regulation [21]. The nodal displacements and CSC results were filtered at CFC 60. Seatbelt and airbag loading with the occupant were also filtered at CFC 60 [55]. The occupant-wall interaction forces measured in the Cavanaugh side impact simulation were filtered with CFC 300. All of the filtered data was then processed using in-house code written in MATLAB 7.12.0 (R2011a, MathWorks, Natick, MA).

Results

Animated results of the overall occupant kinematics are presented as individual d3plots for the start, middle, and end of each simulation (Figure 3-6, Figure 3-7, and Figure 3-8). Total force and moment time histories were created for each simulation from the summation of bone, ligament, active muscle, passive muscle, and soft tissue anatomical components, and discrete element loading contributions, in the rotated LCSYS for each respective cervical level (Figure 3-9, Figure 3-10, and Figure 3-11). A summary of force and moment polarity with respect to head and chest motion based on SAE J211 is presented in Table 3-1 [55]. Maximum and minimum neck forces and moments are summarized in Table 3-2. The individual force and moment contributions of the anatomical components and discrete elements are reported in the Appendices B-D. Force time histories of occupant/restraint systems and occupant/wall interaction are reported in Figure 3-12, Figure 3-13, and Figure 3-14.

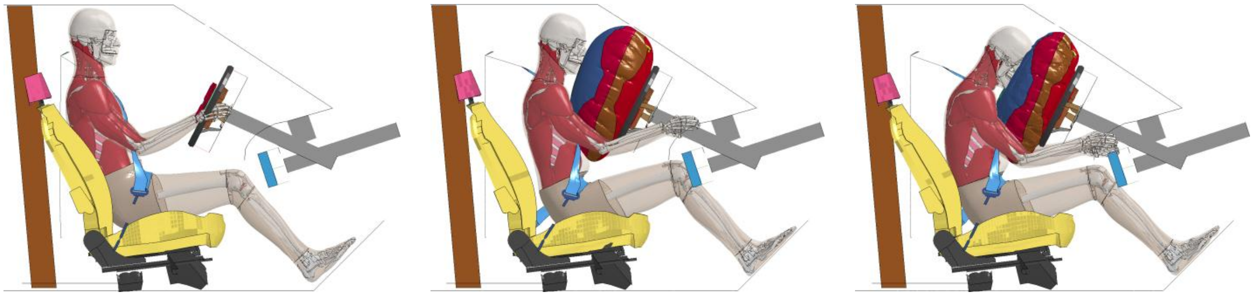
(a) (b) (c)

Figure 3-6: Simulation d3plots for the Forman 13.3 m/s ΔV force-limited, 3-point belted driver frontal impact with airbag deployment at (a) t=0 ms, (b) t=75 ms, and (c) t=150 ms [50].

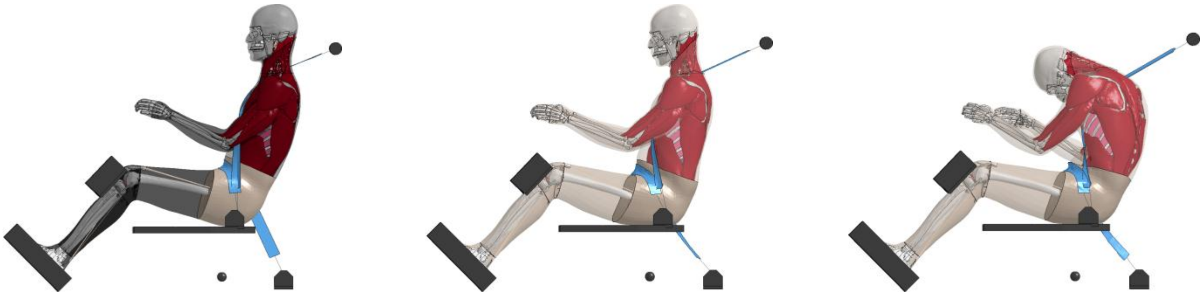
(a) (b) (c)

Figure 3-7: Simulation d3plots for the Shaw 11.1 m/s ΔV 3-point belted (no retractor) passenger frontal impact at (a) t=0 ms, (b) t=75 ms, and (c) t=150 ms [51].


(a) (b) (c)

Figure 3-8: Simulation d3plots for the Cavanaugh 6.7 m/s ΔV lateral impact using a Heidelberg-type seat fixture with no side wall padding at (a) t=0 ms, (b) t=50 ms, and (c) t=100 ms [52-54].

For purposes of the current study, only the total forces and moments will be reported in this section. Many of the local extrema in the force and moment curves correlate with occupant-restraint interactions. In the Forman simulation, maximum engagement of the upper shoulder belt occurred at 70 ms and maximum occupant/airbag interaction at 85 ms. Prior to maximum airbag interaction, the time of maximum engagement with the upper shoulder belt coincided with the largest negative AP shear force in the upper cervical spine and the largest axial tension force at all levels. While AP shear force decreased in magnitude for both C1 and C2 just after the maximum engagement of the upper shoulder belt, an inflection point was noted for both cervical levels at the time of maximum occupant/airbag interaction where AP shear subsequently increased in magnitude (larger negative value). At the approximate time of maximum occupant/airbag interaction, a local axial tension force minimum and local axial moment maximum were reached for all cervical levels.

In the Shaw simulation, maximum engagement of the upper shoulder belt occurred at 90 ms and of the lower shoulder belt at 116 ms. A force plateau was noted between both of these points in time for the lateral shear and axial force, for all levels of the cervical spine. The magnitude of the AP shear force began to increase (larger negative value) at a faster rate from the time of maximum engagement of the upper shoulder belt to that of the lower belt. All levels of the cervical spine experienced a flexion moment for the entire simulation. At maximum engagement of the lower shoulder belt, peak axial moments were experienced in the lower cervical spine (C4-C7).

While there were no restraints in the Cavanaugh simulation, time of maximum occupant-to-wall interaction and estimated maximum lateral neck rotation were reported. Occupant-to-wall force time histories were reported for the upper body (shoulder, thorax, and abdomen forces) and pelvis. The maximum force between the upper body and wall occurred at t=18 ms and between the pelvis and wall at t=19.5 ms. Lateral rotation of the cervical spine in the frontal plane was approximated in LS-PrePost. This estimated maximum lateral rotation was measured between C1 and C7 and occurred at t=55 ms. Lateral shear forces first peaked shortly after pelvis-to-wall contact at all levels of the cervical spine. Peak axial force occurred for all levels at approximately the same time, between maximum pelvis-to-wall contact and maximum lateral cervical spine rotation. Peak lateral moments occurred roughly 10 ms prior to the time of maximum rotation for the lower cervical spine (C5-C7) and at the approximate time of maximum rotation for the upper cervical spine (C1-C4).

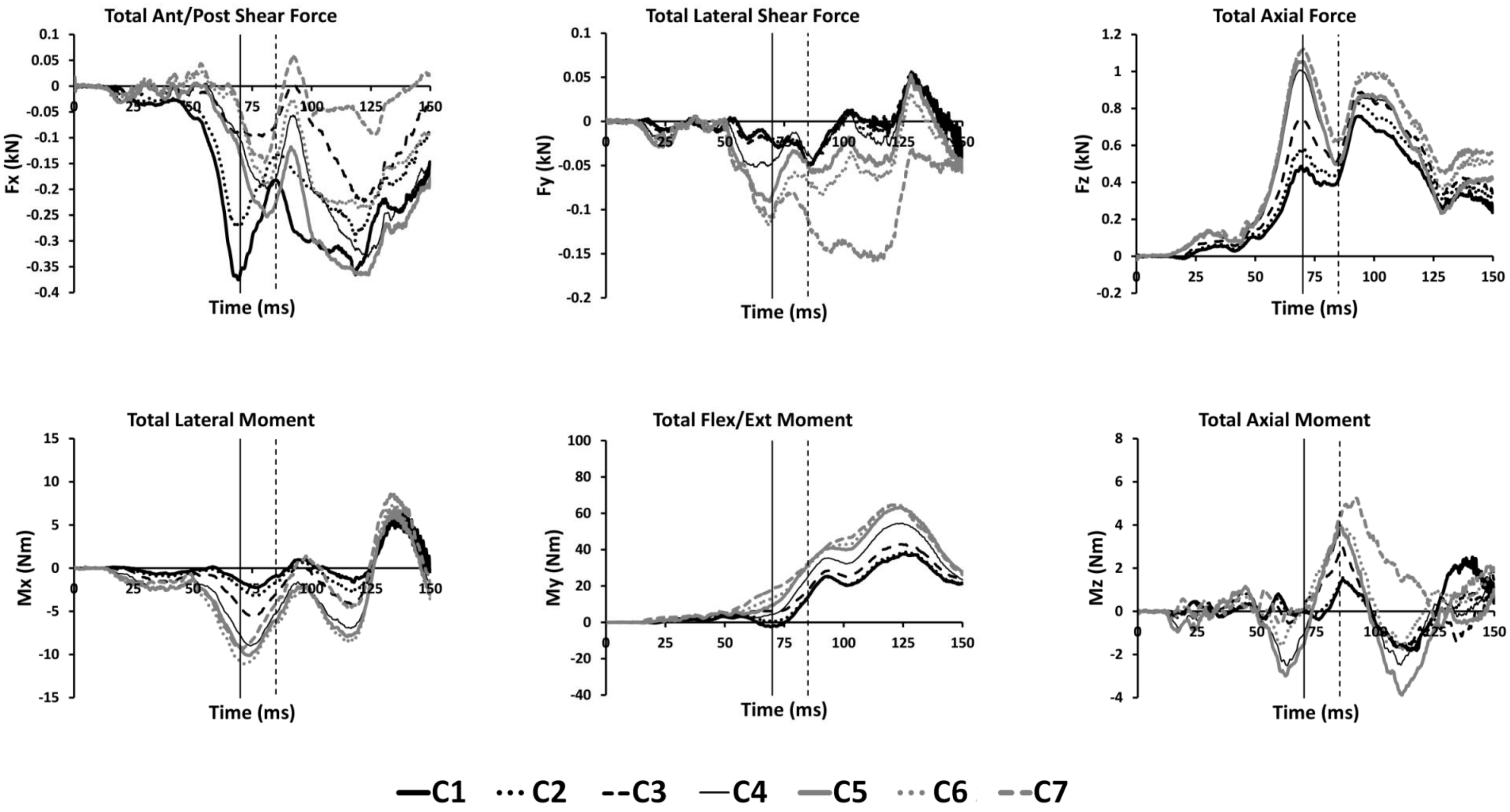

Figure 3-9: Total force and moment time histories from the Forman frontal impact simulation. These total load curves are the summation of bone, ligament, active muscle, passive muscle, soft tissue, and discrete element anatomical component contributions in the rotated, local coordinate system for each respective vertebral level. The vertical solid line corresponds to the time of maximum engagement of the upper shoulder belt (t=70 ms) and the vertical dashed line to the time of maximum occupant/airbag interaction (t=85 ms).

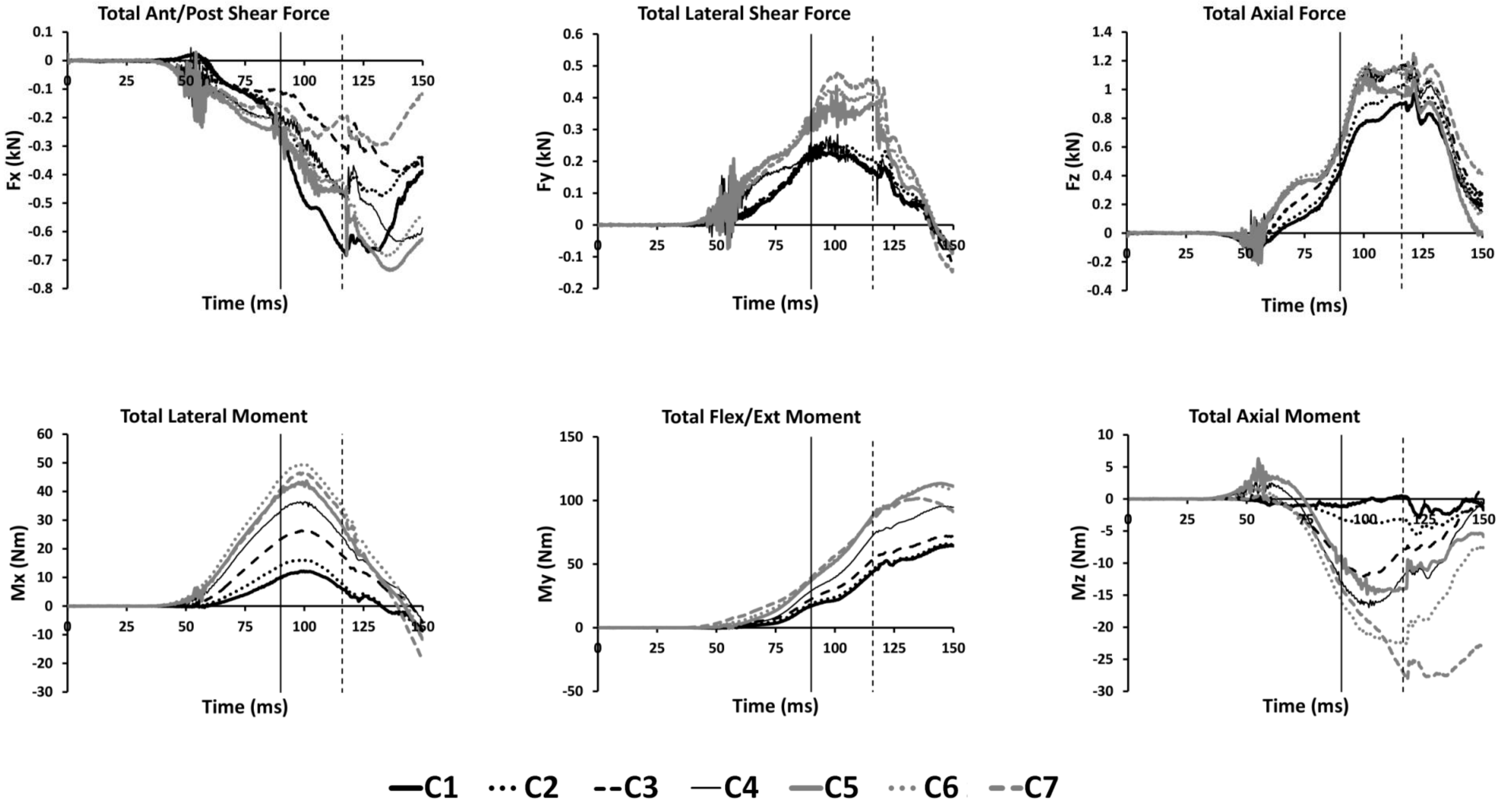

Figure 3-10: Total force and moment time histories from the Shaw frontal impact simulation. These total load curves are the summation of bone, ligament, active muscle, passive muscle, soft tissue, and discrete element anatomical component contributions in the rotated, local coordinate system for each respective vertebral level. The vertical solid line corresponds to the time of maximum engagement of the upper shoulder belt (t=90 ms) and the vertical dashed line to of maximum engagement of the lower shoulder belt (t=116 ms).

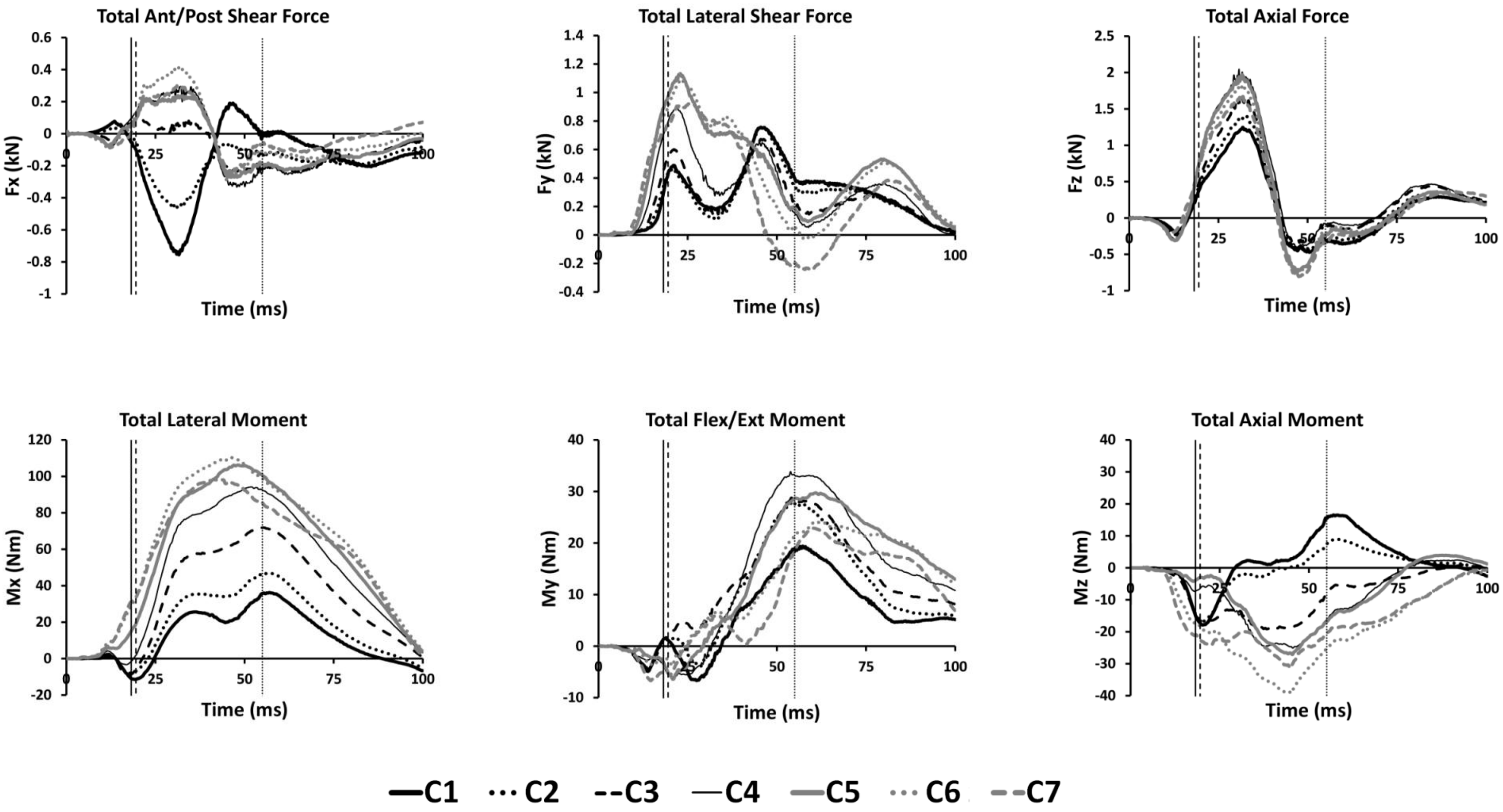

Figure 3-11: Total force and moment time histories from the Cavanaugh side impact simulation. These total load curves are the summation of bone, ligament, active muscle, passive muscle, soft tissue, and discrete element anatomical component contributions in the rotated, local coordinate system for each respective vertebral level. The vertical solid line corresponds to the time of maximum upper body-to-wall contact force (t=18 ms), the vertical dashed line to the time of maximum pelvis-to-wall contact force (t=19.5 ms) and the vertical dotted line to the approximate time of the maximum lateral rotation of C1 with respect to C7 in the frontal plane (t=55 ms).

Table 3-1: Polarity relative to sign convention for the measured neck loads and moments [55].

Parameter	Measurement	Head-Neck Motion	Manipulation for Positive Polarity
Neck Load	Fx	Anterior/Posterior Shear	Head rearward, chest forward
	Fy	Lateral Shear	Head leftward, chest rightward
	Fz	Axial	Head upward, chest downward
Neck Moment	Mx	Lateral	Left ear toward left shoulder
	My	Flexion/Extension	Chin toward sternum (flexion)
	Mz	Axial (Torsion)	Chin toward left shoulder

The time of maximum total axial force and the time of maximum total bending moment were determined for each simulation. Force and moment values for each cervical level corresponding to these two times are presented in Figure 3-15 and Figure 3-16. Adjacent vertebral level ratios, C1/C2, C2/C3, C3/C4, C4/C5, C5/C6, and C6/7, were calculated using these force and moment values (Figure 3-17 and Figure 3-18). D3plot images for these two times (approximate) are presented in Figure 3-19. The Forman simulation produced a maximum axial force of 1.1 kN at the C7 vertebral level (t=70.2 ms) and a maximum flexion moment of 64.6 Nm at the C6 vertebral level (t=122.4 ms). The adjacent vertebral level axial force and flexion moment ratios were 0.80, 0.79, 0.74, 0.95, 0.94, 1.00 and 0.96, 0.88, 0.78, 0.87, 0.97, 1.00, respectively. The Shaw simulation produced a maximum axial force of 1.3 kN at the C7 vertebral level (t=121.3 ms) and a maximum flexion moment of 113.5 Nm at the C5 vertebral level (t=144.9 ms). The adjacent vertebral level axial force and flexion moment ratios were 0.89, 0.91, 1.04, 1.07, 0.87, 0.97 and 0.98, 0.91, 0.75, 0.84, 1.02, 1.15, respectively. The Cavanaugh simulation produced a maximum axial force of 2.0 kN at the C4 vertebral level (t=30.8 ms) and a maximum lateral moment of 110.4 Nm at the C6 vertebral level (t=46.2 ms). The adjacent vertebral level axial force and lateral moment ratios were 0.87, 0.84, 0.80, 1.05, 1.07, 1.11 and 0.60, 0.55, 0.69, 0.85, 0.95, 1.14, respectively.

Table 3-2: Peak neck forces and moments calculated for each cervical spine levels for the (F) Forman, (S) Shaw and (C) Cavanaugh simulations. The IARVs for each loading mode at the OC-C1 and C7-T1 junctions are included for reference [7].

Peak Loading	OC-C1	C7-T1	ID*	C1		C2		C3		C4		C5		C6		C7	
AP Shear F_x (N)	±3100	±3100	F	2.3	-375.1	1.5	-299.2	2.5	-224.6	7.6	-330.8	5.7	-365.6	28.6	-236.8	58.9	-148.5
			S	24.2	-683.5	1.6	-487.6	2.6	-391.1	45.2	-634.7	28.6	-736.4	3.9	-687.4	22.4	-297.0
			C	190.2	-755.0	45.7	-463.8	97.6	-261.7	295.1	-332.5	236.8	-271.5	416.1	-288.0	299.2	-243.7
Lateral Shear F_y (N)	±3100	±3100	F	52.9	-49.1	55.5	-47.6	57.3	-50.2	55.8	-51.6	52.8	-90.9	30.0	-118.7	3.5	-158.0
			S	245.8	-82.4	255.2	-78.3	255.0	-116.7	284.3	-64.9	436.2	-89.7	428.2	-89.5	476.7	-147.5
			C	756.6	-0.8	753.2	-0.9	672.1	-2.2	887.5	-2.0	1132.4	-1.6	1084.7	-26.7	924.2	-241.4
Ten/Comp F_z (N)	4170/ -4000	4170/ -4000	F	758.3	-12.8	827.7	-11.4	888.4	-3.1	1007.8	-1.3	1053.4	-2.1	1121.2	-4.8	1118.0	-19.6
			S	970.0	-112.3	1088.9	-113.3	1199.7	-112.7	1185.5	-224.9	1107.2	-210.8	1232.4	-43.9	1257.1	-54.7
			C	1245.2	-471.8	1397.5	-436.3	1665.0	-354.7	2044.4	-418.8	1969.0	-743.9	1829.8	-757.8	1669.3	-809.4
Lateral Moment M_x (Nm)	±143	±286	F	6.6	-2.2	6.3	-3.2	6.6	-5.6	6.1	-9.0	6.7	-10.1	7.3	-11.1	8.6	-9.4
			S	12.2	-8.6	16.2	-10.9	26.3	-5.8	36.4	-5.1	43.7	-11.6	49.5	-11.4	46.5	-18.7
			C	36.2	-11.4	47.0	-8.0	71.9	-9.4	94.2	-3.3	106.2	-0.1	110.3	-0.1	98.3	-0.1
Flex/Ext Moment M_y (Nm)	190/ -96	380/ -192	F	37.8	-2.4	38.7	-0.1	43.0	0.0	54.6	-0.5	63.4	-0.4	64.6	-0.3	64.6	-0.1
			S	64.8	-0.4	65.9	-0.1	72.1	-0.1	95.5	-1.0	113.5	-0.5	111.7	-0.1	101.7	-0.1
			C	19.4	-6.7	28.0	-4.6	28.8	-5.0	33.8	-6.1	29.7	-6.4	24.2	-3.8	22.9	-6.7
Axial Moment M_z (Nm)	±96	±96	F	2.5	-1.8	1.6	-1.6	3.0	-1.8	3.9	-2.5	4.0	-3.9	4.0	-1.8	5.3	-0.8
			S	0.5	-2.9	0.1	-5.6	2.0	-12.1	3.5	-16.9	6.3	-14.8	2.1	-22.6	0.9	-28.2
			C	16.5	-17.9	9.0	-16.7	0.9	-19.2	2.4	-25.1	3.9	-27.1	0.2	-39.2	0.1	-31.4

*F: Driver, frontal impact, 13.3 m/s ΔV, 3-point force-limited belt, airbag deployment

S: Passenger, frontal impact, 11.1 m/s ΔV, 3-point belt with no retractor, no airbag deployment

C: Heidelberg-type sled test, lateral impact, 6.7 m/s ΔV, no side wall padding

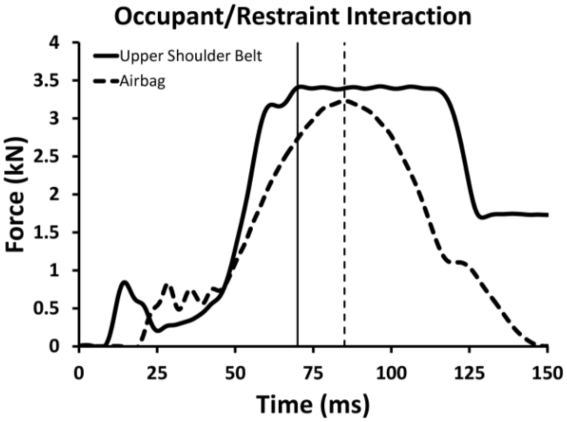

Figure 3-12: Reported interface force time histories of the occupant with the upper shoulder belt and airbag in the Forman simulation. The vertical solid line corresponds to the time of maximum engagement of the upper shoulder belt (t= 70 ms) and the vertical dashed line to the time of maximum occupant/airbag interaction (t= 85 ms).

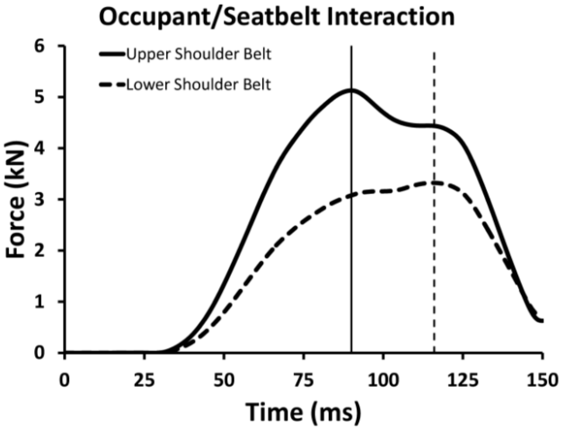

Figure 3-13: Reported interface force time history of the occupant with the upper and lower shoulder belt in the Shaw simulation. The vertical solid line corresponds to the time of maximum engagement of the upper shoulder belt (t=90 ms) and the vertical dashed line to the time of maximum engagement of the lower shoulder belt (t=116 ms).

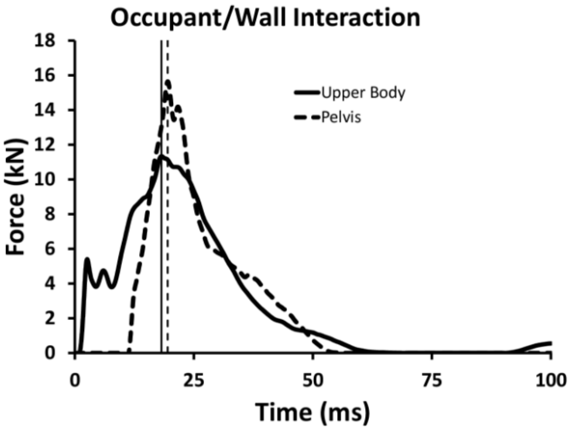

Figure 3-14: Reported interface force time history of the occupant with the wall in the Cavanaugh simulation. The vertical solid line corresponds to the time of maximum upper body-to-wall contact force (t=18 ms) and the vertical dashed line to the time of maximum pelvis-to-wall contact force (t=19.5 ms).

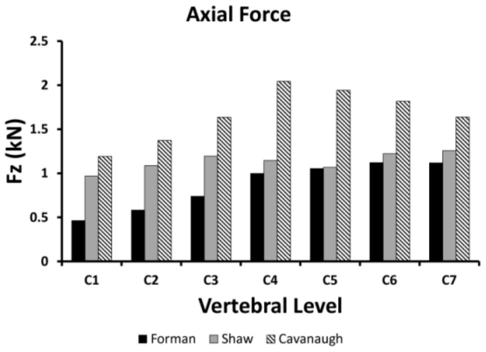

Figure 3-15: Distribution of axial forces for each vertebral level at the time of overall maximum axial force. Time of maximum axial force for the Forman, Shaw and Cavanaugh simulations occurred at t=70.2, 121.3, and 30.8 ms, respectively.

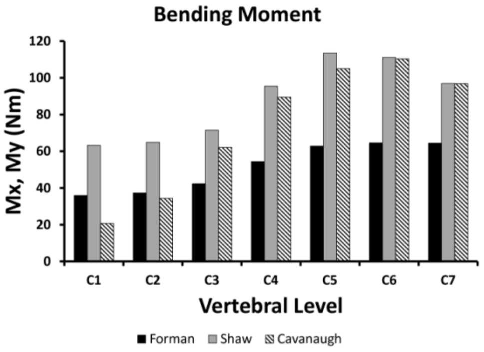

Figure 3-16: Distribution of bending moments for each vertebral level at the time of overall maximum bending moment. Time of maximum bending moment for the Forman, Shaw and Cavanaugh simulations occurred at t=122.4, 144.9, and 46.2 ms respectively. The flexion moment, My, was reported for the frontal Forman and Shaw simulations and the lateral bending moment, Mx, for the lateral Cavanaugh simulation.

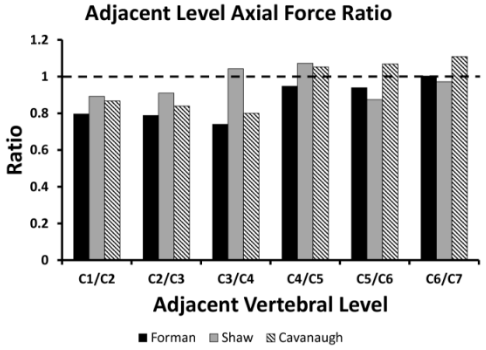

Figure 3-17: Adjacent vertebral level axial force ratio at the time of overall maximum axial force. Time of maximum axial force for the Forman, Shaw and Cavanaugh simulations occurred at t=70.2, 121.3, and 30.8 ms, respectively.

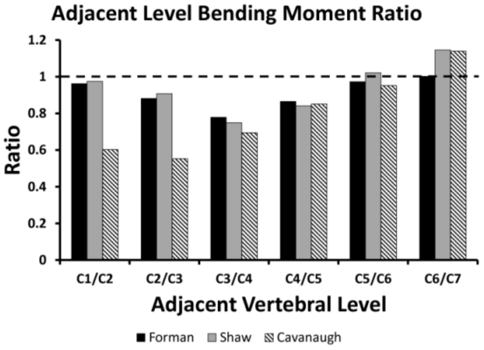

Figure 3-18: Adjacent vertebral level bending moment ratio at the time of overall maximum bending moment. Time of maximum bending moment for the Forman, Shaw and Cavanaugh simulations occurred at t=122.4, 144.9, and 46.2 ms respectively. The flexion moment ratio was reported for the frontal Forman and Shaw simulations and the lateral bending moment ratio for the lateral Cavanaugh simulation.

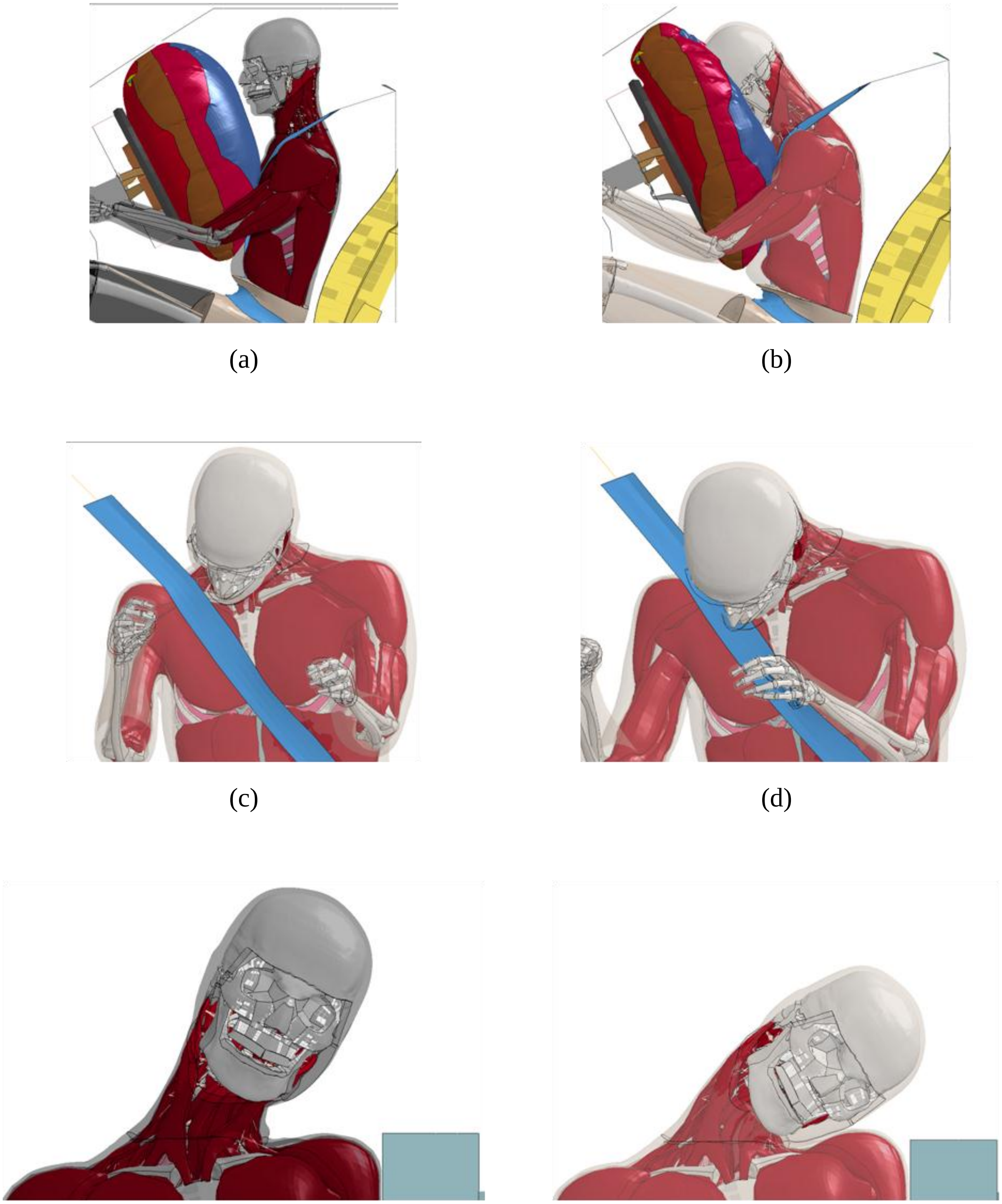

(a) (b)

(c) (d)

(e) (f)

Figure 3-19: D3plots corresponding to the approximate times of maximum neck force and moment for Forman (a) axial force and (b) flexion moment, Shaw (c) axial force and (d) and flexion moment, and Cavanaugh (e) axial force and (f) lateral moment.

Neck tension time-dependent curves were calculated for each simulation at each cervical level (Figure 3-20). None of the calculated curves exceeded the injury tolerance threshold, indicating that serious injury due to neck tension was unlikely. The N_{ij} value was calculated at each cervical level using the axial force and flexion/extension moment for both frontal sled tests and the corresponding critical intercepts (Table 3-3) as specified in FMVSS 208 [21]. The lateral moment replaced the flexion/extension moment in the calculation for the side impact test and the critical moment intercept was changed to match that used in previous lateral impact tests [56-58].

For every point in time, only one of four loading scenarios exists when calculating N_{ij} (Table 3-4). The combined N_{ij} calculations are presented as time histories for each simulation at each cervical level (Figure 3-21). Maximum N_{ij} values for each cervical level are reported in Table 3-5. The maximum N_{ij} values for both frontal simulations were below the FMVSS 208 threshold of 1, corresponding to an approximately 22% risk of serious (AIS 3+) injury (Figure 3-22) [9, 59]. The maximum N_{ij} value for the Forman and Shaw simulations were 0.313 and 0.492 at C7, respectively. The maximum value for the Cavanaugh lateral impact simulation was 1.958 at C6. Neither FMVSS 208 nor its lateral impact counterpart, FMVSS 214 [60], specify a maximum N_{ij} for lateral impacts.

Table 3-3: N_{ij} critical intercept values for the OC-C1 junction as specified FMVSS 208 [21] and for the OC-C1 and C7-T1 junctions as specified by Mertz [7].

N_{ij} Intercept	**OC-C1 (FMVSS 208)**	**OC-C1 (IARV)**	**C7-T1 (IARV)**
Ft	6806	6780	6780
Fc	-6160	-6200	-6200
Mf*	310	305	610
Me*	-135	-133	-266

*Replaced with ±60 for Cavanaugh lateral impact simulation [56-58].

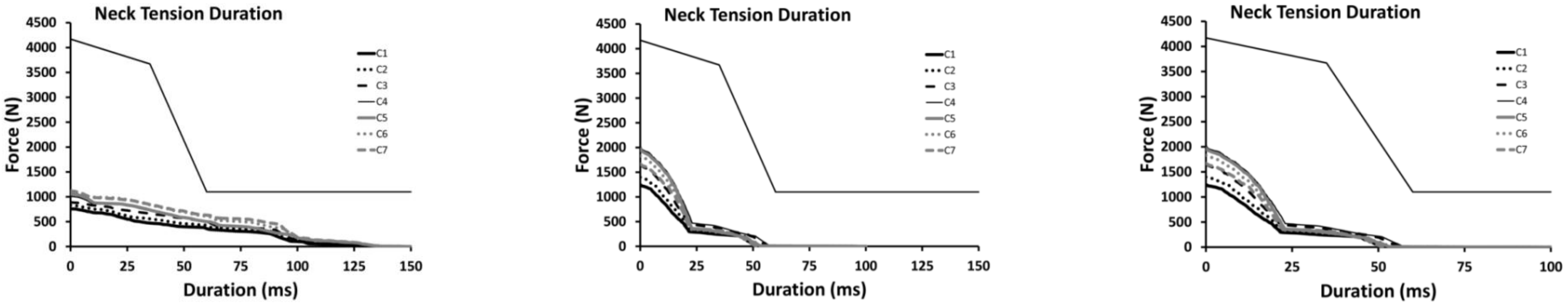

(a) (b) (c)

Figure 3-20: Neck tension duration results at each vertebral level with threshold boundary for the (a) Forman, (b) Shaw, and (c) Cavanaugh simulations.

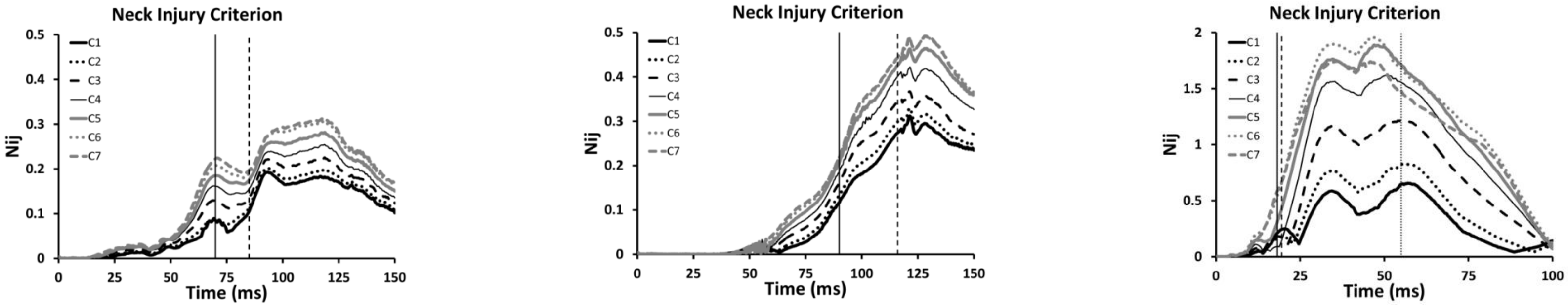

(a) (b) (c)

Figure 3-21: N_{ij} time histories at each vertebral level for the (a) Forman (b) Shaw and (c) Cavanaugh simulations. For the Forman simulation, the vertical solid line corresponds to the time of maximum engagement of the upper shoulder belt (t=70 ms) and the vertical dashed line to the time of maximum occupant/airbag interaction (t=85 ms). For the Shaw simulation, the vertical solid line corresponds to the time of maximum engagement of the upper shoulder belt (t=90 ms) and the vertical dashed line to of maximum engagement of the lower shoulder belt (t=116 ms). For the Cavanaugh simulation, the vertical solid line corresponds to the time of maximum upper body-to-wall contact force (t=18 ms), the vertical dashed line to the time of maximum pelvis-to-wall contact force (t=19.5 ms), and the vertical dotted line to the approximate time of the maximum lateral rotation of C1 with respect to C7 in the frontal plane (t=55 ms).

Table 3-4: Summary of the four possible loading modes of the neck used in calculating N_{ij}.

N_{ij}	Loading Mechanism	Force	Moment
N_{CF}	Compression-Flexion	F<0	M>0
N_{CE}	Compression-Extension	F<0	M<0
N_{TF}	Tension-Flexion	F>0	M>0
N_{TE}	Tension-Extension	F>0	M<0

Table 3-5: Maximum N_{ij} value calculated at each cervical level.

Simulation	C1	C2	C3	C4	C5	C6	C7
Forman	0.193	0.202	0.225	0.255	0.281	0.307	0.313
Shaw	0.312	0.329	0.367	0.422	0.464	0.491	0.492
Cavanaugh	0.656	0.826	1.217	1.618	1.887	1.958	1.744

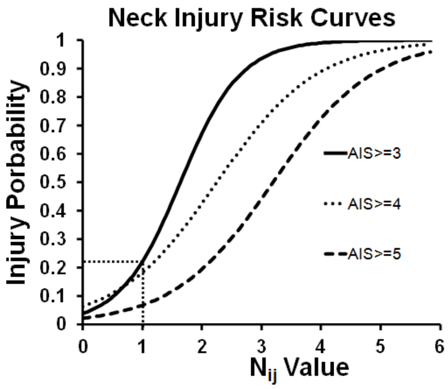

Figure 3-22: N_{ij} risk curves for AIS 3+ to AIS 5+ neck injuries. The FMVSS 208 maximum allowable N_{ij} value of 1 indicates approximately 22% risk for serious (AIS 3+) injury [9, 21].

Discussion

Methodology

This study created and utilized cross sections to calculate forces and moments within the neck of a total human body FE model during simulated frontal and lateral impacts. The local vertebral body coordinate systems were defined in a manner which can be easily replicated in any FE neck model. The nodes defining a LCSYS were constrained to their respective vertebra using *CNRBs, allowing the LCSYS to rotate. Even though the vertebrae were deformable bodies, no deformation was expected to occur for the loading scenarios. Should comparison need to be made between tracked motion of the cadaver cervical spine using high-speed, biplane x-rays, an alternative LCSYS defined by Padgaonkar [61] and utilized by White [5, 62] can be implemented. Using this alternative method, the local origin is placed at the anterior-superior vertebral body in the sagittal plane, not requiring the location of the CG.

The interface definitions created by the *DCSPs contain the elements and nodes associated with the cross sections, ensuring that elements are captured from only one side of each cut. While the best results are obtained when the *DCSP cuts cleanly through the middle of all elements, this automatic interface definition handles irregularities quite well. The captured elements and nodes depend on the part sets defined by the user, as well as the placement of the *DCSPs. For this study, part sets were created based on anatomical components within the neck including bones, IVDs, ligaments, soft tissue, active muscles, and passive muscles. Since none of the *DCSPs cut through the IVDs, no forces or moments were reported for this component. The user can always add in additional *DCSPs to capture IVDs or other structures of interest. Once the nodes and elements for each cross section are captured, they are separated into element sets and used to define *DCSSs. This step allows the user even more control over which elements are included in a cross section. Additionally, the creation of these element sets allows for visualization and inspection of the elements and nodes automatically selected by the *DCSPs.

In LS-PrePost, the SPlane option is an interactive method to report cross-sectional data. Unlike *DCSPs or *DCSSs, the SPlane option reports cross-sectional forces and moments calculated from element stress resultants in the d3plot data. There are three different methods of defining a cross-sectional cut with SPlane. The first two methods allow the section plane to be fixed in space so that it does not move once defined or to be fixed to the model so that it moves with the nodes used to define it. The Lagrangian cut option, most like *DCSP and *DCSS, captures a group of elements in the plane and tracks them throughout the d3plot animation, even if the elements move out of the plane. The SPlane options are considered less accurate than *DCSS or *DCSP which use nodal forces not included in the d3plots to calculate section forces. Additionally, the sampling rate for the SPlane data is limited by the time interval between outputs for the d3plots, which are typically lower than the ASCII outputs due to the large data size of the file.

Simulation Results

Several interesting observations can be made from the force and moment time histories of the three simulations. Axial force tended to progressively increase from the upper to lower cervical levels. A sharp decrease in axial tension occurred at the time of maximum occupant/airbag interaction in the Forman simulation, attributed to interaction with the airbag. No such decrease in axial loading was noted in the Shaw simulation, which did not include an airbag. Significant AP shear forces were observed in C1 and C2 for both the Forman and Cavanaugh simulations. The main contributors of these forces were the ligaments. Unlike C3-C7, more extensive ligamentous structures exist between OC-C1-C2. In general, the flexion moment in the frontal simulations and the lateral moment in the side impact increased caudally. This was expected as the moment arm to the head increases from C1 to C7.

The reported force and moment ratios allow for comparison between adjacent vertebral levels. A ratio less than unity indicates the force or moment at the superior vertebral level is less than the inferior level while a ratio greater than unity indicates the force or moment at the superior vertebral level is greater than the inferior level. The force ratios for the Forman and Cavanaugh simulations suggested a load distribution difference between the upper (C1-C3) and lower (C4-C7) neck. The Forman force ratios indicated the axial forces increased caudally while the Cavanaugh ratios indicated the axial forces increased caudally in the upper neck and cephalically in the lower neck. The force ratios for the Shaw simulation suggested a load distribution difference between the upper (C1-C3), middle (C4-C5), and lower (C6-C7) neck. This simulation used a generic three point seatbelt with no retractor or load limiter, producing a more abrupt deceleration of the occupant than the load limiting retractor in the Forman simulation. The maximum shoulder belt force for the Shaw simulation was approximately 5 kN while it was approximately 3.5 kN in the Forman simulation. The force ratios indicated the axial forces increased caudally in the upper and lower neck and cephalically in the middle neck. This point of inflection in the middle neck may indicate a rotation point where the head begins to wrap around the shoulder belt with no airbag to counteract this motion.

For the Forman and Shaw frontal simulations, the moment ratios decreased between C1/C2 and C3/C4, and then increased up to C6/C7 while the Cavanaugh lateral simulation produced a steady increase in moment ratios from C2/C3 to C6/C7. The moment ratio concavity in the frontal simulations is most likely due to passive restraint interactions with the occupant. The occupant torso and pelvis in the lateral simulation were not restrained. The moment ratios also indicated the moments increased caudally for all levels of the neck in all simulations, except the Cavanaugh C6/C7 and the Shaw C5/C6 and C6/C7 adjacent levels, where they increased cephalically.

None of the maximum or minimum forces and moments reported in Table 3-2 exceeded corresponding IARVs, indicating significant injury to the neck was unlikely. The neck tension duration results were also well below the threshold boundaries. While axial compression and AP shear duration plots could have also been created, it is unlikely that the corresponding injury thresholds would have been exceeded. Only minimal axial compression was noted and AP shear tended to be about half that of axial tension in the simulations. While the N_{ij} criteria is currently used to evaluate injury risk at the OC-C1 junction per FMVSS 208 [21], lower neck critical intercepts do exist [7]. In this study, the N_{ij} criteria were applied to levels of the neck between the OC-C1 junction and T1. Since no critical intercept values currently exist for these levels the FMVSS 208 specified force and moment intercepts were utilized for all levels of the neck as a worst case scenario. While the overall efficacy of N_{ij} in lateral impacts is unknown, it was modified slightly for use in the lateral Cavanaugh simulation [56-58].

It is important to note the contribution of the discrete spring elements to the overall cross-sectional results. As described in the Methods Section, the force and moment contributions of these discrete elements were manually added to the total force and moment plots for completeness. These discrete elements represent the suprahyoid and infrahyoid muscles which suspend the hyoid bone in the GHBMC model. The stiffness values of these elements were chosen for computational purposes only. In a human, the primary actions of these muscles are to elevate and depress the hyoid bone during speaking and swallowing [63], playing a minimal role in the kinematics of the neck. While these muscles can actively create tension in the neck, they do not support compressive loads. The implementation of these discrete elements may seem counterintuitive. For example, during head flexion the discrete elements develop a restoring force which counteracts the flexion moment, creating an extension moment. This is apparent when comparing the discrete element force and moment time histories with the anatomical component time histories. However, both the force and moment contributions of these discrete elements compose only a small fraction of the total forces and moments and are therefore considered negligible. The purpose of this paper was to present a method to measure forces and moments at various levels of an FE human body model neck and demonstrate how this data can be used to evaluate the risk of injury based on IARVs and injury criteria. The described method can always be modified to exclude these discrete elements at the discretion of the user.

Limitations and Future Work

There are several limitations to the current work. One is that there is no direct method to validate the forces and moments calculated at the different levels of the neck, as these values could not be measured in the actual cadaveric experiments. While it is possible to estimate the forces and moments at the OC [19] and T1 [64] using inverse kinematic methods in cadavers, there is no direct measurement method. Traditionally, the inverse kinematic approaches have been acceptable and are therefore the best available data for comparison. The GHBMC T1 is modelled as a rigid body and therefore cannot be included in the cross section definition. Modifications to the GHBMC neck model are underway to make T1 deformable. Converting T1 to a deformable body requires not only changing the material definition, but any associated attachment points. Lastly, the elements initially defined in the *DCSSs for a particular cross section may potentially move out of plane as the neck deforms. Unless there is direct impact to the neck or extreme head motion, the potential for this to occur should be minimal. The reader is cautioned that the force and moment results depend on how the cross-sectional plane, captured elements, and local coordinate system are defined. Care was taken to choose the best cross sections for the intended purpose, and to avoid redundant load measurement axially through the entire neck.

Future work includes studying the effects of both anterior cervical discectomy and fusion (ACDF) and cervical total disc replacement (CTDR) on adjacent vertebral levels using the described cross-sectional technique. Current literature debates whether cervical fusion deleteriously alters the loading of the adjacent segments, increasing adjacent-segment disease (ASD). By preserving motion and loading distribution, some consider CTDRs a method to reduce the likelihood of ASD [65-70]. The use of cross sections to measure load contributions from the cervical zygapophysial and uncovertebral joints will also be investigated in future studies.

Conclusions

This paper described and implemented a method to determine cross-sectional forces and moments at various levels of a human body FE model neck during simulated frontal and lateral MVCs. Total force and moment time histories were reported for each vertebral and compared to established IARVs to determine if significant injury was likely to occur. Adjacent level axial force ratios varied between 0.74 and 1.11 and adjacent level bending moment ratios between 0.55 and 1.15. The individual contribution of neck anatomical components to the total cross-sectional forces and moments were also evaluated. Neck tension time-dependent curves and N_{ij} time histories were calculated for each cervical level and compared to injury threshold standards. The procedure presented in this paper can be applied not only to the neck, but also to other regions of the body. It is helpful for full-body FE models to provide transducer data similar to their physical counterparts, ATDs, to properly evaluate the safety of an automobile.

Acknowledgements

The authors would like to acknowledge the Global Human Body Models Consortium for use of the 50th percentile seated male FE model and the United States Army Medical Research and Materiel Command for funding this research. Special thanks are given to Mr. Adam Golman for his advice on cross section implementation and Mr. Nicholas Vavalle for his work on the GHBMC model. All computations were performed on the Wake Forest University DEAC Cluster, a centrally managed resource with support provided in part by the University.

Chapter 3 References

[1] McElhaney J, Nightingale R, Winkelstein B, Chancey V, Myers B. Biomechanical Aspects of Cervical Trauma. In: Nahum A, Melvin J, editors. Accidental Injury: Biomechanics and Prevention. New York: Springer; 2002. p. 324-73.

[2] National Spinal Cord Injury Statistical Center. The 2011 Annual Statistical Report for the Spinal Cord Injury Model. University of Alabama at Birmingham; 2011.

[3] Yoganandan N, Haffner M, Maiman DJ, Nichols H, Pintar F, Jentzen J, et al. Epidemiology and Injury Biomechanics of Motor Vehicle Related Trauma to the Human Spine. SAE Technical Paper 892438. 1989.

[4] Schmitt K-U, Niederer P, Muser M, Walz F. Trauma Biomechanics: Accidental Injury in Traffic and Sports. 3rd ed. New York: Springer; 2010.

[5] White NA, Begeman P, Hardy W, Yang KH, Ono K, Sato F, et al. Investigation of Upper Body and Cervical Spine Kinematics of Post Mortem Human Subjects (PMHS) During Low-Speed, Rear-End Impacts. SAE Technical Paper 2009-01-0387. 2009.

[6] Mertz HJ. Anthropomorphic Test Device. In: Nahum A, Melvin J, editors. Accidental Injury: Biomechanics and Prevention. New York: Springer; 2002.

[7] Mertz HJ, Irwin AL, Prasad P. Biomechanical and Scaling Bases for Frontal and Side Impact Injury Assessment Reference Values. Stapp car crash journal. 2003;47:155-88.

[8] Society of Automotive Engineers. SAE J1727 - Calculation Guidelines for Impact Testing. 2010.

[9] Eppinger R, Sun E, Bandak F, Haffner M, Khaewpong N, Maltese M, et al. Development of Improved Injury Criteria for the Assessment of Advanced Automobile Restraint Systems - II. NHTSA Docket No. 1999-6407-5. 1999.

[10] Eppinger R, Sun E, Kuppa S, Saul R. Development of Improved Injury Criteria for the Assessment of Advanced Automobile Restraint Systems - II. NHTSA Docket No. 2010-03-19. 2000.

[11] Kleinberger M, Sun E, Eppinger R, Kuppa S, Saul R. Development of Improved Injury Criteria for the Assessment of Advanced Automobile Restraint Systems. NHTSA Docket No. 1998-4405-9. 1998.

[12] Klinich K, Saul R, Auguste G, Backaitis S, Kleinberger M. NHTSA Child Protection Team. Techniques for Developing Child Dummy Protection Reference Values. NHTSA Docket No. 74-14, Notice 97, Item 069. 1996.

[13] Mertz HJ, Nyquist GW, Hodgson VR, Weber DA. Response of Animals Exposed to Deployment of Various Passenger Inflatable Restraint System Concepts for a Variety of Collision Severities and Animal Positions. SAE Technical Paper 826047. 1982.

[14] Mertz HJ, Weber DA. Interpretations of the Impact Responses of a 3-Year-Old Child Dummy Relative to Child Injury Potential. SAE Technical Paper 826048. 1982.

[15] Prasad P, Daniel RP. A Biomechanical Analysis of Head, Neck, and Torso Injuries to Child Surrogates Due to Sudden Torso Acceleration. SAE Technical Paper 841656. 1984.

[16] Bostrom O, Svensson M, Aldman B, Hansson H, Haland Y, Lovsund P, et al. A New Neck Injury Criterion Candidate Based on Injury Findings in the Cervical Ganglia after Experimental Neck Extension Trauma. IRCOBI. 1996.

[17] Schmitt K-U, Muser M, Walz F, Niederer P. Nkm - a Proposal for a Neck Protection Criterion for Low Speed Rear-End Impacts. Traffic Injury Prevention. 2002;3:117-26.

[18] Goldsmith W, Ommaya A. Head and Neck Injury Criteria and Tolerance Levels. In: Aldman B, Chapon A, editors. The Biomechanics of Impact Trauma. Amsterdam: Elsevier Science Publisher; 1984. p. 149-87.

[19] Mertz HJ, Patrick L. Strength and Response of the Human Neck. SAE Technical Paper 710855. 1971.

[20] Heitplatz F, Sferco R, Fay P, Reim J, Kim A, Prasad P. An Evaluation of Existing and Proposed Injury Criteria with Various Dummies to Determine Their Ability to Predict the Levels of Soft Tissue Neck Injury Seen in Real World Accidents. 18th International Technical Conference on the Enhanced Safety of Vehicles (ESV). 2003.

[21] NHTSA. Title 49 Code of Federal Regulations (CFR) Part 571 Section 208, Occupant Crash Protection. Washington, DC: Office of the Federal Register, National Archives and Records Administration; 2008.

[22] United Nations Economic Commission for Europe. Addendum 93, Regulation No. 94, Uniformed Provisions Concerning the Approval of Vehicles with Regard to the Protection of the Occupants in the Event of a Frontal Collision. 2007.

[23] McHenry R. Analysis of the Dynamics of Automobile Passenger-Restraint Systems. 7th Stapp Car Crash Conference. 1963.

[24] Prasad P, Chou CC. A Review of Mathematical Occupant Simulation Models. In: Nahum A, Melvin J, editors. Accidental Injury: Biomechanics and Prevention. 2nd ed. New York: Springer; 2002. p. 121-86.

[25] Yang KH, Hu J, White NA, King AI, Chou CC, Prasad P. Development of Numerical Models for Injury Biomechanics Research: A Review of 50 Years of Publications in the Stapp Car Crash Conference. Stapp car crash journal. 2006;50:429-90.

[26] Hu J. Neck Injury Mechanism in Rollover Crashes - a Systematic Approach for Improving Rollover Neck Protection. Detroit, MI: Wayne State University; 2007.

[27] Saito T, Yamamuro T, Shikata J, Oka M, Tsutsumi S. Analysis and Prevention of Spinal Column Deformity Following Cervical Laminectomy. I. Pathogenetic Analysis of Postlaminectomy Deformities. Spine. 1991;16:494-502.

[28] Camacho D, Nightingale R, Robinette J, Vanguri S, Coates D, Myers B. Experimental Flexibility Measurements for the Development of a Computational Head-Neck Model Validated for near-Vertex Head Impact. SAE Technical Paper 973345. 1997.

[29] Dauvilliers F, Bendjellal F, Weiss M, Lavaste F, Tarrière C. Development of a Finite Element Model of the Neck. SAE Technical Paper 942210. 1994.

[30] de Jager M, Sauren A, Thunnissen J, Wismans J. A Global and a Detailed Mathematical Model for Head-Neck Dynamics. SAE Technical Paper 962430. 1996.

[31] Deng YC, Fu J. Simulation and Identification of the Neck Muscle Activities During Head and Neck Flexion Whiplash. SAE Technical Paper 2002-01-0017. 2002.

[32] Deng YC, Li X, Liu Y. Modeling of the Human Cervical Spine Using Finite Element Techniques. SAE Technical Paper 1999-01-1310. 1999.

[33] Halldin PH, Brolin K, Kleiven S, von Holst H, Jakobsson L, Palmertz C. Investigation of Conditions That Affect Neck Compression- Flexion Injuries Using Numerical Techniques. Stapp car crash journal. 2000;44:127-38.

[34] Kleinberger M. Application of Finite Element Techniques to the Study of Cervical Spine Mechanics. SAE Technical Paper 933131. 1993.

[35] Kumaresan S, Yoganandan N, Pintar F. Age-Specific Pediatric Cervical Spine Biomechanical Responses: Three-Dimensional Nonlinear Finite Element Models. SAE Technical Paper 973319. 1997.

[36] Maurel N, Lavaste F, Skalli W. A Three-Dimensional Parameterized Finite Element Model of the Lower Cervical Spine. Study of the Influence of the Posterior Articular Facets. Journal of biomechanics. 1997;30:921-31.

[37] Meyer F, Bourdet N, Deck C, Willinger R, Raul JS. Human Neck Finite Element Model Development and Validation against Original Experimental Data. Stapp car crash journal. 2004;48:177-206.

[38] Nitsche S, Krabbel G, Appel H, Huag E. Validation of a Finite-Element Model of the Human Neck. International IRCOBI Conference on the Biomechanics of Impacts. Dublin, Ireland. 1996.

[39] van der Horst M, Thunnissen J, Happee R, van Haaster R. The Influence of Muscle Activity on Head-Neck Response During Impact. SAE Technical Paper 973346. 1997.

[40] Yang KH, Zhu F, Luan F, Zhao L, Begeman P. Development of a Finite Element Model of the Human Neck. SAE Technical Paper 983157. 1998.

[41] Zhang QH, Teo EC, Ng HW. Development and Validation of a Co-C7 Fe Complex for Biomechanical Study. Journal of biomechanical engineering. 2005;127:729-35.

[42] Gayzik FS, Moreno DP, Danelson KA, McNally C, Klinich KD, Stitzel JD. External Landmark, Body Surface, and Volume Data of a Mid-Sized Male in Seated and Standing Postures. Annals of biomedical engineering. 2012;40:2019-32.

[43] Gayzik FS, Moreno DP, Geer CP, Wuertzer SD, Martin RS, Stitzel JD. Development of a Full Body CAD Dataset for Computational Modeling: A Multi-Modality Approach. Annals of biomedical engineering. 2011;39:2568-83.

[44] Stitzel JD. Global Human Body Models Consortium (GHBMC) Male 50th Percentile (M50) Occupant Model Manual. Virginia Tech – Wake Forest University Center for Injury Biomechanics; 2011.

[45] DeWit JA, Cronin DS. Cervical Spine Segment Finite Element Model for Traumatic Injury Prediction. Journal of the mechanical behavior of biomedical materials. 2012;10:138-50.

[46] Fice JB, Cronin DS. Investigation of Whiplash Injuries in the Upper Cervical Spine Using a Detailed Neck Model. Journal of biomechanics. 2012;45:1098-102.

[47] Fice JB, Cronin DS, Panzer MB. Cervical Spine Model to Predict Capsular Ligament Response in Rear Impact. Annals of biomedical engineering. 2011;39:2152-62.

[48] Mattucci SF, Moulton JA, Chandrashekar N, Cronin DS. Strain Rate Dependent Properties of Younger Human Cervical Spine Ligaments. Journal of the mechanical behavior of biomedical materials. 2012;10:216-26.

[49] Vavalle NA, Moreno DP, Rhyne AC, Stitzel JD, Gayzik FS. Lateral Impact Validation of a Geometrically Accurate Full Body Finite Element Model for Blunt Injury Prediction. Annals of biomedical engineering. 2012.

[50] Forman J, Lessley D, Kent R, Bostrom O, Pipkorn B. Whole-Body Kinematic and Dynamic Response of Restrained PMHS in Frontal Sled Tests. Stapp car crash journal. 2006;50:299-336.

[51] Shaw G, Parent D, Purtsezov S, Lessley D, Crandall J, Kent R, et al. Impact Response of Restrained PMHS in Frontal Sled Tests: Skeletal Deformation Patterns under Seat Belt Loading. Stapp car crash journal. 2009;53:1-48.

[52] Cavanaugh J, Walilko T, Malhotra A, Zhu Y, King A. Biomechanical Response and Injury Tolerance of the Pelvis in Twelve Sled Side Impacts. SAE Technical Paper 902305. 1990:1-12.

[53] Cavanaugh J, Walilko T, Malhotra A, Zhu Y, King A. Biomechanical Response and Injury Tolerance of the Thorax in Twelve Sled Side Impacts. SAE Technical Paper 902307. 1990:23-38.

[54] Cavanaugh J, Zhu Y, Huang Y, King A. Injury and Response of the Thorax in Side Impact Cadaveric Tests. SAE Technical Paper 933127. 1993:199-221.

[55] Society of Automotive Engineers. SAE J211/1 - Instrumentation for Impact Test-Part 1-Electronic Instrumentation. 2007.

[56] DeWeese R, Moorcroft D, Green T, Philippens MMGM. Assessment of Injury Potential in Aircraft Side-Facing Seats Using the Es-2 Anthropomorphic Test Dummy. Federal Aviation Administration, DOT/FAA/AM-07/132007.

[57] Green T, Barth T. Injury Evaluation and Comparison of Lateral Impacts When Using Conventional and Inflatable Restraints. Creswell, OR: SAFE Association. 2006.

[58] Soltis S. An Overview of Existing and Needed Neck Impact Injury Criteria for Sideward Facing Aircraft Seats. Proceedings of the Third Triennial International Aircraft Fire and Cabin Safety Research Conference. 2001.

[59] Association for the Advancement of Automotive Medicine. Abbreviated Injury Scale © 2005 Update 2008. In: Gennarelli TA, Wodzin E, editors. Barrington, IL2008.

[60] NHTSA. Title 49 Code of Federal Regulations (CFR) Part 571 Section 214, Side Impact Protection. Washington, DC: Office of the Federal Register, National Archives and Records Administration; 2008.

[61] Padgaonkar AJ. Validation Study of a Three-Dimensional Crash Victim Simulator for Pedestrian-Vehicle Impact. Detroit, MI: Wayne State University; 1976.

[62] White NA, Hu J, Yang KH. Conceptual Development of a Personalised Whiplash Protection System. International Journal of Vehicle Safety. 2008;3:163-78.

[63] Moore KL, Agur AMR. Essential Clinical Anatomy. New York: Lippincott, Williams and Wilkins; 2002.

[64] Pintar FA, Yoganandan N, Maiman DJ. Lower Cervical Spine Loading in Frontal Sled Tests Using Inverse Dynamics: Potential Applications for Lower Neck Injury Criteria. Stapp car crash journal. 2010;54:133-66.

[65] Galbusera F, Bellini CM, Brayda-Bruno M, Fornari M. Biomechanical Studies on Cervical Total Disc Arthroplasty: A Literature Review. Clinical biomechanics. 2008;23:1095-104.

[66] Baaj AA, Uribe JS, Vale FL, Preul MC, Crawford NR. History of Cervical Disc Arthroplasty. Neurosurgical focus. 2009;27:E10.

[67] Bartels RH, Donk R, Verbeek AL. No Justification for Cervical Disk Prostheses in Clinical Practice: A Meta-Analysis of Randomized Controlled Trials. Neurosurgery. 2010;66:1153-60; discussion 60.

[68] Fekete TF, Porchet F. Overview of Disc Arthroplasty-Past, Present and Future. Acta neurochirurgica. 2010;152:393-404.

[69] Kishen TJ, Diwan AD. Fusion Versus Disk Replacement for Degenerative Conditions of the Lumbar and Cervical Spine: Quid Est Testimonium? The Orthopedic clinics of North America. 2010;41:167-81.

[70] Uschold TD, Fusco D, Germain R, Tumialan LM, Chang SW. Cervical and Lumbar Spinal Arthroplasty: Clinical Review. AJNR American journal of neuroradiology. 2011.

Appendix A: Cross-Sectional Visualization

Projected cross-sectional visualization of the neck at each vertebral level (C1-T1) including the bone, passive muscles, and soft tissue. Beam (ligaments and active muscles) and discrete elements are not shown. While included for completeness, forces and moments were not calculated at the level of T1 since this vertebra is currently defined as a rigid body and cannot be included in a cross-section.

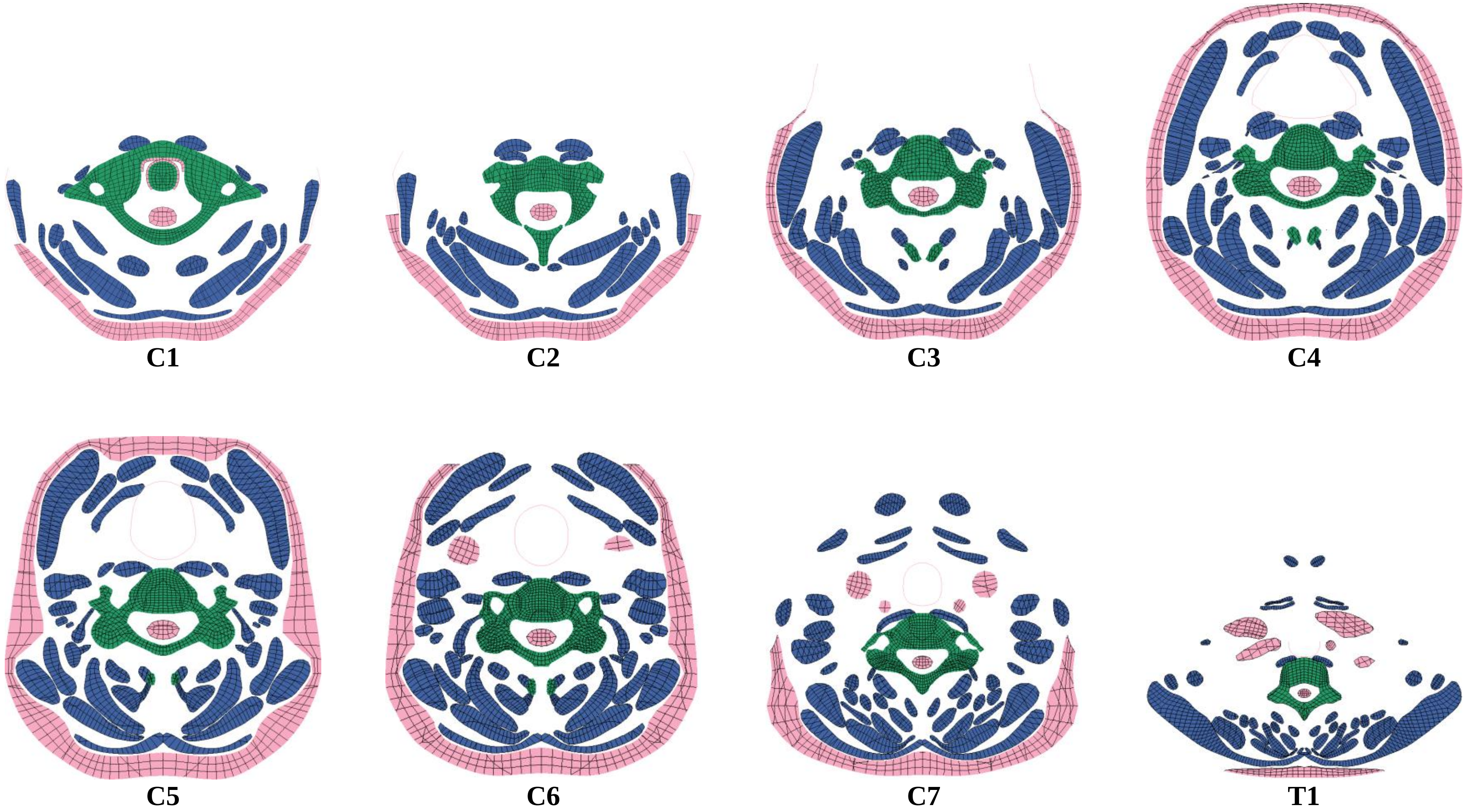
C1 **C2** **C3** **C4**

C5 **C6** **C7** **T1**

Appendix B: Forman frontal impact simulation

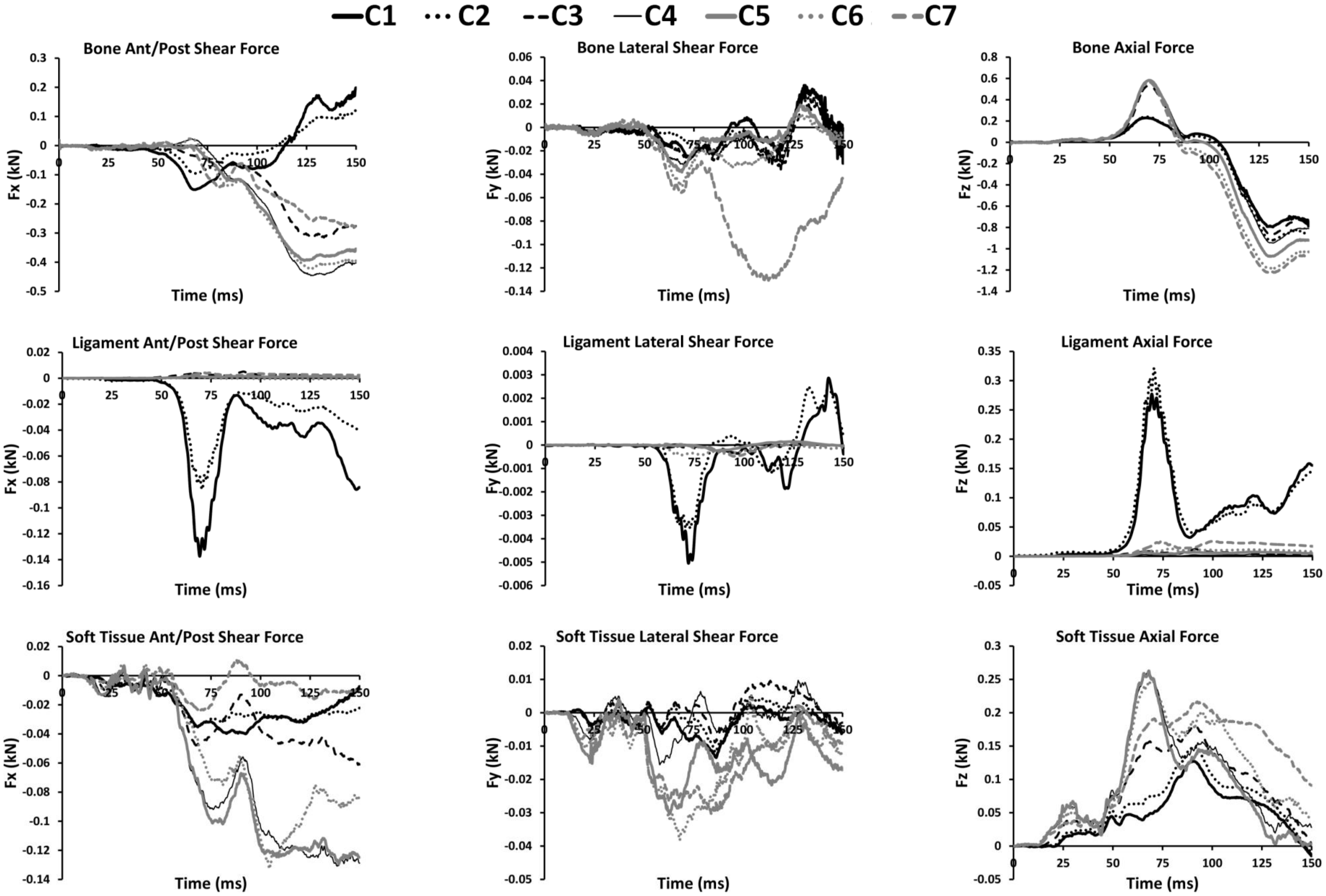

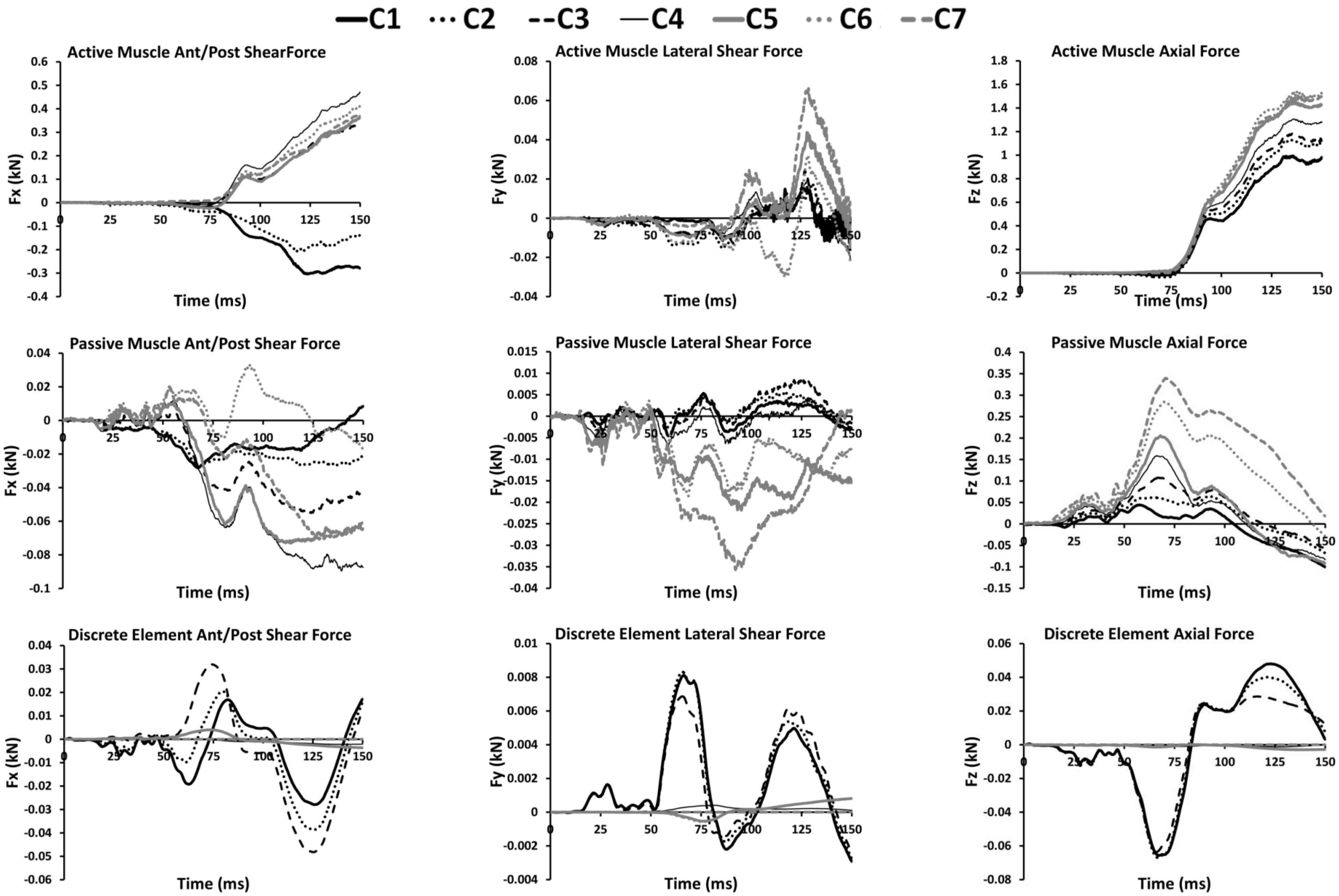
C1
C2
C3
C4
C5
C6
C7
Active Muscle Ant/Post ShearForce
Fx (kN)
0.6
0.5
0.4
0.3
0.2
0.1
0
-0.1
-0.2
-0.3
-0.4
0
25
50
75
100
125
150
Time (ms)
Active Muscle Lateral Shear Force
Fy (kN)
0.08
0.06
0.04
0.02
0
-0.02
-0.04
Time (ms)
Active Muscle Axial Force
Fz (kN)
1.8
1.6
1.4
1.2
1
0.8
0.6
0.4
0.2
0
-0.2
Time (ms)
Passive Muscle Ant/Post Shear Force
Fx (kN)
0.04
0.02
0
-0.02
-0.04
-0.06
-0.08
-0.1
Time (ms)
Passive Muscle Lateral Shear Force
Fy (kN)
0.015
0.01
0.005
0
-0.005
-0.01
-0.015
-0.02
-0.025
-0.03
-0.035
-0.04
Time (ms)
Passive Muscle Axial Force
Fz (kN)
0.4
0.35
0.3
0.25
0.2
0.15
0.1
0.05
0
-0.05
-0.1
-0.15
Time (ms)
Discrete Element Ant/Post Shear Force
Fx (kN)
0.04
0.03
0.02
0.01
0
-0.01
-0.02
-0.03
-0.04
-0.05
-0.06
Time (ms)
Discrete Element Lateral Shear Force
Fy (kN)
0.01
0.008
0.006
0.004
0.002
0
-0.002
-0.004
Time (ms)
Discrete Element Axial Force
Fz (kN)
0.06
0.04
0.02
0
-0.02
-0.04
-0.06
-0.08
Time (ms)

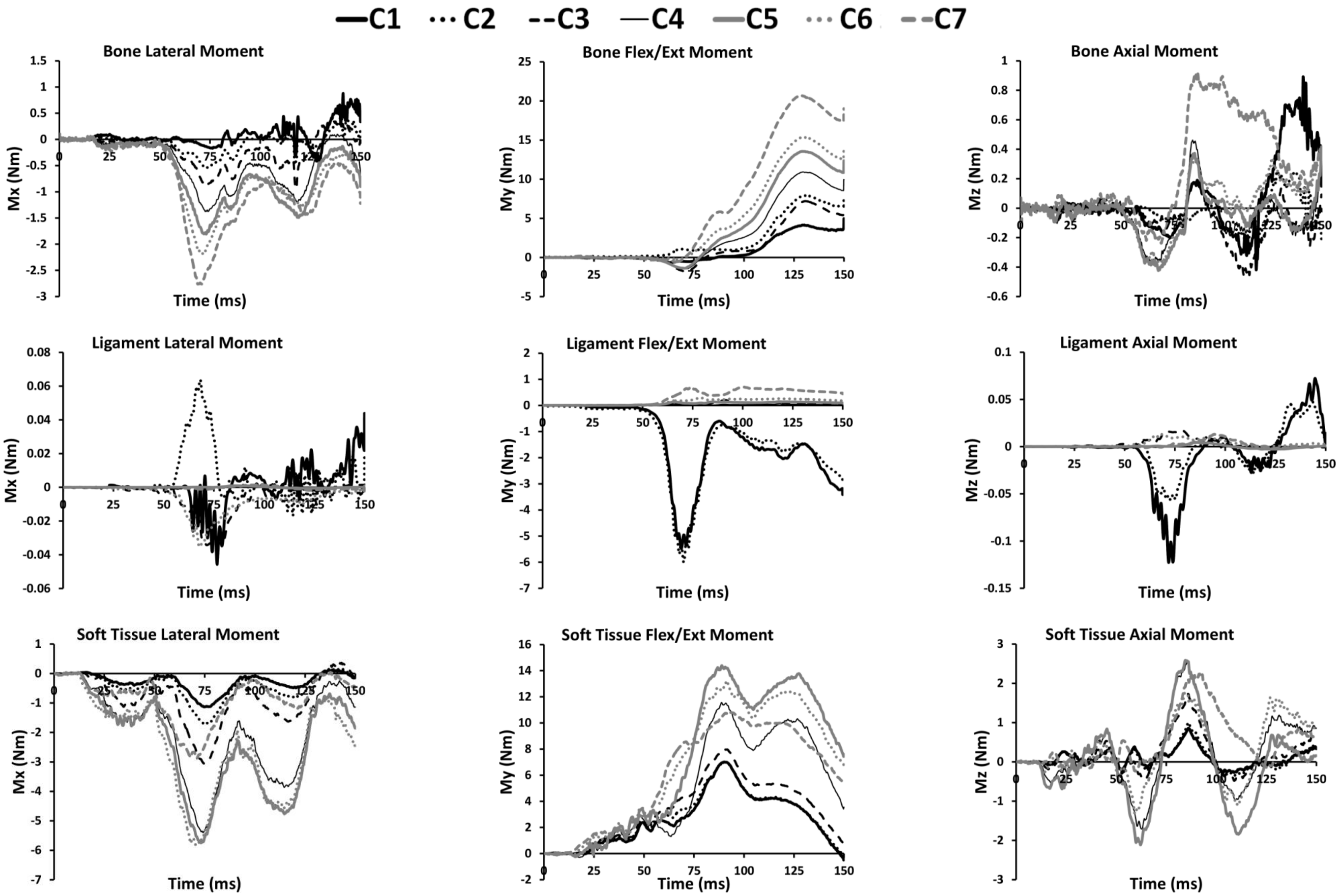
C1
C2
C3
C4
C5
C6
C7
Bone Lateral Moment
Mx (Nm)
1.5
1
0.5
0
-0.5
-1
-1.5
-2
-2.5
-3
0
25
50
75
100
125
150
Time (ms)
Bone Flex/Ext Moment
My (Nm)
25
20
15
10
5
0
-5
0
25
50
75
100
125
150
Time (ms)
Bone Axial Moment
Mz (Nm)
1
0.8
0.6
0.4
0.2
0
-0.2
-0.4
-0.6
0
25
50
75
100
125
150
Time (ms)
Ligament Lateral Moment
Mx (Nm)
0.08
0.06
0.04
0.02
0
-0.02
-0.04
-0.06
0
25
50
75
100
125
150
Time (ms)
Ligament Flex/Ext Moment
My (Nm)
2
1
0
-1
-2
-3
-4
-5
-6
-7
0
25
50
75
100
125
150
Time (ms)
Ligament Axial Moment
Mz (Nm)
0.1
0.05
0
-0.05
-0.1
-0.15
0
25
50
75
100
125
150
Time (ms)
Soft Tissue Lateral Moment
Mx (Nm)
1
0
-1
-2
-3
-4
-5
-6
-7
0
25
50
75
100
125
150
Time (ms)
Soft Tissue Flex/Ext Moment
My (Nm)
16
14
12
10
8
6
4
2
0
-2
0
25
50
75
100
125
150
Time (ms)
Soft Tissue Axial Moment
Mz (Nm)
3
2
1
0
-1
-2
-3
0
25
50
75
100
125
150
Time (ms)

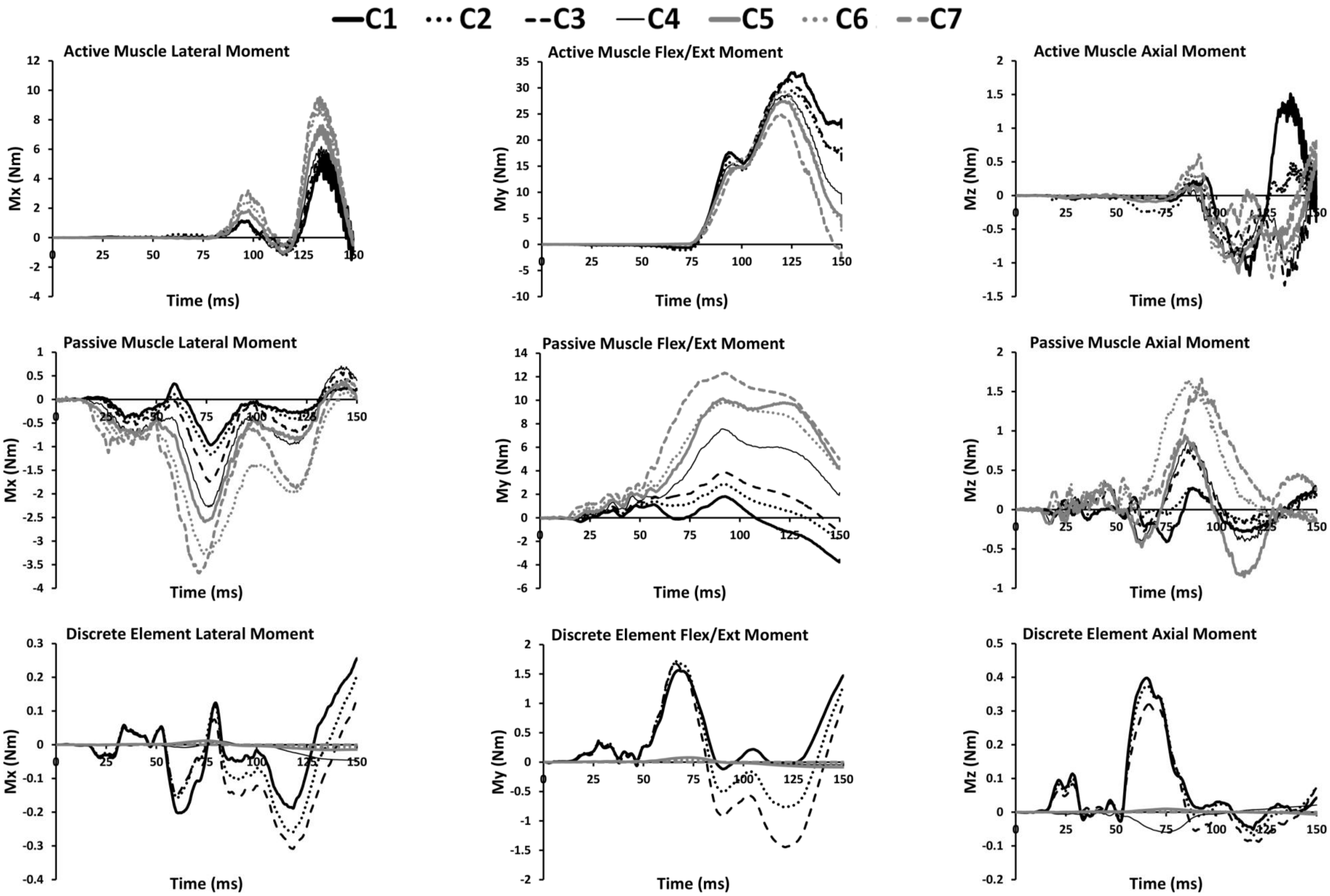
C1
C2
C3
C4
C5
C6
C7
Active Muscle Lateral Moment
Mx (Nm)
12
10
8
6
4
2
0
-2
-4
0
25
50
75
100
125
150
Time (ms)
Active Muscle Flex/Ext Moment
My (Nm)
35
30
25
20
15
10
5
0
-5
-10
0
25
50
75
100
125
150
Time (ms)
Active Muscle Axial Moment
Mz (Nm)
2
1.5
1
0.5
0
-0.5
-1
-1.5
0
25
50
75
100
125
150
Time (ms)
Passive Muscle Lateral Moment
Mx (Nm)
1
0.5
0
-0.5
-1
-1.5
-2
-2.5
-3
-3.5
-4
0
25
50
75
100
125
150
Time (ms)
Passive Muscle Flex/Ext Moment
My (Nm)
14
12
10
8
6
4
2
0
-2
-4
-6
0
25
50
75
100
125
150
Time (ms)
Passive Muscle Axial Moment
Mz (Nm)
2
1.5
1
0.5
0
-0.5
-1
0
25
50
75
100
125
150
Time (ms)
Discrete Element Lateral Moment
Mx (Nm)
0.3
0.2
0.1
0
-0.1
-0.2
-0.3
-0.4
0
25
50
75
100
125
150
Time (ms)
Discrete Element Flex/Ext Moment
My (Nm)
2
1.5
1
0.5
0
-0.5
-1
-1.5
-2
0
25
50
75
100
125
150
Time (ms)
Discrete Element Axial Moment
Mz (Nm)
0.5
0.4
0.3
0.2
0.1
0
-0.1
-0.2
0
25
50
75
100
125
150
Time (ms)

Appendix C: Shaw frontal impact simulation

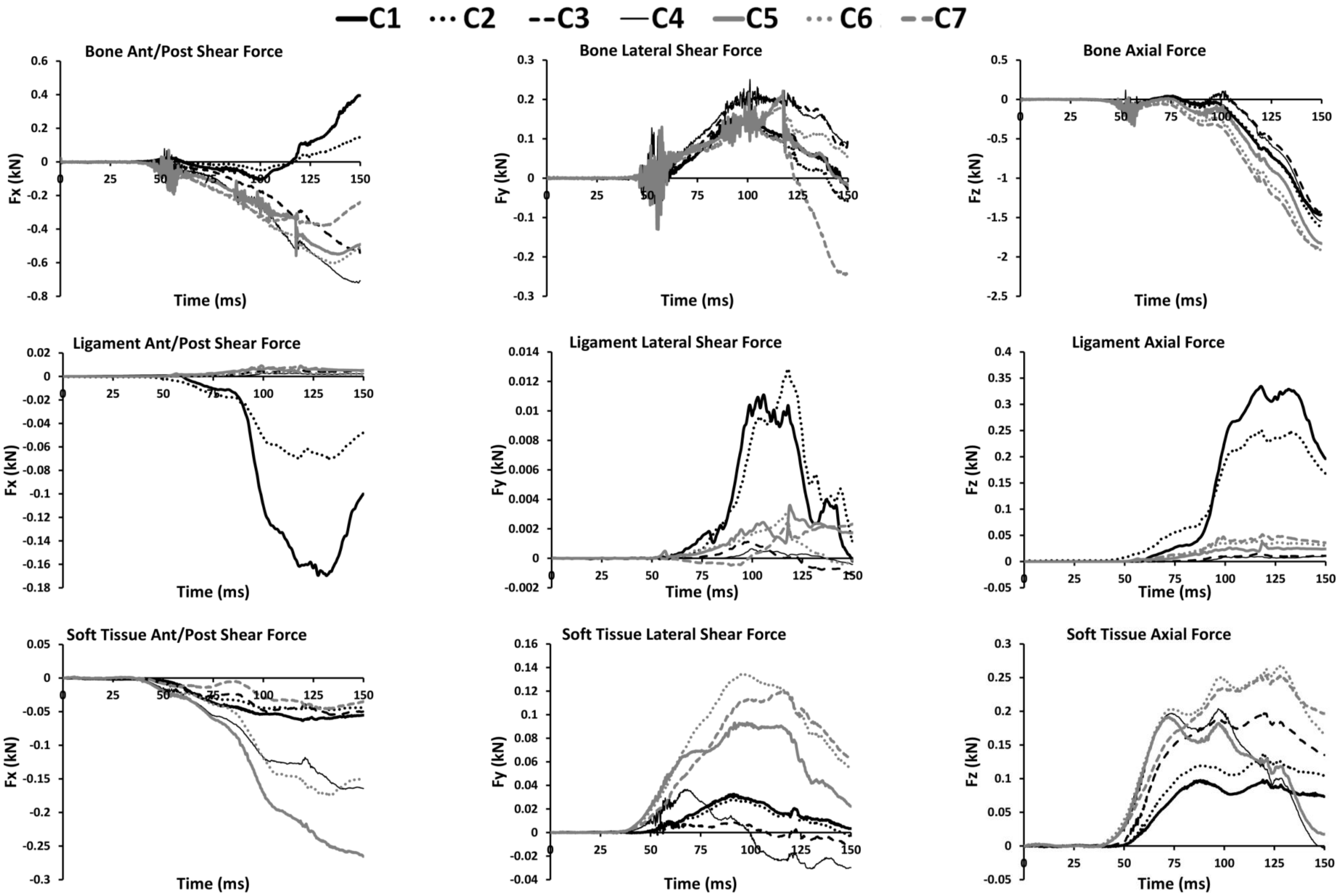

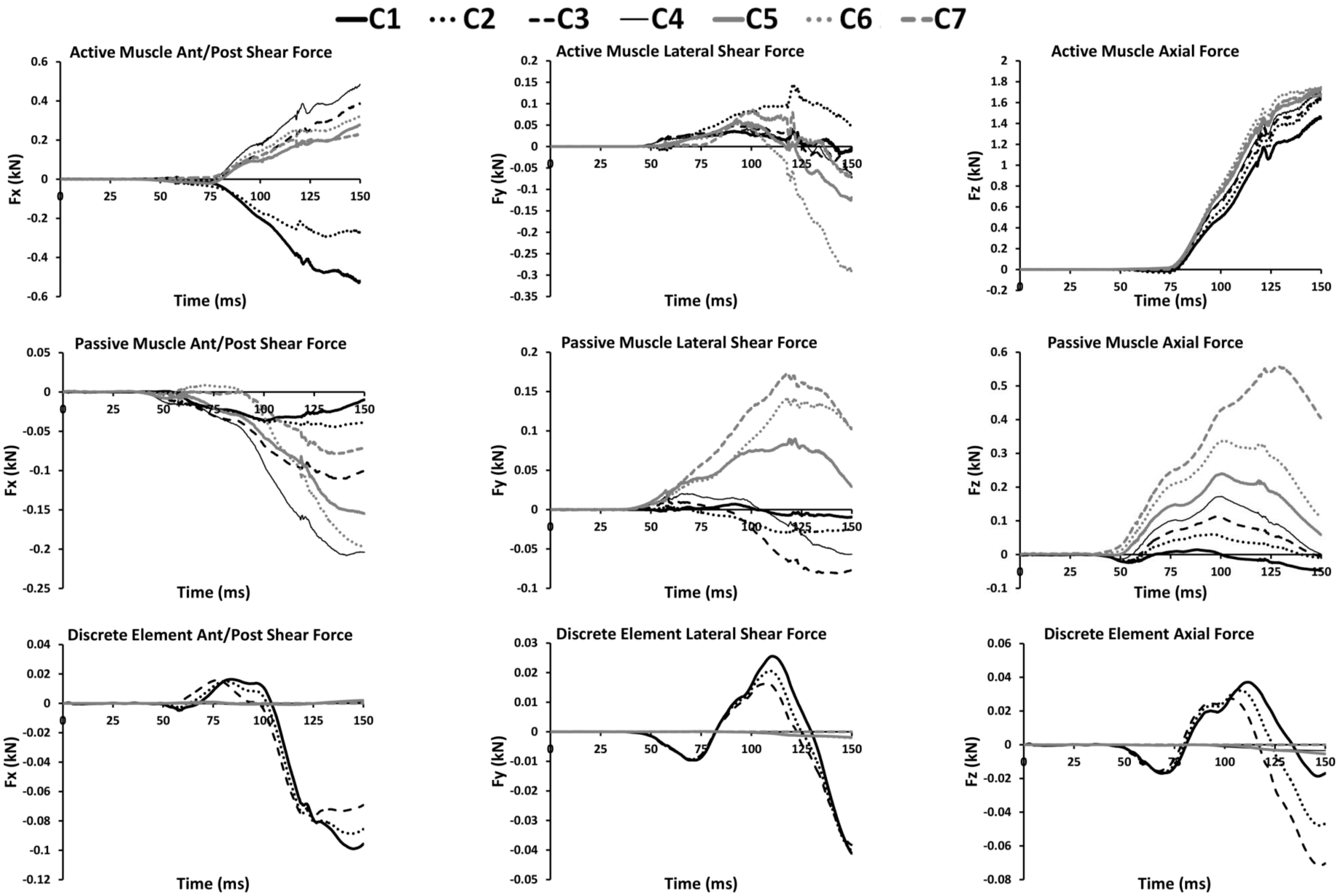
C1
C2
C3
C4
C5
C6
C7
Active Muscle Ant/Post Shear Force
Fx (kN)
Time (ms)
Active Muscle Lateral Shear Force
Fy (kN)
Time (ms)
Active Muscle Axial Force
Fz (kN)
Time (ms)
Passive Muscle Ant/Post Shear Force
Fx (kN)
Time (ms)
Passive Muscle Lateral Shear Force
Fy (kN)
Time (ms)
Passive Muscle Axial Force
Fz (kN)
Time (ms)
Discrete Element Ant/Post Shear Force
Fx (kN)
Time (ms)
Discrete Element Lateral Shear Force
Fy (kN)
Time (ms)
Discrete Element Axial Force
Fz (kN)
Time (ms)
0
25
50
75
100
125
150

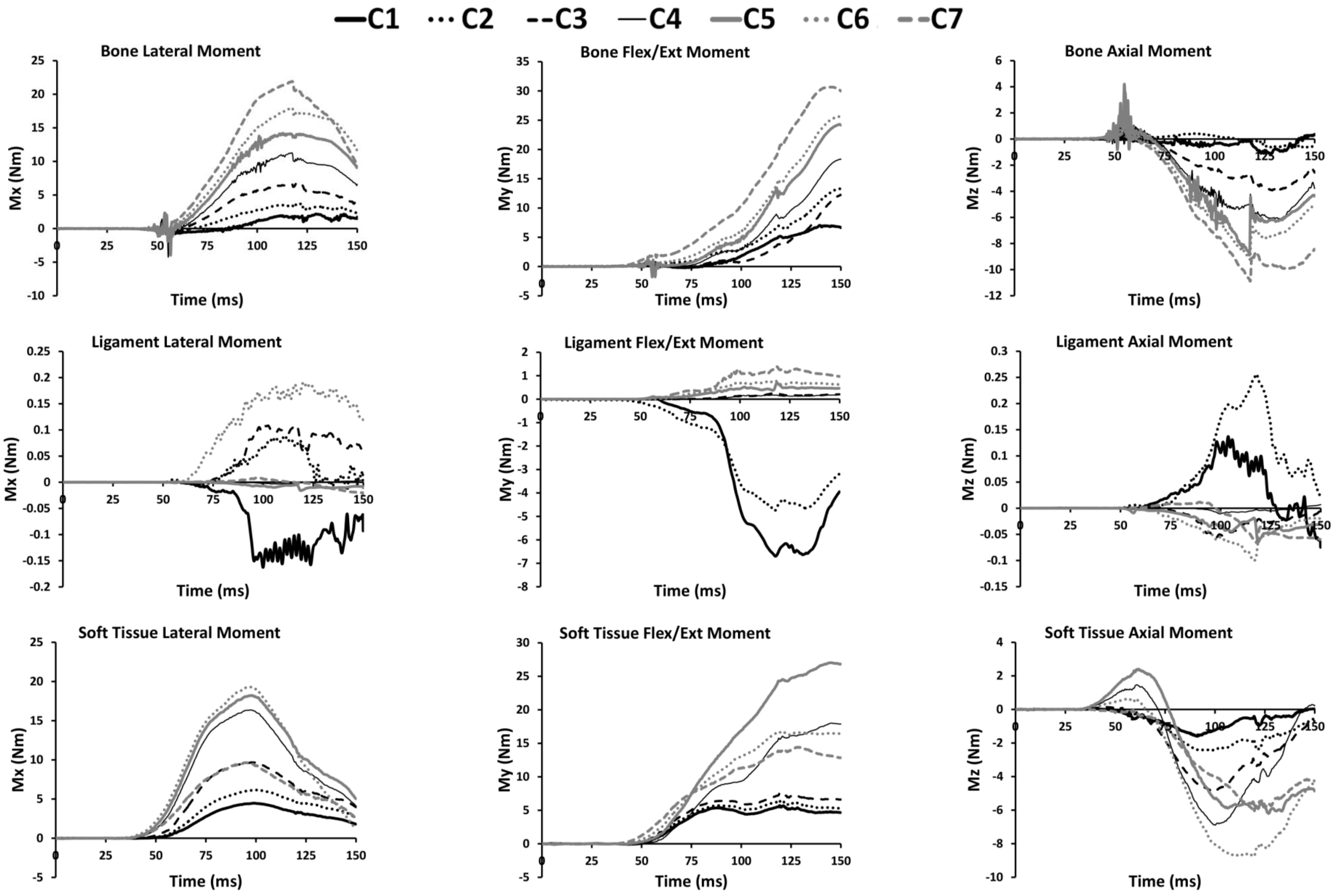

C1
C2
C3
C4
C5
C6
C7
Bone Lateral Moment
Mx (Nm)
25
20
15
10
5
0
-5
-10
0
25
50
75
100
125
150
Time (ms)
Bone Flex/Ext Moment
My (Nm)
35
30
25
20
15
10
5
0
-5
Time (ms)
Bone Axial Moment
Mz (Nm)
6
4
2
0
-2
-4
-6
-8
-10
-12
Time (ms)
Ligament Lateral Moment
Mx (Nm)
0.25
0.2
0.15
0.1
0.05
0
-0.05
-0.1
-0.15
-0.2
Time (ms)
Ligament Flex/Ext Moment
My (Nm)
2
1
0
-1
-2
-3
-4
-5
-6
-7
-8
Time (ms)
Ligament Axial Moment
Mz (Nm)
0.3
0.25
0.2
0.15
0.1
0.05
0
-0.05
-0.1
-0.15
Time (ms)
Soft Tissue Lateral Moment
Mx (Nm)
25
20
15
10
5
0
-5
Time (ms)
Soft Tissue Flex/Ext Moment
My (Nm)
30
25
20
15
10
5
0
-5
Time (ms)
Soft Tissue Axial Moment
Mz (Nm)
4
2
0
-2
-4
-6
-8
-10
Time (ms)

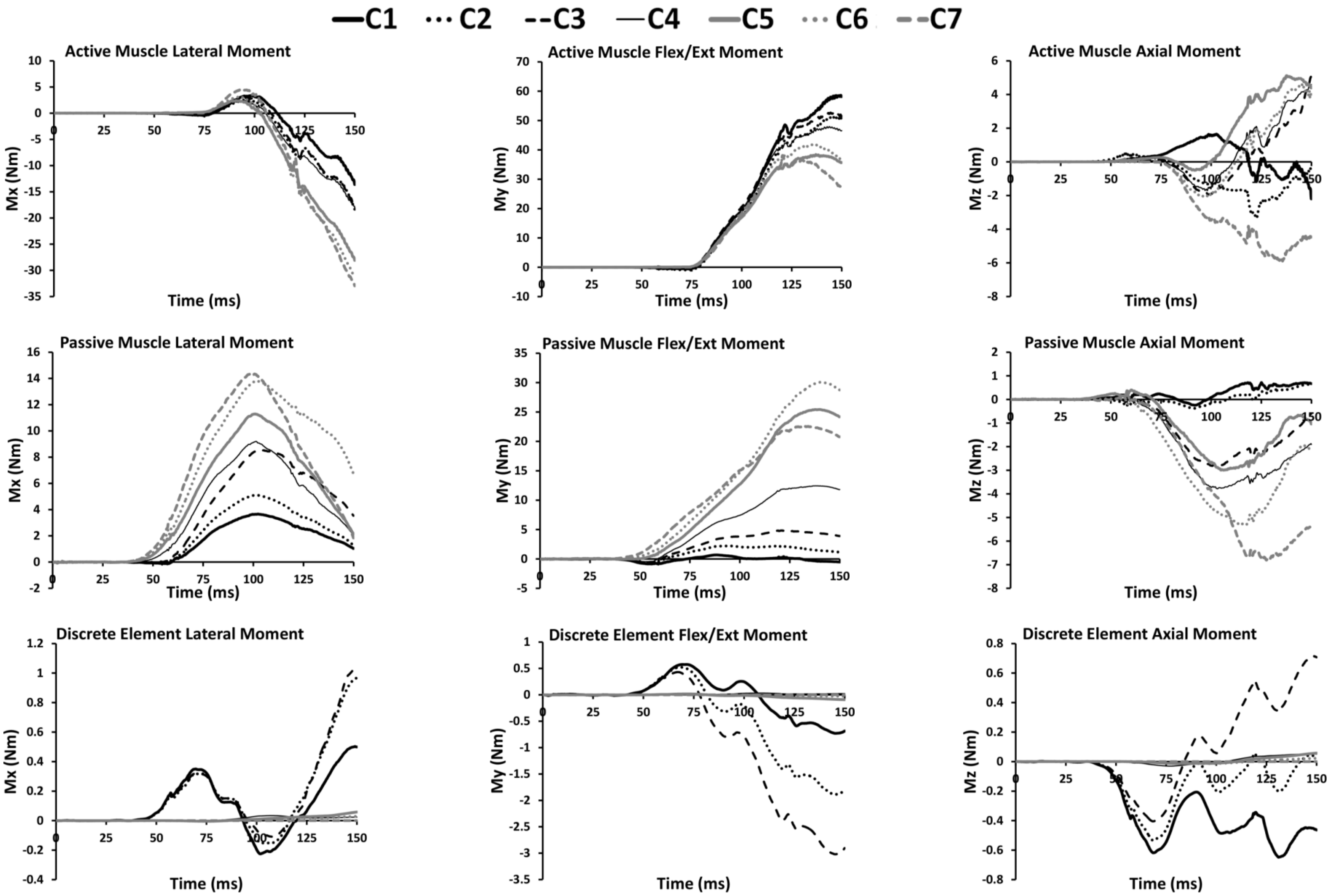
C1
C2
C3
C4
C5
C6
C7
Active Muscle Lateral Moment
Mx (Nm)
10
5
0
-5
-10
-15
-20
-25
-30
-35
0
25
50
75
100
125
150
Time (ms)
Active Muscle Flex/Ext Moment
My (Nm)
70
60
50
40
30
20
10
0
-10
Time (ms)
Active Muscle Axial Moment
Mz (Nm)
6
4
2
0
-2
-4
-6
-8
Time (ms)
Passive Muscle Lateral Moment
Mx (Nm)
16
14
12
10
8
6
4
2
0
-2
Time (ms)
Passive Muscle Flex/Ext Moment
My (Nm)
35
30
25
20
15
10
5
0
-5
Time (ms)
Passive Muscle Axial Moment
Mz (Nm)
2
1
0
-1
-2
-3
-4
-5
-6
-7
-8
Time (ms)
Discrete Element Lateral Moment
Mx (Nm)
1.2
1
0.8
0.6
0.4
0.2
0
-0.2
-0.4
Time (ms)
Discrete Element Flex/Ext Moment
My (Nm)
1
0.5
0
-0.5
-1
-1.5
-2
-2.5
-3
-3.5
Time (ms)
Discrete Element Axial Moment
Mz (Nm)
0.8
0.6
0.4
0.2
0
-0.2
-0.4
-0.6
-0.8
Time (ms)

Appendix D: Cavanaugh side impact simulation

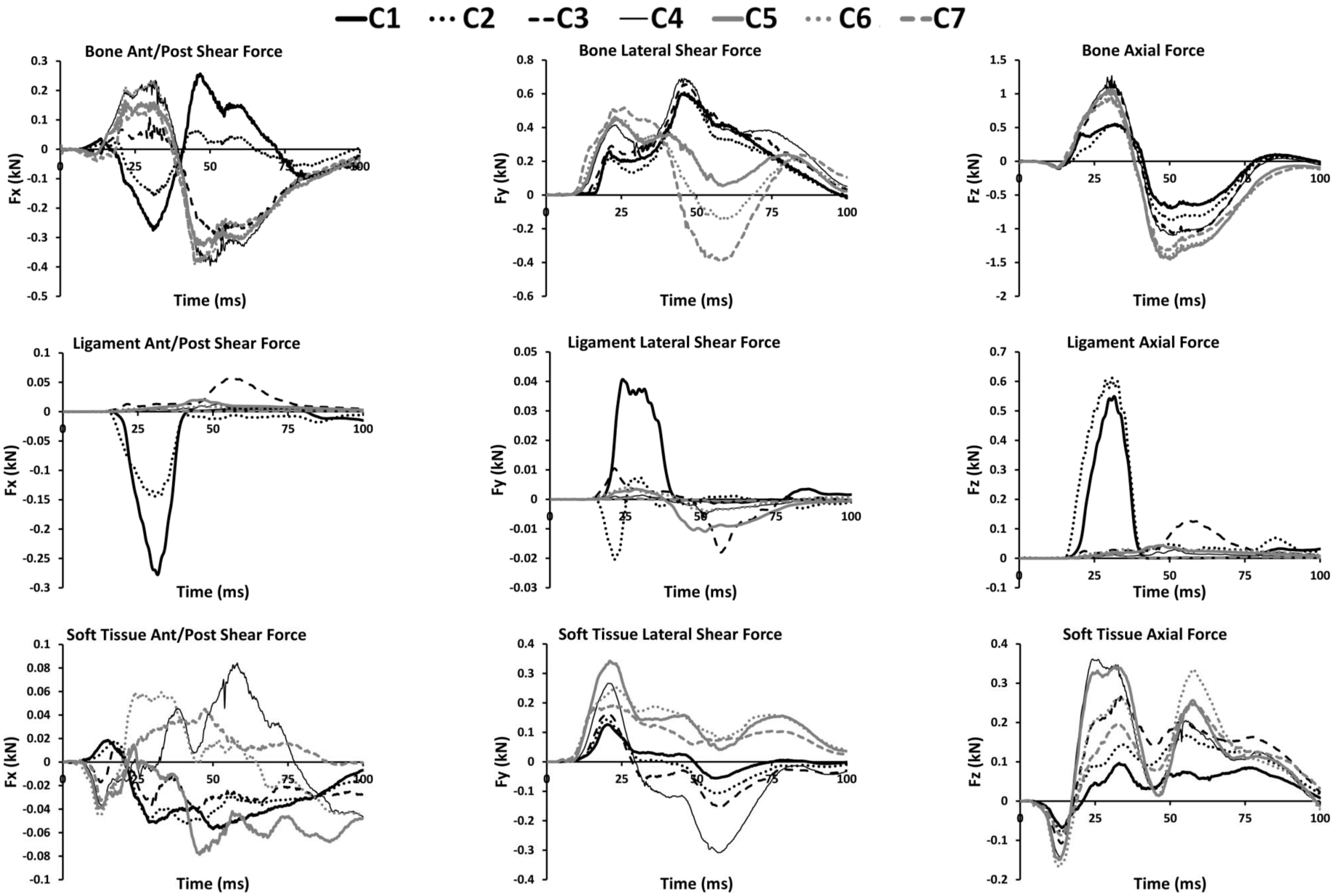

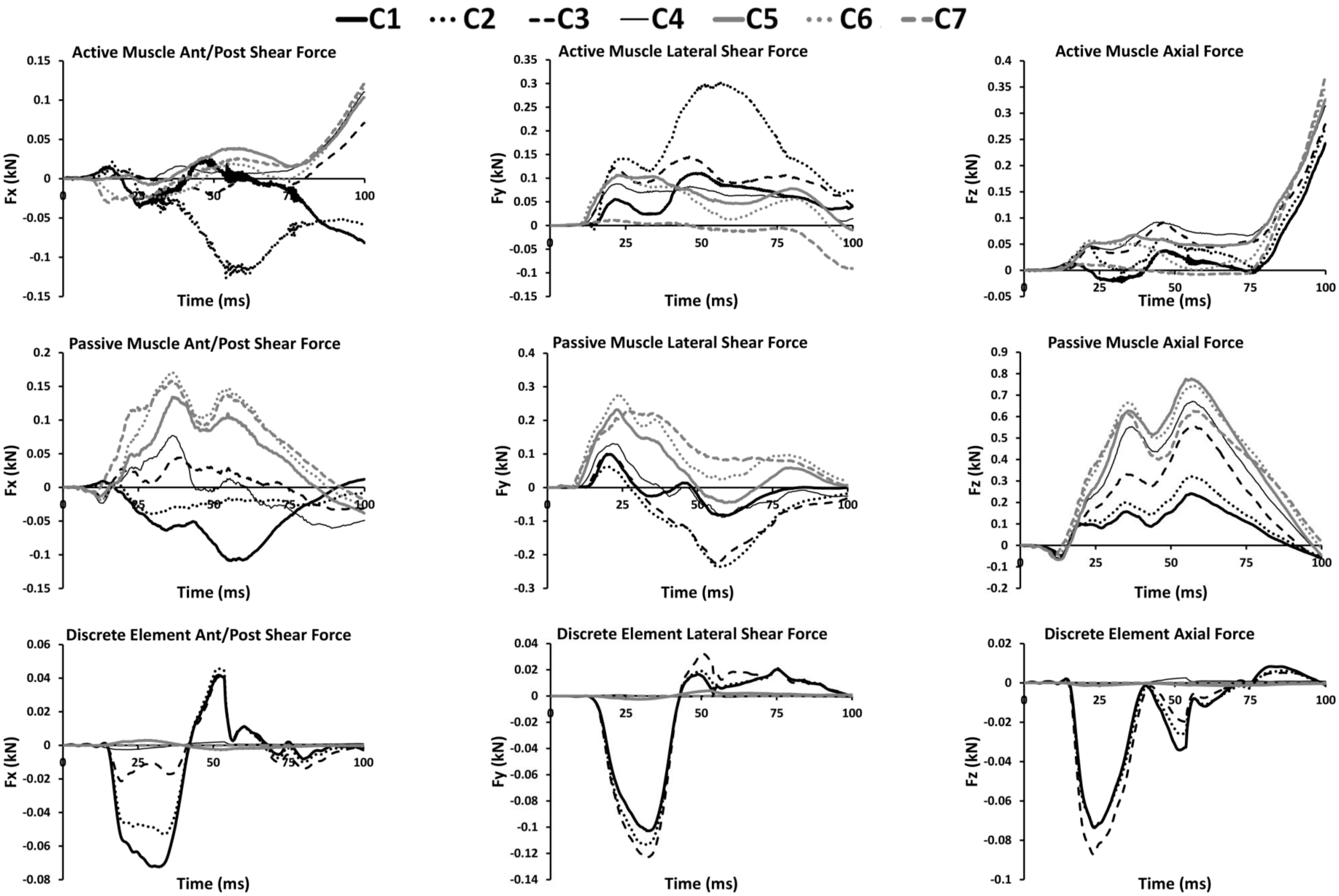
C1
C2
C3
C4
C5
C6
C7
Active Muscle Ant/Post Shear Force
Fx (kN)
0.15
0.1
0.05
0
-0.05
-0.1
-0.15
0
25
50
75
100
Time (ms)
Active Muscle Lateral Shear Force
Fy (kN)
0.35
0.3
0.25
0.2
0.15
0.1
0.05
0
-0.05
-0.1
-0.15
0
25
50
75
100
Time (ms)
Active Muscle Axial Force
Fz (kN)
0.4
0.35
0.3
0.25
0.2
0.15
0.1
0.05
0
-0.05
0
25
50
75
100
Time (ms)
Passive Muscle Ant/Post Shear Force
Fx (kN)
0.2
0.15
0.1
0.05
0
-0.05
-0.1
-0.15
0
25
50
75
100
Time (ms)
Passive Muscle Lateral Shear Force
Fy (kN)
0.4
0.3
0.2
0.1
0
-0.1
-0.2
-0.3
0
25
50
75
100
Time (ms)
Passive Muscle Axial Force
Fz (kN)
0.9
0.8
0.7
0.6
0.5
0.4
0.3
0.2
0.1
0
-0.1
-0.2
0
25
50
75
100
Time (ms)
Discrete Element Ant/Post Shear Force
Fx (kN)
0.06
0.04
0.02
0
-0.02
-0.04
-0.06
-0.08
0
25
50
75
100
Time (ms)
Discrete Element Lateral Shear Force
Fy (kN)
0.04
0.02
0
-0.02
-0.04
-0.06
-0.08
-0.1
-0.12
-0.14
0
25
50
75
100
Time (ms)
Discrete Element Axial Force
Fz (kN)
0.02
0
-0.02
-0.04
-0.06
-0.08
-0.1
0
25
50
75
100
Time (ms)

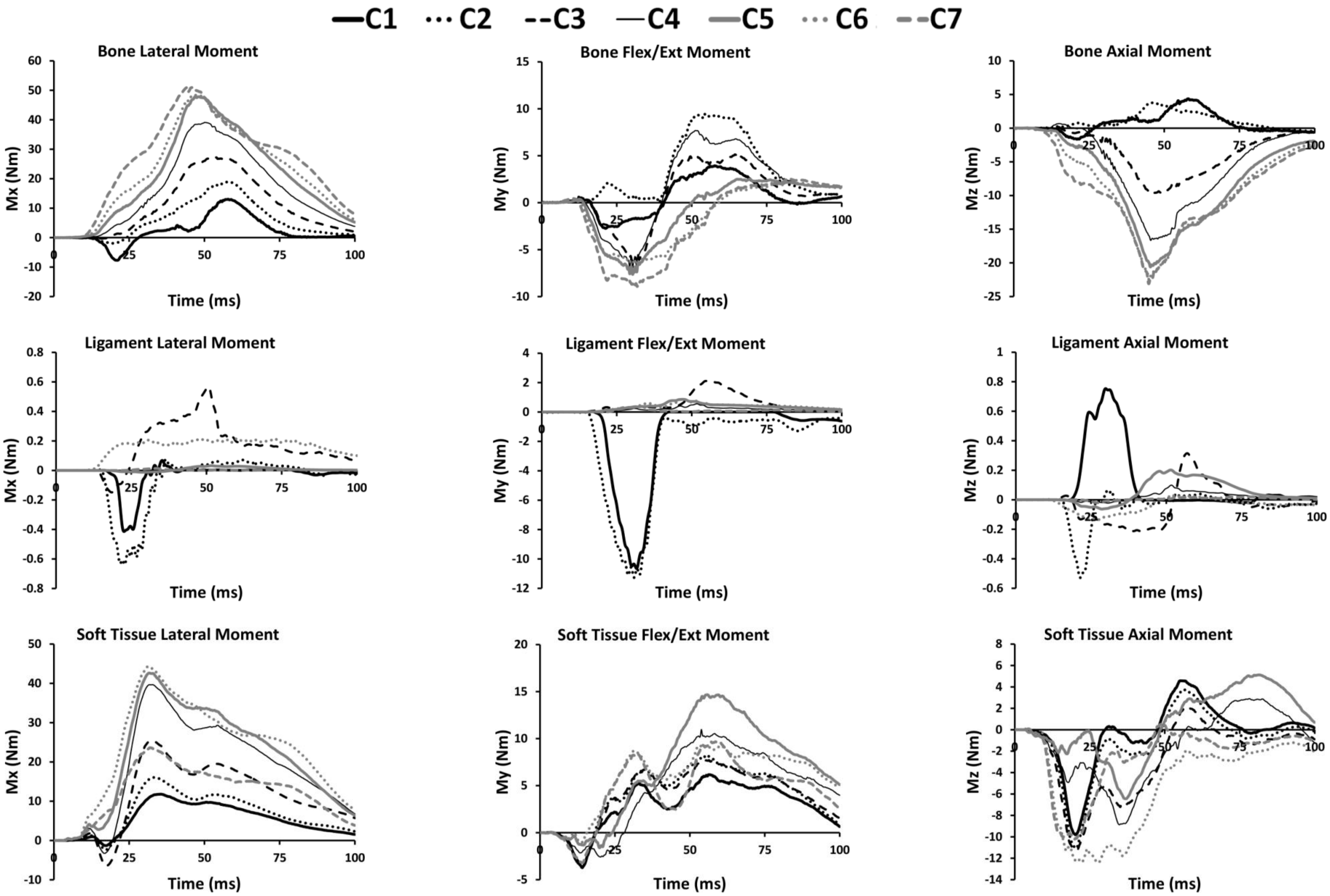
C1
C2
C3
C4
C5
C6
C7
Bone Lateral Moment
Mx (Nm)
Time (ms)
Bone Flex/Ext Moment
My (Nm)
Time (ms)
Bone Axial Moment
Mz (Nm)
Time (ms)
Ligament Lateral Moment
Mx (Nm)
Time (ms)
Ligament Flex/Ext Moment
My (Nm)
Time (ms)
Ligament Axial Moment
Mz (Nm)
Time (ms)
Soft Tissue Lateral Moment
Mx (Nm)
Time (ms)
Soft Tissue Flex/Ext Moment
My (Nm)
Time (ms)
Soft Tissue Axial Moment
Mz (Nm)
Time (ms)
0
25
50
75
100

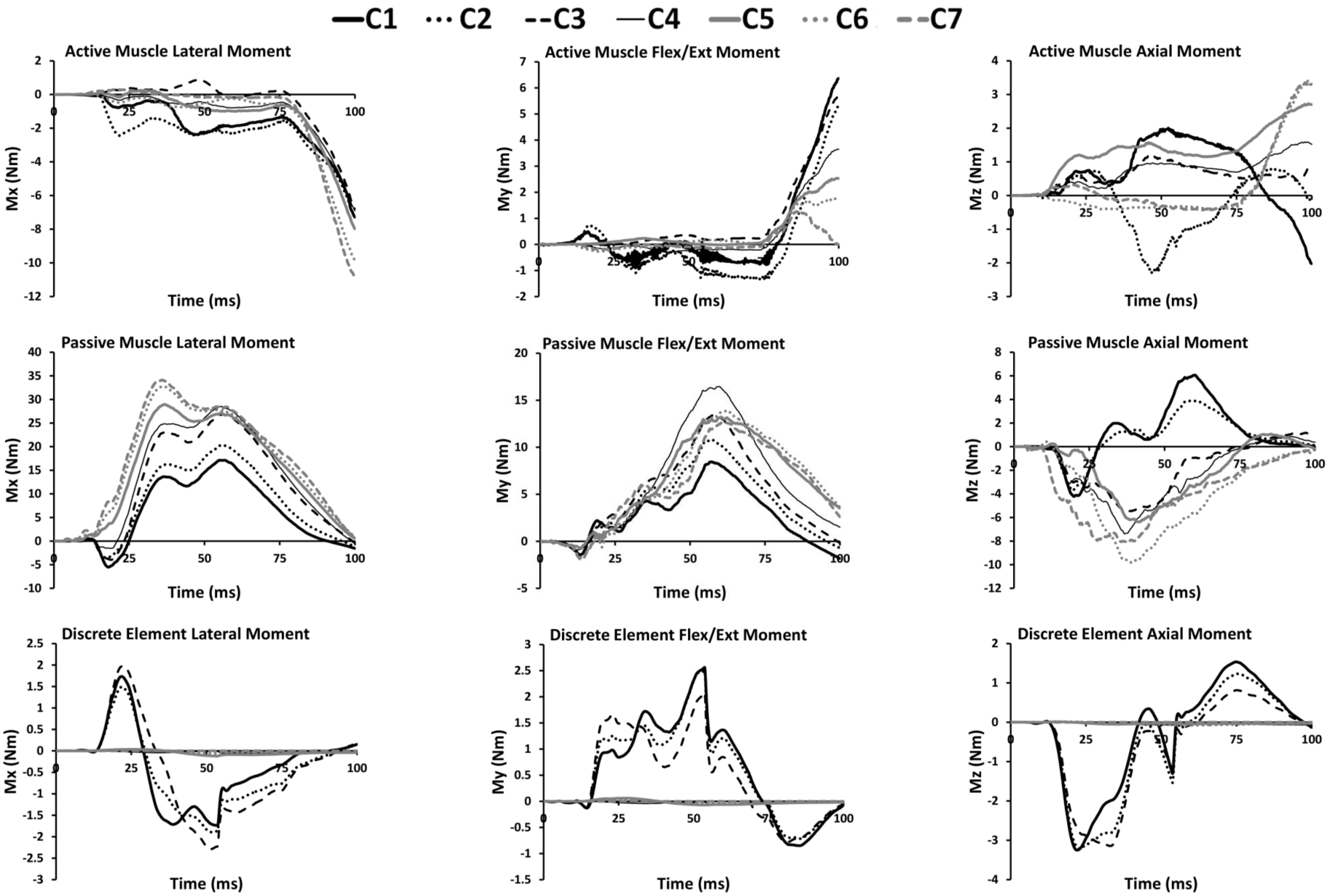

C1
C2
C3
C4
C5
C6
C7
Active Muscle Lateral Moment
Mx (Nm)
Time (ms)
Active Muscle Flex/Ext Moment
My (Nm)
Time (ms)
Active Muscle Axial Moment
Mz (Nm)
Time (ms)
Passive Muscle Lateral Moment
Mx (Nm)
Time (ms)
Passive Muscle Flex/Ext Moment
My (Nm)
Time (ms)
Passive Muscle Axial Moment
Mz (Nm)
Time (ms)
Discrete Element Lateral Moment
Mx (Nm)
Time (ms)
Discrete Element Flex/Ext Moment
My (Nm)
Time (ms)
Discrete Element Axial Moment
Mz (Nm)
Time (ms)
0
25
50
75
100

Chapter 4: Implant Finite Element (FE) Models

Overview

Both arthrodesis and arthroplasty were modeled at the C5-6 level of the cervical spine. Arthrodesis was modeled using two different methods: Constrained Nodal Rigid Bodies (CNRBs) and implantation of a generic cage, core, and anterior plate. Arthroplasty was modeled with the Prestige ST (Medtronic, Memphis, TN) and ProDisc-C (Synthes Spine, Paoli, PA) cervical total disc replacements (CTDRs). The geometries of the CTDRs were reverse engineered from physical implants obtained from their respective manufacturers.

Modifications to the C5-6 Level

To accurately model the cervical arthrodesis and arthroplasty, modifications similar to those performed during an actual surgery were made to C5 and C6 vertebral bodies (VBs). The intervertebral disc (IVD), endplates, and anterior longitudinal ligaments (ALL) associated with this level of the cervical spine were removed. The C5 and C6 vertebrae were placed into a separate keyword file, facilitating implant-specific modifications and contact definitions. Geometric modifications to these vertebrae, allowing proper fit for the implants, were accomplished through a combination of select element deletion and advanced morphing techniques using HyperMesh (v11.0, Altair, Troy, MI).

Cervical Arthrodesis

Constrained Nodal Rigid Bodies

The CNRB fusion rigidly constrained over 100 individual node sets from the inferior VB surface of C5 to the superior VB surface of C6 (Figure 4-1). The geometries of VB surfaces were not modified and no additional contacts were required since a physical implant was not modeled. The anterior plate of the fusion was similarly simulated with a series of CNRBs, connecting the anterior-inferior VB of C5 to the anterior-superior VB of C6.

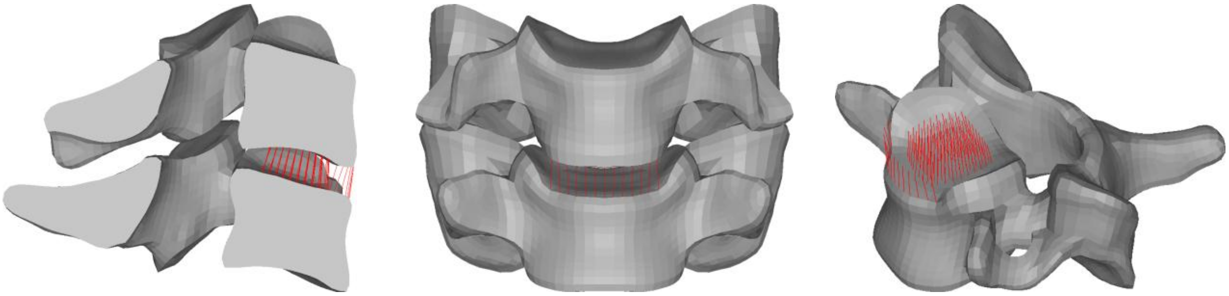
(a) (b) (c)

Figure 4-1: Cervical arthrodesis of C5-6 modeled with CNRBs between C5-6: (a) midsagittal, (b) anteroposterior, and (c) oblique views.

Cage, Core, and Anterior Plating

The fusion implant was modeled as a 14x15x6 mm solid organic polymer PEEK (polyether ether ketone) cage, 1 mm thick, and a solid trabecular bone core (Figure 4-2). The C5 and C6 VBs were modified to create surfaces parallel and coincident with the implant. The cage and core were constrained to the vertebrae using the *CONTACT_TIED card. Titanium (Ti-6Al-4V) shell elements were used to model a simplified anterior plate by connecting the anteroinferior VB of C5 to the anterosuperior VB of C6. Material and element properties are listed in Table 4-1.

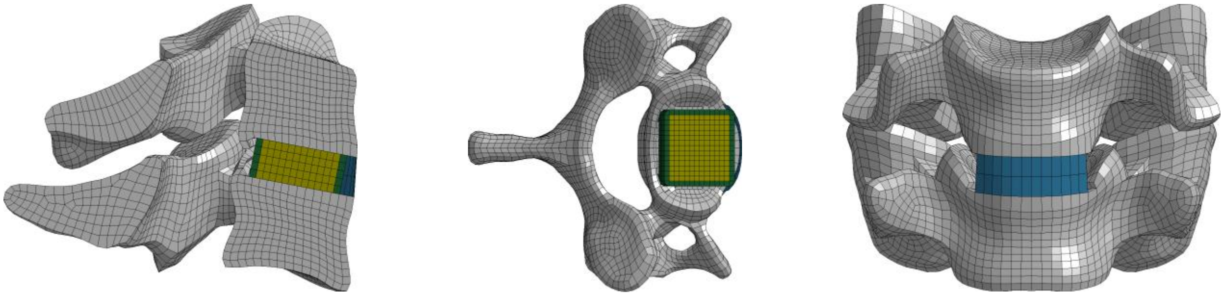
(a) (b) (c)

Figure 4-2: Cervical arthrodesis of C5-6 modeled as a cage (green), core (yellow), and anterior plate (blue): (a) midsagittal, (b) superoinferior, and (c) anteroposterior views.

Table 4-1: Material and element properties for the cage, core, and anterior plate cervical arthrodesis FE model.

Part	**Material**	**ASTM Standard**	**Material Model**	**Element Type**	**ρ (kg/mm^3)**	**E (GPa)**	**ν**	**Ref**
Cage	PEEK	F2026-02	Elastic	Solid Hex	1.30E-06	3.6	0.4	[1, 2]
Core	Trabecular Bone	N/A	Plastic-Kinematic	Solid Hex	1.10E-06	0.4	0.3	[3]
Plate	Ti-6Al-4V	F136	Elastic	Shell	4.43E-06	116	0.3	[2, 4]

Cervical Arthroplasty

Model Generation

A Prestige ST and a ProDisc-C CTDR were obtained from their respective manufacturers. Their geometries were reverse engineered through meticulous hand measurements to create solid models. Stainless-steel, 3D replicas of both implants were produced from these solid models using a Direct Metal Laser Sintering (DMLS) process. The geometries of these physical replicas were compared with the actual implants for dimensional accuracy. The solid models were converted into meshed FE models and assigned appropriate material properties. These CTDRs were then incorporated into the neck at the C5-6 level.

Prestige ST

The solid model of the Prestige ST is presented in Figure 4-3 and comparison between the actual implant and 3D replica in Figure 4-4. The nominally 16 mm deep, 7 mm high CTDR was modeled with rigid shells and initial position of the ball at the center of the trough (Figure 4-5). Material and element properties are reported in Table 4-2. The C5 and C6 VBs were modified to create surfaces parallel and coincident with the implant. The implant was constrained to the vertebrae using a *CONTACT_TIED card and ball-to-trough contact was defined using the *AUTOMATIC_SURFACE_TO_SURFACE card. The intervertebral screws were not modeled.

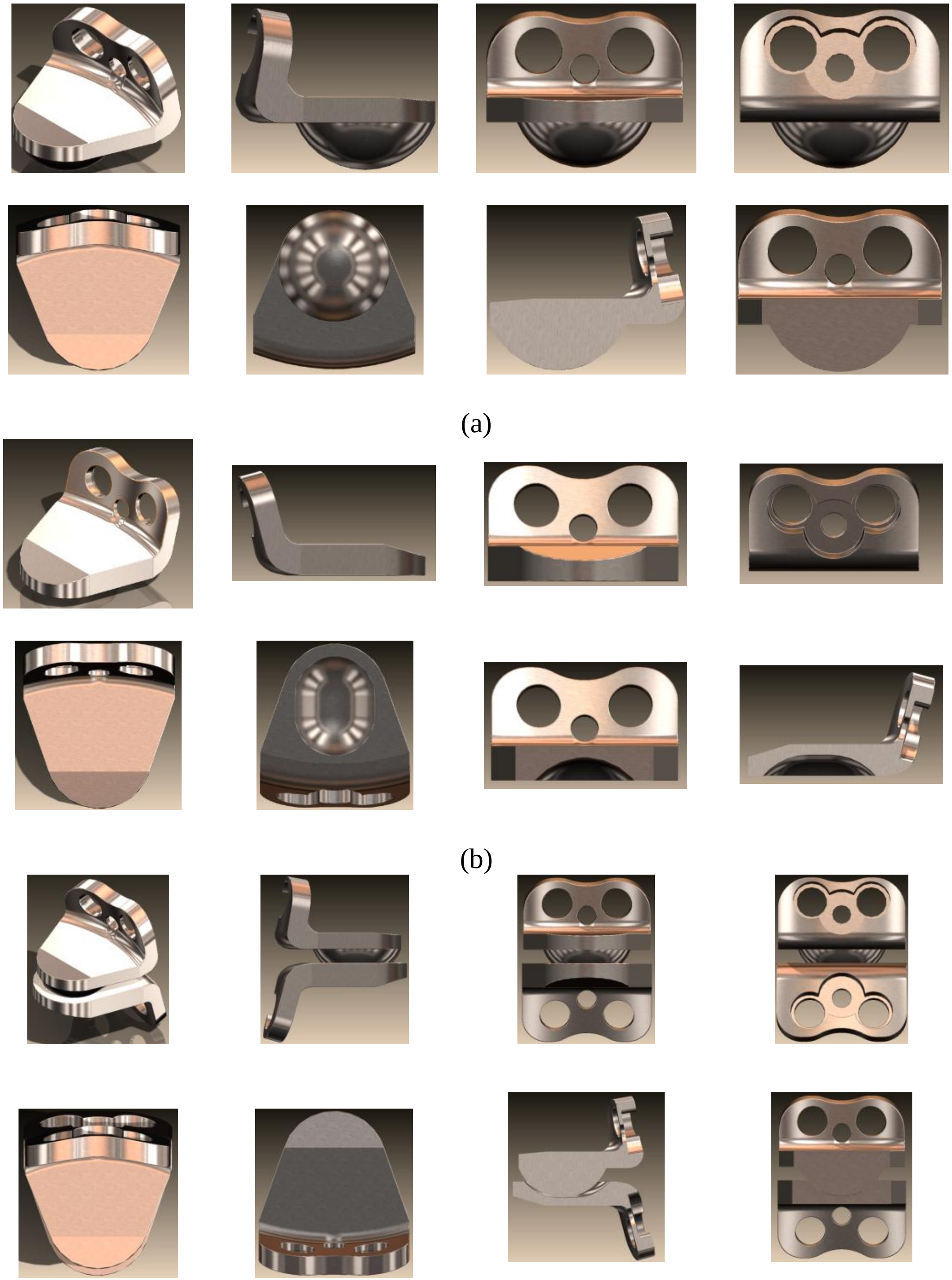

(a)

(b)

(c)

Figure 4-3: Solid model of the Prestige ST (a) ball, (b) trough, and (c) assembly.

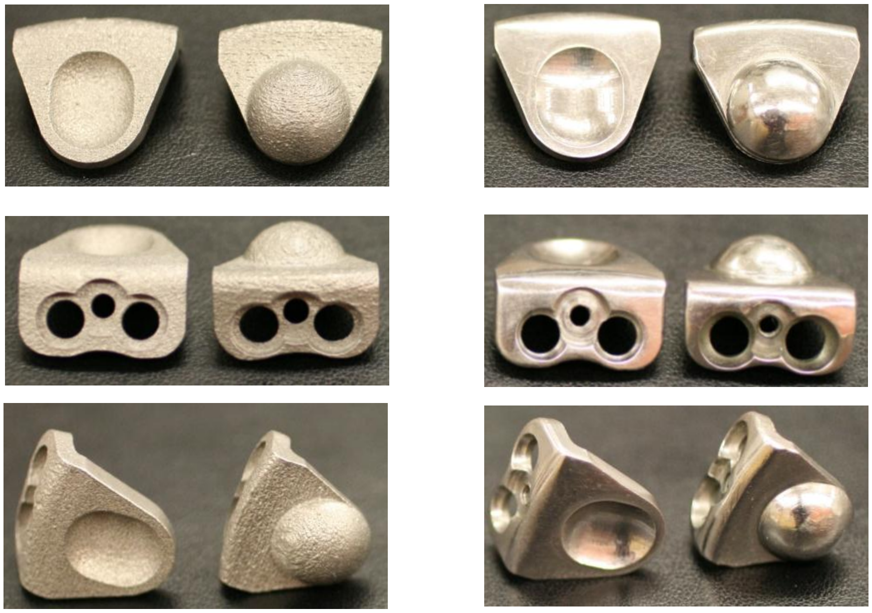

Figure 4-4: DMLS stainless-steel 3D print (left) and actual Prestige ST (right).

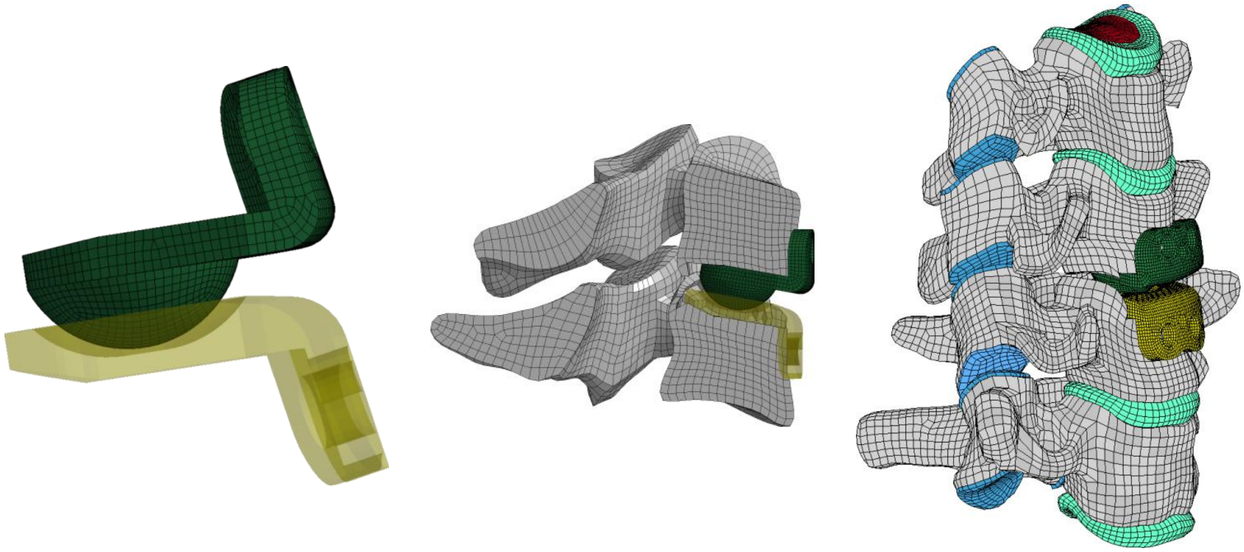

(a) (b) (c)

Figure 4-5: FE model of the Prestige ST: (a) lateral view, (b) midsagittal view at C5-6, and (c) oblique view of C4-C7.

Table 4-2: Material and element properties for Prestige ST FE model.

Part	Material	ASTM Standard	Material Model	Element Type	ρ (kg/mm3)	E (GPa)	ν	Ref
Endplates	316L SST	F138	Rigid	Shell	8.00E-06	190	0.3	[2, 5]

ProDisc-C

The solid model of the ProDisc-C is presented in Figure 4-6 and comparison between the actual CTDR and 3D replica in Figure 4-7. The nominal dimensions of this implant are 14x15x6 mm. The endplates were modeled with rigid shells and the semi-spherical inlay with deformable tetrahedrons (Figure 4-8). Material and element properties are reported in Table 4-3. The C5 and C6 VBs were modified to create surfaces parallel and coincident with the implant, as well as channels matching the geometry of the central keels. The *CONTACT_TIED card was used to constrain the endplates to the VBs and the semi-spherical inlay to the bottom endplate. Ball-to-socket contact was defined using the *AUTOMATIC_SURFACE_TO_SURFACE card with the assistance of a null surface overlaying the deformable ball.

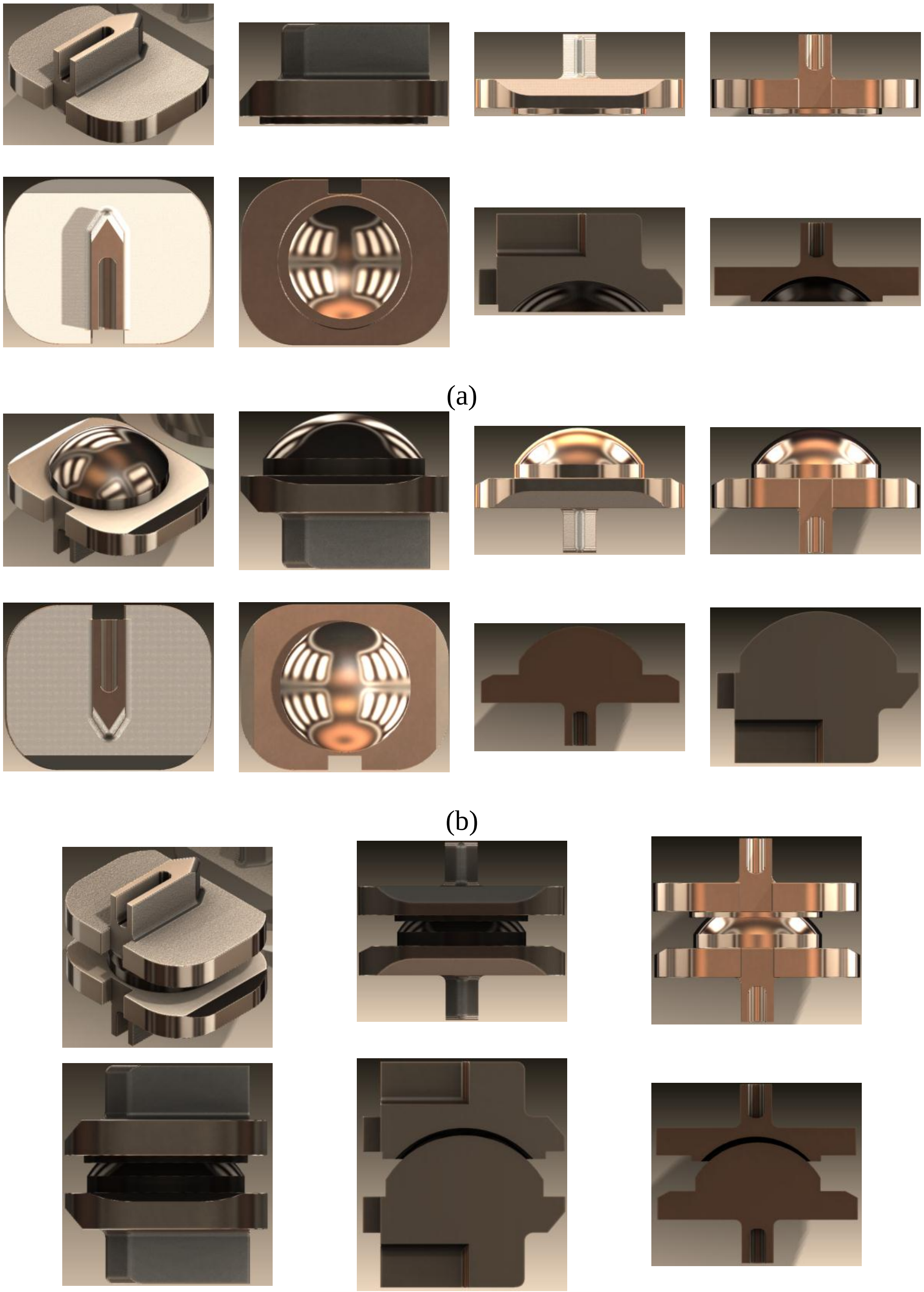

(a)

(b)

(c)

Figure 4-6: Solid model of the ProDisc-C (a) socket, (b) ball, and (c) assembly.

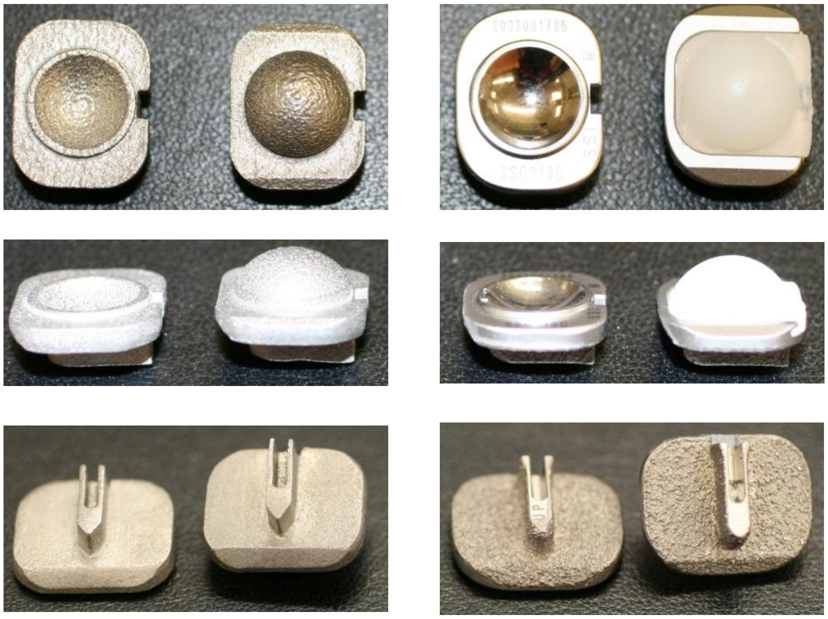

Figure 4-7: DMLS stainless-steel 3D print (left) and actual ProDisc-C (right).

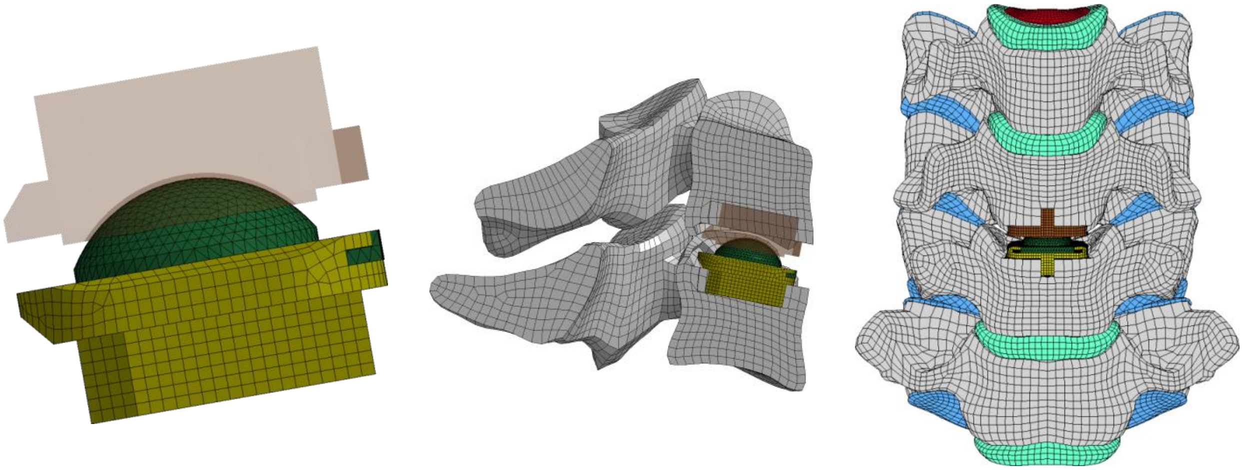

(a) (b) (c)

Figure 4-8: FE model of the ProDisc-C: (a) lateral view, (b) midsagittal view at C5-6, and (c) anteroposterior view of C4-C7.

Table 4-3: Material and element properties for ProDisc-C FE model.

Part	Material	ASTM Standard	Material Model	Element Type	ρ (kg/mm3)	E (GPa)	ν	Ref
Endplates	CoCrMo	F75	Rigid	Shell	8.30E-06	210	0.3	[2]
Insert	UHMWPE	F648	Elastic	Solid Tetrahedron	9.36E-07	1.3	0.3	[2, 6, 7]

Conclusions

Cervical arthrodesis and arthroplasty of C5-6 was simulated in a human body FE model. Modifications, consistent with actual surgical procedure, were made to the C5 and C6 VBs. Geometry and material properties of the FE implants were consistent with their real-life counterparts. The contact definitions allowed for realistic kinematics in the CTDR models; rotation and translation of the Prestige ST and rotation and spherical inlay deformation in the ProDisc-C.

Chapter 4 References

[1] Goyal RK, Tiwari AN, Mulik UP, Negi YS. Novel High Performance Al2O3/Poly(Ether Ether Ketone) Nanocomposites for Electronics Applications. Composites Science and Technology. 2007;67:1802-12.

[2] Hallab NJ, Wimmer M, Jacobs JJ. Material Properties and Wear Analysis. In: Yue JJ, Bertagnoli R, McAfee PC, An HS, editors. Motion Preservation Surgery of the Spine: Advanced Techniques and Controversies. Philadelphia: Saunders; 2008. p. 52-62.

[3] Stitzel JD. Global Human Body Models Consortium (GHBMC) Male 50th Percentile (M50) Occupant Model Manual. Virginia Tech – Wake Forest University Center for Injury Biomechanics; 2011.

[4] eFunda. Ti-6al-4v. Web. April 8 2013. <http://www.efunda.com/materials/alloys/titanium/show_titanium.cfm?ID=T18_AB&prop=all&Page_Title=Ti-6Al-4V>.

[5] eFunda. AISI Type 316l. Web. April 8 2013. <http://www.efunda.com/materials/alloys/stainless_steels/show_stainless.cfm?ID=AISI_Type_316L&show_prop=all&Page_Title=AISI%20Type%20316L>.

[6] DIN ISO 5834-2:2007-12. Implants for Surgery: Ultra-High-Molecular-Weight-Polyethylene, Part 2: Moulded Forms (Iso 5834-2:2006). Berlin, Germany2007.

[7] Womack W, Leahy PD, Patel VV, Puttlitz CM. Finite Element Modeling of Kinematic and Load Transmission Alterations Due to Cervical Intervertebral Disc Replacement. Spine. 2011;36:E1126-33.

Chapter 5: Effects of Cervical Arthrodesis and Arthroplasty on Neck Response during a Simulated Frontal Automobile Collision

Nicholas A. White, Daniel P. Moreno, Philip J. Brown, F. Scott Gayzik, Wesley Hsu, Alexander Powers, and Joel D. Stitzel

Submitted to: *The Spine Journal*, September 2013.

Structured Abstract

Background Context: While arthrodesis is the most common surgical intervention for treatment of symptomatic cervical degenerative disc disease (CDDD), arthroplasty has become increasingly more popular over the past decade. While literature exists comparing the effects of anterior cervical discectomy and fusion (ACDF) and cervical total disc replacement (CTDR) on neck kinematics and loading, the vast majority of these studies apply only quasi-static, non-injurious loading conditions to a segment of the cervical spine.

Purpose: The objective of this study was to investigate the effects of arthrodesis and arthroplasty on biomechanical neck response during a simulated frontal automobile collision with airbag deployment.

Study Design: This study uses a full-body, 50th percentile seated male finite element (FE) model to study neck response during a dynamic impact event. The cervical spine was modified to simulate either an arthrodesis or an arthroplasty procedure at C5-6.

Methods: Five simulations of a belted driver, subjected to a 13.3 m/s ΔV frontal impact with airbag deployment, were run in LS-DYNA with the Global Human Body Models Consortium (GHBMC) full-body FE model. The first simulation used the original model, with no modifications to the neck, while the remaining four were modified to represent either interbody arthrodesis or arthroplasty of C5-6. The arthrodesis was modeled as either a series of Constrained Nodal Rigid Bodies (CNRBs) or as a generic cage, core, and anterior plate, while the arthroplasty was modeled with either a Prestige ST or ProDisc-C CTDR. Cross-sectional forces and moments at the C5 and C6 cervical level of the neck, along with interbody and facet forces between C5 and C6, were reported. Midsagittal rotations of C5 and C6 about their respective centers of gravity were also reported.

Results: Adjacent-level, cross-sectional neck loading was maintained in all simulations without exceeding any established injury thresholds. Interbody compression was greatest for the CTDRs, and interbody tension occurred only in the fused and non-modified spines. Some interbody separation occurred between the superior and inferior components of the CTDRs during flexion-induced tension of the cervical spine, increasing facet load and strain.

Conclusions: This is the first study to evaluate the effects of a C5-6 cervical arthrodesis and arthroplasty on neck response during a simulated frontal automobile impact. While cervical arthrodesis and arthroplasty at C5-6 did not appear to significantly alter the adjacent-level, cross-sectional neck responses during a simulated frontal automobile impact, key differences were noted in the interbody loading, facet loading, and facet strain.

Keywords: Arthrodesis, Arthroplasty, ProDisc-C, Prestige ST, Finite Element Analysis (FEA), Frontal Impact

Introduction

Cervical spondylosis refers to the age-related degeneration of the cervical spine, which can include cervical degenerative disc disease (CDDD) [1-4]. The clinical presentation of symptomatic CDDD includes axial neck pain, radiculopathy, myelopathy or any combination of the three [5, 6], most often originating in the lower cervical spine between C5 and C6 [1-4, 7]. Anterior cervical discectomy and fusion (ACDF) has been the gold standard in treatment for this condition for over fifty years [8-13]. However, adjacent segment degeneration (ASD) following an ACDF is not an uncommon occurrence [14-16]. In an effort to decrease the rate of ASD, cervical total disc replacements (CTDRs) were introduced to maintain same-level and adjacent-level physiologic motion and loading [17-23]. While the efficacy of CTDRs with respect to their long-standing ACDF counterpart is subject to debate [11, 13, 23-33], the number of cervical arthroplasty procedures has increased over time [34].

The use of finite element (FE) methods for orthopedic applications, particularly those involving the cervical spine, began over twenty years ago with a simple 2D model used to study post-laminectomy deformities [35]. The first finite element study of an anterior cervical spine fusion was conducted by Kumaresan et al. to evaluate the effects of fusion materials and surgical procedure on the biomechanical response of a C4-C6 spine model [36]. Since this publication, close to two dozen additional FE studies have been conducted, evaluating the effects of both ACDFs and CTDRs on the biomechanics of the cervical spine [37-59]. Typically, the implant was modeled between either C4-5 or C5-6, and the simulations were run as quasi-static events using an implicit FE solver. A summary of these publications including implant type, implant location, modeled vertebrae, and FE code is reported in Table 5-1.

Dang et al. evaluated the effects of single and double-level fusions on the anterior longitudinal ligaments of the Toyota Human Body Model for Safety (THUMS) during a simulated low-speed, rear-end impact [42]. To the best of the authors' knowledge, this is the only dynamic impact FE study on the effects of cervical fusion, as well as the only study to use a full-body model for such purposes. The neck model employed herein has a higher degree of anatomical detail compared to THUMS. The current study uses this state-of-the-art full body FE model to evaluate neck kinematics and loading, with simulated arthrodesis and arthroplasty at the C5-6 level, during a frontal automobile collision.

Table 5-1: Literature review of FE simulations involving cervical arthrodesis and arthroplasty.

Author/Year	**Ref**	**Implant**	**Implant Location**	**Model**	**FE Code**
Kumaresan, 1997	[36]	Fusion	C4-5	C4-6	NASTRAN
Maiman, 1999	[37]	Fusion	C4-5, C5-6	C4-6	NASTRAN
Natarajan, 2000	[38]	Fusion	C5-6	C5-6	ADINA
Galbusera, 2006	[39]	BRYAN	C5-C6	C5-6	ABAQUS
Ha, 2006	[40]	Elastomer Disc, Fusion	C4-5	C3-6	ANSYS
Lopez-Espina, 2006	[41]	Fusion	C3-4, C4-5, C5-6, C6-7 C3-5, C4-6, C5-7	C3-7	ANSYS
Dang, 2008	[42]	Fusion	C2-3, C3-4, C4-5, C5-6, C6-7 C2-4, C3-5, C4-6, C5-7	THUMS	LS-DYNA
Galbusera, 2008	[43]	BRYAN	C5-6	C4-7	ANSYS
Rousseau, 2008	[44]	Ball & Socket	C5-6	C5-6	ANSYS
Faizan, 2009	[45]	Ball & Socket	C5-6	C3-7	ABAQUS
Lin, 2009	[46]	BRYAN, Prestige LP ProDisc-C	C5-6	C5-6	Voxelcon
Womack, 2009	[47]	ProDisc-C	C4-5	C3-7	ABAQUS
Crawford, 2010	[48]	Prestige ST, ProDisc-C Synergy	C5-6	C3-7	ABAQUS
Galbusera, 2010	[49]	Spherical Joint	C5-6	C5-6	ANSYS
Kang, 2010	[50]	BRYAN, Prestige LP ProDisc-C	C5-6	C5-6	Voxelcon
Kulkarni, 2010	[51]	Prestige ST, ProDisc-C Synergy	C5-6	C3-7	ABAQUS
Li, 2010	[52]	Fusion, Nucleus	C5-6	C1-7	ABAQUS
Bhattacharya, 2011	[53]	Prestige ST, ProDisc-C	C5-6	C5-6	ABAQUS
Bhattacharya, 2011	[54]	ProDisc-C	C5-6	C5-6	ABAQUS
Faizan, 2011	[55]	Discover, Fusion	C4-5, C5-6	C3-7	ABAQUS
Fernandes, 2011	[56]	Fusion	C5-6	C5-6	ABAQUS
Lee, 2011	[57]	ProDisc-C, Mobi-C	C5-6	C2-7	ABAQUS
Womack, 2011	[58]	ProDisc-C	C4-5	C3-7	ABAQUS
Zhao, 2012	[59]	ProDisc-C, Fusion	C4-5, C5-6, C4-6	C3-7	ABAQUS

THUMS: Toyota Human Model for Safety

Methods and Materials

General Model Overview

The Global Human Body Models Consortium (GHBMC) 50th percentile seated male FE model (v3.5) is used to study the cervical spine response due to a simulated arthrodesis and arthroplasty [60, 61]. This high fidelity human body model, specifically designed for crash simulation, is the product of a team of research university centers of excellence (COEs) from around the world. The neck is comprised of over 25,000 deformable elements composing the seven cervical vertebrae, intervertebral discs (IVDs), ligaments, musculature, and soft tissue (Figure 5-1). The geometry of the neck was developed at Wake Forest University (WFU) School of Medicine [62] and further developed into an FE model at the University of Waterloo in Ontario, Canada [63, 64]. The biofidelity of the neck has been rigorously validated both at individual cervical segment levels and for the full cervical spine [63-66]. Additionally, whole body validation has been conducted for a number a different impact scenarios [67-70].

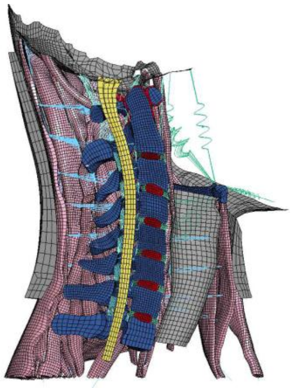

Figure 5-1: Midsagittal cross section of the GHBMC neck including the C1-T1 vertebrae, IVDs, ligaments, musculature, and soft tissue.

Cervical Spine Modifications for ACDF and CTDR

Several modifications were made to the GHBMC neck allowing for simulation of C5-6 cervical arthrodesis and arthroplasty. To mimic actual surgical technique for these procedures, the IVD, endplates, and anterior longitudinal ligaments (ALL) associated with this level of the cervical spine were removed from the model. Vertebral body (VB) geometric modifications consistent with these surgeries were accomplished through a combination of select element deletion and advanced morphing techniques using HyperMesh (v11.0, Altair Engineering, Troy, MI). The geometries of both CTDRs used in this study were reverse engineered from the corresponding physical implants. The modeled implants and C5-6 modifications were then reviewed and approved by WFU neurosurgeons. The ACDF and CTDRs were secured to the VBs using tied nodes to surface offset contacts. Material properties for the IVDs, ACDF, and CTDRs are reported in Table 5-2 [58, 71-76].

Arthrodesis at the C5-6 cervical level was modeled using two different methods, one involving Constrained Nodal Rigid Bodies (CNRBs) and the other, a cage, core, and anterior plate (ACDF). The CNRB fusion rigidly constrained over 100 individual node sets from the inferior VB surface of C5 to the superior VB surface of C6. The geometries of VB surfaces were not modified and no additional contacts were required since a physical implant was not modeled. The anterior plate of the fusion was simulated with a series of CNRBs, connecting the anterior-inferior VB of C5 to the anterior-superior VB of C6. The ACDF was modeled as a 14x15x6 mm solid organic polymer PEEK (polyether ether ketone) cage, 1 mm thick, and a solid trabecular bone core (Figure 5-2a). The C5 and C6 VBs were modified to create surfaces parallel to and coincident with the implant. Titanium shell elements were used to model a simplified anterior plate by again connecting the anterior-inferior VB of C5 to the anterior-superior VB of C6.

Arthroplasty at the C5-6 cervical level was modeled with the Prestige ST and ProDisc-C cervical total disc replacements (CTDRs). The Prestige ST is a 2-piece, ball-and-trough design with one point of articulation. This stainless steel, metal-on-metal implant is capable of rotation in all three axes, as well as translation in the AP direction, allowing for a mobile, instantaneous center of rotation. The nominally 16 mm deep, 7 mm high CTDR was modeled with rigid shells, with the ball positioned at the center of the trough (Figure 5-2b). To simplify the analyses, the locking screws were not modeled. The C5 and C6 VBs were modified to create surfaces parallel and coincident with the implant.

The ProDisc-C is a 3-piece, ball-and-socket design with one point of articulation. The endplates are constructed of cobalt-Chromium molybdenum (CoCrMo) and the polymer insert of ultra-high-molecular-weight polyethylene (UHMWPE), creating a metal-on-polymer articulation. This design encourages three-axis rotation, thus establishing a nearly fixed center of rotation. The CTDR is press-fit between adjoining vertebrae, with central keels nested into the VBs. The nominal dimensions of this implant were 14x15x6 mm (Figure 5-2c). The endplates were modeled with rigid shells and the semi-spherical inlay with deformable tetrahedrons. The C5 and C6 VBs were modified to create surfaces parallel and coincident with the implant, as well as channels matching the geometry of the central keels.

Table 5-2: Material and model properties for the FE models of the ACDF, Prestige ST, and ProDisc-C.

Implant	**Part**	**Material**	**Material Model**	**Element Type**	**ρ (kg/mm^3)**	**E (GPa)**	**ν**	**Ref**
ACDF	Cage	PEEK	Elastic	Solid Hex	1.30E-06	3.6	0.4	[74, 75]
	Core	Trabecular Bone	Plastic-Kinematic	Solid Hex	1.10E-06	0.4	0.3	[61]
	Plate	Ti-6Al-4V	Elastic	Shell	4.43E-06	116	0.3	[72, 75]
Prestige ST	End Plates	316L SST	Rigid	Shell	8.00E-06	190	0.3	[73, 75]
ProDisc-C	End Plates	CoCrMo	Rigid	Shell	8.30E-06	210	0.3	[75, 76]
	Insert	UHMWPE	Elastic	Solid Tet	9.36E-07	1.3	0.3	[58, 71, 75]

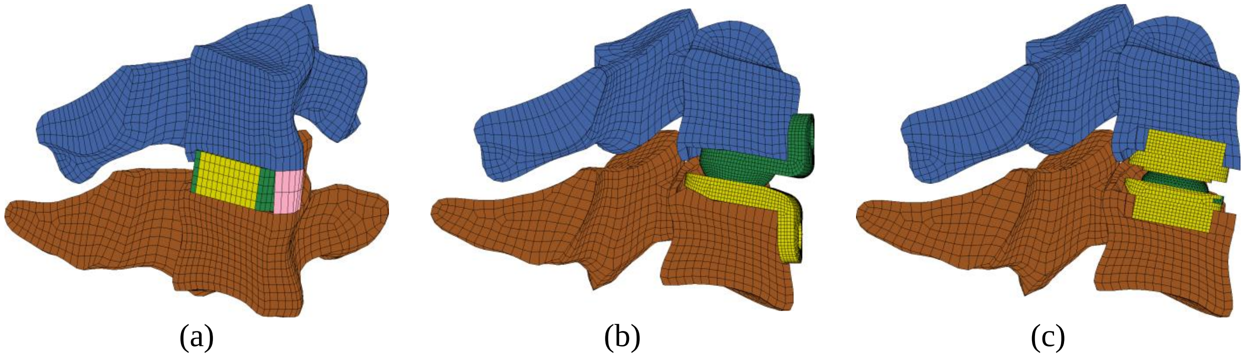
(a) (b) (c)

Figure 5-2: Midsagittal cross section of the C5 and C6 vertebrae with an (a) ACDF, (b) Prestige ST CTDR, and (c) ProDisc-C CTDR. The cross section extends through the ACDF showing the cage, core, and plate while CTDRs were left intact for better visualization.

Simulation

Five simulations of a belted driver, subjected to a 13.3 m/s ΔV frontal impact with airbag deployment, were run with the GHBMC model in LS-DYNA (LSTC, Livermore, CA) (Figure 5-4) [77]. The first simulation used the original model, with no modifications to the neck [60, 61, 78]. The remaining four simulations included a CNRB fusion, ACDF, Prestige ST implant, or ProDisc-C implant at the C5-6 cervical level. A series of cross sections were included to capture the forces and moments at each cervical level of the neck in their respective local coordinate systems (LCSYS) using a methodology previously described by White, et al. [78]. A LCSYS was defined for each cervical vertebrae with its origin located at the center of gravity (CG) of the respective vertebrae. Each LCSYS was oriented according to SAE J211 [79], with positive-x directed to the midpoint of the superior and inferior portion of the anterior VB and positive-z directed inferiorly to the VB in the midsagittal plane. Effectively, these cross sections passed through the middle of their respective VBs. Cross sections were also used to capture forces transmitted though the C5-6 IVD of the non-modified neck, the cage, core, and plate of the ACDF neck, and C5-6 facets for all neck models Figure 5-3.


(a) (b)

Figure 5-3: Representative cross section set used to capture the load transmission through the (a) IVDs and (b) solid cartilage and beam ligaments of the facets.

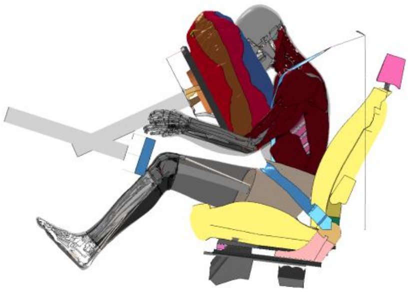

Figure 5-4: Belted driver subjected to a frontal impact with 13.3 m/s ΔV and airbag deployment.

Data Analysis

The simulation results were post-processed using Oasys T/HIS (v10.2. Arup, London, UK). Cross-sectional forces were filtered at CFC 1000 and moments at CFC 600 [79]. The outputs from the nodal force groups were filtered at CFC 1000 and the nodal displacements used to calculate VB rotation at CFC 60. The filtered data was then processed using in-house code written in MATLAB (v7.12.0, MathWorks, Natick, MA). A quantitative validation method developed by Sprague & Geers was used to compare time history plots [80]. This method computes the magnitude (M) and phase (P) contributions to the total error (difference between the benchmark and experimental curves) and combines these metrics into a single comprehensive metric (C) [81, 82]. For example, a perfect magnitude and phase match between two curves would yield zero values for M, P, and C. An experimental curve with twice the magnitude of the benchmark would yield M=1, indicating a 100% larger magnitude. An experimental curve 180° out of phase with the benchmark would yield P=1. The comprehensive metric, C, is the square root of the sum of the squares of M and P. For clarity, all values of M, P, and C are reported as percentages throughout this manuscript.

Results

Overview

The simulation time histories are separated into two categories, fusion (CNRB/ACDF) and CTDR (Prestige ST/ProDisc-C), with the non-modified (IVD) simulation results reported in both categories as a baseline. Positive polarities for the different loading modes reported in these time histories are illustrated in Figure 5-5 [79]. Each time history plot includes vertical lines indicating the approximate time of maximum shoulder belt loading (70 ms) and maximum contact force between the airbag and the occupant (85 ms). These times were determined from the time histories of the seatbelt force from the upper shoulder belt and contact force between the airbag and the occupant (Figure 5-6). Each time history plot also includes two vertical dotted lines indicating the window of time (t=119-124 ms) where the maximum C5 and C6 cross-sectional bending moments occurred for all simulations.

Midsagittal rotation of C5 and C6 about their respective CG are reported in Figure 5-7 with peak rotations reported in Table 5-3. Interbody loading between C5 and C6 was captured via cross-sectional forces measured through the IVD and ACDF, and contact forces from both CTDRs with respect to the C6 LCSYS (Figure 5-8). Facet loading between C5 and C6 was captured via cross-sectional forces measured through the left and right superior C6 facet cartilage and capsule ligament. The distraction of each C5-6 cervical facet capsule beam element was extracted and divided by the neutral ligament length to calculate the strain. The facet forces are reported with respect to C6 in Figure 5-9. Peak interbody forces and peak facet forces and strains are reported in Table 5-4 and Table 5-5.

Adjacent-level, cross-sectional anterior-posterior (AP) shear and axial forces and flexion/extension moments about VB CGs are reported at the C5 and C6 cervical level in their respective LCSYS (Figure 5-10, Figure 5-11, and Figure 5-12) with peak loading reported in Table 5-3. These forces and moments are derived from the total contribution of bone, ligament, active muscle, passive muscle, and soft tissue anatomical components. Pertinent results are described in a timeline fashion, broken into three distinct phases based on the maximum occupant/restraint contact times: Phase 1 from 0-70 ms, Phase 2 from 70-85 ms, and Phase 3 from 85-150 ms. Phase 1 begins at the onset of sled acceleration, continuing up to the approximate time of maximum shoulder belt loading. At this point in time, Phase 2 begins and continues up to the time of maximum contact force between the airbag and the occupant. Phase 3 represents the remainder of the simulation time.

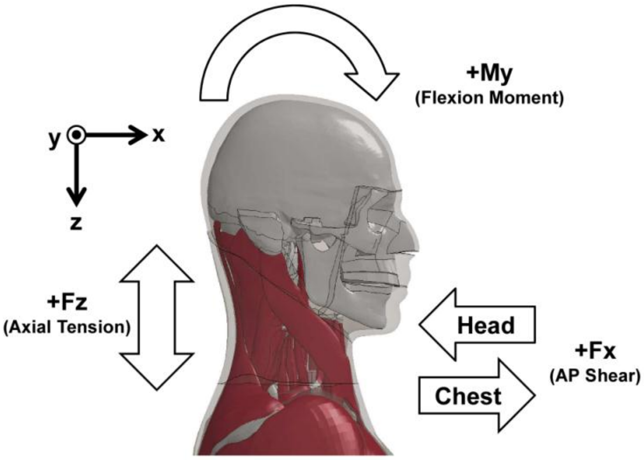

Figure 5-5: Relative head and chest motion corresponding to SAEJ211 standards for positive neck AP shear force, axial force, and bending moment.

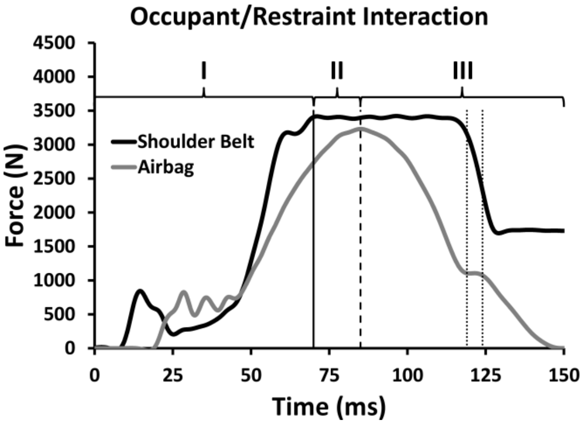

Figure 5-6: Representative time histories of the shoulder belt loading and contact force between the airbag and occupant. The vertical solid line corresponds to the time of maximum upper shoulder belt loading (t=70 ms) and the vertical dashed line to the time of maximum contact force between the airbag and occupant (t=85 ms). These two points of maximum occupant/restraint interaction are used to separate the time histories into three distinct phases. The two vertical dotted lines in Phase III indicate the window of time (t=119-124 ms) where the maximum C5 and C6 cross-sectional bending moments occurred for all simulations.

Table 5-3: Peak adjacent-level, cross-sectional loading through the C5 and C6 VB level with respect to the corresponding LCSYS. Maximum midsagittal rotation was taken about the VB CG.

Simulation	VB	± AP Shear (N)		Ten/Comp (N)		Flex/Ext (Nm)		Rot (deg)
IVD	C5	5.7	-365.6	1053.4	-2.1	63.4	-0.4	-39.0
	C6	28.6	-236.8	1121.2	-4.8	64.6	-0.3	-34.2
ACDF	C5	8.5	-403.1	1053.2	-2.4	62.6	-0.4	-36.4
	C6	35.3	-234.6	1121.9	-4.2	65.0	-0.3	-36.6
CNRB	C5	13.5	-415.5	1059.1	-2.2	62.8	-0.4	-35.5
	C6	37.9	-222.3	1125.2	-3.9	65.7	-0.3	-35.8
Prestige ST	C5	8.7	-395.8	1052.6	-3.1	62.8	-0.3	-37.6
	C6	31.2	-247.3	1125.7	-6.9	64.9	-0.3	-35.2
ProDisc-C	C5	10.2	-397.0	1058.3	-2.2	62.8	-0.3	-38.6
	C6	35.7	-268.7	1127.5	-2.7	65.1	-0.3	-34.0

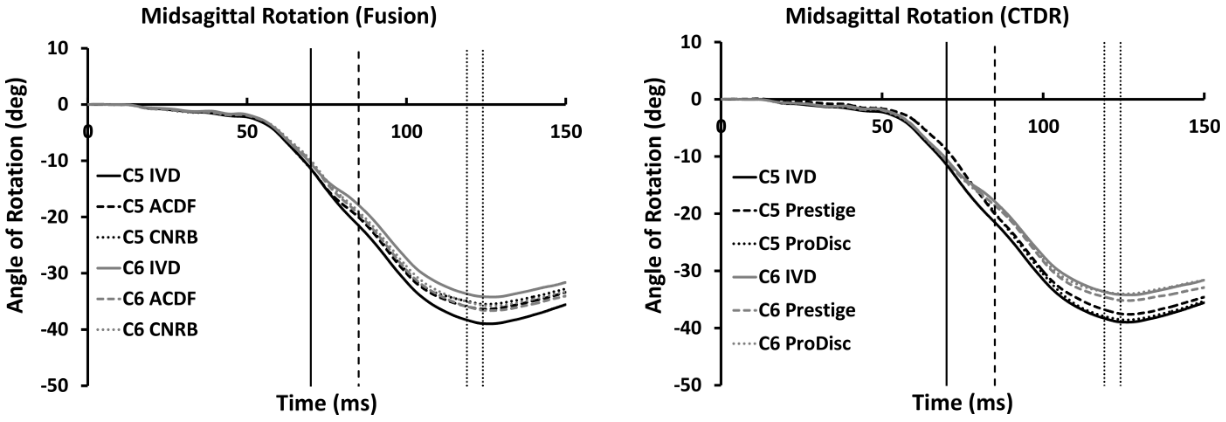

(a) (b)

Figure 5-7: Midsagittal rotation of C5 and C6 about their CGs for the (a) fusion and (b) CTDR simulations. The vertical solid line corresponds to the time of maximum upper shoulder belt loading (t=70 ms) and the vertical dashed line to the time of maximum contact force between the airbag and occupant (t=85 ms). The two vertical dotted lines indicate the window of time (t=119-124 ms) where the maximum C5 and C6 cross-sectional bending moments occurred for all simulations.

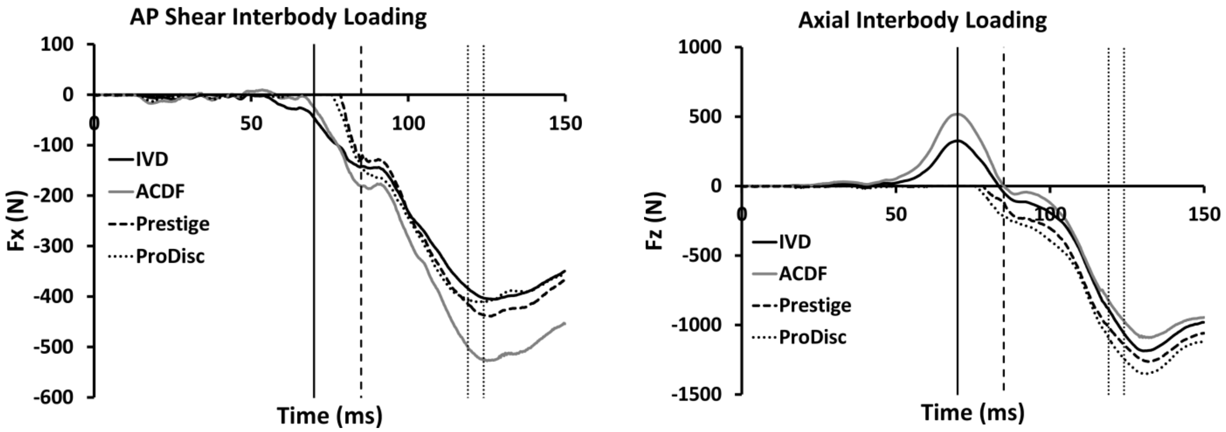

(a) (b)

Figure 5-8: Interbody (a) AP shear and (b) axial force time histories between C5 and C6 reported in the C6 LCSYS. The forces for the IVD and ACDF are reported from cross sections and the CTDRs from contact forces. The vertical solid line corresponds to the time of maximum upper shoulder belt loading (t=70 ms) and the vertical dashed line to the time of maximum contact force between the airbag and occupant (t=85 ms). The two vertical dotted lines indicate the window of time (t=119-124 ms) where the maximum C5 and C6 cross-sectional bending moments occurred for all simulations.

Table 5-4: Peak interbody loading between C5 and C6 with respect to the C6 LCSYS. Cross sections were used to capture the interbody loading for the IVD and ACDF and contact forces for the CTDRs.

Simulation	**Peak Interbody Load (N)**			
	AP Shear		**Ten/Comp**	
IVD	0.5	-405.4	325.8	-1187.0
ACDF	9.6	-527.4	517.3	-1091.7
Prestige ST	0.4	-439.0	0.6	-1263.3
ProDisc-C	0.1	-411.0	0.0	-1351.9

Table 5-5: Peak facet loading and average maximum facet strain between C5 and C6 with respect to the C6 LCSYS.

		AP Shear (+Fx)		**AP Shear (-Fx)**		**Tension (+Fz)**		**Compression (-Fz)**		**Average Maximum Strain (%)**
Simulation	**Facet**	**Time (ms)**	**Force (N)**	**Time (ms)**	**Force (N)**	**Time (ms)**	**Force (N)**	**Time (ms)**	**Force (N)**	
IVD	Left	66.4	8.1	149.8	-20.7	71.6	64.9	149.8	-11.2	14.7±1.8
	Right	66.4	3.9	149.8	-40.8	66.2	19.9	149.8	-37.1	9.1±1.3
ACDF	Left	72.8	4.0	149.9	-12.3	70.1	26.0	149.9	-13.4	9.5±1.7
	Right	69.2	1.7	149.9	-27.0	69.2	7.4	149.9	-28.0	5.7±1.3
Prestige ST	Left	36.6	1.3	78.2	-17.5	72.0	110.3	17.5	-4.8	19.8±3.5
	Right	67.1	2.1	149.9	-37.3	69.3	53.0	149.9	-29.3	13.0±2.4
ProDisc-C	Left	90.2	2.7	76.0	-13.6	72.2	111.1	16.2	-3.4	20.1±3.3
	Right	62.6	1.5	81.1	-26.4	70.6	50.6	21.2	-3.1	13.7±1.6

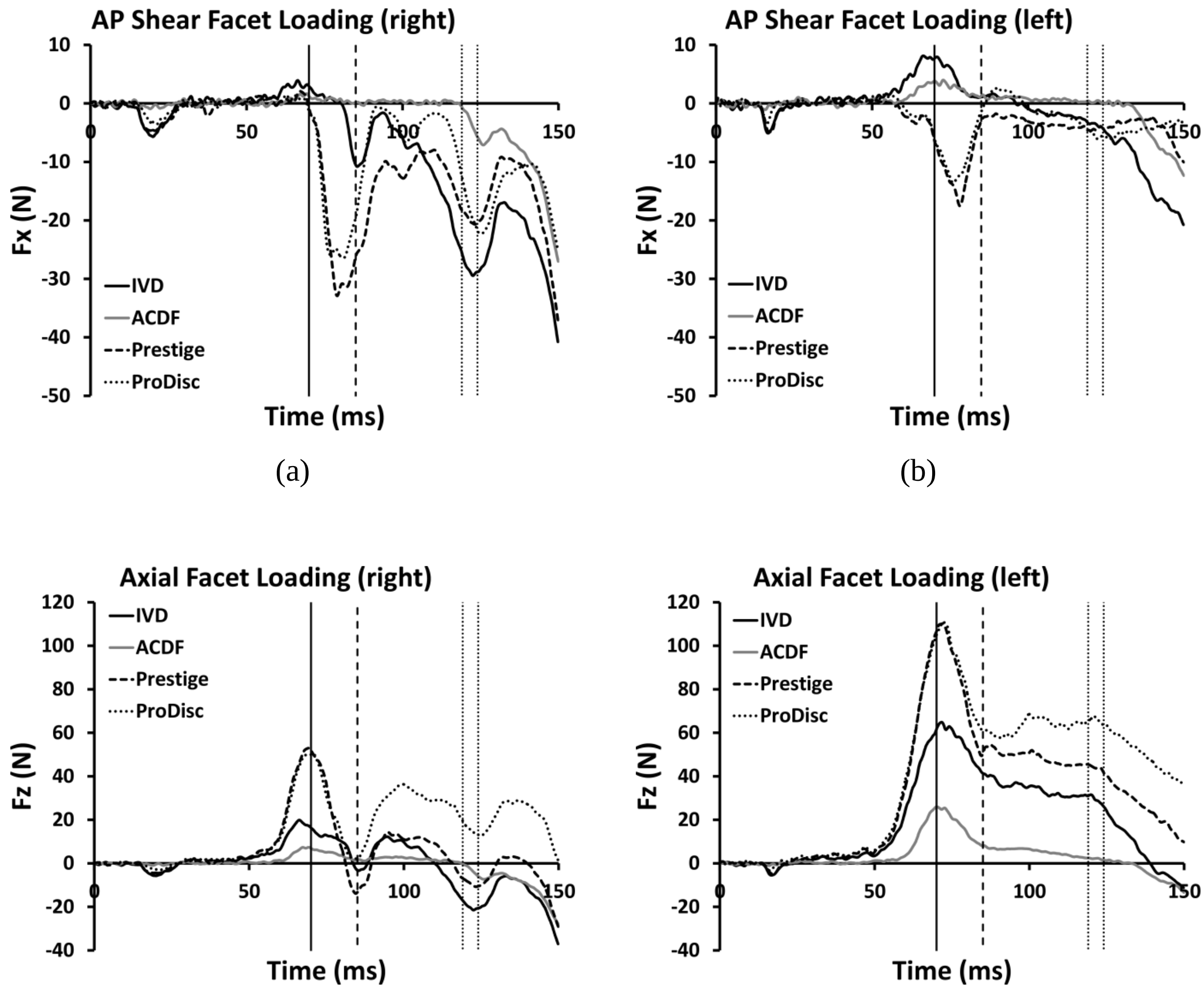

(a) (b)

(c) (d)

Figure 5-9: Facet (a-b) AP shear and (c-d) axial force time histories between C5 and C6 reported in the C6 LCSYS. The vertical solid line corresponds to the time of maximum upper shoulder belt loading (t=70 ms) and the vertical dashed line to the time of maximum contact force between the airbag and occupant (t=85 ms). The two vertical dotted lines indicate the window of time (t=119-124 ms) where the maximum C5 and C6 cross-sectional bending moments occurred for all simulations.

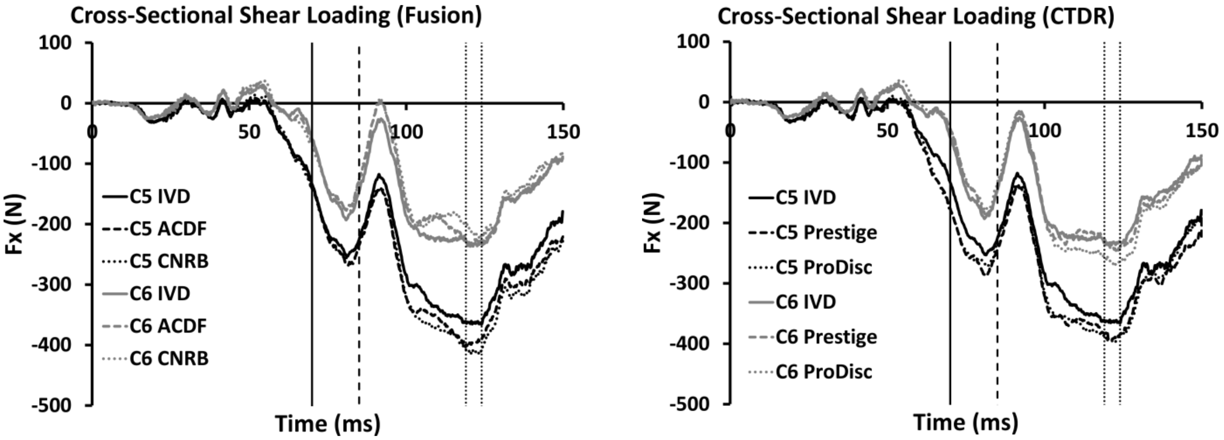

(a) (b)

Figure 5-10: Adjacent-level, cross-sectional AP shear force time histories for the (a) fusion and (b) CTDR simulations. The forces are reported in their respective VB LCSYS. The vertical solid line corresponds to the time of maximum upper shoulder belt loading (t=70 ms) and the vertical dashed line to the time of maximum contact force between the airbag and occupant (t=85 ms). The two vertical dotted lines indicate the window of time (t=119-124 ms) where the maximum C5 and C6 cross-sectional bending moments occurred for all simulations.

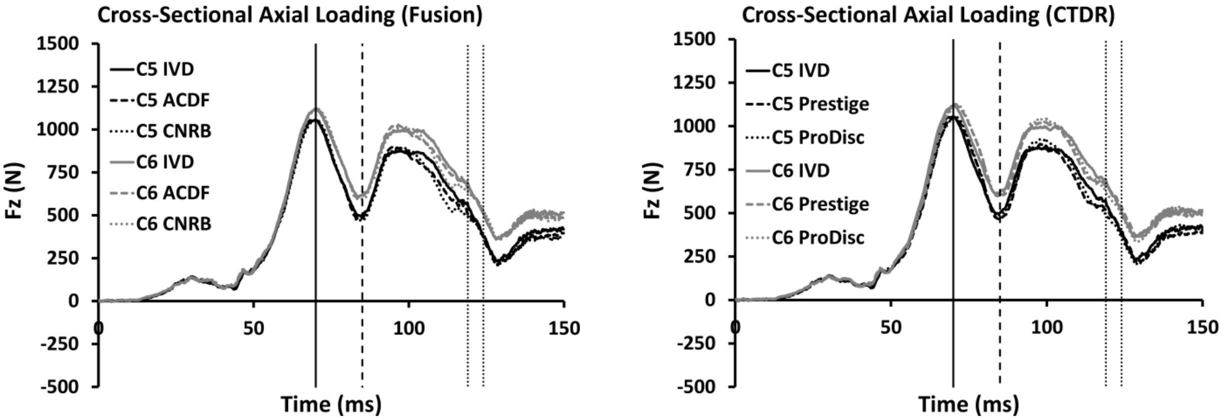

(a) (b)

Figure 5-11: Adjacent-level, cross-sectional axial force time histories for the (a) fusion and (b) CTDR simulations. The forces are reported in their respective VB LCSYS. The vertical solid line corresponds to the time of maximum upper shoulder belt loading (t=70 ms) and the vertical dashed line to the time of maximum contact force between the airbag and occupant (t=85 ms). The two vertical dotted lines indicate the window of time (t=119-124 ms) where the maximum C5 and C6 cross-sectional bending moments occurred for all simulations.

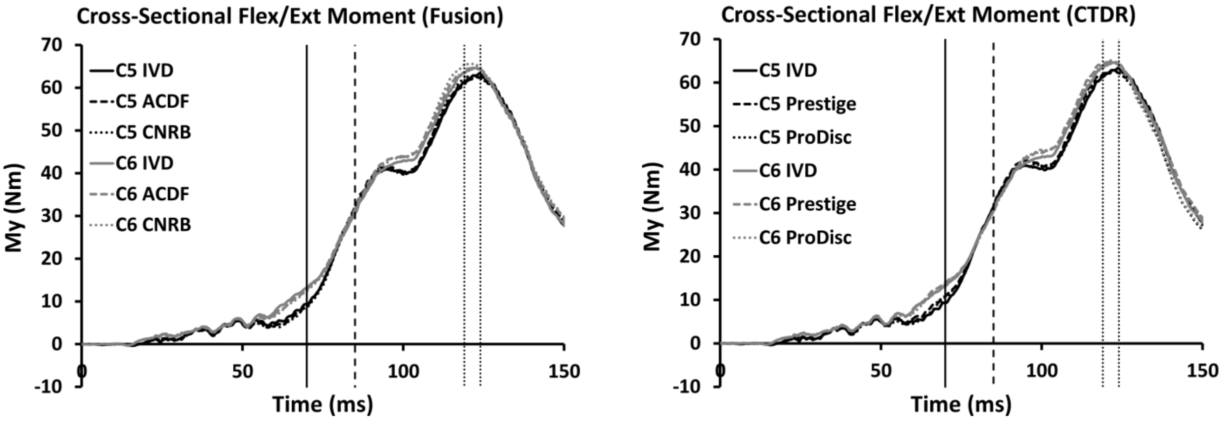

(a) (b)

Figure 5-12: Adjacent-level, cross-sectional bending moment time histories for the (a) fusion and (b) CTDR simulations. The moments are taken about the VB CG and are reported in their respective VB LCSYS. The vertical solid line corresponds to the time of maximum upper shoulder belt loading (t=70 ms) and the vertical dashed line to the time of maximum contact force between the airbag and occupant (t=85 ms). The two vertical dotted lines indicate the window of time (t=119-124 ms) where the maximum C5 and C6 cross-sectional bending moments occurred for all simulations.

Phase 1 (0-70 ms)

Midsagittal rotations of both C5 and C6 VBs begin early in this phase and are almost identical for all simulations (Figure 5-7). An exception to this observation occurs between 50 and 70 ms where the C5 VB rotations from the CTDR simulations are slightly lower than the other VB rotations.

AP shear and axial interbody loading (Figure 5-8) is negligible for the CTDRs in this phase. Negative AP shear interbody loading in the IVD and ACDF begins at approximately 55 ms, becoming more noticeable just prior to the end of the phase. Interbody tension in both the IVD and ACDF begins at approximately 50 ms, reaching global peaks of 325.8 N and 517.3 N, respectively.

The AP shear facet loading (Figure 5-9) is negligible for the CTDRs in this phase. Positive AP shear facet loading in the IVD and ACDF begins at approximately at 55 ms, reaching global peaks of 8.1 N and 4.0 N, respectively. Peak total facet global tension is achieved for all simulations towards the end of the phase. The CTDR total facet tension traces are almost identical, reaching a peak value of 110.3 N for the Prestige ST and 111.1 N for the ProDisc-C. Peak total facet tension for the IVD and ACDF are 64.9 N and 26.0 N, respectively.

Cross-sectional negative AP shear (Figure 5-10) begins at approximately 55 ms for all simulations. Cross-sectional tension (Figure 5-11) is produced for all simulations with global peaks reached at the end of the phase. Peak tension ranged between 1052.6 N and 1059.1 N at the C5 VB level and between 1121.2 N and 1127.5 N at the C6 VB level. A cross-sectional flexion bending moment (Figure 5-12) is experienced at both levels in all simulations, with a noticeable increase at approximately 50 ms.

Phase 2 (70-85 ms)

During this phase, the C5 and C6 rotation of the IVD VBs begin to differentiate, with C6 rotating less than C5 (Figure 5-7). The relative difference in rotation between C5 and C6 in both fusion simulations remains negligible, with the traces running midway between the IVD C5 and C6 traces. The C5 rotations of the CTDRs surpass the C6 rotations during this phase.

Approximately halfway through this phase the CTDRs begin to experience interbody negative AP shear loading and compression (Figure 5-8). Interbody tension decreases to approximately zero for both the IVD and ACDF by the end of this phase. The global peak negative AP shear facet loads for the CTDRs are achieved during this phase; -37.3 N for the Prestige ST and -26.4 N for the ProDisc-C. The facet axial loading is decreasing during this phase for all simulations. The same is true for the adjacent-level, cross-sectional axial loading (Figure 5-10, Figure 5-11, and Figure 5-12).

Phase 3 (85-150 ms)

Peak rotation of C5 and C6 occurs between 121 ms and 128 ms for all simulations (Figure 5-7). For the IVD, rotation of C5 is always greater than C6, with a maximum relative difference of 4.8˚ between to the two VBs. As would be expected, C5 and C6 rotation are almost identical for the fusions. The fusion traces run midway between the IVD C5 and C6 rotations. The CTDR traces follow the IVD traces much closer. The maximum relative difference in rotation between C5 and C6 is 2.4˚ for the Prestige ST and 4.6˚ for the ProDisc-C.

Peak negative AP shear interbody loading occurs between 118 ms and 128 ms, and peak compressive interbody loading between 130 ms and 132 ms for all simulations (Figure 5-8). Peak negative AP shear ranged from -405.4 N for the IVD to -527.7 N for the ACDF while peak compression ranged from -1091.7 N for the ACDF to -1351.9 N for the ProDisc-C.

The peak adjacent-level, cross-sectional negative AP shear force occurs between 118 ms and 124 ms for all simulations (Figure 5-10). The peak flexion moment occurs between 119 ms and 124 ms (Figure 5-12). The larger negative AP shear force occurs at the C5 level, ranging from -365.6 N for the IVD to -415.5 N for the CNRB. The greatest flexion moment occurs at the C6 level, ranging from 64.6 Nm for the IVD to 65.7 Nm for the CNRB.

Several observations are made during the five-second window where the maximum cross-sectional C5 and C6 bending moments occurs (t=119-124 ms). Within this window of time, shoulder belt loading sharply decreases while occupant to airbag contact force plateaus (Figure 5-6). The majority of the peak adjacent-level, cross-sectional negative AP shear forces occur within this window (Figure 5-10). A point of inflection in the right AP shear facet loading occurs for all simulations immediately after this window (Figure 5-9a).

Quantitative Comparison

Two separate quantitative comparisons of the adjacent-level, cross-sectional loading and VB rotational time histories were conducted using the Sprague & Geers method. The first analysis compares the ACDF (benchmark) to the CNRB (experiment) with results reported in Table 5. The second analysis compares the IVD (benchmark) to the fusions and CTDRs (experiments) with results reported in Table 6. The entire time history is evaluated in these comparisons, with a time interval of t=0-150 ms. As stated in the Methods section of this manuscript, the magnitude, phase, and comprehensive errors are reported as percentages. Another example is given to reemphasize the physical meaning and interpretation of these comparative metrics. A magnitude error of 10% would indicate the magnitude of the experimental curve is 10% greater than the magnitude of the benchmark curve. A phase error of 50% would indicate the experimental curve was 50% (90°) out of phase with the benchmark curve. The comprehensive error is the square root of the sum of the squares of the magnitude and phase errors; 51% for this example.

In the fusion analysis, the largest comprehensive errors occur at the C6 level. These errors ranged from 4.53% for AP shear loading to 0.78% for moment loading. The magnitude was underestimated by the CNRBs for AP shear loading, axial loading, and midsagittal rotation. For the non-modified versus modified neck analysis, the magnitude error factor typically contributes more to the comprehensive error than the phase shift error factor. Additionally, the largest comprehensive errors occur in the CNRB and Prestige ST simulations. The largest errors for the adjacent-level, cross-sectional AP shear loading occur at the C5 level with 11.82% for the CNRB and 10.22% for the Prestige ST. In both cases, the magnitudes overestimate the IVD response. The largest axial loading and rotational comprehensive errors also occur at the C5 level with magnitudes underestimating the IVD response. The axial force and rotation errors are 3.83% and 7.70% for the CNRB and 3.26% and 4.73% for the Prestige ST, respectively. The largest compressive error for flexion/extension moment is 2.24% for the CNRB and 1.54% for the Prestige ST, both occurring at the C6 level. In both cases the magnitudes overestimate the IVD response.

Table 5-6: Quantitative comparison analysis of the two fusion simulations. Sprague and Geers magnitude (M), phase (P) and comprehensive (C) error factors are expressed as a percentage for the cross-sectional loading and VB rotation time histories. The corresponding ACDF curve was defined as the benchmark data and the CNRB curve as the experimental data.

Loading	**C5**			**C6**		
	M	**P**	**C**	**M**	**P**	**C**
AP Shear	2.70	0.94	2.86	-4.06	2.02	4.53
Axial	-1.13	1.09	1.57	-1.30	0.99	1.64
Moment	0.19	0.50	0.53	0.63	0.47	0.78
Rotation	-1.82	0.24	1.83	-2.28	0.08	2.28

Discussion

General

A series of five frontal automobile collisions with airbag deployment were simulated with a belted 50th percentile male human body FE model. The C5-6 level of the spine was modified in four of the cases to simulate either a cervical arthrodesis or arthroplasty. The arthrodesis modifications were modeled with either a cluster of CNRBs joining the superior and inferior VBs or a simplified cage, core, and anterior plate ACDF. The arthroplasty modifications were modeled with either a Prestige ST, allowing for rotation and anterior-posterior translation, or a

ProDisc-C, allowing for rotation only. The kinematics and kinetics of C5-6 functional spinal unit were examined using adjacent-level, cross-sectional loading, VB rotation, interbody loading, and facet loading and strain.

ACDF vs. CNRBs

Implementation of CNRBs into the neck to simulate a fusion between adjacent VBs was a less time consuming and computationally less expensive approach than modeling an ACDF. However, it is important that the CNRB neck response adequately mimics a realistic ACDF response. With the ACDF as the benchmark data and CNRBs as the experimental data, the Sprague & Geers method was utilized to compare the two fusion methods. Both fusion methods yielded negligible relative rotation between C5 and C6, as would be expected. While the VB rotations of the CNRB model were less than the ACDF model, the largest rotation difference between fusion methods was less than 1˚ and considered negligible. One of the major drawbacks of the CNRB method was that interbody shear and axial forces were not available for comparison with IVD results.

For adjacent-level, cross-sectional loading the comprehensive errors were less than 2% for the axial loading and 1% for the moment for both vertebral levels. Difference in bending moment was negligible for both VB levels. Current Federal Motor Vehicle Safety Standards (FMVSS) include the N_{ij} neck injury criteria to evaluate the risk of neck injury from frontal motor vehicle collisions (MVCs) using a linear combination of normalized axial loading and bending moment [83, 84]. With minimal difference in the axial and moment loading between the

Table 5-7: Quantitative comparison analysis of the non-modified and modified neck simulations. Sprague and Geers magnitude (M), phase (P), and comprehensive (C) error factors expressed as a percentage for the cross-sectional loading and VB rotation time histories. The corresponding IVD curve was defined as the benchmark to which all others curves were compared.

VB Level	**Simulation**	**Shear**			**Axial**			**Moment**			**Rotation**		
		M	**P**	**C**	**M**	**P**	**C**	**M**	**P**	**C**	**M**	**P**	**C**
C5	ACDF	8.80	1.09	8.87	-2.28	1.23	2.59	0.34	0.49	0.59	-5.96	0.39	5.98
	CNRB	11.73	1.39	11.82	-3.38	1.80	3.83	0.53	0.65	0.84	-7.67	0.59	7.70
	Prestige ST	10.08	1.68	10.22	-2.80	1.67	3.26	1.13	0.62	1.29	-4.59	1.13	4.73
	ProDisc-C	8.78	1.64	8.93	-0.78	1.64	1.82	-1.13	0.85	1.41	-2.37	1.31	2.71
C6	ACDF	-5.77	2.66	6.35	-0.85	0.86	1.21	1.51	0.55	1.61	7.05	0.42	7.07
	CNRB	-9.59	3.21	10.12	-2.14	1.41	2.56	2.14	0.66	2.24	4.61	0.46	4.63
	Prestige ST	1.13	2.08	2.37	-1.06	1.41	1.77	1.47	0.46	1.54	3.11	0.16	3.12
	ProDisc-C	7.73	2.87	8.25	-0.36	1.45	1.49	-0.31	0.86	0.91	0.59	0.46	0.75

CNRB and ACDF, N_{ij} calculations should not vary greatly. While N_{ij} is routinely used to evaluate injury risk at the junction of the occipital condyle and C1, lower neck critical intercepts exist [85].

Prestige ST vs. ProDisc-C

Rotation of both VB levels matched between CTDRs up to the time of maximum occupant/airbag interaction; the end of phase 2. The simulation kinematics revealed the Prestige ST reached its maximum AP translation at this time. The ProDisc-C allowed more rotation, as well as some additional AP translation due to deformation of the semi-spherical inlay. The maximum relative rotational difference between C5 and C6 of the ProDisc-C was within 0.2˚ of the IVD rotation, closer than for the Prestige ST. Along with the lower rotational comprehensive error for both VB levels, it is apparent that the C5 and C6 rotation of the ProDisc-C followed the IVD rotation more closely than did the Prestige ST.

For adjacent-level, cross-sectional loading, the peak negative AP shear forces for both CTDRs were almost identical at the C5 level and 8.0% greater for the ProDisc-C at the C6 level. Peak negative AP interbody shear force was 6.8% greater for the Prestige ST than for the ProDisc-C. At the time of peak negative AP shear, the simulation kinematics reveal the superior socket of the ProDisc-C catching on the semi-sphere inlay, deforming it slightly. The non-deformable Prestige ST reached its maximum AP translation much earlier and was purely rotating at this point in time.

The peak adjacent-level, cross-sectional tensile force was almost identical between CTDRs and IVD for both VB levels. As neither of the CTDRs was capable of supporting interbody tension, the axial interbody forces remained negligible until compression occurred.

During this period, a physical separation between the inferior and superior CTDR components was visualized in the simulation. Interbody compression followed a similar trend for both CTDRs with a peak compression force 7.0% greater for the ProDisc-C than for the Prestige ST.

For adjacent-level, cross-sectional loading, the peak bending moment was almost identical between CTDRs and IVD for both VB levels. The comprehensive errors were all less than 2%, indicating minimal difference in bending moment between the modified and non-modified cervical spines.

Fusion vs. CTDRs

Biomechanical injury assessment reference values (IARVs) for the junction between the head and neck and the neck and torso of 50th percentile male occupant have been previously defined [85]. Peak loading below these thresholds minimizes the risk of neck injury. The force thresholds for the upper and lower neck are ±3100 N for AP shear, 4170 N for axial tension and -4000 N for axial compression. The bending moment thresholds for the upper neck are 190 Nm for flexion and -96 Nm for extension and for the lower neck are 380 Nm for flexion and -192 Nm for extension. The peak adjacent-level, cross-sectional shear and axial loading at C5 and C6 fell well below these IARVs for all simulations.

As would be expected, the CTDRs maintained midsagittal rotation of the C5 and C6 VBs closer to the IVD than the fusions. Rotation was best preserved by the ProDisc-C in terms of peak rotation, peak relative rotation, and comprehensive error. The largest comprehensive error was less than 12% for all adjacent-level, cross-sectional loading time histories with the majority less than 5%. This indicates that the overall neck loading time histories adjacent to a simulated arthrodesis or arthroplasty were not greatly altered. There was negligible difference between simulations for peak bending moment and peak tension. The largest comprehensive errors for all simulations occurred for AP shear loading. Both fusions created a stiff interface between adjacent VBs, thereby altering the shear loading. When the translation of the superior ball of the Prestige ST reached the anterior end of the trough only rotation could occur, increasing the shear force at the C5 and C6 VB levels. The ProDisc-C did not allow for translation, other than that due to minor deformation of the semi-spherical inlay which increased the shear force at adjacent VB levels.

The largest interbody AP shear force occurred in the ACDF, followed by the Prestige ST, ProDisc-C, and then IVD. The cage, core, and anterior plate of the ACDF prevented relative AP displacement between C5 and C6, therefore creating the greatest shear forces. The Prestige ST allowed for some AP translation; however, once maximum translation was reached, shear force increased. The Prestige ST shear force remained lower than the ACDF.

While the ProDisc-C is not designed to allow AP translation, the increased VB rotation and some deformation of the semi-spherical inlay created a shear force larger than the IVD, but less than the ACDF and Prestige ST. The increase in adjacent-level translation in both CTDRs increased the AP shear facet loading. Interbody tension occurred only in ACDF and IVD. Without a firm connection between the inferior C5 and superior C6 VB surfaces, interbody tension was not supported through the CTDRs, allowing for a period of VB separation during the simulations. This separation almost doubled the amount of tension measured in the facets versus the tension measured in the IVD simulation. Lee and Winkelstein [86] reported the response of the human cervical facet capsular ligament during failure from quasi-static retraction of one joint. Average gross failure was reported at 61.81 ± 26.40 N, partial failure at 45.81 ± 22.99 N and ligament yielding at 30.65 ± 25.54 N. Mattucci et al. [64] reported the response of the human cervical facet from dynamic testing at 250 s^{-1}, equivalent to the strain rate experienced during a 22g frontal car crash scenario. Average failure was reported at 286 ± 73 N and 111.0±46% strain. The reported right and left facet tension and average maximum strain in the current study, for the CTDR simulations, are below these gross failure levels for dynamic loading.

The ACDF experienced the least amount of interbody compression, even less than the IVD. However, it is important to note that the peak shear and tension occurred at approximately the same time for the IVD and ACDF. The difference in the resultant force between the IVD and ACDF interbody forces is much less than the difference in individual force components, indicating similar loading through the interbody space. The difference in relative rotations between the VBs in these two simulations most likely accounts for the mismatch in peak shear and compression. Both CTDRs produced greater interbody axial compression than the IVD and ACDF, potentially due to the change in center of rotation and facet loading.

Comparison to Quasi-Static Experiments

While the vast majority of cervical arthrodesis and arthroplasty experimental studies are quasi-static, they give insight into the change in kinematics and loading from these procedures. Attention is given to flexion as it was the primary bending mode in the current study. Biomechanical studies conducted by DiAngelo et al. investigated the change in motion patterns of C2-T1 cadaveric cervical spines after surgical implantation of an ACDF, Prestige ST, and ProDisc-C at C5-6 using a displacement controlled method [87, 88]. The motion patterns at the operated and adjacent levels were not altered during physiological flexion for both CTDRs, unlike the ACDF in which motion was decreased. The motion preservation experimentally observed in the CTDR specimens corresponds well with observations from the current study. In

2007 Chang et al. conducted a series of tests on C3-T2 cadaveric cervical spines using a load-control, pure moment method to investigate the effect on load transmission through the IVDs and facets after surgical implantation of an ACDF, Prestige ST, and ProDisc-C at C6-7 [89]. The adjacent-level IVD pressure did not vary greatly between the intact spine and CTDRs; however, the pressure did increase for the ACDF in flexion at the proximal level. There was no significant change in facet loading noted in flexion. Cadaveric studies conducted by Jaumard et al. [90] and Bauman et al. [91] reported that a ProDisc-C arthroplasty did not significantly alter facet joint contact pressure during lateral, axial or sagittal bending.

While adjacent-level IVDs were not investigated in the current study, the cross-sectional axial loading gives insight into the change in adjacent-level loading. The peak tension adjacent to the implant site was almost identical for the IVD, fusions, and CTDRs, indicating that there would be little change in adjacent IVD pressure. It is important to note, however, that the reported cross-sectional forces include contributions from other load-bearing tissue structures besides the skeleton. A finite element study by Womack et al. utilized a C3-7 lower cervical spine model to investigate alterations in kinematics and load transmission from a ProDisc-C modeled between C4-5 [58]. Implant size was found to strongly affect the facet and interbody implant forces. The increase in CTDR interbody loading for the current study may be explained by this finding.

Future Work

Future work includes examining the effects of arthrodesis and arthroplasty throughout the entire cervical spine using the current impact simulation along with side and rear impact configurations. A more detailed analysis of cross-sectional load distribution will be conducted on the IVD and ACDF, reporting the individual contributions of the annulus fibrosus, nucleus pulposus, and anterior longitudinal ligament of the IVD and the PEEK cage, trabecular bone core, and titanium anterior plate of the ACDF. Cross-sectional loading contributions from different anatomical structures, including bone, ligaments, and musculature will also be examined. Future experimental ACDF and CTDRs endeavors will include kinematic studies of intact cervical spines using a six-degree-of-freedom force-torque controlled industrial robotic arm and full body or regional post mortem human subject (PMHS) tests with a high-speed, biplane x-ray system.

Conclusions

This study is the first dynamic finite element analysis of a frontal automobile impact to evaluate the effects of a C5-6 cervical arthrodesis and arthroplasty on neck response. Cross-sectional loading above and below C5-6 interbody space was maintained in all simulations without exceeding any IARVs. The midsagittal rotation of the C5 and C6 VBs were maintained well with the CTDRs. Interbody compression was greatest for the CTDR cases, possibly due to a change in center of rotation and its effects on facet loading. Interbody tension occurred only in the ACDF and IVD, as the superior and inferior components of the CTDRs were independent of one another. The design of the CTDRs allowed for some interbody separation to occur between the superior and inferior components during flexion-induced tension of the cervical spine, subsequently increasing the facet tension and strain. While cervical arthrodesis and arthroplasty at C5-6 did not appear to significantly alter the adjacent-level, cross-sectional neck responses during a simulated frontal automobile impact, key differences were noted in the interbody loading, facet loading, and maximum facet strain.

Acknowledgements

The authors would like to acknowledge the United States Army Medical Research and Materiel Command for funding this research and the Global Human Body Models Consortium for use of the 50th percentile seated male FE model. The authors would also like to acknowledge Medtronic Sofamor Danek (Memphis, TN) for supplying a Prestige ST implant and Synthes Spine (West Chester, PA) for supplying a ProDisc-C implant for reverse engineering purposes. All computations were performed on the Wake Forest University DEAC Cluster, a centrally managed resource with support provided in part by the University.

Chapter 5 References

[1] Gore DR, Sepic SB, Gardner GM. Roentgenographic Findings of the Cervical Spine in Asymptomatic People. Spine. 1986;11:521-4.

[2] Gore DR. Roentgenographic Findings in the Cervical Spine in Asymptomatic Persons: A Ten-Year Follow-Up. Spine. 2001;26:2463-6.

[3] Boden SD, McCowin PR, Davis DO, Dina TS, Mark AS, Wiesel S. Abnormal Magnetic-Resonance Scans of the Cervical Spine in Asymptomatic Subjects. A Prospective Investigation. The Journal of bone and joint surgery American volume. 1990;72:1178-84.

[4] Roh JS, Teng AL, Yoo JU, Davis J, Furey C, Bohlman HH. Degenerative Disorders of the Lumbar and Cervical Spine. The Orthopedic clinics of North America. 2005;36:255-62.

[5] Habela NM, McAfee PC. Indications and Contraindications for Cervical Nonfusion Surgery: Patient Selection. In: Yue JJ, Bertagnoli R, McAfee PC, An HS, editors. Motion Preservation Surgery of the Spine: Advanced Techniques and Controversies. Philadelphia: Saunders; 2008. p. 80-4.

[6] Matan AJ, Connolly PJ. Concepts of Cervical Decompression. In: Herkowitz HN, editor. The Cervical Spine Surgery Atlas. 2 ed. Philadelphia: Lippincott Williams & Wilkins; 2004. p. 123-38.

[7] Montgomery DM, Brower RS. Cervical Spondylotic Myelopathy. Clinical Syndrome and Natural History. The Orthopedic clinics of North America. 1992;23:487-93.

[8] Bailey RW, Badgley CE. Stabilization of the Cervical Spine by Anterior Fusion. The Journal of bone and joint surgery American volume. 1960;42-A:565-94.

[9] Cloward RB. The Anterior Approach for Removal of Ruptured Cervical Disks. Journal of neurosurgery. 1958;15:602-17.

[10] Smith GW, Robinson RA. The Treatment of Certain Cervical-Spine Disorders by Anterior Removal of the Intervertebral Disc and Interbody Fusion. The Journal of bone and joint surgery American volume. 1958;40-A:607-24.

[11] Fallah A, Akl EA, Ebrahim S, Ibrahim GM, Mansouri A, Foote CJ, et al. Anterior Cervical Discectomy with Arthroplasty Versus Arthrodesis for Single-Level Cervical Spondylosis: A Systematic Review and Meta-Analysis. PloS one. 2012;7:e43407.

[12] Helgeson MD, Bevevino AJ, Hilibrand AS. Update on the Evidence for Adjacent Segment Degeneration and Disease. The spine journal : official journal of the North American Spine Society. 2013;13:342-51.

[13] Mummaneni PV, Amin BY, Wu JC, Brodt ED, Dettori JR, Sasso RC. Cervical Artificial Disc Replacement Versus Fusion in the Cervical Spine: A Systematic Review Comparing Long-Term Follow-up Results from Two FDA Trials. Evidence-based spine-care journal. 2012;3:59-66.

[14] Goffin J, Geusens E, Vantomme N, Quintens E, Waerzeggers Y, Depreitere B, et al. Long-Term Follow-up after Interbody Fusion of the Cervical Spine. Journal of spinal disorders & techniques. 2004;17:79-85.

[15] Gore DR, Sepic SB. Anterior Cervical Fusion for Degenerated or Protruded Discs. A Review of One Hundred Forty-Six Patients. Spine. 1984;9:667-71.

[16] Hilibrand AS, Carlson GD, Palumbo MA, Jones PK, Bohlman HH. Radiculopathy and Myelopathy at Segments Adjacent to the Site of a Previous Anterior Cervical Arthrodesis. The Journal of bone and joint surgery American volume. 1999;81:519-28.

[17] Matsunaga S, Kabayama S, Yamamoto T, Yone K, Sakou T, Nakanishi K. Strain on Intervertebral Discs after Anterior Cervical Decompression and Fusion. Spine. 1999;24:670-5.

[18] Eck JC, Humphreys SC, Lim TH, Jeong ST, Kim JG, Hodges SD, et al. Biomechanical Study on the Effect of Cervical Spine Fusion on Adjacent-Level Intradiscal Pressure and Segmental Motion. Spine. 2002;27:2431-4.

[19] Albert TJ, Eichenbaum MD. Goals of Cervical Disc Replacement. The spine journal : official journal of the North American Spine Society. 2004;4:292S-3S.

[20] Traynelis VC. Cervical Arthroplasty. Clinical neurosurgery. 2006;53:203-7.

[21] Anderson PA, Sasso RC, Riew KD. Update on Cervical Artificial Disk Replacement. Instructional course lectures. 2007;56:237-45.

[22] Baaj AA, Uribe JS, Vale FL, Preul MC, Crawford NR. History of Cervical Disc Arthroplasty. Neurosurgical focus. 2009;27:E10.

[23] Tharin S, Benzel EC. Cervical Spine Arthroplasty: Fact or Fiction: The Absence of Need for Arthroplasty. Clinical neurosurgery. 2012;59:82-90.

[24] McAfee PC, Reah C, Gilder K, Eisermann L, Cunningham B. A Meta-Analysis of Comparative Outcomes Following Cervical Arthroplasty or Anterior Cervical Fusion: Results from 4 Prospective Multicenter Randomized Clinical Trials and up to 1226 Patients. Spine. 2012;37:943-52.

[25] Mummaneni PV, Burkus JK, Haid RW, Traynelis VC, Zdeblick TA. Clinical and Radiographic Analysis of Cervical Disc Arthroplasty Compared with Allograft Fusion: A Randomized Controlled Clinical Trial. Journal of neurosurgery Spine. 2007;6:198-209.

[26] Upadhyaya CD, Wu JC, Trost G, Haid RW, Traynelis VC, Tay B, et al. Analysis of the Three United States Food and Drug Administration Investigational Device Exemption Cervical Arthroplasty Trials. Journal of neurosurgery Spine. 2012;16:216-28.

[27] Yin S, Yu X, Zhou S, Yin Z, Qiu Y. Is Cervical Disc Arthroplasty Superior to Fusion for Treatment of Symptomatic Cervical Disc Disease? A Meta-Analysis. Clinical orthopaedics and related research. 2013;471:1904-19.

[28] Boselie TF, Willems PC, van Mameren H, de Bie R, Benzel EC, van Santbrink H. Arthroplasty Versus Fusion in Single-Level Cervical Degenerative Disc Disease. The Cochrane database of systematic reviews. 2012;9:CD009173.

[29] Chen J, Fan SW, Wang XW, Yuan W. Motion Analysis of Single-Level Cervical Total Disc Arthroplasty: A Meta-Analysis. Orthopaedic surgery. 2012;4:94-100.

[30] Ding C, Hong Y, Liu H, Shi R, Hu T, Li T. Intermediate Clinical Outcome of Bryan Cervical Disc Replacement for Degenerative Disk Disease and Its Effect on Adjacent Segment Disks. Orthopedics. 2012;35:e909-16.

[31] Nunley PD, Jawahar A, Kerr EJ, 3rd, Gordon CJ, Cavanaugh DA, Birdsong EM, et al. Factors Affecting the Incidence of Symptomatic Adjacent-Level Disease in Cervical Spine after Total Disc Arthroplasty: 2- to 4-Year Follow-up of 3 Prospective Randomized Trials. Spine. 2012;37:445-51.

[32] Rollinghoff M, Zarghooni K, Hackenberg L, Zeh A, Radetzki F, Delank KS. Quality of Life and Radiological Outcome after Cervical Cage Fusion and Cervical Disc Arthroplasty. Acta orthopaedica Belgica. 2012;78:369-75.

[33] Yang B, Li H, Zhang T, He X, Xu S. The Incidence of Adjacent Segment Degeneration after Cervical Disc Arthroplasty (Cda): A Meta Analysis of Randomized Controlled Trials. PloS one. 2012;7:e35032.

[34] Nesterenko SO, Riley LH, 3rd, Skolasky RL. Anterior Cervical Discectomy and Fusion Versus Cervical Disc Arthroplasty: Current State and Trends in Treatment for Cervical Disc Pathology. Spine. 2012;37:1470-4.

[35] Saito T, Yamamuro T, Shikata J, Oka M, Tsutsumi S. Analysis and Prevention of Spinal Column Deformity Following Cervical Laminectomy. I. Pathogenetic Analysis of Postlaminectomy Deformities. Spine. 1991;16:494-502.

[36] Kumaresan S, Yoganandan N, Pintar FA. Finite Element Analysis of Anterior Cervical Spine Interbody Fusion. Bio-medical materials and engineering. 1997;7:221-30.

[37] Maiman DJ, Kumaresan S, Yoganandan N, Pintar FA. Biomechanical Effect of Anterior Cervical Spine Fusion on Adjacent Segments. Bio-medical materials and engineering. 1999;9:27-38.

[38] Natarajan RN, Chen BH, An HS, Andersson GB. Anterior Cervical Fusion: A Finite Element Model Study on Motion Segment Stability Including the Effect of Osteoporosis. Spine. 2000;25:955-61.

[39] Galbusera F, Fantigrossi A, Raimondi MT, Sassi M, Fornari M, Assietti R. Biomechanics of the C5-C6 Spinal Unit before and after Placement of a Disc Prosthesis. Biomechanics and modeling in mechanobiology. 2006;5:253-61.

[40] Ha SK. Finite Element Modeling of Multi-Level Cervical Spinal Segments (C3-C6) and Biomechanical Analysis of an Elastomer-Type Prosthetic Disc. Medical engineering & physics. 2006;28:534-41.

[41] Lopez-Espina CG, Amirouche F, Havalad V. Multilevel Cervical Fusion and Its Effect on Disc Degeneration and Osteophyte Formation. Spine. 2006;31:972-8.

[42] Dang AB, Hu SS, Tay BK. Biomechanics of the Anterior Longitudinal Ligament During 8 G Whiplash Simulation Following Single- and Contiguous Two-Level Fusion: A Finite Element Study. Spine. 2008;33:607-11.

[43] Galbusera F, Bellini CM, Raimondi MT, Fornari M, Assietti R. Cervical Spine Biomechanics Following Implantation of a Disc Prosthesis. Medical engineering & physics. 2008;30:1127-33.

[44] Rousseau MA, Bonnet X, Skalli W. Influence of the Geometry of a Ball-and-Socket Intervertebral Prosthesis at the Cervical Spine: A Finite Element Study. Spine. 2008;33:E10-4.

[45] Faizan A, Goel VK, Garfin SR, Bono CM, Serhan H, Biyani A, et al. Do Design Variations in the Artificial Disc Influence Cervical Spine Biomechanics? A Finite Element Investigation. European spine journal : official publication of the European Spine Society, the European Spinal Deformity Society, and the European Section of the Cervical Spine Research Society. 2009.

[46] Lin CY, Kang H, Rouleau JP, Hollister SJ, Marca FL. Stress Analysis of the Interface between Cervical Vertebrae End Plates and the Bryan, Prestige Lp, and Prodisc-C Cervical Disc Prostheses: An in Vivo Image-Based Finite Element Study. Spine. 2009;34:1554-60.

[47] Womack WJ. Computational Modeling of the Lower Cervical Spine Facet Cartilage Distribution and Disc Replacement: Colorado State University; 2009.

[48] Crawford NR, Arnett JD, Butters JA, Ferrara LA, Kulkarni N, Goel VK, et al. Biomechanics of a Posture-Controlling Cervical Artificial Disc: Mechanical, in Vitro, and Finite-Element Analysis. Neurosurgical focus. 2010;28:E11.

[49] Galbusera F, Anasetti F, Bellini CM, Costa F, Fornari M. The Influence of the Axial, Antero-Posterior and Lateral Positions of the Center of Rotation of a Ball-and-Socket Disc Prosthesis on the Cervical Spine Biomechanics. Clinical biomechanics (Bristol, Avon). 2010;25:397-401.

[50] Kang H, Park P, La Marca F, Hollister SJ, Lin CY. Analysis of Load Sharing on Uncovertebral and Facet Joints at the C5-6 Level with Implantation of the Bryan, Prestige Lp, or Prodisc-C Cervical Disc Prosthesis: An in Vivo Image-Based Finite Element Study. Neurosurgical focus. 2010;28:E9.

[51] Kulkarni N. Effects of Implant Design Parameters on Cervical Disc Arthroplasty Performance and Sagittal Balance - a Finite Element Investigation: The University of Toledo; 2010.

[52] Li Y, Lewis G. Influence of Surgical Treatment for Disc Degeneration Disease at C5-C6 on Changes in Some Biomechanical Parameters of the Cervical Spine. Medical engineering & physics. 2010;32:595-603.

[53] Bhattacharya S. Predictive Finite Element Modeling of Artificial Cervical Discs in a Ligamentous Functional Spinal Unit: The University of Toledo; 2011.

[54] Bhattacharya S, Goel VK, Liu X, Kiapour A, Serhan HA. Models That Incorporate Spinal Structures Predict Better Wear Performance of Cervical Artificial Discs. The spine journal : official journal of the North American Spine Society. 2011;11:766-76.

[55] Faizan A, Goel VK, Biyani A, Garfin SR, Bono CM. Adjacent Level Effects of Bi Level Disc Replacement, Bi Level Fusion and Disc Replacement Plus Fusion in Cervical Spine--a Finite Element Based Study. Clinical biomechanics (Bristol, Avon). 2012;27:226-33.

[56] Fernandes PC, Fernandes PR, Folgado JO, Levy Melancia J. Biomechanical Analysis of the Anterior Cervical Fusion. Computer methods in biomechanics and biomedical engineering. 2012;15:1337-46.

[57] Lee SH, Im YJ, Kim KT, Kim YH, Park WM, Kim K. Comparison of Cervical Spine Biomechanics after Fixed- and Mobile-Core Artificial Disc Replacement: A Finite Element Analysis. Spine. 2011;36:700-8.

[58] Womack W, Leahy PD, Patel VV, Puttlitz CM. Finite Element Modeling of Kinematic and Load Transmission Alterations Due to Cervical Intervertebral Disc Replacement. Spine. 2011;36:E1126-33.

[59] Zhao Y, Li Q, Mo Z, Sun Y, Fan Y. Finite Element Analysis of Cervical Arthroplasty Combined with Fusion against 2-Level Fusion. Journal of spinal disorders & techniques. 2013;26:347-50.

[60] Gayzik FS. Completion of Phase I Development of the Global Human Body Consortium Mid-Sized Male Full Body Finite Element Model. SAE Government Industry Meeting: Society of Automotive Engineers; 2012.

[61] Stitzel JD. Global Human Body Models Consortium (GHBMC) Male 50th Percentile (M50) Occupant Model Manual. Virginia Tech – Wake Forest University Center for Injury Biomechanics; 2011.

[62] Gayzik FS, Moreno DP, Geer CP, Wuertzer SD, Martin RS, Stitzel JD. Development of a Full Body CAD Dataset for Computational Modeling: A Multi-Modality Approach. Annals of biomedical engineering. 2011;39:2568-83.

[63] DeWit JA, Cronin DS. Cervical Spine Segment Finite Element Model for Traumatic Injury Prediction. Journal of the mechanical behavior of biomedical materials. 2012;10:138-50.

[64] Mattucci SF, Moulton JA, Chandrashekar N, Cronin DS. Strain Rate Dependent Properties of Younger Human Cervical Spine Ligaments. Journal of the mechanical behavior of biomedical materials. 2012;10:216-26.

[65] Fice JB, Cronin DS. Investigation of Whiplash Injuries in the Upper Cervical Spine Using a Detailed Neck Model. Journal of biomechanics. 2012;45:1098-102.

[66] Fice JB, Cronin DS, Panzer MB. Cervical Spine Model to Predict Capsular Ligament Response in Rear Impact. Annals of biomedical engineering. 2011;39:2152-62.

[67] Gayzik FS, Moreno DP, Vavalle NA, Rhyne AC, Stitzel JD. Development of a Full Human Body Finite Element Model for Blunt Injury Prediction Utilizing a Multi-Modality Medical Imaging Protocol. 12th Int'l LS-DYNA User Conf Dearborn, MI. 2012.

[68] Rhyne AC, Moreno DP, Vavalle NA, Stitzel JD, Galbusera F. Validation of Simulated Chestband Data in Frontal and Lateral Loading Using a Human Body Finite Element Model. Traffic Injury Prevention. 2013; IN PRESS.

[69] Vavalle NA, Jelen BC, Moreno DP, Stitzel JD, Gayzik FS. An Evaluation of Objective Rating Methods for Full-Body Finite Element Model Comparison to PMHS Tests. Traffic Inj Prev. 2013;14 Suppl:S87-94.

[70] Vavalle NA, Moreno DP, Rhyne AC, Stitzel JD, Gayzik FS. Lateral Impact Validation of a Geometrically Accurate Full Body Finite Element Model for Blunt Injury Prediction. Annals of biomedical engineering. 2013;41:497-512.

[71] DIN ISO 5834-2:2007-12. Implants for Surgery: Ultra-High-Molecular-Weight-Polyethylene, Part 2: Moulded Forms (Iso 5834-2:2006). Berlin, Germany2007.

[72] eFunda. Ti-6al-4v. Web. April 8 2013. <http://www.efunda.com/materials/alloys/titanium/show_titanium.cfm?ID=T18_AB&prop=all&Page_Title=Ti-6Al-4V>.

[73] eFunda. Aisi Type 316l. Web. April 8 2013. <http://www.efunda.com/materials/alloys/stainless_steels/show_stainless.cfm?ID=AISI_Type_316L&show_prop=all&Page_Title=AISI%20Type%20316L>.

[74] Goyal RK, Tiwari AN, Mulik UP, Negi YS. Novel High Performance Al2O3/Poly(Ether Ether Ketone) Nanocomposites for Electronics Applications. Composites Science and Technology. 2007;67:1802-12.

[75] Hallab NJ, Wimmer M, Jacobs JJ. Material Properties and Wear Analysis. In: Yue JJ, Bertagnoli R, McAfee PC, An HS, editors. Motion Preservation Surgery of the Spine: Advanced Techniques and Controversies. Philadelphia: Saunders; 2008. p. 52-62.

[76] ASM International. Materials and Coatings for Medical Devices - Cardiovascular. 1 ed. Materials Park, OH: ASM International; 2009.

[77] Forman J, Lessley D, Kent R, Bostrom O, Pipkorn B. Whole-Body Kinematic and Dynamic Response of Restrained PMHS in Frontal Sled Tests. Stapp car crash journal. 2006;50:299-336.

[78] White NA, Moreno DP, Gayzik FS, Stitzel JD. Cross-Sectional Neck Response of a Total Human Body Fe Model During Simulated Frontal and Side Automobile Impacts. Computer methods in biomechanics and biomedical engineering. 2013.

[79] Society of Automotive Engineers. SAE J211/1 - Instrumentation for Impact Test-Part 1-Electronic Instrumentation. 2007.

[80] Sprague MA, Geers TL. A Spectral-Element Method for Modelling Cavitation in Transient Fluid–Structure Interaction. International Journal for Numerical Methods in Engineering. 2004;60:2467-99.

[81] Mongiardini M, Ray M, Anghileri M. Development of a Software for the Comparison of Curves During the Verification and Validation of Numerical Models. 7th European LS-DYNA Conference. Milan, Italy: DYNAmore GmbH; 2009.

[82] Moorcroft D. Selection of Validation Metrics for Aviation Seat Models. The Fifth Triennial International Aviation Fire and Cabin Safety Research Conference2007.

[83] NHTSA. Title 49 Code of Federal Regulations (CFR) Part 571 Section 214, Side Impact Protection. Washington, DC: Office of the Federal Register, National Archives and Records Administration; 2008.

[84] Eppinger R, Sun E, Kuppa S, Saul R. Development of Improved Injury Criteria for the Assessment of Advanced Automobile Restraint Systems - II. NHTSA Docket No. 2010-03-19. 2000.

[85] Mertz HJ, Irwin AL, Prasad P. Biomechanical and Scaling Bases for Frontal and Side Impact Injury Assessment Reference Values. Stapp car crash journal. 2003;47:155-88.

[86] Lee DJ, Winkelstein BA. The Failure Response of the Human Cervical Facet Capsular Ligament During Facet Joint Retraction. Journal of biomechanics. 2012;45:2325-9.

[87] DiAngelo DJ, Foley KT, Morrow BR, Schwab JS, Song J, German JW, et al. In Vitro Biomechanics of Cervical Disc Arthroplasty with the Prodisc-C Total Disc Implant. Neurosurgical focus. 2004;17:E7.

[88] DiAngelo DJ, Roberston JT, Metcalf NH, McVay BJ, Davis RC. Biomechanical Testing of an Artificial Cervical Joint and an Anterior Cervical Plate. Journal of spinal disorders & techniques. 2003;16:314-23.

[89] Chang UK, Kim DH, Lee MC, Willenberg R, Kim SH, Lim J. Changes in Adjacent-Level Disc Pressure and Facet Joint Force after Cervical Arthroplasty Compared with Cervical Discectomy and Fusion. Journal of neurosurgery Spine. 2007;7:33-9.

[90] Jaumard NV, Bauman JA, Guarino BB, Gokhale AJ, Lipschutz DE, Weisshaar CL, et al. Prodisc Cervical Arthroplasty Does Not Alter Facet Joint Contact Pressure During Lateral Bending or Axial Torsion. Spine. 2013;38:E84-93.

[91] Bauman JA, Jaumard NV, Guarino BB, Weisshaar CL, Lipschutz DE, Welch WC, et al. Facet Joint Contact Pressure Is Not Significantly Affected by Prodisc Cervical Disc Arthroplasty in Sagittal Bending: A Single-Level Cadaveric Study. The spine journal : official journal of the North American Spine Society. 2012;12:949-59.

Chapter 6: Head and Neck Response of a Finite Element Anthropomorphic Test Device and Human Body Model during a Simulated Rotary-Wing Aircraft Impact

Nicholas A. White, Kerry A. Danelson, F. Scott Gayzik, and Joel D. Stitzel

Submitted to: *The Journal of Biomechanical Engineering*, Submitted November 2013.

Abstract

A finite element simulation environment has been developed to investigate aviator head and neck response during a simulated rotary-wing aircraft impact using both an anthropomorphic test device (ATD) and a human body model. The simulation setup was based on a series of experimental sled tests reported in the literature which studied the effects of ATD size, head-supported mass, and sled pulse on neck response during such an event. The first ATD simulation was successfully validated against one of these experimental sled tests. The majority of the transducer time histories received a CORrelation and Analysis (CORA) rating of 0.7 or higher, indicating good overall correlation between the simulation and the experiment response. A second ATD simulation was conducted to examine the effects of initial position on head and neck response. Neck angle and foot-to-floor contact were found to influence the magnitude of the head and neck response, but not the timing. The human body model simulated a more biofidelic head and neck response than the ATD model, including the change in neck curvature. Shear force, axial force, and bending moment were reported for each level of the cervical spine, providing further insight into the biomechanical loading of the neck during a rotary-wing aircraft impact.

Keywords: Helicopter, Neck Kinematics, Cervical Spine, GHBMC, ATD

Introduction

Background

Since WWII, rotary-wing aircraft have become a staple in all major military conflicts including the Korean War, Vietnam War, Gulf War, and the War on Terror [1]. Pilot training is a very time-consuming and expensive process, typically requiring 1.5 to 2.5 years of preparation and costing U.S. taxpayers as much as $2 million per pilot [2]. Due to the large investment required to produce these highly skilled pilots, as well as the obvious concern for loss of life or injury, it is very important these individuals are protected in the event of a crash. A total of 96 Army flight accidents were reported for the 2012 fiscal year, corresponding to 8.135 accidents per 100,000 flight hours [3]. While these figures are not separated into aircraft type, fixed or rotary-winged, the vast majority of the Army aviation fleet is composed of helicopters [2, 4]. A retrospective study of injuries sustained by U.S. Army personnel from ground-impact rotary-wing aircraft mishaps reported a total of 672 mishaps between 1980 and 1994 [5]. Of the 2,337 occupants involved in these mishaps, 11.3% suffered at least one neck injury. A more recent study examined all U.S. military personnel injured during Operation Enduring Freedom and Operation Iraqi Freedom from 2001 to 2009 [6]. This study reported the relative distribution of noncontiguous spine injuries with respect to mechanism of injury. The greatest percentage of these injuries resulted from a helicopter crash.

Experimental Crash Testing

Since the 1970s, full-scale crash tests of rotary-wing aircraft have been conducted to evaluate crashworthiness at the Impact Dynamics Research Facility (IDRF) located at the NASA Langley Research Center (Hampton, VA) [7]. Many of these full-scale tests evaluated the effectiveness of energy absorption systems, crew restraint systems, and occupant response [7-15]. While these full-scale experiments are extremely valuable in evaluating the crashworthiness of a rotary-wing aircraft, they can be quite involved. When seat and occupant response are of primary interest, an alternative experimental approach is to mount the fuselage or seat directly to a crash sled and apply an acceleration or deceleration pulse comparable to an actual crash pulse.

For over thirty years, both cadavers and anthropomorphic test devices (ATDs) have been used to evaluate occupant response during helicopter crash sled tests. Between 1979 and 1985, a series of 15 cadaver sled tests were conducted at the Wayne State University Bioengineering Center (Detroit, MI) to determine the load threshold of spinal injury during simulated helicopter impacts [16, 17]. In 1998, the Federal Aviation Administration's (FAA) Civil Aeromedical Institute (Oklahoma City, OK) conducted a series of 8 deceleration sled tests using an H-58 helicopter fuselage and two ATDs. [18, 19]. The purpose of these tests was two-fold: to evaluate the effectiveness of a new energy absorption seat in mitigating back injury, and to study potential head impact with a new pilot display unit (PDU). Between 2002 and 2004, four series of head-supported mass (HSM) tests were performed at the University of Virginia Center for Applied Biomechanics (Charlottesville, VA) [20, 21]. Head-neck component and whole-body experiments were conducted with cadavers and two types of ATDs. The purpose of these tests was to investigate the effects of HSM on cervical spine injury during experimentally simulated rotary-wing aircraft impacts and to subsequently develop a new injury criterion for the lower neck. In 2004, an extensive series of sled tests were performed at the Naval Air Warfare Center (NAWC) Aircraft Division Horizontal Accelerator facility (Patuxent River, MD) to study ATD neck kinematics resulting from rotary-wing aircraft impacts [22, 23]. The ATD size, helmet mass properties, and impact severity were varied for each of the 43 sled tests.

Crash Modeling and Simulation

Computational modeling has been used to evaluate aircraft crashworthiness, particularly helicopter crashworthiness, for close to four decades [7, 24-27]. Most of the more recent crash simulation studies used explicit time integration finite element (FE) programs, including MSC.Dytran (MSC Software Corporation, Santa Ana, CA) and LS-DYNA (LSTC, Livermore, CA) [26]. These codes allow for analysis of high-speed, dynamic impacts involving large deformations. In the current study, three low-severity rotary-wing aircraft impacts have been simulated in LS-DYNA using either an FE ATD or human body model aviator surrogate. The seat geometry, belt configuration, and sled pulse were based on a previously conducted experimental sled test using a 50th percentile ATD with added head mass. The first simulation included an ATD positioned according to the experimental sled test. Its primary purpose was to validate the simulation configuration, ensuring the ATD head, chest, and neck response were similar to the experimental response. The second simulation used the human body model in its seated, automotive driving posture. The purpose of this simulation was to capture a more biofidelic response of the head and neck during a simulated rotary-wing aircraft impact and compare it to the response of the ATD. Due to the difference in initial position between the ATD and human body model in the first two simulations, a third ATD simulation was conducted. In this simulation, the ATD was prepositioned to closer match the initial position of the human body model. The head, neck, and chest response from the experiment and simulations were compared to each other.

Materials and Methods

Overview

In the current study, three low-severity, rotary-wing aircraft impact FE simulations were conducted in LS-DYNA (R4.2.1, LSTC, Livermore, CA) to examine the head and neck response of an ATD and human body model. The sled pulse (Figure 6-1), seat geometry (Figure 6-2), and belt preload were based on the low-severity, 7.62 m/s delta-V, sled test (#530) conducted by Paskoff et al. [22, 23]. This experimental test used a 50th percentile Hybrid III ATD with 1.8 kg of additional head mass representing a helmet. The additional head mass did not significantly alter the head center of gravity (CG) for this particular test.

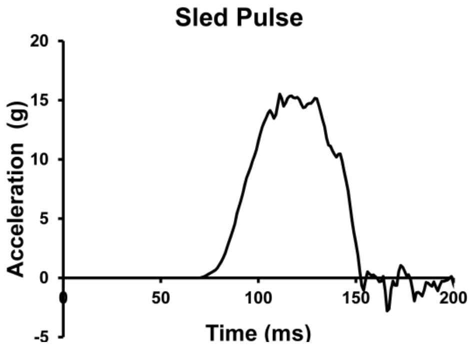

Figure 6-1: Horizontal sled acceleration pulse used for all simulations. This time history was digitized from low-severity experimental sled test reported by Paskoff et al. [22, 23]. The pulse was shifted 70 ms forward in time to allow for proper restraint preloading.

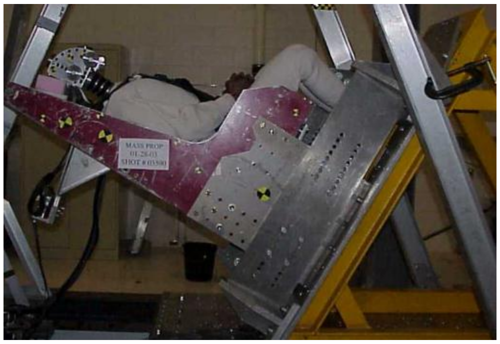

Figure 6-2: Experimental test setup for the #530 low-severity test [22, 23].

Surrogate Models

The Humanetics (Plymouth, MI) 50th percentile Hybrid III ATD FE model (v8.0) was used in two of the three simulations. This model has been extensively validated on the component, sub-assembly, and whole ATD levels [28]. Neck validation included flexion and extension pendulum certification tests, as well as inline and offset mass mini sled tests. The whole model has been validated in two belted frontal impact tests. Lumped mass elements were equally distributed around the head accelerometer mounting block (Figure 6-3), representing the additional head mass in the experimental sled test. Neck forces were extracted from the upper and lower load cell transducers. Using the appropriate transformation equations, upper neck moments were reported about the occipital condyles (OC) and lower neck moments about the base of the neck.

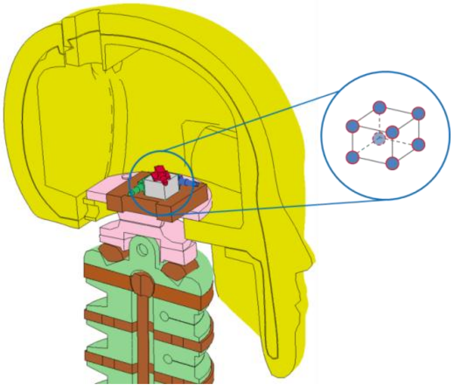

Figure 6-3: Midsagittal cut of the Humanetics ATD head and neck, leaving the head accelerometer block and accelerometers intact. The additional mass simulating a helmet was equally distributed to the eight corners of the accelerometer block, effectively maintaining the original head CG.

The Global Human Body Models Consortium (GHBMC) seated, 50th percentile male model (v3.5) was used in one of the simulations [29-31]. This state-of-the-art human body model was developed by an international team of research institutions to investigate injury to the human body during dynamic impact events. The neck was developed at University of Waterloo in Ontario, Canada [32] with geometry supplied by the Wake Forest University (WFU) School of Medicine [30]. It has been validated on both segmental and full cervical spine levels [32-35]. Additionally, whole body validation has been conducted in a number of different impact scenarios [36-39]. The LS-PrePost (v4.0, LSTC, Livermore, CA) mass trimming function was used to equally distribute the additional head mass about the skull while maintaining the original head CG (Figure 6-4). To capture neck loading, cross sections were defined at each cervical level of the neck using a methodology previously developed by White et al. [40]. For each cervical level, a local coordinate system (LCSYS) was defined according to SAEJ211 sign convention [41] with the origin located at the CG of the corresponding vertebra (Figure 6-5). The positive x-direction was directed along the midsagittal plane from the origin to the midpoint of the anterior vertebral body (VB). The positive z-direction was directed inferiorly from the origin, coplanar with and orthogonal to the local x-axis. All cross-sectional forces and moments were reported in their respective LCSYS, with moments calculated about the local origin. These forces and moments include the loading contributions from the bones, ligaments, active muscles, passive muscles, and soft tissue.

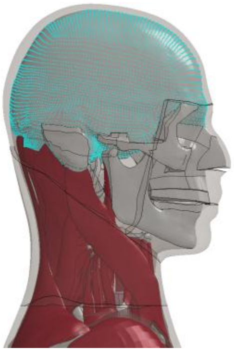

Figure 6-4: The additional mass simulating a helmet was added to the GHBMC skull using the LS-PrePost mass trimming function. This built in function distributed the mass about the skull while maintaining the original head CG.

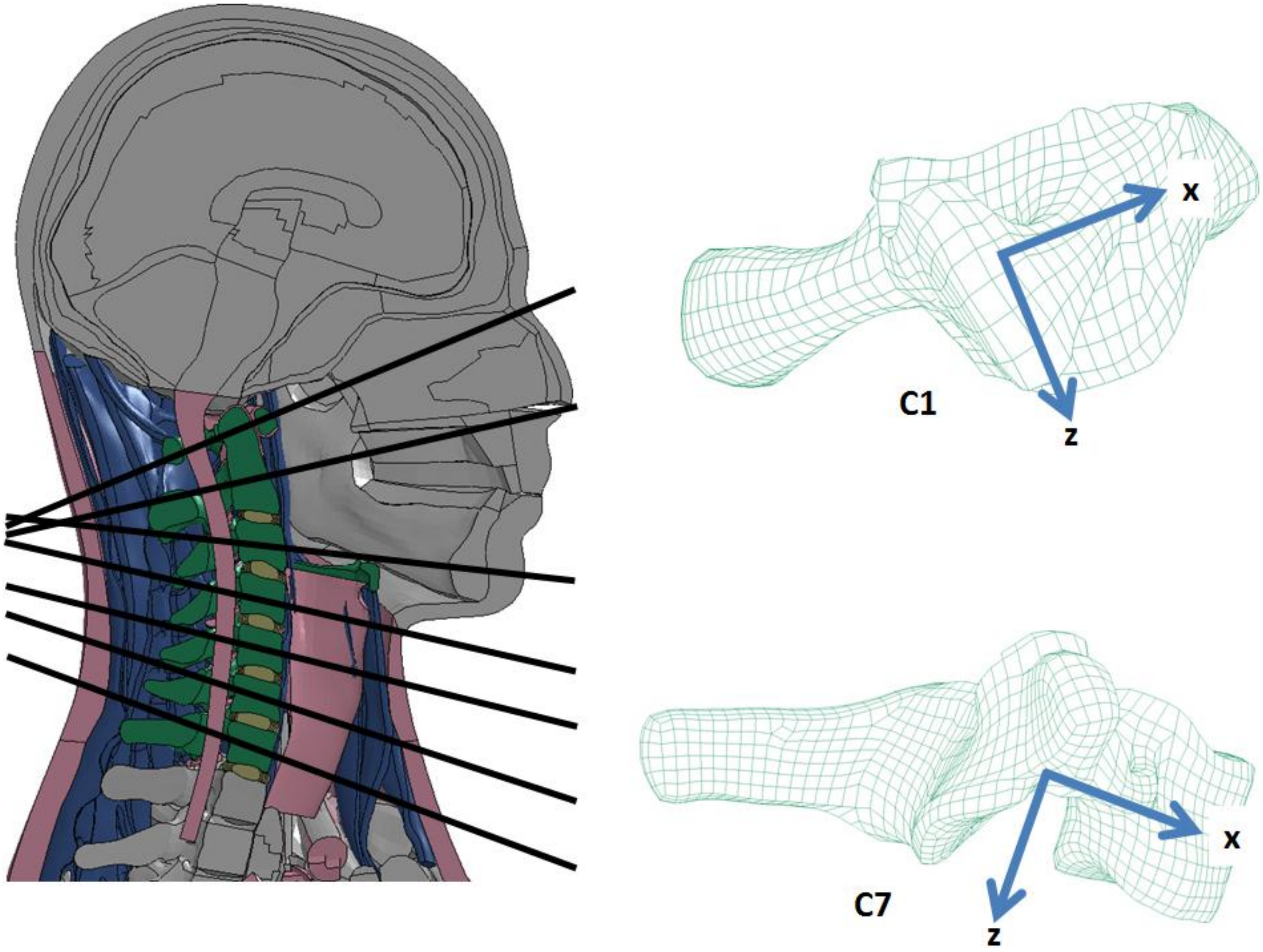

Figure 6-5: Midsagittal cut of the GHBMC head and neck with transverse cross sections indicated by the solid lines [40].

Simulations

The first simulation included the ATD model in the experimental sled test initial position and will be referred to as ATD_{exp}. The original seated, driving posture of the ATD model was modified, increasing the neck extension angle by 15° and the thorax extension angle by 3°. These modifications aligned the ATD model more closely to the experimental initial position. The initial positions of the neck and thorax were achieved using a three-step procedure which avoided any initial penetrations [42]. First, the angles of the lower neck and upper thorax were incrementally modified until the desired initial configuration was achieved using the ATD positioning feature in LS-PrePost. Second, these desired ATD angles were used as inputs into a pre-simulation model. This model used boundary prescribed motions to rotate the neck and thorax to the desired angles while capturing any deformation associated with these rotations. Third, the nodal coordinates of the original ATD model were replaced with the nodal coordinates from the deformed, pre-simulation run. Since the pre-simulation model used in this procedure does not allow initial positioning of the upper arms and the lower legs, the second step of the above procedure was omitted for these body parts. The upper arms were rotated until they were in line with the torso and the lower legs were flexed until the feet were parallel with the sled floor. The second simulation included the GHBMC model in its original seated, driving posture [29]. The third simulation included the ATD model initially positioned according to the GHBMC seated posture and will be referred to as $\text{ATD}_{\text{ghbmc}}$. The original seated, driving posture of the ATD model was modified, increasing the thorax angle by 3° without any modification to the neck or lower leg angles.

A generic five-point restraint system was modeled in each simulation according to established military aircraft personnel restraint design principles (Figure 6-6) [43]. In order to simulate the experimental preloading of the restraint system, modeled pretensioners applied approximately 181N of belt loading prior to any sled acceleration. To allow this initial belt tension to be achieved, as well as model settling due to gravity, each simulation was run for 70 ms prior to the initiation of the sled pulse (Figure 6-7). Retractors with generic loading/unloading curves were included as a method to control the belt loading during the impact event.

(a) (b)

Figure 6-6: Front view of a generic five-point restraint system for the (a) ATD_{exp} and (b) GHBMC simulations at t=0 ms. The lap belt and shoulder harness were modeled as a combination of shell and seat belt elements, while the center lap belt tiedown was modeled solely as seatbelt elements.

Data Analysis

The results of each simulation were post-processed using Oasys T/HIS (v11, Arup, London, UK). For consistency with the reported experimental results, all simulation data was filtered using a 100Hz, 8-pole Butterworth filter. The filtered cross-sectional force and moment results from the GHBMC model were then processed using in-house code written in MATLAB (v7.12.0, R2011a, MathWorks, Natick, MA).

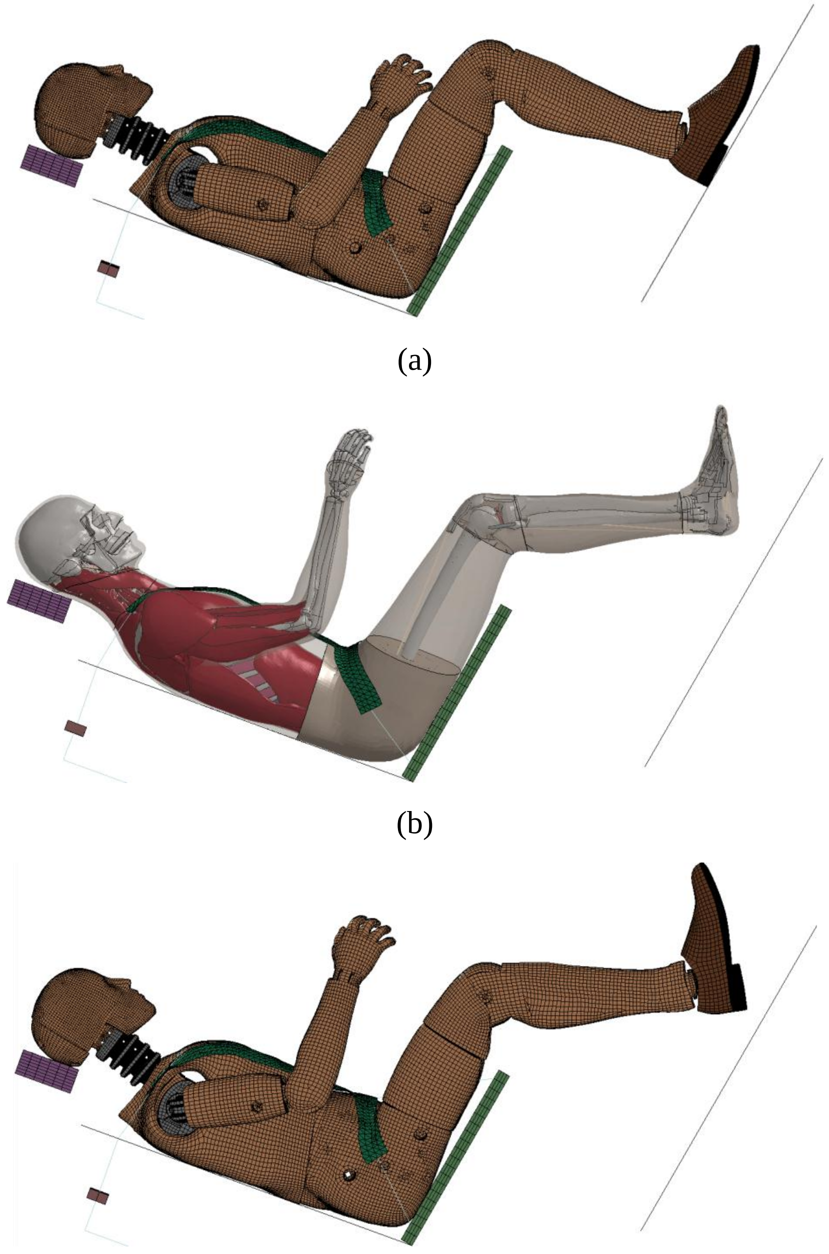
(a)

(b)

(c)

Figure 6-7: Positioning at the time of sled pulse initiation (t=70 ms) for the (a) ATD_{exp}, (b) GHBMC, and (c) ATD_{ghbmc} simulations. Pretensioning of the restraint system was achieved by this time.

Quantitative Analysis

A quantitative comparison analysis was conducted to compare the experimental results with the ATD_{exp} simulation results using CORA (CORrelation and Analysis, v3.6.1, Partnership for Dummy Technology and Biomechanics, Germany). Prior to the analysis, the experimental data was zeroed and time shifted 70 ms, matching the start time of the simulation sled pulse. The time intervals for analysis were defined from 70-270 ms for acceleration and force data and 70-290 ms for moment data. These time intervals were chosen since they focus on the most relevant parts of the respective time histories.

The CORA analysis uses two different methods to quantitatively compare signals [44-46]. The corridor method rates, from 0 to 1, how well the experimental curve fits within a narrow inner corridor and a wide outer corridor, both defined about the benchmark curve. A rating of 1 is assigned if the experimental curve falls completely within the narrow corridor and a 0 if it falls completely outside of the wide corridor. The cross correlation method analytically analyzes the characteristics of the signal including phase shift, size, and shape using individual weighing factors. For each of the three sub-methods, a rating between 0 and 1 is also calculated. An overall, global rating is then calculated as the weighted sum of the corridor and correlations ratings, ranging from 0 for a poor match to 1 for a perfect match. While there is no definitive rating indicative of a “good” match, correlations with a score of 0.7 or greater have been assumed as “good” in past studies [45]. It is important to note that the CORA rating is dependent on the control variables within the program. Default global settings were used for both the corridor and cross-correlation methods.

Results

Overview

The head and neck response is reported for the experimental and simulated rotary-wing aircraft impacts, with the upper and lower neck load polarities reported in accordance with SAE J211 [41] sign convention (Figure 6-8). Data is only reported prior to the time of head to head restraint contact. Maximum head and chest accelerations are reported in Table 6-1. Global extrema for neck loading and calculated N_{ij} values are reported in Table 6-2. The N_{ij} for the upper neck was calculated using critical intercepts defined in FMVSS 208 [47] and for the lower neck using critical intercepts reported in Mertz et al. [48]. Results of the quantitative comparison analyses between the experimental test and corresponding ATD_{exp} simulation are reported in Table 6-3.

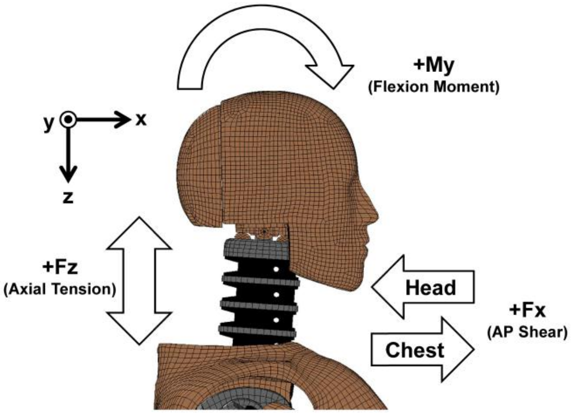

Figure 6-8: Schematic representation of the relative head and chest motion corresponding to SAEJ211 standards for positive neck AP shear force, axial force, and bending moment [41]. Positive polarity for AP shear corresponds to the head moving rearward and the chest moving forward. Positive polarity for axial loading (tension) corresponds to the head moving upward and the chest moving downward. Positive polarity for bending moment (flexion) corresponds to the chin moving towards the sternum.

Table 6-1: Maximum head and chest acceleration magnitudes for the experiment and simulations. Two distinct periods of head acceleration occurred, one during the first half of the simulation and the other during the second half. The peak accelerations during both of these periods are reported as a1 and a2. Time is reported in milliseconds.

	Parameter	Exp	ATD$_{exp}$	ATD$_{ghbmc}$	GHBMC
Head Acceleration (g)	t	134	121	121	135
	a1	26.5	26.3	22.1	19.4
	t	178	175	170	176
	a2	10.8	16.5	20.2	22.5
Chest Acceleration (g)	t	131	120	121	128
	a	27.2	28.4	22.3	21.1

Table 6-2: Maximum upper and lower neck loads for the experiment and simulation along with established IARVs [48]. The simulation maximum values occurred between the start of the sled pulse (t=70 ms) and the end of the simulation. Time is reported in milliseconds.

	Loading Mode	IARV	Parameter	Exp$_{530}$	ATD$_{exp}$	ATD$_{ghbmc}$	GHBMC
Upper Neck Loading	AP Shear F_x (N)	3100	t max	132	124	121	136
			F_x max	496.6	371.6	334.1	790.3
		-3100	t min	204	204	202	176
			F_x min	-538.6	-690.2	-929.9	-678.8
	Ten/Comp F_z (N)	4170	t max	178	174	171	182
			F_z max	665.5	809.4	1011.2	735.5
		-4000	t min	134	121	121	134
			F_z min	-1604.5	-1560.1	-1319.3	-898.2
	Flex/Ext Moment M_y (Nm)	190	t max	192	211	209	189
			M_y max	53.7	63.8	76.8	77.2
		-96	t min	142	146	160	149
			M_y min	-34.1	-20.9	-19.3	-1.6
	N_{ij}	1	t max	136	122	210	188
			N_{ij} max	0.36	0.32	0.28	0.35
Lower Neck Loading	AP Shear F_x (N)	3100	t max	126	90	92	180
			F_x max	182.9	46.1	63.5	198.8
		-3100	t min	202	204	186	136
			F_x min	-731.7	-594.3	-759.6	-491.9
	Ten/Comp F_z (N)	4170	t max	178	174	168	179
			F_z max	752.3	908.3	1121.3	1416.7
		-4000	t min	133	121	121	134
			F_z min	-1945.4	-2261.5	-1847.7	-1312.7
	Flex/Ext Moment M_y (Nm)	380	t max	213	206	203	196
			M_y max	128.8	155.8	185.8	110.5
		-192	t min	127	127	290	146
			M_y min	-33.2	-25.6	-24.6	-25.5
	N_{ij}	1	t max	134	122	201	183
			N_{ij} max	0.32	0.44	0.44	0.36

Table 6-3: Quantitative comparisons between the benchmark experimental data and the ATD$_{exp}$ simulation data.

Transducer		CORA		
		Corridor	**Correlation**	**Overall**
Acceleration (magnitude)	Head	0.761	0.803	0.782
	Chest	0.826	0.849	0.838
Upper Neck Loading	F_X	0.736	0.903	0.819
	F_Z	0.721	0.751	0.736
	M_Y	0.589	0.818	0.704
Lower Neck Loading	F_X	0.578	0.577	0.578
	F_Z	0.698	0.701	0.700
	M_Y	0.803	0.914	0.858

Head Rotation

While not reported in the experimental test, midsagittal head rotations for the three simulations are presented in Figure 6-9. Maximum rotations are reported in Table 6-4 with images of each simulation at the approximate time of maximum head rotation presented in Figure 6-10. Head rotation remained minimal prior to 70 ms, during the settling phase of the simulations. While the GHBMC head underwent approximately 11° of extension during the beginning of the sled acceleration, head flexion was the primary form of rotation for all simulations. Both ATD simulations reached maximum head flexion simultaneously while the GHBMC model reached maximum head flexion 16 ms later. Chin to chest contact occurred at maximum flexion in the ATD$_{ghbmc}$ simulation, but not in the other two simulations.

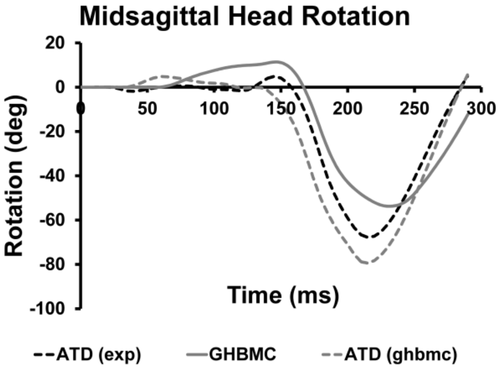

Figure 6-9: Midsagittal head rotation for the three simulations. Head rotation from the experimental sled test was not available for comparison.

Table 6-4: Maximum midsagittal head rotation for the simulations. Head rotation from the experimental sled test was not available for comparison.

	Flexion Start Time (ms)	**Time of Max Flexion (ms)**	**Max Flexion (degrees)**
ATD_{exp}	158	215	-67.8
ATD_{ghbmc}	130	215	-79.4
GHBMC	167	231	-53.8

Head Acceleration

The head CG resultant linear accelerations are presented in Figure 6-11. The global peak accelerations occurred during the first half of the time history plot for both the experimental test and ATD simulations. The global peak acceleration occurred during the second half for the GHBMC simulation. Unlike the simulations, the global peak in the experimental test exhibited bimodal-behavior. The global peak accelerations of the experimental test and ATD_{exp} simulation were almost identical in magnitude. The overall CORA rating between the experimental test and ATD_{exp} simulation head accelerations indicated good correlation between the two time histories.

Chest Acceleration

The peak chest resultant linear accelerations were very similar in magnitude between the experimental test and ATD_{exp} simulation (Figure 6-12). The overall CORA rating indicated good correlation between the two acceleration time histories. A bimodal-peak occurred for both the experimental test and GHBMC simulation, around the time of peak chest acceleration. The peak accelerations were very similar between the GHBMC and ATD_{ghbmc} simulations.

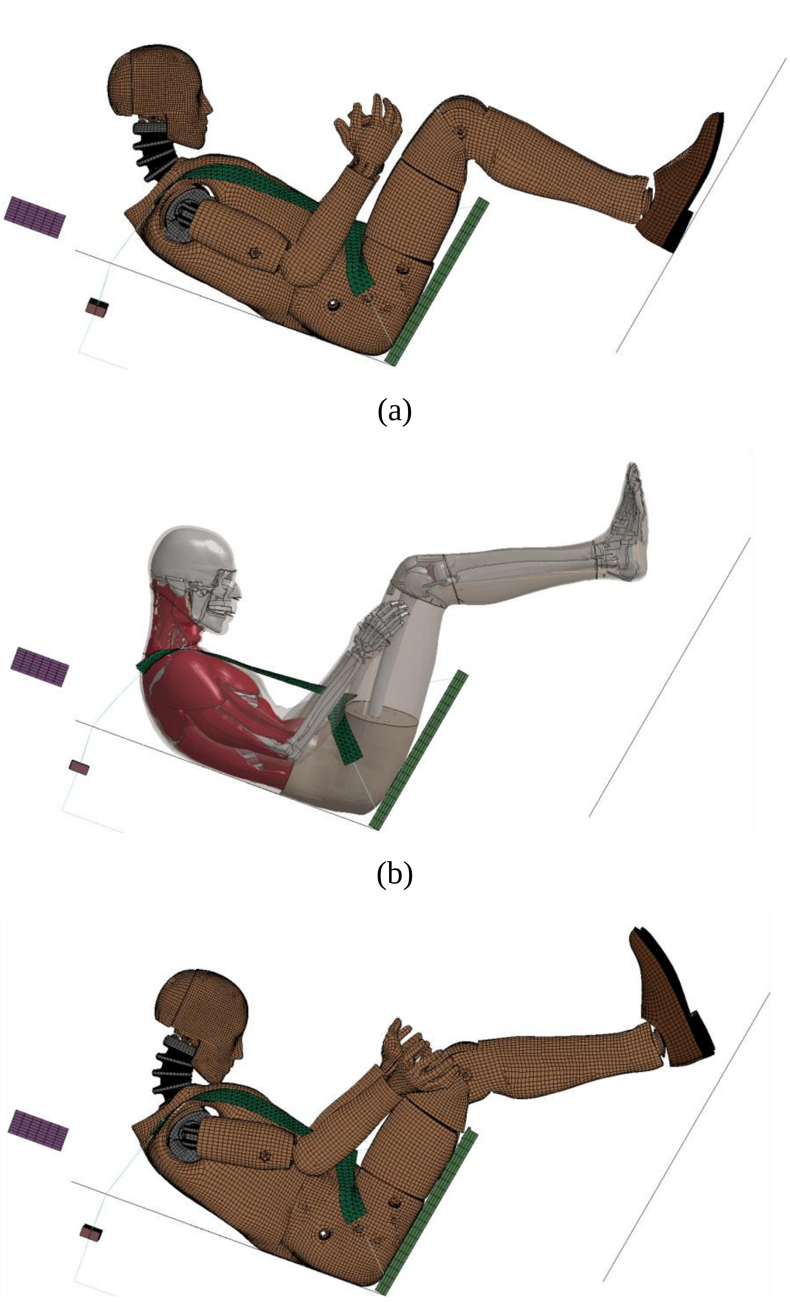

(a)

(b)

(c)

Figure 6-10: Simulation kinematics at the time of maximum midsagittal head rotation for the (a) ATD_{exp} (t=215 ms), (b) GHBMC (t=231 ms), and (c) $\text{ATD}_{\text{ghbmc}}$ (t=215 ms).

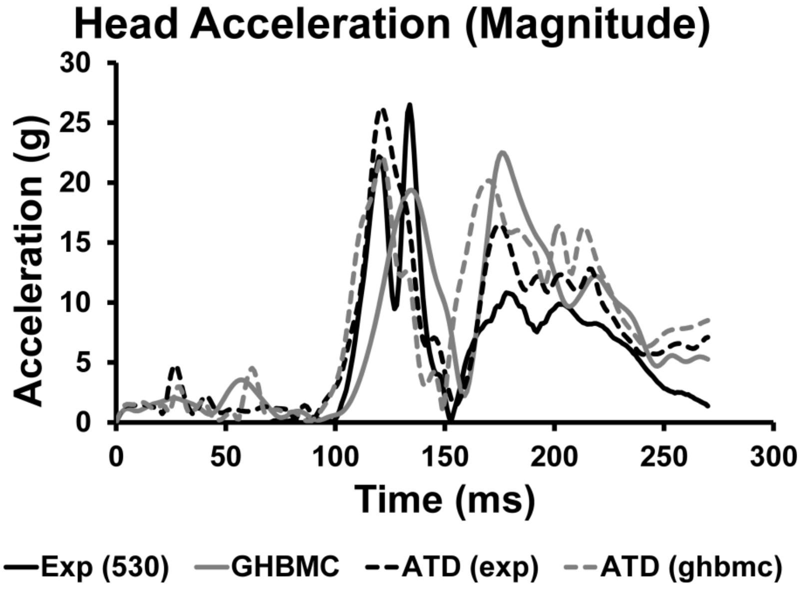

Figure 6-11: Head CG acceleration magnitude for the experiment and simulations.

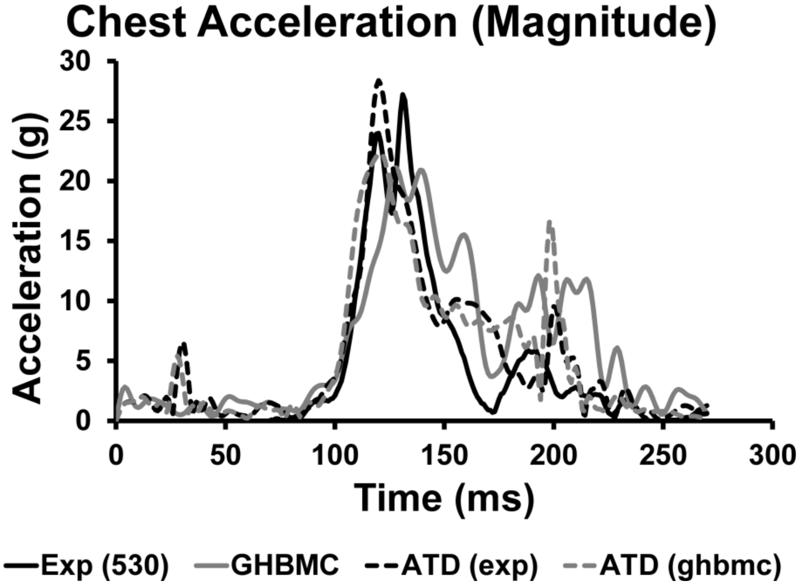

Figure 6-12: Chest acceleration magnitude for the experiment and simulations.

Neck Loading

Upper neck loading is reported in Figure 6-13, Figure 6-14, and Figure 6-15. The CORA analysis of the upper neck loading showed good agreement between the experimental test and ATD_{exp} simulation time histories for all loading modes. A period of positive AP shear and compression followed by a period of negative AP shear and tension occurred in the experiment and simulation data. The change in load direction appeared to correlate with head rotation for the simulations. During compression, the experimental test exhibited bimodal-behavior, similar to the head acceleration time history. The experimental test and both ATD simulations experienced a short period of extension followed by a more pronounced flexion moment, while the GHBMC simulation experienced primarily a flexion moment.

Lower neck loading is reported in Figure 6-16, Figure 6-17, and Figure 6-18. The CORA analysis of the lower neck loading showed good agreement between the experimental test and ATD_{exp} simulation for both the axial force and bending moment time histories. The degree of agreement between AP shear time histories was less clear. The experimental test and simulations experienced a period of compression followed by tension, similar to the upper neck axial loading. Again, the change in load direction appeared to correlate with head rotation. A small extension moment occurred in the experimental test and simulations, followed by a more pronounced flexion moment.

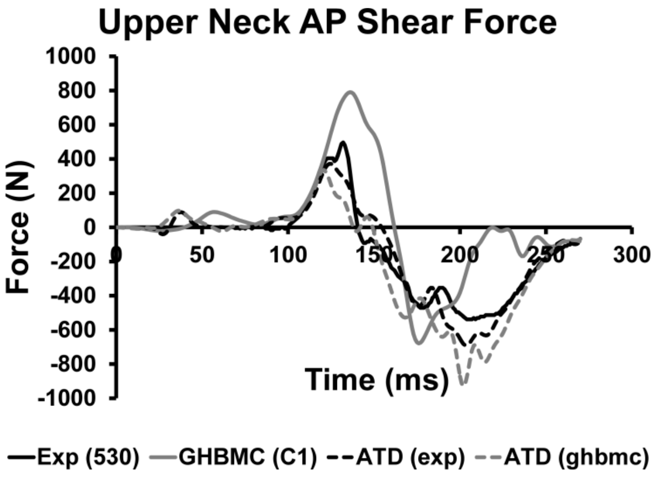

Figure 6-13: Upper neck AP shear force for the experiment and simulations.

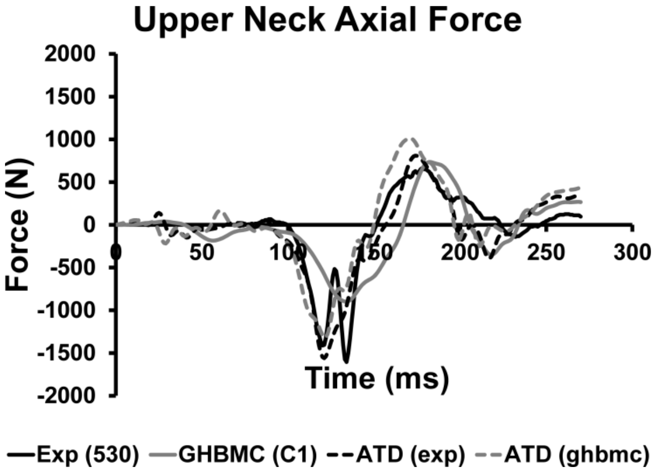

Figure 6-14: Upper neck axial force for the experiment and simulations.

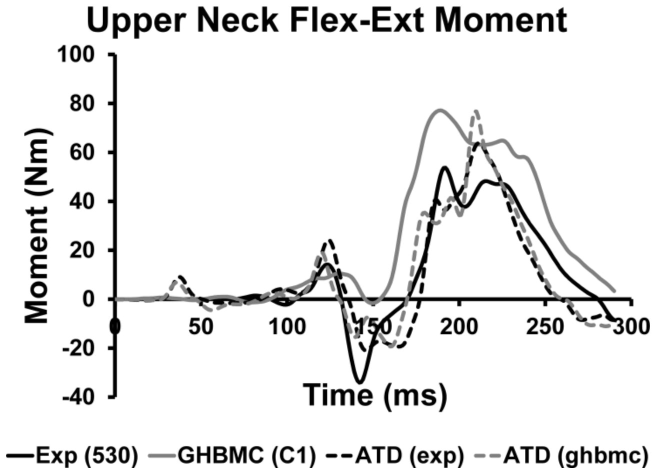

Figure 6-15: Upper neck bending moment for the experiment and simulations.

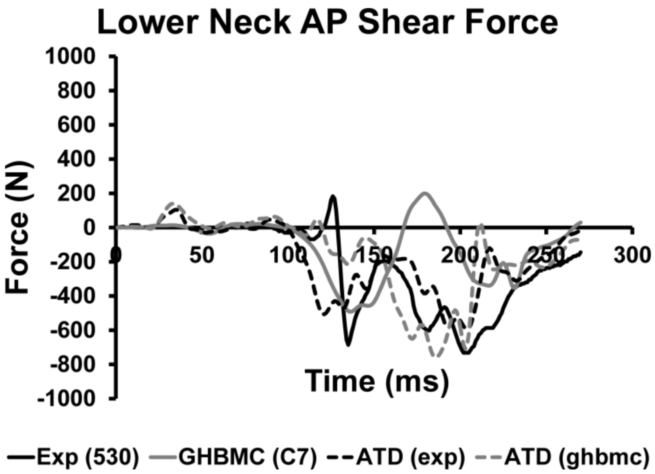

Figure 6-16: Lower neck AP shear force for the experiment and simulations.

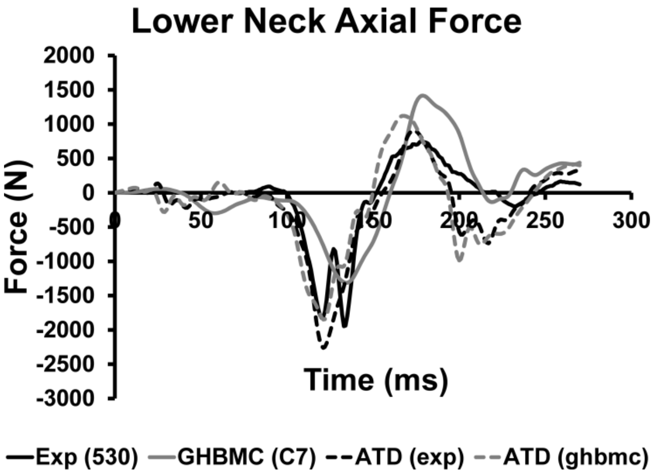

Figure 6-17: Lower neck axial force for the experiment and simulations.

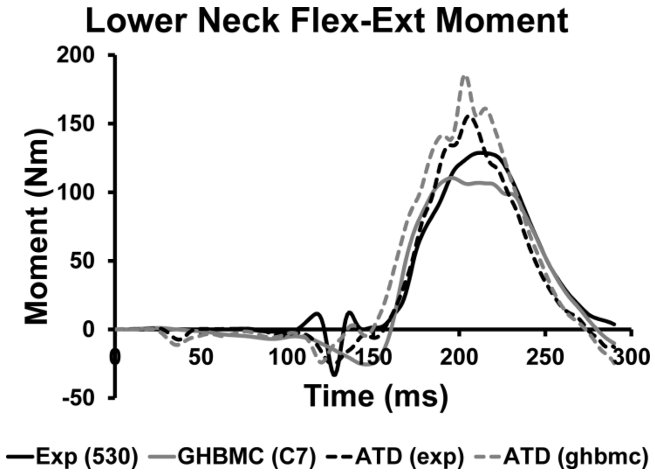

Figure 6-18: Lower neck bending moment for the experiment and simulations.

GHBMC Neck Response

To further investigate the loading distribution throughout the entire neck, cross-sectional AP shear forces (Figure 6-19), axial forces (Figure 6-20), and bending moments (Figure 6-21) are reported for each cervical level in the GHBMC simulation. The solid vertical line (t=167 ms) indicates the initiation of primary head rotation and the dashed vertical line (t=231 ms) indicates maximum head rotation. The lower cervical levels tended to experience greater axial forces and bending moments than the upper levels. Incremental, midsagittal neck kinematics with respect to the C7 local origin are presented in Figure 6-22 [49]. This kinematic representation illustrates the change in cervical spine curvature during the different phases of loading.

Forces and moments corresponding to the time of maximum C7 loading were used to calculate adjacent-level, loading ratios: C1/C2, C2/C3, C3/C4, C4/C5, C5/C6 and C6/C7 (Figure 6-23, Table 6-5) [40]. The time of maximum C7 loading (Table 6-6) did not necessarily match the time of maximum loading for the other vertebral levels (Table 6-7); however, the largest overall loading typically occurred at the C7 level. An adjacent-level ratio less than 1 indicated that the loading at the superior vertebral level was less than the inferior level. An adjacent-level ratio greater than 1 indicated that the loading at the superior vertebral level was greater than the inferior level.

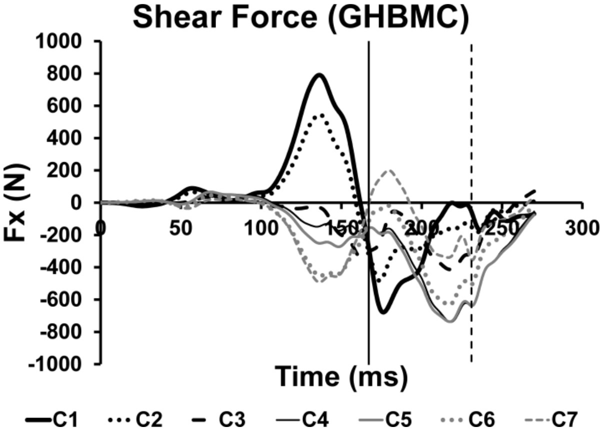

Figure 6-19: Cross-sectional AP shear force for each cervical level of the GHBMC simulation. The forces are reported in their respective LCSYS.

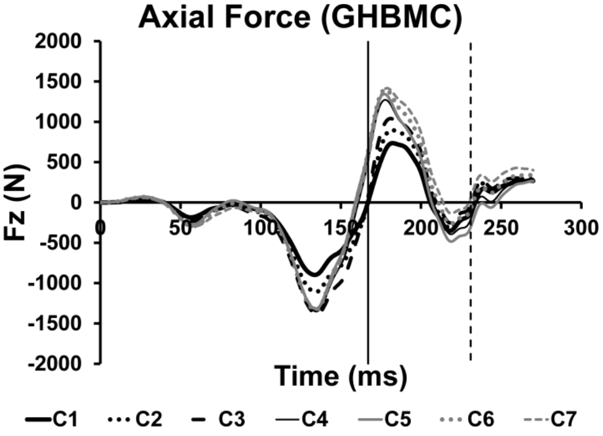

Figure 6-20: Cross-sectional axial force for each cervical level of the GHBMC simulation. The forces are reported in their respective LCSYS.

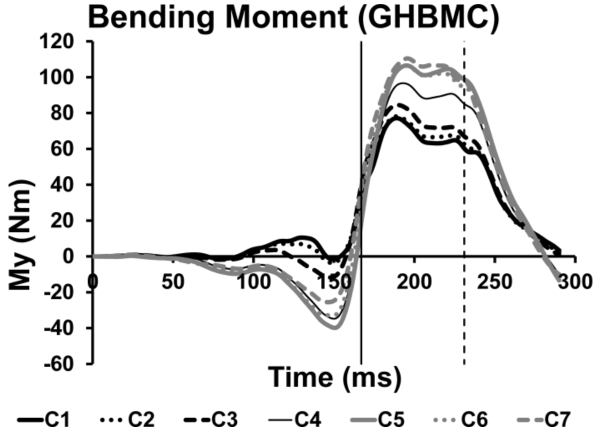

Figure 6-21: Cross-sectional bending moment for each cervical level of the GHBMC simulation. Each moment is reported about the CG of its LCSYS.

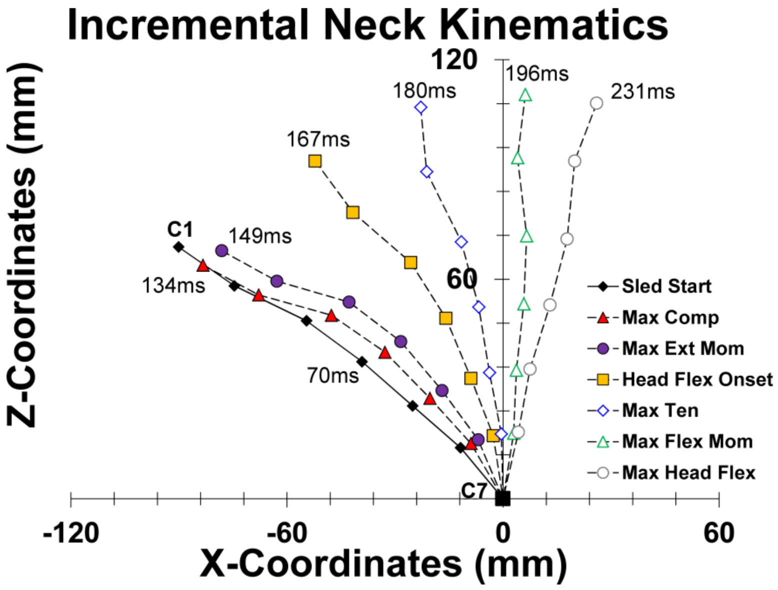

Figure 6-22: Incremental, midsagittal neck kinematics of the GHBMC simulation. The position of the local origin for each vertebra is plotted with respect to the C7 local origin, at different points in time: sled pulse onset (t=70 ms), maximum compression (t=134 ms), maximum extension moment (t=146 ms), head flexion onset (t=167 ms), maximum tension (t=179 ms), maximum flexion moment (t=196 ms), and maximum head flexion (t=231 ms).

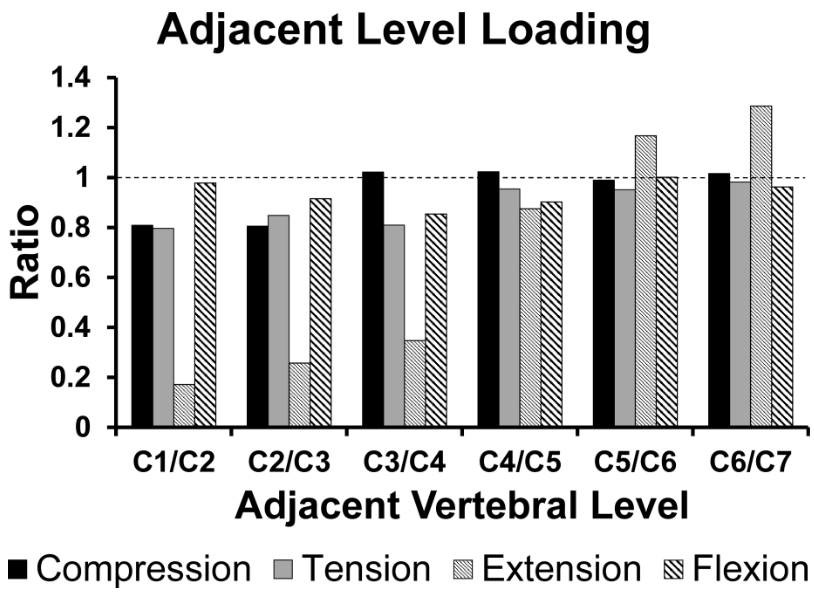

Figure 6-23: Adjacent-level loading ratios calculated at the time of maximum cross-sectional C7 loading for compression (t=134 ms), tension (t=179 ms), extension (t=146 ms), and flexion (t=196 ms).

Table 6-5: Adjacent-level loading calculated at the time of maximum cross-sectional C7 loading for compression (t=134 ms), tension (t=179 ms), extension (t=146 ms), and flexion (t=196 ms) in the GHBMC simulation. A ratio less than unity indicates the loading at the superior vertebral level is less than the loading at the inferior vertebral level. A ratio greater than unity indicates the loading at the superior vertebral level is greater than the loading at the inferior vertebral level.

Loading	**C1/C2**	**C2/C3**	**C3/C4**	**C4/C5**	**C5/C6**	**C6/C7**
Compression	0.81	0.81	1.02	1.02	0.99	1.02
Tension	0.80	0.85	0.81	0.95	0.95	0.98
Extension	0.17	0.26	0.35	0.88	1.17	1.29
Flexion	0.98	0.92	0.85	0.90	1.00	0.96

Table 6-6: Cross-sectional loading for each cervical level in the GHBMC simulation at the time of maximum cross-sectional C7 loading.

Level	**Compression (N) (t=134 ms)**	**Tension (N) (t=179 ms)**	**Extension (Nm) (t=146 ms)**	**Flexion (Nm) (t=196 ms)**
C1	-898.2	691.1	-0.5	73.4
C2	-1110.9	867.4	-3.0	75.1
C3	-1379.5	1022.3	-11.7	82.0
C4	-1350.3	1262.5	-33.6	96.0
C5	-1319.9	1323.0	-38.3	106.4
C6	-1334.0	1391.1	-32.8	106.3
C7	-1312.7	1416.7	-25.5	110.5

Table 6-7: Maximum cross-sectional loading for each cervical level in the GHBMC simulation.

	Compression		**Tension**		**Extension**		**Flexion**	
Level	**Time (ms)**	**Fz (N)**	**Time (ms)**	**Fz (N)**	**Time (ms)**	**My (Nm)**	**Time (ms)**	**My (Nm)**
C1	134	-898.2	182	735.5	149	-1.6	189	77.2
C2	134	-1110.9	182	900.3	149	-3.6	189	78.1
C3	135	-1383.9	181	1040.4	148	-11.8	190	84.5
C4	135	-1352.0	178	1271.6	150	-34.8	193	96.7
C5	134	-1319.9	177	1344.3	150	-39.9	195	106.5
C6	134	-1334.0	178	1399.6	149	-33.0	195	106.4
C7	134	-1312.7	179	1416.7	146	-25.5	196	110.5

Discussion

Simulation Configuration

Of the rotary-wing aircraft sled tests reported in the literature, those tests conducted by Paskoff et al. [22, 23] were most conducive to FE simulation. A total of 43 experiments were conducted varying ATD size, sled pulse severity, and added head mass configuration. The current study simulated experimental test #530 which subjected a 50th percentile ATD, with 1.8 kg added head mass, to a low-severity crash pulse. The location of the CG for this head mass configuration remained relatively close to the original head CG. From a simulation standpoint, CG location was an important consideration. Since the material cards for the ATD FE model are encrypted by the developer, the LS-PrePost mass trimming function could not be used to distribute the additional head mass in the same configuration as the experiment. In other words, the location of the head CG with additional mass could not be easily controlled by the user. To circumvent this potential pitfall, 0.225 kg of additional mass was attached to the eight corners of the head accelerometer block in the FE model. This method effectively added the 1.8 kg of head mass, while maintaining the head CG location. For consistency, the GHBMC model head CG was also maintained with the addition of the head mass. Since added head mass and CG location had no statistically significant effect of the magnitude of the measured forces or moments for the experimental tests, the difference in CG location for the simulations was considered negligible.

Each simulation was allowed to settle under the effects of gravity and belt pretensioning for 70 ms, prior to the onset of the sled acceleration pulse. While some head and chest acceleration and neck loading occurred during the settling phase of the simulation, almost all of the time histories returned to zero at the onset of the sled acceleration pulse (t=70 ms). Combining both the settling and sled acceleration into a single simulation allowed for the initial stresses, particularly the belt pretensioning, to be maintained. This process avoided some of the complications associated with applying initial stress and nodal positioning obtained from separate settling runs.

Difference between the ATD and GHBMC Models

Several fundamental differences between the GHBMC and Hybrid III ATD models must be highlighted. The GHBMC model was developed as a biofidelic surrogate based on the anthropometry of a 50th percentile male in a seated position. The seven cervical vertebrae, intervertebral discs (IVDs), ligaments, musculature, and soft tissue of the neck were modeled in great detail. Muscle activation was included in the GHBMC neck simulation in an effort to capture a more accurate head and neck response. The Hybrid III ATD neck, while designed to produce a biofidelic mechanical response during frontal impacts, does not include the anatomical complexity of the human neck, nor does it try to incorporate the effects of muscle response. The neck of the ATD is a single-piece elastomer component with three interleaving aluminum disc elements and two aluminum end plates [50]. Rotation of the head occurs about a pin-joint, representing the approximate location of the OC-C1 interface, on the cephalic endplate. A pair of nodding blocks on this endplate limits the head flexion and extension. Axial tension of the neck is augmented through a central steel cable while compression is predominantly the product of the compressive properties of the elastomer. The different flexion and extension response of the neck are due to the asymmetrical cross-sectional geometry and three anterior slits built into the geometry of the elastomer. The natural lordotic curvature of the human cervical spine is not replicated in the ATD neck, unlike in the GHBMC model. Another difference in spinal curvature exists in the lumbar spine, which is curved in the Hybrid III ATD unlike the GHBMC model.

Other ATDs with more accurate lumbar spine orientation exist for aviation crash testing, such as the Hybrid II and FAA Hybrid III ATDs [51]. The ATD torso was stiffer in the midsagittal plane than the GHBMC vertebral column as is evident in Figure 6-10. This finding was similar to that reported by Putnam and Untaroiu [52] in which the THUMS and THOR-NT FE models were subjected to simulated vertical impacts.

While upper and lower neck loading are reported for both the ATD and GHBMC simulations, there are several differences in the method of data extraction. The ATD neck load cells were defined as zero length linear elastic discrete beams, effectively acting as stiff translational and rotational springs [53]. The loads from these transducers were transformed with the upper neck loading reported at the OC in the head LCSYS and lower neck loading at the base of the neck in its respective LCSYS. The GHBMC neck load cells were defined using cross sections, capturing the total force and moment contributions from the bones, ligaments, muscles, and soft tissue [40]. The upper neck loading was reported at the C1 level with bending moment reported about the CG of the C1 vertebra. Unlike the upper neck load LCSYS in the ATD, which rotated with the head, the C1 loads were reported in a LCSYS that rotated with the vertebra. This method of reporting upper neck loading provided a more realistic load response in the human body model since the majority of the neck loading was transmitted through the bony skeleton, either directly or indirectly through muscle and ligament attachments. The lower neck loading was reported at the C7 level with bending moment reported about the CG of the C7 vertebra.

Experiment vs. ATD$_{exp}$ Simulation

From a visual standpoint, the salient features of the experimental time histories appeared to be adequately simulated by the ATD$_{exp}$ model. This observation is supported by the quantitative analysis where an overall CORA score of 0.7 or greater was achieved for all acceleration, force, and moment time histories, except for lower neck shear loading. The chest acceleration, upper neck shear loading, and lower neck bending moment received an overall score of greater than 0.8.

Between 100 and 150 ms, distinct bimodal-peaks occurred in the experimental head and chest accelerations, as well as the upper and lower neck axial loading. The magnitude of the second peak was always larger than the first peak and the local minimum between these peaks occurred at approximately 130 ms. Even though this bimodal-peak behavior was not reproduced by the ATD_{exp} model, the simulation peaks always aligned in time with the first, smaller peaks of the experimental bimodal-response. While the experimental belt loading was not reported in the literature, it was examined in the ATD_{exp} simulation. It appeared that the ATD_{exp} began to pitch forward and load the shoulder harness at around 130 ms, the same time the local minimum occurs in the experimental bimodal-response. Due to the high degree of correlation between the experiment and simulation in terms of head and neck response, it is reasonable to deduce that the simulated belt loading approximated the experimental loading. Therefore, the bimodal-response in the experiment data may be the result of the initial shoulder harness interaction with the ATD, creating a sharp, momentary deceleration of the upper torso. Minor differences in belt placement, pretensioning, and friction properties may explain why the bimodal-response was not produced in the simulation.

The largest discrepancy between the experiment and simulation response occurred for the lower neck AP shear, as was evident by the low overall CORA score. A clear, visual difference between the experiment and simulation responses occurred between 100 and 150 ms. In the experiment, a short duration positive AP shear peak occurred at 126 ms, just prior to a large, almost instantaneous reverse in polarity at approximately 130 ms. The simulation produced neither this distinct positive AP shear peak nor such a sharp polarity change. The disparity in simulation and experiment responses was most likely due to a difference in initial shoulder harness interaction with the ATD.

Effects of Initial Position

The purpose of the $\mathrm{ATD}_{\mathrm{ghbmc}}$ simulation was to examine the effects of initial positioning on aviator response, comparing results to the $\mathrm{ATD}_{\mathrm{exp}}$ simulation. In general, initial positioning had the greatest effect on the magnitude of peak response, not the timing. The maximum midsagittal head flexion rotation occurred simultaneously for both simulations. However, the $\mathrm{ATD}_{\mathrm{ghbmc}}$ peak rotation was 17.1% greater in magnitude, allowing chin to chest contact to occur (Figure 6-10). Peak response was increased between 19.3% and 37.7% for upper neck positive AP shear, upper and lower neck tension and flexion, and lower neck AP shear. Peak response was decreased between 10.1% and 21.5% for head and chest accelerations, upper and lower neck compression and upper neck positive AP shear.

While the increased flexion angle of the $\mathrm{ATD}_{\mathrm{ghbmc}}$ neck may have allowed for greater rotation of the head, the lack of foot-to-floor contact had a greater role in altering the ATD overall response. In the $\mathrm{ATD}_{\mathrm{exp}}$ simulation, the lower legs were flexed so that the feet where parallel with the sled floor. During this simulation, the foot-to-floor contact stabilized the trunk, preventing the more pronounced forward excursion of the torso, neck, and head seen in the $\mathrm{ATD}_{\mathrm{ghbmc}}$ simulation. The sustained contact and load distribution through the lower extremities was evident from the $\mathrm{ATD}_{\mathrm{exp}}$ tibia load cell output. The lack of sustained contact with the floor increased the $\mathrm{ATD}_{\mathrm{ghbmc}}$ torso flexion, subsequently increasing the peak belt loading by 32.3%.

GHBMC Response

The GHBMC simulation head, chest, and neck response matched the ATD_{ghbmc} time histories closer than the ATD_{exp} time histories. The two main exceptions were for upper neck AP shear force and lower neck bending moment which can be attributed to some of the fundamental differences between the ATD and human body models. Maximum head rotation occurred later for the GHBMC simulation than in either the ATD simulations. Additionally, the head rotated less in the human body model than in the ATD models. Muscle activation and the pliability of the human thorax (Figure 6-10) were most likely the reasoning behind the difference in head rotation magnitude and timing.

Similar to the upper and lower neck loads reported at the C1 and C7 levels, the AP shear, axial, and bending moment loads were also reported for the C2-C6 levels; effectively capturing the response of the entire GHBMC neck. Prior to onset of head flexion rotation, all levels underwent axial compression with peak levels occurring at approximately the same time, between 134 and 135 ms. Maximum compression was noticeably larger for C3-C7 levels than for the C1 and C2 levels. At approximately 136 ms, the C1 and C2 levels experienced maximum positive AP shear as the C3-C7 levels experienced a local peak negative AP shear. From the incremental kinematics (Figure 6-22), it appeared that the cervical spine took on an S-shaped curvature during this period of time, with the transition in curvature occurring between the C3 and C4 levels. This transition was even more pronounced at the time of maximum extension moment, t=146 ms. Similar observations in spinal curvature were reported in the cadaver component and sled tests by Bass et al. [21]. This S-shaped curvature can be explained using basic beam deflection theory. From the simulation animation, it was observed that the global head CG translation from the onset of the sled pulse to the onset of head flexion occurred almost exclusively in the horizontal direction. This creates a paradigm where the neck can be represented as a beam fixed at the C7 level and free, but guided, at the C1 level. From the corresponding beam deflection equation, it can be shown that the beam, in this case the neck, will bend into a sigmoidal shape. Transition of the curvature occurs at the midpoint of the beam, which would correspond most closely to the C4 level. These findings were supported by the adjacent level loading ratios (Figure 6-23). At the time of maximum extension moment, the ratio was 0.35 for C3/C4 and 0.88 for C4/C5. The relatively large difference in these adjacent level loading ratios corresponded with the transition of the spinal curvature.

The onset of axial tension began at approximately 160 ms for the C4-C7 levels and 167 ms for C1-C3 levels. This delay between the lower and upper levels appeared in the incremental kinematics illustration, where the lower vertebrae began to straighten out prior to the onset of head flexion. Straightening in the upper levels occurred by the time of maximum tension, creating a C-shaped curve in the cervical spine, indicative of simple beam bending. Maximum tension was reached at approximately the same time for all levels, with the C4-C7 levels reaching greater peak values than the C1-C3 levels. This difference in peak values between the upper and lower levels was also apparent in the adjacent level loading ratios. Shortly after maximum tension occurred, maximum flexion moment was achieved for all levels. The largest peak moments were achieved at the C5-C7 levels, due to the longer moment arm from these levels to the head. Peak flexion moments were smallest for the C1-C3 levels, due to the shorter moment arm. The C4 level maximum flexion moment value was midway between the C1 and C7 values while a dip in adjacent level loading ratio occurred for C3/C4.

Evaluation of Potential Neck Injury

The upper and lower neck peak loading and N_{ij} values were reported for the experiment and all simulations. None of the peak loading values approached established injury threshold levels [48]. The N_{ij} was originally developed to assess the risk of upper neck injury during a frontal automotive crash through a linear combination of normalized axial and sagittal bending moments. Federal regulations set a threshold of 1.0 for the N_{ij} in the upper neck, corresponding to a 22% risk of a serious injury [47]. All calculated upper neck N_{ij} values were well below this threshold. While no Federal Standard exists for lower neck N_{ij}, critical intercepts have been established for the C7-T1 junction with a threshold of 1.0 [48]. Other injury criteria, potentially more suitable for combined vertical-frontal loading scenarios, are being evaluated and may be utilized in future studies [20, 21, 54].

Limitations and Future Work

The ATD_{exp} simulation head and neck response were compared to the response of a single experimental test. Additional experiments using the same boundary conditions would provide better average responses for comparison with the simulation response. The CORA quantitative analysis method was designed as an objective method to compare time histories; however, the degree of this objectivity is limited to the user specified inputs, particularly the time interval under evaluation. The time intervals specified in the current study included both the positive and negative portion of the neck response. Potentially the user may wish to compare the response for a particular polarity. For example, two quantitative analyses could be conducted with different time intervals on axial neck loading, separately comparing the major tension and compression components.

The GHBMC human body model gave further insight into the neck response during a simulated rotary-wing aircraft impact. While there is no direct method to validate the cross-sectional loads reported at each level of the cervical spine, the upper and lower neck loads appear to correlate with both the experimental and ATD responses. Full body cadaver tests should be conducted in a similar testing configuration and compared with the GHBMC model response without muscle activation. The use of high-speed, biplane x-ray to capture the cervical spine kinematics of the cadaver during the impact would also prove useful from a validation standpoint. Future rotary-wing aircraft impact studies using the GHBMC model will be conducted to evaluate the neck response using different HSM configurations and sled acceleration pulses. Loading through the facets and the intervertebral discs will be investigated along with the effects of muscle activation. Additionally, the effects of simulated surgical arthrodesis and arthroplasty at the C5-C6 level on neck response will be evaluated.

Conclusions

The head and neck response of an FE ATD during a simulated rotary-wing aircraft impact was successfully validated against experimental test data. A quantitative analysis was conducted to compare the responses of the simulation and experiment. All but one time history received a CORA rating of 0.7 or higher, indicating good overall correlation. Initial positioning of the ATD was found to affect the peak acceleration and loading, though the overall timing of these responses were typically not altered to a large degree. The neck response of a human body FE model was also investigated during a simulated rotary-wing aircraft impact. Detailed neck loading for each cervical level was reported and key kinematic features, including change in spinal curvature, were captured. Sigmoidal curvature of the cervical spine was most prominent during the early part of the simulation when compression and extension moment were greatest. The S-shaped bending may indicate a potential mechanism of injury during this phase of the impact. This observation highlights the importance of human body modeling in understanding the underlying biomechanics of potential neck injury, a much harder task to achieve when using an ATD.

Acknowledgements

The authors would like to acknowledge the Global Human Body Models Consortium for use of the 50th percentile seated male FE model and the United States Army Medical Research and Materiel Command for funding this research. The authors would also like to thank Glenn Paskoff for his assistance with experimental inquiries. All computations were performed on the Wake Forest University DEAC Cluster, a centrally managed resource with support provided in part by the University.

Chapter 6 References

[1] Dorr R. Chopper: A History of American Military Helicopter Operations from WWII to the War on Terror. New York, NY: The Berkley Publishing Group; 2005.

[2] Gebicke ME, Farrell BS. Military Personnel: Actions Needed to Better Define Pilot Requirements and Promote Retention. U.S. General Accounting Office. B-283075. 1999.

[3] U.S. Army Combat Readiness/Safety Center. U.S. Army Accident Information Aviation Accident Statistics - Year End, 01 October through 30 September. Web. 10 July 2013. <https://safety.army.mil/statisticsdata/ARMYSTATISTICSREPORTS/tabid/373/Default.aspx>.

[4] U.S. Army. U.S. Army Fact Files: Aircraft. Web. 15 July 2013. <http://www.army.mil/factfiles/equipment/aircraft/index.html>.

[5] Shannon SG, Albano JP, Mason KT, Licina JR. Head Injury Risk in Us Army Rotary-Wing Mishaps: Changes since 1980. Fort Rucker, AL: US Army Aeromedical Research Laboratory. USAARL Report No. 98-13. 1998.

[6] Patzkowski JC, Blair JA, Schoenfeld AJ, Lehman RA, Hsu JR, Skeletal Trauma Research C. Multiple Associated Injuries Are Common with Spine Fractures During War. The spine journal : official journal of the North American Spine Society. 2012;12:791-7.

[7] Jackson KE, Boitnott RL, Fasanella EL, Jones LE, Lyle KH. A History of Full-Scale Aircraft and Rotorcraft Crash Testing and Simulation at NASA Langley Research Center. Fourth Triennial International Fire and Cabin Safety Research Conference. 2004.

[8] Boitnott RL, Jackson KE, Fasanella EL, Kellas S. Full-Scale Crash Test of the Sikorsky Advanced Composite Airframe Program Helicopter. Proceedings of the American Helicopter Society Forum 56. Virginia Beach, VA. 2000.

[9] Burrows L, Lane R, McElhenney J. Ch-47 Crash Test (T-40) Structural, Cargo Restraint, and Aircrew Inflatable Restraint Experiments. USARTL-TR-78-22. 1978.

[10] Cronkhite JD, Mazza LT. Bell ACAP Full-Scale Aircraft Crash Test and Krash Correlation. Proceedings of the 44th Annual Forum of the American Helicopter Society. Washington, D.C. 1988.

[11] Perschbacher JP, Clarke C, Furnes K, Carnell B. Advanced Composite Airframe Program (ACAP) Militarization Test and Evaluation (MT&E) Volume V- Airframe Drop Test. USAATCOM TR 88-D-22E. 1996.

[12] Singley GT, III. Full-Scale Crash Testing of a CH-47C Helicopter. Proceedings of the 32nd V/STOL Forum of the American Helicopter Society. Washington, D.C. 1976.

[13] Smith KF. Full-Scale Crash Test (T-41) of the YAH-63 Attack Helicopter. USAAVSCOM TR-86-D-2. 1986.

[14] Thomson DT, Clarke CW. Advanced Composite Airframe Program (ACAP) Militarization Test and Evaluation (MT&E) Volume I- Landing Gear Drop Test. USAAVSCOM TR-88-D-22A. 1989.

[15] Jackson KE, Fasanella EL, Boitnott RL, McEntire BJ, Lewis A. Occupant Responses in a Full-Scale Crash Test of the Sikorsky ACAP Helicopter. NASA/TM-2002-211733 (ARL-TR-2735). 2002.

[16] Coltman JW, Van Ingen C, Selker F. Crash-Resistant Crewseat Limit-Load Optimization through Dynamic Testing with Cadavers. Fort Eustis, VA: US Army Aviation Systems Command. USAAVSCOM TR-85-D-11. 1986.

[17] Coltman JW. Design and Test Criteria for Increased Energy-Absorbing Seat Effectiveness. USAAVRADCOM-TR-82-D-42. 1983.

[18] Haley Jr. JL, Palmer RW. Evaluation of a Retrofit OH-58 Pilot's Seat to Prevent Back Injury. Fort Rucker, AL: US Army Aeromedical Research Laboratory. USAARL Report No. 95-9. 1994.

[19] Haley JL, Jr., McEntire BJ. OH-58 Pilot Display Unit (PDU) Simulated Crash Tests. Fort Rucker, AL: United States Army Aeromedical Research Laboratory. USAARL Report No. 95-10. 1994.

[20] Bass CR, Donnellan L, Salzar R, Lucas S, Folk B, Davis M, et al. A New Neck Injury Criterion in Combined Vertical/Frontal Crashes with Head Supported Mass. International Research Council on Biomechanics of Injury. Madrid, Spain. 2006.

[21] Bass CR, Salzar R, Donnellan L, Lucas H. Injury Risk from HSM Loading (HM 2,3,4,5 Series). Charlottesville, VA.: University of Virginia Center for Applied Biomechanics. Report HEADMASS2. 2004.

[22] Paskoff GR. Cervical Injury Risk Resulting from Rotary Wing Impact: Assessment of Injury Based Upon Aviator Size, Helmet Mass Properties and Impact Severity. Patuxent River, Maryland. . NAWCADPAX/RTR-2004/86. 2004.

[23] Paskoff GR, Sieveka E. Influence of Added Head Mass Properties on Head/Neck Loads During Standard Helicopter Impact Conditions. Forty Second Annual SAFE Association Symposium. Salt Lake City, Utah. 2004.

[24] Fasanella EL, Carden HC, Boitnott RL, Hayduk RJ. A Review of the Analytical Simulation of Aircraft Crash Dynamics. NASA Technical Memorandum (TM) 102595. 1990.

[25] Fasanella EL, Jackson KE. Best Practices for Crash Modeling and Simulation. U.S. Army Research Laboratory. ARL-TR-2849. 2002.

[26] Jackson KE, Fasanella EL, Lyle KH. Crash Certification by Analysis – Are We There Yet? American Helicopter Society 62nd Annual Forum. Phoenix, AZ. 2006.

[27] Jackson K, Fuchs Y, Kellas S. Overview of the National Aeronautics and Space Administration Subsonic Rotary Wing Aeronautics Research Program in Rotorcraft Crashworthiness. Journal of Aerospace Engineering. 2009;22:229-39.

[28] Humanetics. Hybrid III 50th Dummy Dyna Model Technical Report, Release Version 8.0. Plymouth, MI. 2013.

[29] Gayzik FS, Moreno DP, Danelson KA, McNally C, Klinich KD, Stitzel JD. External Landmark, Body Surface, and Volume Data of a Mid-Sized Male in Seated and Standing Postures. Annals of biomedical engineering. 2012;40:2019-32.

[30] Gayzik FS, Moreno DP, Geer CP, Wuertzer SD, Martin RS, Stitzel JD. Development of a Full Body CAD Dataset for Computational Modeling: A Multi-Modality Approach. Annals of biomedical engineering. 2011;39:2568-83.

[31] Stitzel JD. Global Human Body Models Consortium (GHBMC) Male 50th Percentile (M50) Occupant Model Manual. Virginia Tech – Wake Forest University Center for Injury Biomechanics; 2011.

[32] DeWit JA, Cronin DS. Cervical Spine Segment Finite Element Model for Traumatic Injury Prediction. Journal of the mechanical behavior of biomedical materials. 2012;10:138-50.

[33] Fice JB, Cronin DS. Investigation of Whiplash Injuries in the Upper Cervical Spine Using a Detailed Neck Model. Journal of biomechanics. 2012;45:1098-102.

[34] Fice JB, Cronin DS, Panzer MB. Cervical Spine Model to Predict Capsular Ligament Response in Rear Impact. Annals of biomedical engineering. 2011;39:2152-62.

[35] Mattucci SF, Moulton JA, Chandrashekar N, Cronin DS. Strain Rate Dependent Properties of Younger Human Cervical Spine Ligaments. Journal of the mechanical behavior of biomedical materials. 2012;10:216-26.

[36] Gayzik FS, Moreno DP, Vavalle NA, Rhyne AC, Stitzel JD. Development of a Full Human Body Finite Element Model for Blunt Injury Prediction Utilizing a Multi-Modality Medical Imaging Protocol. 12th International LS-DYNA User Conference. Dearborn, MI. 2012.

[37] Hayes AR, Vavalle NA, Moreno DP, Stitzel JD, Gayzik FS. Validation of Simulated Chestband Data in Frontal and Lateral Loading Using a Human Body Finite Element Model. Traffic Injury Prevention. 2013.

[38] Vavalle NA, Jelen B, Stitzel JD, Gayzik FS. An Evaluation of Objective Rating Methods for Full Body Finite Element Model Comparison to PMHS Tests. Traffic Injury Prevention. 2013;14:S87-S94.

[39] Vavalle NA, Moreno DP, Rhyne AC, Stitzel JD, Gayzik FS. Lateral Impact Validation of a Geometrically Accurate Full Body Finite Element Model for Blunt Injury Prediction. Annals of biomedical engineering. 2013;41:497-512.

[40] White NA, Moreno DP, Gayzik FS, Stitzel JD. Cross-Sectional Neck Response of a Total Human Body Fe Model During Simulated Frontal and Side Automobile Impacts. Computer methods in biomechanics and biomedical engineering. 2013.

[41] Society of Automotive Engineers. SAE J211/1 - Instrumentation for Impact Test-Part 1-Electronic Instrumentation. 2007.

[42] Humanetics. Hybrid III 50th Dummy LS-DYNA Model, Pre-Simulation Positioning, Version 8.0. Plymouth, MI. 2013.

[43] Zimmerman RE, Merritt NA. Aircraft Crash Survival Design Guide. Volume 1. Design Criteria and Checklists. DTIC Document; 1989.

[44] Gehre C, Gades H, Wernicke P. Objective Rating of Signals Using Test and Simulation Responses. 21st International Technical Conference on the Enhanced Safety of Vehicles. Stuttgart, Germany. 2009.

[45] Gehre C, Stahlschmidt S. Assessment of Dummy Models by Using Objective Rating Methods. 22nd International Technical Conference on the Enhanced Safety of Vehicles. Washington, DC. 2011.

[46] Thunert C. CORA Release 3.6 User's Manual. Germany: GNS mbH; 2012.

[47] National Highway Traffic Safety Administration. Title 49 Code of Federal Regulations (CFR) Part 571 Section 208, Occupant Crash Protection. 2008.

[48] Mertz HJ, Irwin AL, Prasad P. Biomechanical and Scaling Bases for Frontal and Side Impact Injury Assessment Reference Values. Stapp car crash journal. 2003;47:155-88.

[49] White NA, Begeman P, Hardy W, Yang KH, Ono K, Sato F, et al. Investigation of Upper Body and Cervical Spine Kinematics of Post Mortem Human Subjects (PMHS) During Low-Speed, Rear-End Impacts. SAE Technical Paper 2009-01-0387. 2009.

[50] Foster J, Kortge J, Wolanin M. Hybrid III-a Biomechanically-Based Crash Test Dummy. SAE Technical Paper 770938. 1977.

[51] Pellettiere J, Moorcroft D, Olivares G. Anthropomorphic Test Dummy Lumbar Load Variation. 22nd Enhanced Safety of Vehicles Conference. Washington, DC. 2011.

[52] Putnam JB, Untaroiu CD. Investigation of Human Kinematics and Risk of Injury During a Vertical Impact Using Dummy and Human Finite Element Models. The Ohio State University’s 9th Annual Injury Biomechanics Symposium. Columbus, OH. 2013.

[53] Humanetics. User’s Guide for the Hybrid III 50th Percentile Male Dummy LS-DYNA Model Version 8.0. Plymouth, MI. 2013.

[54] Kartal A, Yildiran I, Senkoylu A, Korkusuz F. Soccer Causes Degenerative Changes in the Cervical Spine. European spine journal : official publication of the European Spine Society, the European Spinal Deformity Society, and the European Section of the Cervical Spine Research Society. 2004;13:76-82.

[55] Nichols JP. Overview of Ejection Neck Injury Criteria. Forty Fourth Annual SAFE Association Symposium. 2006.

Chapter 7: Effects of Cervical Arthroplasty on Neck Response during a Simulated Rotary-Wing Aircraft Impact

Nicholas A. White, Kerry A. Danelson, F. Scott Gayzik, Wesley Hsu, Alexander Powers, and Joel D. Stitzel

Abstract

Three simulations were conducted using a human body finite element model to study the effects of cervical arthroplasty on neck response during a rotary-wing aircraft ground impact. One simulation was run as a baseline with no modifications to the neck. The remaining two simulations included neck modifications to represent a C5-6 interbody arthroplasty with either a Prestige ST or ProDisc-C cervical total disc replacement (CTDR). Cross sections were implemented at each cervical level to capture neck loading. In the three simulations, neck injury criteria (N_{ij}) ranged between 0.35 and 0.36 for the upper neck and the Beam Criterion (BC) ranged between 0.98 and 1.05 for the lower neck. The adjacent-level, cross-sectional loading for the C5-6 segment was not greatly altered by the CTDRs, as indicated by CORrelation and Analysis (CORA) ratings of 0.988 for the Prestige ST and 0.909 for the ProDisc-C. The CTDRs increased the interbody range of motion, altering both the interbody and cervical facet loading. While the facet capsules experienced increased tension in both CTDR simulations, established injury threshold levels were not reached. Overall, cervical arthroplasty at the C5-6 level did not appear to have a deleterious effect on the dynamic neck response during a simulated rotary-wing aircraft impact.

Keywords: Arthroplasty, Rotary-Wing Aircraft, Helicopter, Neck Kinematics, GHBMC, Finite Element

Introduction

While degeneration of the intervertebral discs (IVDs) is part of the normal aging process, it typically remains asymptomatic in most individuals [1-4]. However, surgical intervention may be required should clinical symptoms manifest, such as axial neck pain, radiculopathy, or myelopathy. Several previous studies have investigated the epidemiology of degenerative disc disease (DDD) in active-duty military personnel. Between 2001 and 2010, DDD was diagnosed in 131,986 active-duty U.S. military personnel with an overall incidence rate of 9.51 per 1,000 person-years [5]. During this ten-year timespan, DDD-specific and DDD-related medical encounters resulted in a total of 90,855 lost duty days. Pilot and aircrew personnel composed 5,505 of those individuals diagnosed with DDD, corresponding to a 9.87 per 1,000 person-years incident rate. An earlier study reported the incidence rate of herniated nucleus pulposus to be 1 per 1,000 aviator-years in U.S. Army aviators [6]. Flight status was permanently revoked in approximately 7.4% of the diagnosed aviators.

Between 2000 and 2009, cervical radiculopathy was diagnosed in 24,742 active-duty U.S. military personnel, corresponding to an incidence rate of 1.79 per 1,000 person-years [7]. Even though cervical radiculopathy may result from cervical spondylosis or spinal stenosis, it has been reported that 56% of surgeries to treat degenerative cervical spine disease involved DDD [8]. When non-operative treatment fails to adequately control the symptoms of DDD, fusion or arthroplasty may be required. Anterior cervical discectomy and fusion (ACDF) has remained the primary surgical treatment for symptomatic cervical degenerative disc disease (CDDD) for more than half a century [9-12]. While ACDF is an effective treatment for CDDD, the procedure does alter the biomechanics of the cervical spine, potentially increasing the occurrence of adjacent segment degeneration (ASD) [13, 14]. In an effort to maintain same-level and adjacent-level physiologic motion and loading, cervical arthroplasty has become more common as an alternative to ACDF [11, 15-17]. Even though experimental and computational studies have supported the functional equivalence between a cervical total disc replacement (CTDR) and an IVD [18-22], there is still much debate on the efficacy of cervical arthroplasty in preventing ASD [23-35]. Irrespective of the ASD mitigation abilities of CTDRs, several studies have reported greater improvement in neurological symptoms and a shorter post-operative recovery time for cervical arthroplasty as compared to fusion [29, 36, 37].

Military spine surgeons have shown an increased interest in cervical arthroplasty as a means to safely expedite recovery time in members of the armed forces afflicted with CDDD [38, 39]. While some medical waiver guidelines have been established to determine the physical readiness of a service member after CDDD surgery [40-42], final discretion lies with the surgeon. Unlike the general population, military personnel are subjected to many physically demanding tasks, potentially increasing their risk of spinal injury [43-46]. It is important to ensure that surgical treatment for CDDD does not place these individuals at a greater risk of injury. Preliminary studies have indicated that military recipients of cervical arthroplasty were able to return to full unrestricted duty with little to no complications [38, 39]. However, more research is required to evaluate dynamic neck response post-arthroplasty, particularly for military helicopter pilots [47, 48].

The current study investigated the effects of cervical arthroplasty on neck response during a simulated rotary-wing aircraft ground impact using a finite element (FE) human body model. The first simulation was run as a baseline, with no modifications to the neck. Two more simulations were run with the neck modified to represent a C5-6 interbody arthroplasty. These simulations modeled experimental sled tests conducted by the Naval Air Warfare Center Aircraft

Division (Patuxent River, MD), which evaluated the effects of varying helmet weight and center of gravity (CG) on aviator neck response during rotary-wing aircraft crashes [49, 50]. A rigid, crashworthy seat system was mounted to a horizontal accelerator, oriented to represent a 30° pitch-down impact scenario. The surrogate was a Hybrid III 5th, 50th, or 95th percentile anthropomorphic test device (ATD) with custom head fixture. The fixture allowed the head mass and CG to be varied, simulating the effects of a helmet and accessories. Three different severity crash pulses were evaluated, each representing the crash pulse experienced by an actual rotary-wing aircraft stroking seat. For the current study, experiment test #530 was simulated. This test used a Hybrid III 50th percentile ATD with 1.81 kg of additional head mass. The prescribed crash pulse produced a 7.62 m/s delta-V and 16.25 g peak acceleration.

Methods

The Global Human Body Models Consortium (GHBMC) 50th percentile seated, male model (v3.5) was used as the aviator surrogate in the current study (Figure 7-1). This high-fidelity model was developed to investigate human body response during dynamic impact events and has been validated in various impact scenarios [51-54]. The neck has been validated on a segmental level, as well as on the full cervical spine level [55-59]. Segmental physiological range of motion (ROM) has been validated for axial rotation, lateral bending, anteroposterior (AP) shear, flexion/extension, compression, and tension. Traumatic loading at the segmental level has been validated for compression, tension, and flexion/extension in terms of vertebral fracture, IVD injury, and ligament injury. Full cervical spine validation included both frontal and rear impacts. Developed at the University of Waterloo (Ontario, Canada) using geometry supplied by the Wake Forest University (WFU) School of Medicine (Winston-Salem, NC) [51], the neck is composed of the seven cervical vertebrae with detailed facet joints and intervertebral discs. It also includes non-linear, rate dependent ligaments, 3D passive muscles, and 1D active muscles. The additional head mass used in the experiment was distributed about the skull of the GHBMC model using the mass trimming function in LS-PrePost (4.0, LSTC, Livermore, CA).

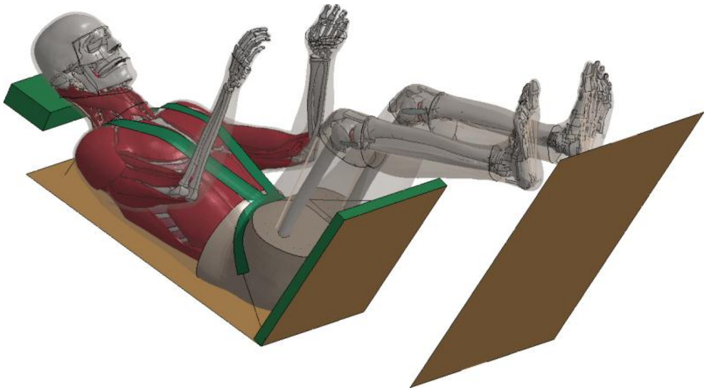

Figure 7-1: Initial position of the GHBMC model, including the five-point restraint system.

In the current study, a total of 3 FE simulations were conducted in LS-DYNA (R4.2.1, LSTC, Livermore, CA) to evaluate the effects of cervical arthroplasty on neck response during a rotary-aircraft crash. Experimental preloading of the restraint system was simulated using a pretensioner system in the model. To allow for settling due to gravity and initial belt tensioning, the simulation was run for 70 ms prior to the start of the sled pulse. The first simulation was run as a baseline, with no modification to the GHBMC neck. The two remaining simulations included a C5-6 CTDR; either the Prestige ST (Medtronic, Minneapolis, MN) or the ProDisc-C (Synthes, West Chester, PA). The Prestige ST is a metal-on-metal implant capable of three-axis rotation and AP translation due to its ball-and-trough design (Figure 7-2a). The ProDisc-C is a metal-on-polymer implant with a ball-and-socket design, allowing for three-axis rotation (Figure 7-2b). The geometries of both these CTDRs were reverse engineered from a physical implant with material properties listed in Table 7-1 [22, 60-62]. Prior to insertion of these CTDRs, several modifications consistent with the actual surgical procedure were made to the neck model. The IVD, endplates, and anterior longitudinal ligaments (ALL) associated with this level of the cervical spine were removed. The geometry of the C5 and C6 vertebral bodies were modified using select element deletion and advanced morphing techniques (Figure 7-3). The CTDRs were secured to the vertebrae using tied node contacts. The modeled CTDRs and C5-6 modifications were then reviewed and approved by board certified neurosurgeons.


(a) (b)

Figure 7-2: Lateral view of the (a) Prestige ST and (b) ProDisc-C finite element models.

Table 7-1: Material properties assigned to the cervical implants.

Implant	Part	Material Model	Element	ρ (kg/mm^3)	E (GPa)	ν	Ref
Prestige ST	End Plates	Rigid - 316L SST	Shell	8.00E-06	190	0.3	[61, 62]
ProDisc-C	End Plates	Rigid - CoCrMo	Shell	8.30E-06	210	0.3	[62, 63]
	Insert	Elastic - UHMWPE	Solid	9.36E-07	1.3	0.3	[22, 60, 62]

SST: Stainless Steel
CoCrMo: Cobalt-Chromium-Molybdenum
UHMWPE: Ultra-High-Molecular-Weight-Polyethylene

Cross sections were defined at each cervical level to capture neck forces and moments using a method previously described by White, et al. [64]. A local coordinate system (LCS) was defined for each cervical vertebrae with its origin located at the center of gravity (CG) of the respective vertebrae. Positive-x was directed to the midpoint of the superior and inferior portion of the anterior vertebral body in the midsagittal plane. Positive-z was directed inferiorly to the vertebra along the midsagittal plane, orthogonal to the local x-axis. A cross section was then defined for each local xy-plane, with forces and moments reported in the LCS. Force and moment polarity, according to head-chest manipulation, are described in Table 7-2 [65]. Cross sections were also used to capture forces transmitted though the C5-6 IVD of the unmodified neck and C5-6 facets for all neck models. The IVD and facet cross-sectional forces, as well as the implant contact forces, were reported in the C6 LCS. The cross-sectional results were post-processed using Oasys T/HIS (v11, Arup, London, UK) and MATLAB (v7.12.0, R2011a, MathWorks, Natick, MA). The forces and moments were filtered in accordance with SAE J211 [65].

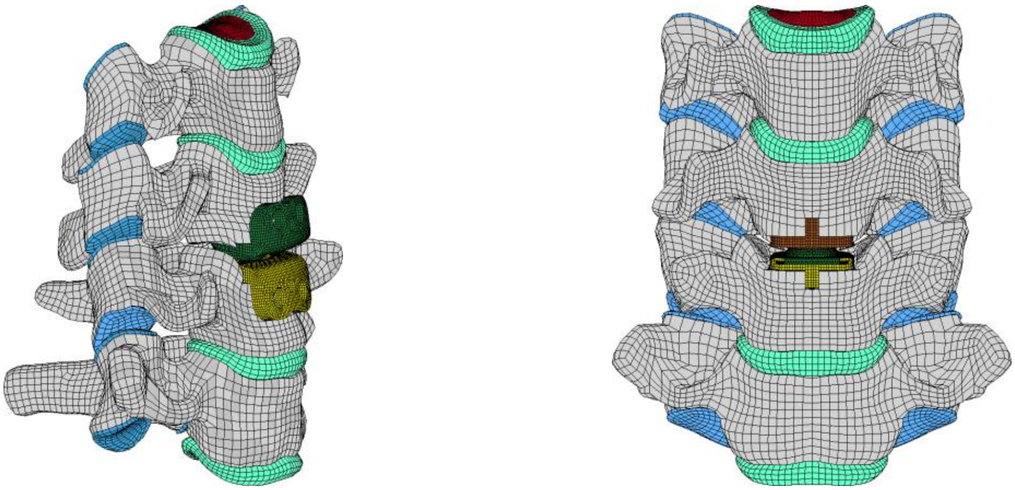

(a) (b)

Figure 7-3: The intervertebral disc and anterior longitudinal ligament between C5 and C6 were removed from the GHBMC neck. The inferior vertebral body of C5 and superior vertebral body of C6 were modified to accept the (a) Prestige ST and (b) ProDisc-C implants.

Table 7-2: Polarity of the cross-sectional forces and moments according to the relative motion between the head and chest.

Load Type	Transducer	Polarity	Head-Chest Manipulation	Load Name
AP Shear Force	Fx	+	Head rearward, chest forward	Positive AP Shear
		-	Head forward, chest rearward	Negative AP Shear
Axial Force	Fz	+	Head upward, chest downward	Tension
		-	Head downward, chest upward	Compression
Bending Moment	My	+	Chin toward chest	Flexion
		-	Chin away from chest	Extension

The N_{ij} neck injury criterion was calculated for the upper neck using the C1 cross-sectional loading [66, 67]. An N_{ij} value of 1.0 corresponds to a 22% risk of an AIS 3+ (Abbreviated Injury Scale) neck injury [66, 68]. The Beam Criterion (BC) was calculated for the lower neck using the C7 cross-sectional loading [69, 70]. A BC value of 1.0 corresponds to a 50% risk of AIS 2+ neck injury.

The axial force and bending moment for each cervical level were used to calculate adjacent-level, cross-sectional ratios: C1/C2, C2/C3, C3/C4, C4/C5, C5/C6, and C6/C7 [64]. These ratios were calculated at the time of maximum tension, compression, extension, and flexion for the C7 level. Loading at the superior level was less than at the inferior level for ratios less than 1 and greater than at the inferior level for ratios greater than 1.

A quantitative analysis was conducted using CORA (v3.6.1, Partnership for Dummy Technology and Biomechanics, Germany) to compare the cross-sectional loading reported in the implant simulations with the loading in the baseline simulation [71-73]. CORA rates the correlation of a signal with a baseline using two different methods: a corridor method and a cross correlation method. An overall score is then calculated between 0 (no correlation) and 1 (perfect match) from the weighted sum of these two ratings.

The neck kinematics in the midsagittal plane were captured for both the entire cervical spine and for the C5 and C6 vertebrae. Changes in cervical spine curvature were depicted by plotting the CG coordinates of each vertebra with respect to C7 [74]. Linkages between these points created a visual interpretation of the spinal curvature at a given time. Interbody relative motion of C5-6 was captured using the points that defined the local x-axes for both vertebrae. The coordinates of these points were plotted with respect to the C6 CG and rotated so the C6 local x-axis always remained horizontal. Linkages between these points created a visual interpretation of the shear, axial, and rotational relative motion between these adjacent vertebrae at a given time.

Results

Neck Loading

Cross-sectional AP shear force, axial force, and bending moment were captured at each cervical level of the neck with peak values reported in Table 7-3. None of these peak values approached established neck injury thresholds for the mid-sized male [75]. The calculated injury criterion values did not vary greatly between the three simulations (Table 7-4). The N_{ij} calculation predicated a 7.5% risk of AIS 3+ neck injury in the upper neck while the BC calculation predicted close to a 50% risk of AIS 2+ injury for the lower neck.

The C5 and C6 cross-sectional AP shear forces, axial force, and bending moment time histories are reported for each simulation (Figure 7-4 and Figure 7-5). Adjacent-level, cross-sectional loading was adequately maintained in both implant simulations as evidenced by the total CORA ratings of 0.988 for the Prestige ST and 0.909 for the ProDisc-C (Table 7-5). AP shear force remained predominantly negative throughout each simulation. Both cervical levels initially experienced a period of compression and extension followed by a period of

Table 7-3: Peak cross-sectional forces and moments reported at each cervical level in the respective local coordinate system.

		AP Shear (+Fx)		AP Shear (-Fx)		Tension (+Fz)		Compression (-Fz)		Flexion (+My)		Extension (-My)	
VB	**Simulation**	**Time (ms)**	**Force (N)**	**Time (ms)**	**Force (N)**	**Time (ms)**	**Force (N)**	**Time (ms)**	**Force (N)**	**Time (ms)**	**Moment (Nm)**	**Time (ms)**	**Moment (Nm)**
C1	GHBMC	136	793.8	177	-694.5	183	751.4	134	-929.0	189	77.4	300	-5.6
	Prestige ST	135	794.4	177	-691.0	182	738.9	135	-928.2	189	77.4	300	-5.6
	ProDisc-C	138	786.8	177	-679.9	182	755.3	134	-907.5	192	78.2	300	-6.6
C2	GHBMC	135	542.8	174	-485.4	183	918.9	135	-1132.2	192	78.2	300	-5.4
	Prestige ST	135	545.7	174	-478.2	182	910.1	135	-1138.6	189	78.7	300	-5.5
	ProDisc-C	135	541.1	174	-478.6	184	933.4	134	-1113.7	193	79.0	300	-6.6
C3	GHBMC	284	124.3	217	-415.7	183	1050.3	135	-1404.6	192	84.7	148	-11.7
	Prestige ST	282	128.4	228	-432.1	181	1064.3	135	-1412.3	190	85.0	148	-11.5
	ProDisc-C	272	124.1	218	-460.0	183	1068.5	134	-1383.1	193	86.4	148	-12.5
C4	GHBMC	297	162.8	219	-740.1	178	1286.1	135	-1372.1	193	96.8	150	-35.1
	Prestige ST	300	192.8	227	-781.3	178	1275.3	135	-1395.1	193	97.4	150	-35.0
	ProDisc-C	300	225.2	219	-790.1	180	1276.7	135	-1359.0	195	101.5	150	-36.4
C5	GHBMC	300	149.3	217	-740.8	178	1348.7	134	-1345.9	195	106.7	150	-40.3
	Prestige ST	300	173.5	226	-782.2	178	1347.2	135	-1367.7	196	107.7	150	-40.4
	ProDisc-C	300	197.7	219	-797.5	178	1344.6	134	-1329.6	222	116.2	150	-41.9
C6	GHBMC	293	143.7	215	-636.9	178	1415.5	134	-1363.4	195	106.7	149	-33.7
	Prestige ST	300	158.7	226	-674.6	178	1409.8	135	-1373.7	195	108.3	149	-33.9
	ProDisc-C	300	210.9	217	-655.8	180	1403.6	134	-1329.9	218	114.5	149	-35.3
C7	GHBMC	179	204.7	138	-504.9	180	1426.0	134	-1344.7	196	110.7	149	-26.4
	Prestige ST	180	221.0	138	-535.0	180	1392.8	135	-1411.6	197	112.1	149	-26.2
	ProDisc-C	293	183.0	137	-540.8	181	1443.6	134	-1337.6	217	120.0	149	-27.5

Table 7-4: Neck injury criteria calculated for the upper and lower cervical spine. The Nij was calculated for the upper neck (C1) and the Beam Criterion was calculated for the lower neck (C7).

Simulation	C1 FMVSS 208	C7 BC
GHBMC	0.35	0.98
Prestige ST	0.35	0.98
ProDisc-C	0.36	1.05

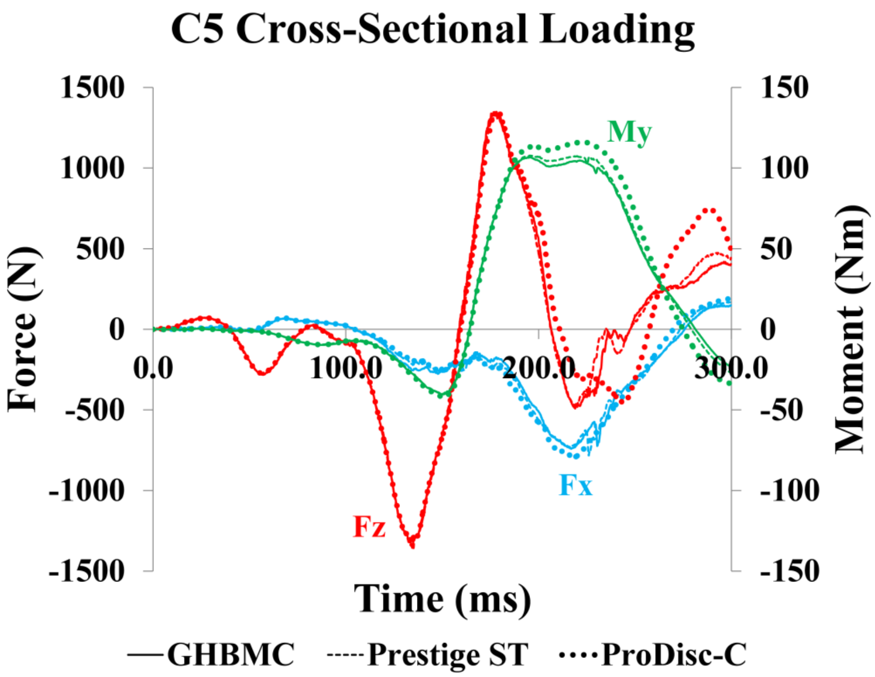

Figure 7-4: Cross-sectional AP shear forces, axial forces, and bending moments for the C5 level.

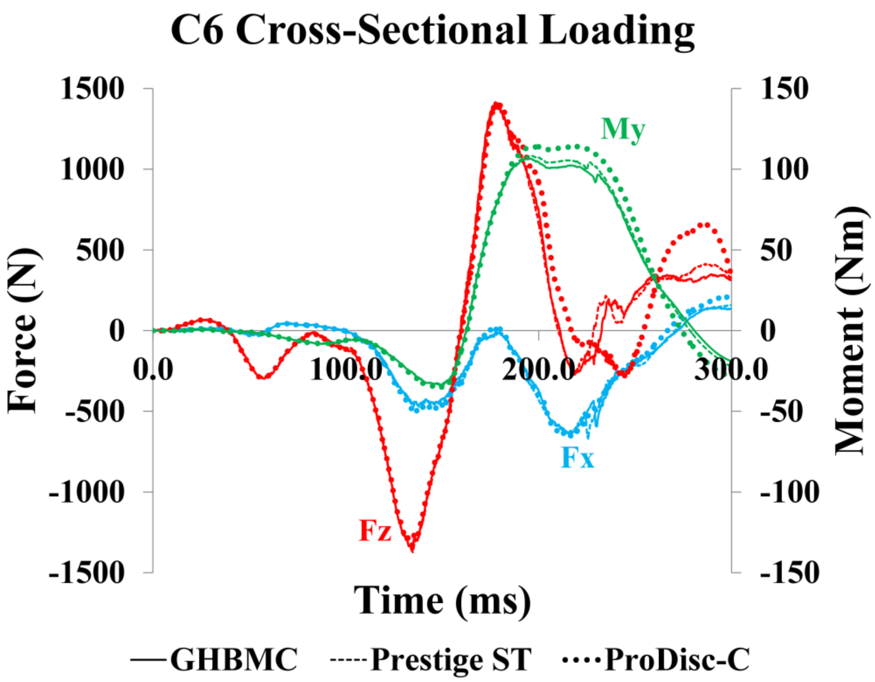

Figure 7-5: Cross-sectional AP shear forces, axial forces, and bending moments for the C6 level.

Table 7-5: Quantitative analysis of the cross-sectional neck loading response of the Prestige ST and ProDisc-C models to the baseline GHBMC model.

Simulation	Total Rating	VB Level	Transducer	Corridor	Correlation	Overall
Prestige ST	0.988	C5	Fx	0.986	0.985	0.985
			Fz	0.984	0.992	0.988
			My	0.999	0.989	0.994
		C6	Fx	0.981	0.977	0.979
			Fz	0.988	0.992	0.990
			My	0.998	0.987	0.992
ProDisc-C	0.909	C5	Fx	0.940	0.953	0.946
			Fz	0.788	0.886	0.837
			My	0.897	0.948	0.922
		C6	Fx	0.963	0.965	0.964
			Fz	0.805	0.903	0.854
			My	0.906	0.949	0.928

predominantly tension and flexion. A plateau in flexion moment occurred between t=195-234 ms, ending at the approximate time of maximum head flexion.

Adjacent-level loading ratios were similar between simulations for each level (Figure 7-6, Table 7-6). Noticeable changes occurred in load ratios between the C3/C4 and C4/C5 adjacent-levels at maximum tension and extension, and C2/C3 and C3/C4 adjacent-levels at maximum compression. The lower level ratios approached or exceeded 1.0, while the upper level ratio remained less than 1.0. At the maximum flexion moment, adjacent-levels in the upper and lower neck approached a ratio of 1.0 while a noticeable dip in ratio occurred in the middle levels.

AP shear and axial interbody loads between C5 and C6 are presented in Figure 7-7 with peak loads reported in Table 7-7. Negative AP shear force was the predominant shear loading in the implant simulations, while sustained periods of both positive and negative shear occurred in the non-modified simulation. The timing of peak negative AP shear was similar for all three simulations, but the implant simulations experienced a larger peak load. The interbody axial loading remained in compression for the duration of all simulations with the largest peak value occurring in the unmodified simulation.

AP shear and axial loading between the inferior C5 and superior C6 facets are presented in Figure 7-8 with peak loads and average maximum capsule ligament strains reported in Table 7-8. The facets experienced primarily negative AP shear and compression with peak values occurring within 4 ms of one another. Up to approximately 175 ms, the difference between left and right facet loading were negligible for a given simulation. A departure between left and right side loading occurred after this point. The right facet experienced noticeably larger negative AP shear and compressive loads than the left facet. Obvious axial tension occurred in the left facets toward the end of both implant simulations.

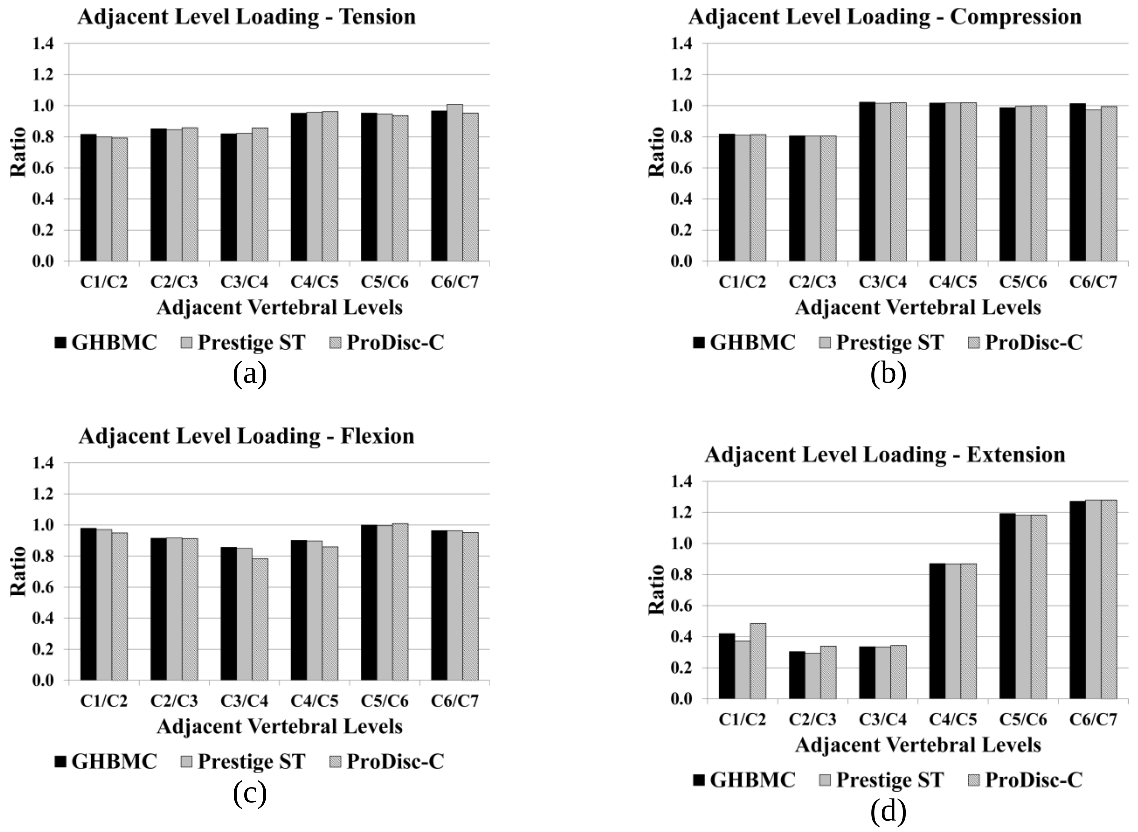

(a) (b) (c) (d)

Figure 7-6: Adjacent-level loading ratios at the time of maximum C7 cross-sectional (a) tension, (b) compression, (c) flexion, and (d) extension.

Table 7-6: Adjacent-level, cross-sectional loading ratios calculated at the times of maximum C7 tension, compression, flexion, and extension.

Loading	**Simulation**	**C1/C2**	**C2/C3**	**C3/C4**	**C4/C5**	**C5/C6**	**C6/C7**
Tension	GHBMC	0.82	0.85	0.82	0.95	0.95	0.97
	Prestige ST	0.80	0.85	0.82	0.96	0.95	1.01
	ProDisc-C	0.79	0.86	0.86	0.96	0.94	0.95
Compression	GHBMC	0.82	0.81	1.02	1.02	0.99	1.01
	Prestige ST	0.81	0.81	1.02	1.02	1.00	0.97
	ProDisc-C	0.81	0.81	1.02	1.02	1.00	0.99
Flexion	GHBMC	0.98	0.92	0.86	0.90	1.00	0.96
	Prestige ST	0.97	0.92	0.85	0.90	1.00	0.96
	ProDisc-C	0.95	0.91	0.78	0.86	1.01	0.95
Extension	GHBMC	0.42	0.30	0.33	0.87	1.19	1.27
	Prestige ST	0.37	0.29	0.33	0.87	1.18	1.28
	ProDisc-C	0.49	0.34	0.34	0.87	1.18	1.28

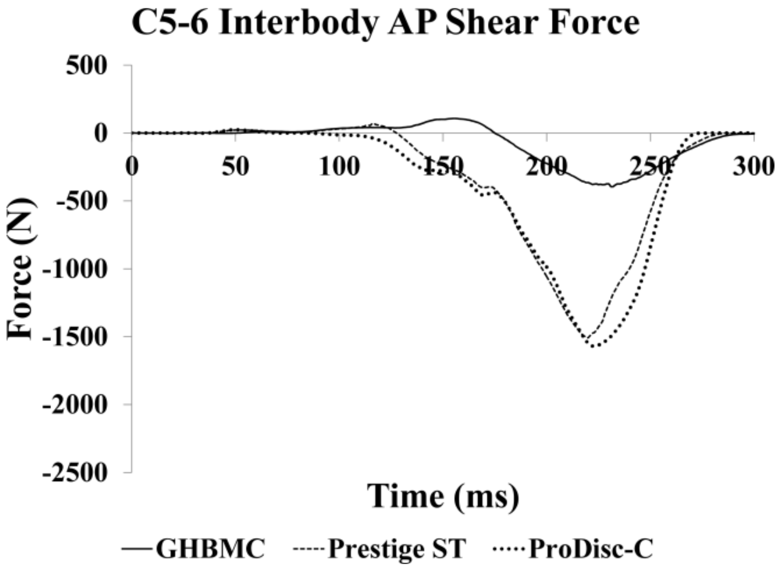

(a)

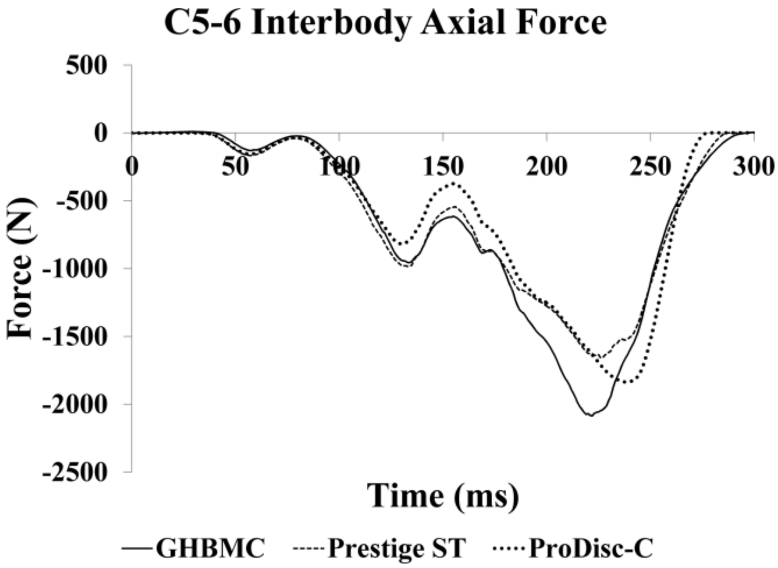

(b)

Figure 7-7: Interbody (a) AP shear force and (b) axial force reported in the C6 LCS. These forces were reported as cross-sectional forces from the IVD in the non-modified GHBMC simulation and as contact forces for both implant simulations.

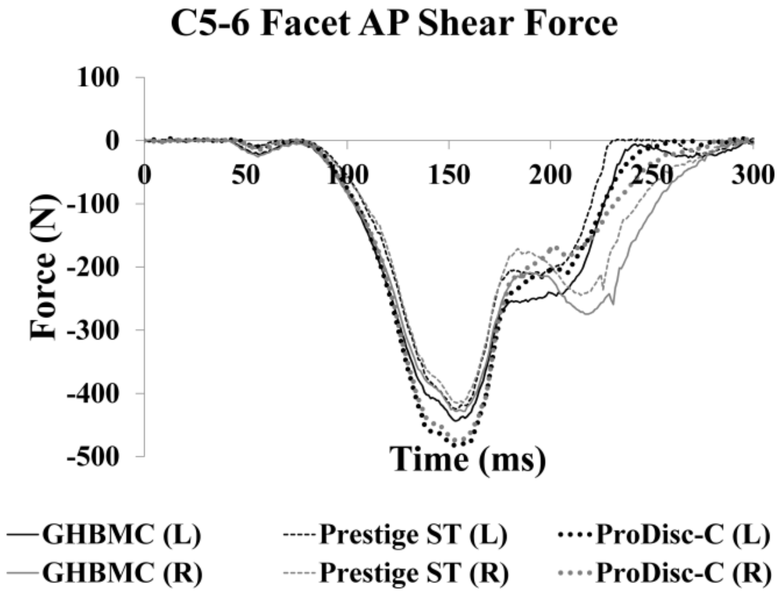

(a)

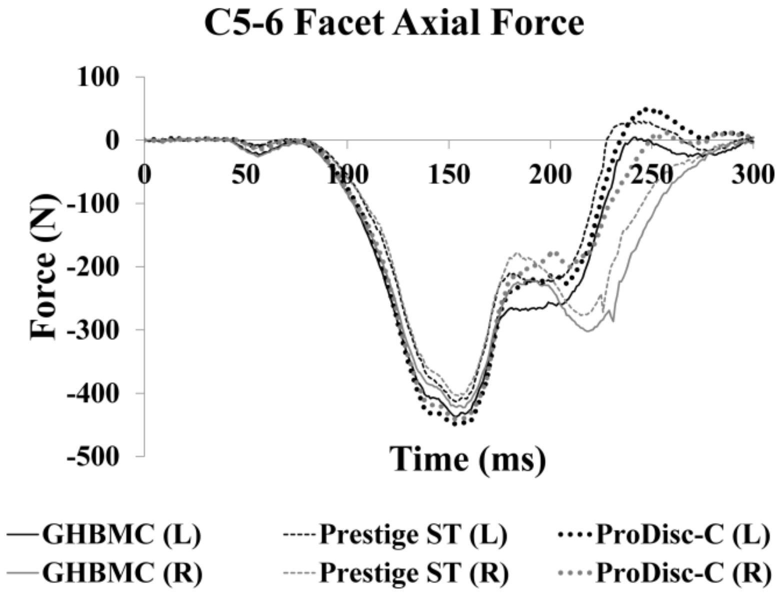

(b)

Figure 7-8: Left and right C5-6 cervical facet (a) AP shear force and (b) axial force reported in the C6 LCS.

Table 7-7: Peak C5-6 interbody loading reported in the C6 LCS.

	AP Shear (+Fx)		AP Shear (-Fx)		Compression (-Fz)	
Simulation	**Time (ms)**	**Force (N)**	**Time (ms)**	**Force (N)**	**Time (ms)**	**Force (N)**
GHBMC	156	107.2	232	-395.3	222	-2085.2
Prestige ST	116	70.9	220	-1507.7	227	-1658.4
ProDisc-C	49	24.1	223	-1570.0	238	-1836.3

Table 7-8: Peak cross-sectional C5-6 cervical facet loading reported in the C6 LCS and average maximum capsule ligament strain.

		AP Shear (-Fx)		Tension (+Fz)		Compression (-Fz)		
Simulation	**Facet**	**Time (ms)**	**Force (N)**	**Time (ms)**	**Force (N)**	**Time (ms)**	**Force (N)**	**Average Maximum Strain (%)**
GHBMC	Left	153	-443.4	242	4.4	153	-437.0	6.4±2.9
	Right	157	-428.2	-	-	157	-422.6	3.9±1.9
Prestige ST	Left	154	-424.4	246	29.9	154	-413.1	10.0±2.5
	Right	154	-415.0	300	3.3	155	-403.9	5.6±1.6
ProDisc-C	Left	153	-482.0	249	50.1	153	-448.3	14.1±3.3
	Right	154	-475.1	258	12.5	154	-441.4	12.2±2.7

Head and Neck Kinematics

Midsagittal head rotations were similar for the three simulations with an initial period of extension followed by a more pronounced period of flexion (Figure 7-9). Maximum head extension was almost identical for all simulations. Maximum head flexion was almost identical between the unmodified and Prestige ST simulations, while the flexion magnitude was approximately 4.5° greater in the ProDisc-C simulation (Table 7-9).

The spine curvature was reported at specific points in time corresponding to major loading and kinematic events in the unmodified simulation (Table 7-10). Comparison of cervical spine incremental kinematics between the unmodified and implant simulations is presented in Figure 7-10. Peak cross-sectional loading at the C7 level was used. The overall curvature did not vary greatly between the unmodified and implant simulations. For all simulations, an S-shaped curvature was produced during neck compression followed by a C-shaped curvature during neck tension. The most notable difference in curvature was seen at the time of maximum head flexion for the ProDisc-C simulation. There appeared to be an increase in rotation of C5 with respect to C6, increasing flexion of the entire neck.

Interbody relative motion of C5-6 with respect to C6 is presented for each simulation in Figure 7-11, Figure 7-12, and Figure 7-13. The motion is described relative to the initial midsagittal orientation of C5 with respect to C6 at t=0 ms. Minimal relative motion occurred in the simulations during the initial 70 ms settling phase. Extension of the C5-6 interbody space occurred for the first 180 ms in all simulations, with the greatest rotation occurring in the implant simulations. By the time of maximum flexion moment, t=196 ms, the implant extension angles were minimal. The time of maximum flexion moment for the ProDisc-C simulation did not occur until t=217 ms, 10-11 ms later than the unmodified and Prestige ST simulations. Interbody flexion increased up to the time of maximum head flexion, t=231 ms, most noticeably in the ProDisc-C simulation.

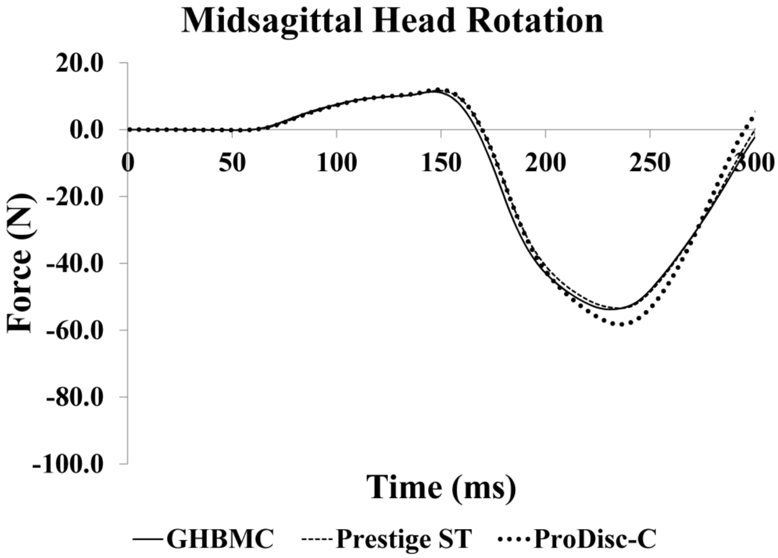

Figure 7-9: Rotation of the head center of gravity in the midsagittal plane.

Table 7-9: Peak midsagittal head rotation for extension and flexion.

	Maximum Head Extension		Maximum Head Flexion	
Simulation	**Time (ms)**	**Rotation (deg)**	**Time (ms)**	**Rotation (deg)**
GHBMC	146	11.3	231	-53.8
Prestige ST	147	11.7	234	-53.4
ProDisc-C	147	11.9	234	-58.3

Table 7-10: Timing of major loading and kinematic events for the non-modified GHBMC simulation.

Event	Time (ms)
Sled Pulse Initiation	70
Max Compression	134
Max Extension Moment	149
Onset of Head Flexion	167
Max Tension	180
Max Flexion Moment	196
Max Head Flexion	231

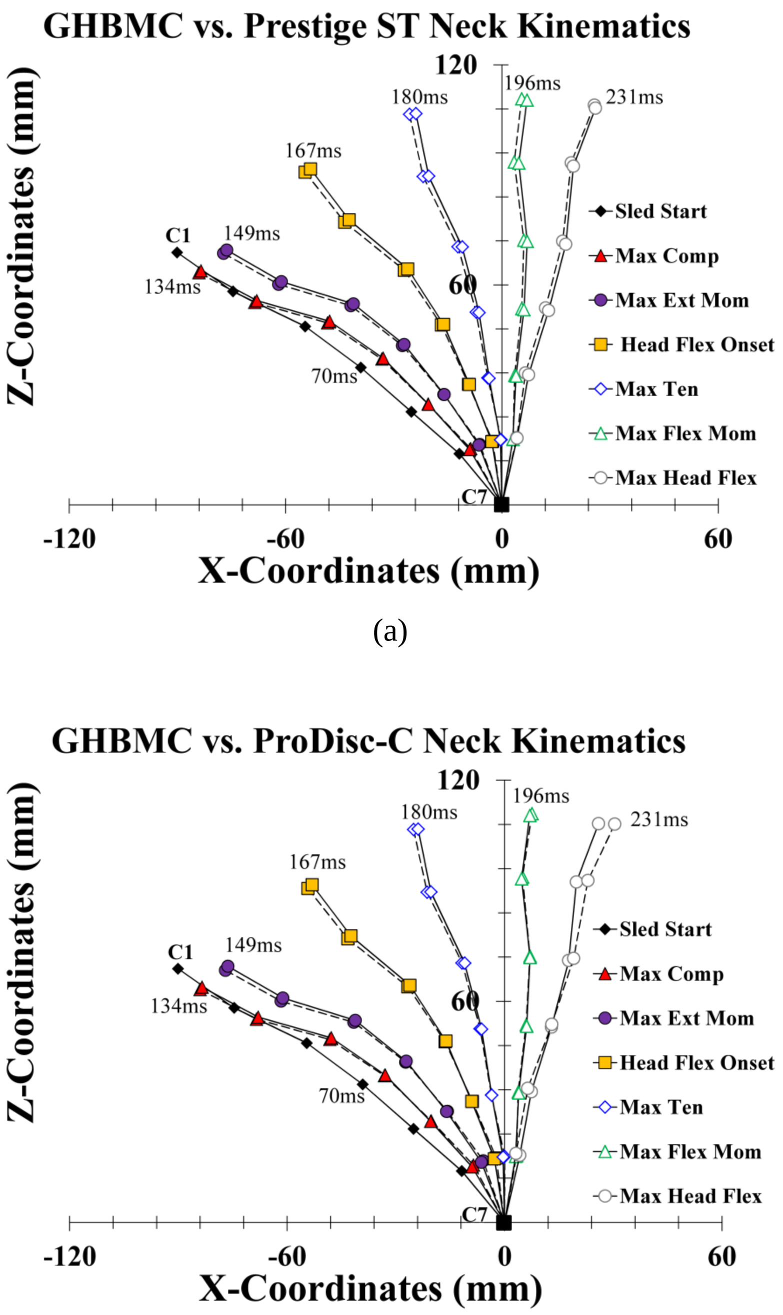

(a)

(b)

Figure 7-10: Incremental, midsagittal kinematics of the cervical spine for the (a) Prestige ST and (b) ProDisc-C simulations. The position of the local origin for each vertebra is plotted with respect to the C7 local origin, at different points in time. The solid lines represent the kinematics of the non-modified GHBMC simulation while the dashed lines represent the kinematics of the respective implant simulation

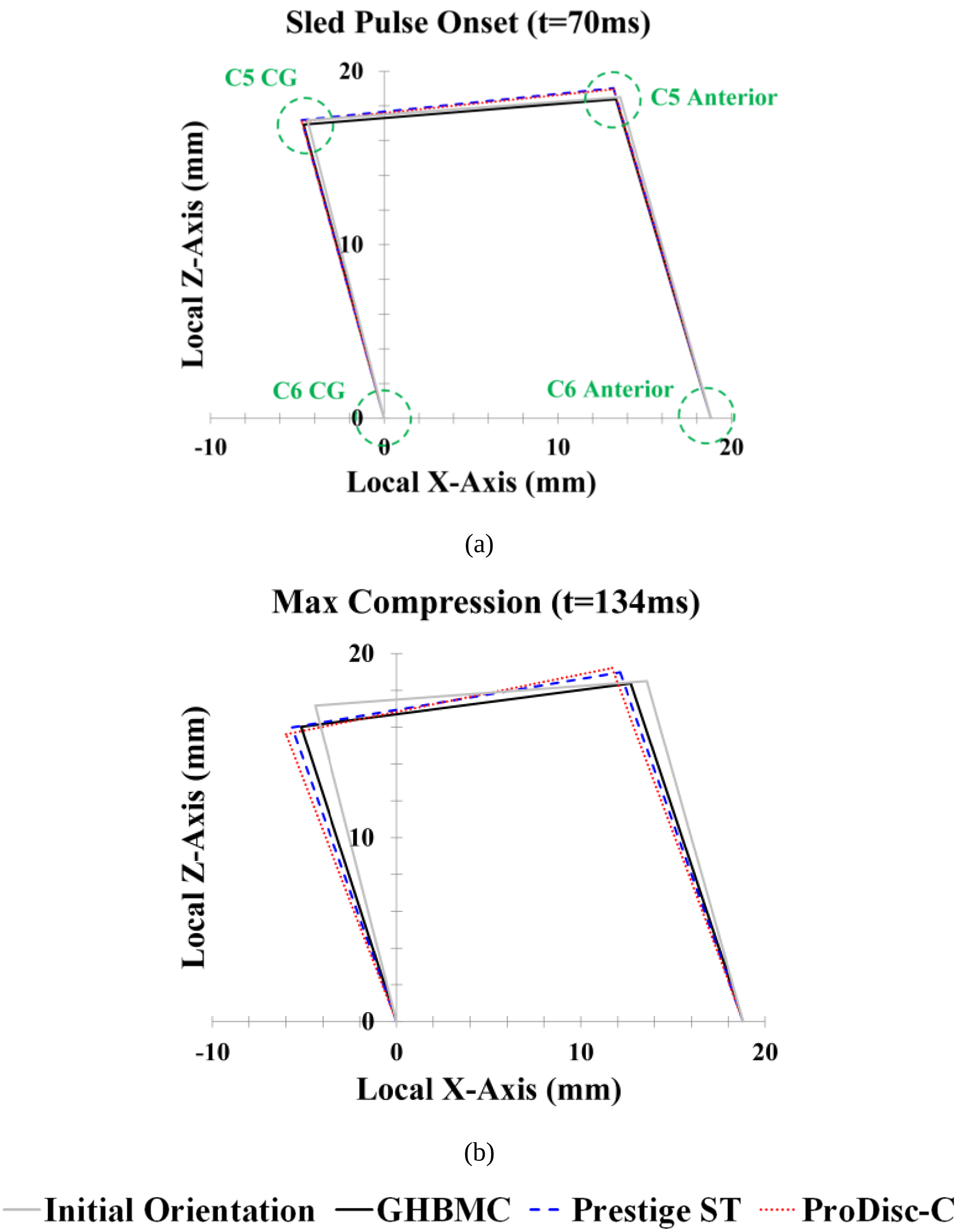

(a)

(b)

Figure 7-11: Relative C5-6 interbody midsagittal motion with respect to C6 at (a) sled pulse onset and (b) maximum compression.

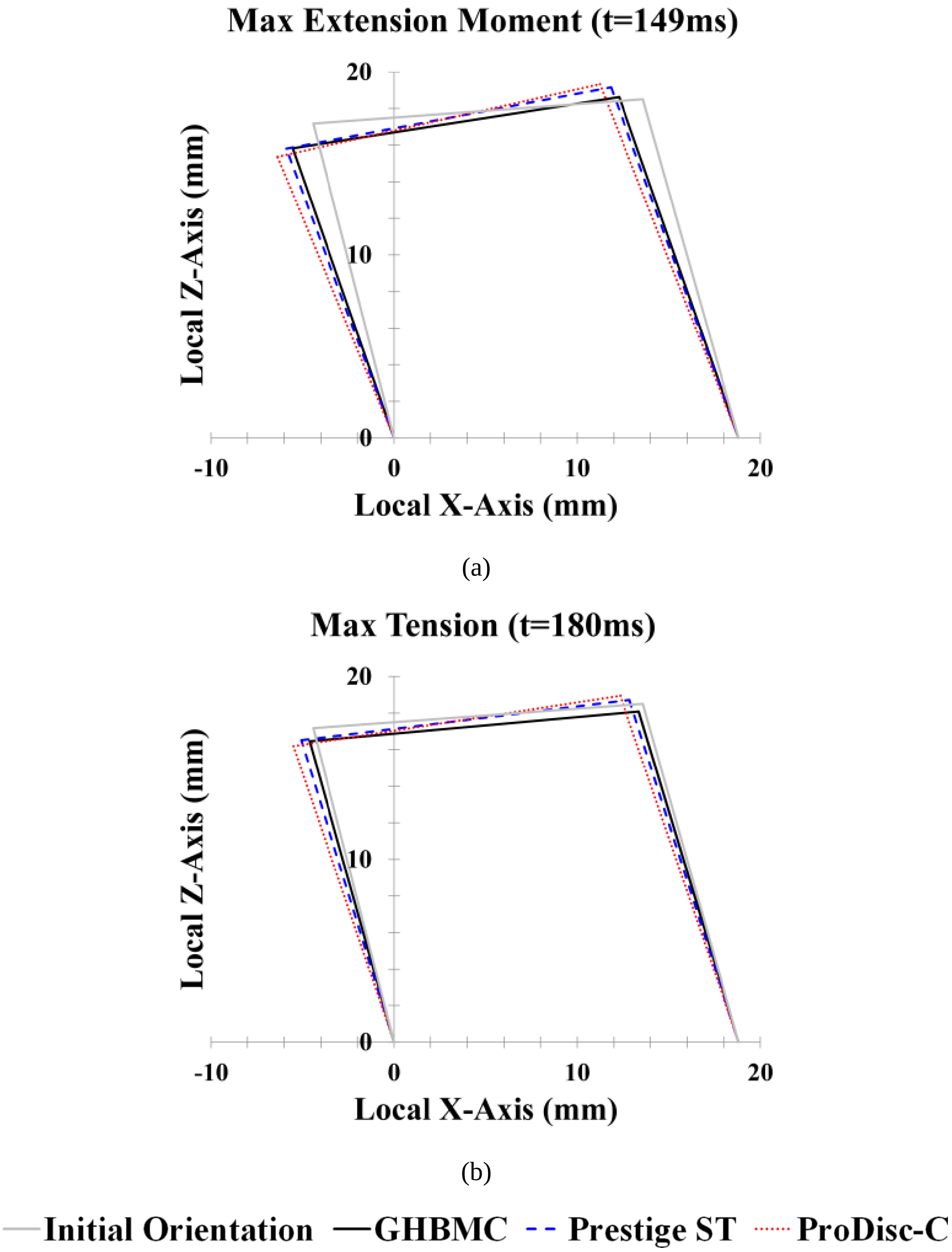

(a)

(b)

Figure 7-12: Relative C5-6 interbody midsagittal motion with respect to C6 at (a) maximum extension moment and (b) maximum tension.

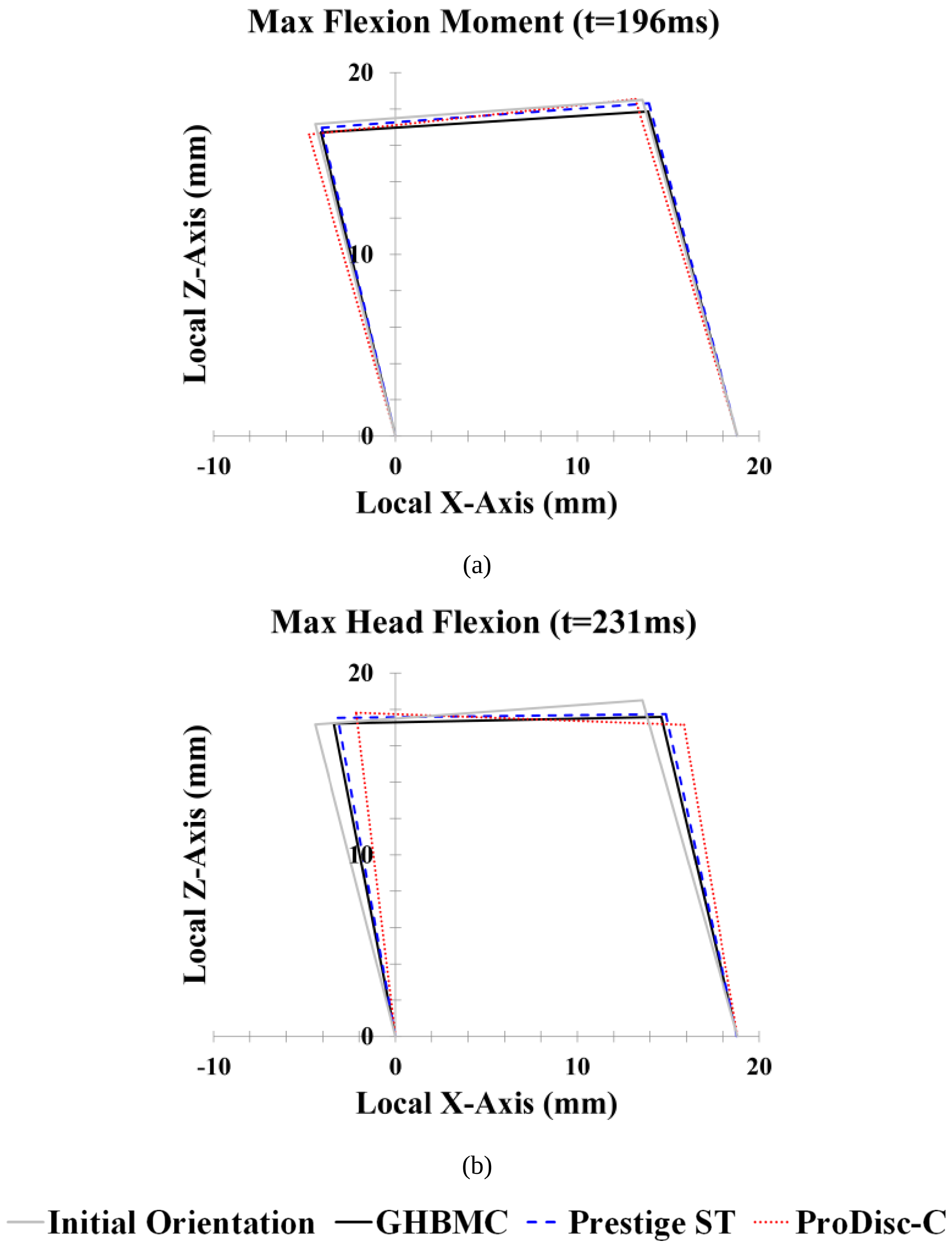

Figure 7-13: Relative C5-6 interbody midsagittal motion with respect to C6 at (a) maximum flexion moment (GHBMC and Prestige ST simulations) and (f) maximum head flexion.

Discussion

Overall Neck Response

The introduction of a CTDR at the C5-6 level did not appear to greatly alter the global neck response during a simulated rotary-wing aircraft impact. Midsagittal head rotation in the implant simulations was maintained in both extension and flexion, though the peak flexion in the ProDisc-C simulation was slightly larger than for the other two simulations. The incremental, midsagittal cervical spine kinematics for the implant simulations were almost identical to the unmodified simulation up to the time of maximum head flexion. Both S-shaped and C-shaped bending were reported during the simulations, similar to observations made in previous cadaver studies [69, 70]. Minimal difference was noted in the simulation for adjacent-level loading ratios, indicating load transmission through the neck was maintained. Injury criteria calculations in the upper and lower neck were almost identical in all simulations, indicating the risk of injury did not appear to change due to the CTDRs. The calculated BC values in all simulations correspond to a probability of an AIS 2+ neck injury, indicating that this type of impact, while survivable, is not benign.

Adjacent-Level Response

The C5-6 adjacent-level, cross-sectional loading was maintained with the CTDRs, as was evident by the quantitative analysis comparison. The largest discrepancy occurred in the axial loading phase of the ProDisc-C simulation, most notably during the last 100 ms of the event. All simulations produced a similar flexion moment plateau period, however, the moment in the ProDisc-C simulation remained larger than the other simulations during this time. Additionally, the peak flexion moment occurred at the end of the plateau for the ProDisc-C simulation, unlike in the unmodified and Prestige ST simulations. Some of the differences in adjacent-level loading may be explained by the C5-6 relative motion.

While the initial 70 ms of settling and belt pretensioning had a negligible effect on the unmodified C5-6 orientation, minimal extension occurred in both implant simulations. The C5-6 segment in both implant simulations remained more mobile than the unmodified simulation throughout time, with the ProDisc-C segment producing the greatest rotation and translation. This increase in mobility and subsequent change in segment kinematics is most likely responsible for any deviation in adjacent-level, cross-sectional loading from the unmodified simulation.

Increased mobility at the implant level has been previously reported in cadaver, volunteer, and FE studies. Chang et al. [76] evaluated the ROM of cadaver cervical spines with a Prestige II and ProDisc-C implanted at the C6-7 level. The ROM increased at the surgically treated segment in both implant specimens as compared to the intact spine, with the ProDisc-C producing the greatest increase in flexion and extension. FE studies have also found that introduction of a CTDR increased the ROM in midsagittal bending [77, 78]. A volunteer, in vivo study conducted by Kowalczyk et al. [79] investigated the effect of arthroplasty on spinal kinematics. The Prestige LP implant was found to preserve segmental ROM, while the ProDisc-C either maintained or increased the ROM. A similar finding was reported by Bertagnoli et al. [80] where flexion ROM was evaluated pre- and post-arthroplasty. Segmental rotation was found to increase from 4° to 12° with implantation of the ProDisc-C.

Interbody Loading

Many of the peak interbody loads correspond to distinct events visualized in the simulation. In the Prestige ST simulation, positive AP shear force starts with the onset of the sled pulse at 70 ms and peaks at 116 ms when the implant ball reaches the posterior end of the trough. Unable to translate any farther, the ball rotates in place until approximately 128 ms. The AP shear force polarity reverses at this point as the ball translates anteriorly. The ball contacts the end of the trough at 220 ms, corresponding with the peak negative AP shear force. The implant continues to rotate in place, flexing the C5-6 segment. As this implant is unable to sustain any tension by design, compression was the sole mode of axial loading. Peak compression occurred 7 ms after the peak negative AP shear force, the apparent time of maximum implant rotation. Interbody loading decreases to zero at approximately 287 ms, at which point separation between the ball and trough was visualized. Tension in adjacent-level, cross sections, caused by the relative motion of the head with respect to the torso, was responsible for this separation. Separation did not occur earlier in the simulation due to flexion-induced compression experienced by the implant.

Unlike the Prestige ST simulation, the ProDisc-C simulation produced negligible AP shear force between t=70 ms and t=100 ms. During this 30 ms time period, rotation in the form of extension occurred, producing only axial compression. As the extension moment increases at both vertebral levels, the interbody AP shear force becomes negative, corresponding to the compression of the posterior aspect of the semi-spherical inlay. The negative AP shear force increased with onset of flexion in the neck, reaching its peak at 223 ms. Both the peak rotation and axial load occurred approximately 15 ms later. While the design of the ProDisc-C allows for rotation only, some AP translation occurred as a result of inlay deformation. Interbody loading decreased to zero at approximately 278 ms, at which point separation between the ball and socket was visualized. Tension in adjacent-level, cross sections, caused by relative head motion, was responsible for this separation. As with the Prestige ST simulation, separation did not occur earlier in the ProDisc-C simulation due to flexion-induced compression experienced by the implant.

Interbody loading though the IVD in the unmodified simulation differed from the loading in the implant simulations. The IVD allowed for simultaneous points of attachment to the adjacent vertebrae as opposed to the single point of contact for the CTDRs. A positive AP shear force was produced for the first 175 ms followed by a negative AP shear force lower in magnitude than for the implant simulations. The peak compression was noticeably larger in the unmodified simulation, aligning closer in time with the Prestige ST peak than the ProDisc-C peak. The larger compressive force helped to limit the overall rotation of the vertebral segment, potentially protecting the facets from increased loading. Unlike the CTDRs, the IVD was capable of supporting tension, though only approximately 5 N of tension occurred at the end of the simulation.

Facet Loading

Due to geometrical symmetry, purely midsagittal motion of the head and neck should produce equal loading of the left and right facets for any given cervical level. However, a divergence in loading between the left and right facets at C5-6 was noted for all simulations. Midsagittal head and neck flexion was the dominant form of motion in the simulations; however, a small amount of lateral rotation occurred at the C5-6 segment. This lateral rotation accounted for the difference in facet loading, most notably in the unmodified and Prestige ST simulations.

All three simulations experienced tension in the facet capsules; however, this load was much more prominent in the implant simulations, particularly for the left facets. The increased midsagittal rotation of the C5-6 segment with either implant appears to have increased the facet tension.

Failure from quasi-static retraction of the human cervical facet capsule ligament has been previously reported [81]. The average load for gross failure, partial failure, and ligament yielding was 61.81 ± 26.40 N, 45.81 ± 22.99 N, and 30.65 ± 25.54 N, respectively. While both the Prestige ST and ProDisc-C left facet tension reached these potentially injurious levels in the simulations, it should be noted that this loading only lasted for approximately 40 ms. Due to this dynamic loading environment, it may not be best to compare the loads with those of a quasi-static experiment run at 0.5 mm/s. Dynamic tests conducted at 150-250 s^{-1}, comparable to the actual strain rate experienced in the cervical facet during a 20 g frontal automobile impact, have yielded a failure force of 286±73 N [58]. These simulated facet loads fell well below the dynamic failure range.

Ligament failure is built into the cervical facet capsule material model such that sequential beam deletion occurs at predefined average failure distraction levels [59]. Failure of the C5-6 facet capsule did not occur in any of the simulations. Cervical facet strain is also a common metric used to predict both ligament failure and potential for persistent neck pain. In the simulations, the distraction of each C5-6 cervical capsule beam element was extracted and divided by the neutral ligament length to calculate the strain [59, 82]. The results of dynamic experimental tests found the average failure strain of the cervical facet capsule to be 111.0±46%, well above the average maximum strains calculated in the simulations [58]. Facet capsule strain of 45.0±15.1% has been shown to correlate with persistent nerve afterdischarge in the caprine surrogate model, leading to persisting pain [83, 84]. Again, the maximum tensile strain in the simulations did not approach this injurious range. While any tension in the cervical facet capsule has potential to cause injury, the increased loads in the CTDR simulations did not appear to reach injurious levels.

Future Work

The current study provided insight into the effects of CTDRs on neck response during a simulated rotary-wing aircraft impact; however, dynamic experimental work is still required to further validate these findings. Such experimental work may include kinematic studies of intact cervical spines using a six-degree-of-freedom force-torque control or full body post mortem human subject (PMHS) tests with a high-speed, biplane x-ray system. Future work may also include modeling the screws in the Prestige ST simulation, allowing for evaluation of stress concentrations within the vertebrae. Other contact options for the press-fit ProDisc-C may also be evaluated to investigate the potential of the implant dislodging from AP shear loading. A parametric study to determine the effects of active muscle loading on neck response would also be of interest. Future simulations should also include combined impact loading modes involving more axial torsion and lateral bending of the neck in order to further investigate the effects of CTDRs on facet loading.

Conclusions

The effects of cervical arthroplasty on neck response during a simulated rotary-wing aircraft impact have been examined. Upper and lower neck loading and head kinematics were only minimally affected with the introduction of a CTDR at the C5-6 cervical level. Neck injury criteria calculations were almost identical between the unmodified and implant simulation. Quantitative analysis of the adjacent-level, cross-sectional neck loading above and below the site of the CTDRs showed very little difference with the adjacent-level loading of the IVD in the unmodified simulation. The AP shear C5-6 interbody force was greater for the CTDRs than IVD, though the axial compression was greatest for the IVD. The C5-6 interbody kinematics were slightly altered with the CTDRs, with an increase in ROM in both flexion and extension. Additionally, the CTDRs were incapable of supporting tension, allowing for interbody separation to occur. This increased mobility created tension in the C5-6 facets not seen in the unmodified simulation. While tension in the facet capsules may lead to injury, the reported loads and strains did not appear to reach any established injury thresholds. Overall, cervical arthroplasty at the C5-6 level did not appear to have a deleterious effect on the dynamic neck response during a simulated rotary-wing aircraft impact.

Acknowledgements

The authors would like to acknowledge the Global Human Body Models Consortium for use of the 50th percentile seated male FE model and the United States Army Medical Research and Materiel Command for funding this research. The authors would also like to acknowledge Medtronic Sofamor Danek (Memphis, TN) for supplying a Prestige ST implant and Synthes Spine (West Chester, PA) for supplying a ProDisc-C implant for reverse engineering purposes. All computations were performed on the Wake Forest University DEAC Cluster, a centrally managed resource with support provided in part by the University.

Chapter 7 References

[1] Boden SD, McCowin PR, Davis DO, Dina TS, Mark AS, Wiesel S. Abnormal Magnetic-Resonance Scans of the Cervical Spine in Asymptomatic Subjects. A Prospective Investigation. The Journal of bone and joint surgery American volume. 1990;72:1178-84.

[2] Lehto IJ, Tertti MO, Komu ME, Paajanen HE, Tuominen J, Kormano MJ. Age-Related MRI Changes at 0.1 T in Cervical Discs in Asymptomatic Subjects. Neuroradiology. 1994;36:49-53.

[3] Matsumoto M, Fujimura Y, Suzuki N, Nishi Y, Nakamura M, Yabe Y, et al. MRI of Cervical Intervertebral Discs in Asymptomatic Subjects. The Journal of bone and joint surgery British volume. 1998;80:19-24.

[4] Roh JS, Teng AL, Yoo JU, Davis J, Furey C, Bohlman HH. Degenerative Disorders of the Lumbar and Cervical Spine. The Orthopedic clinics of North America. 2005;36:255-62.

[5] Mydlarz D. Degenerative Disc Disease, Active Component, U.S. Armed Forces, 2001-2011. Msmr. 2012;19:6-9.

[6] Mason KT, Harper JP, Shannon SG. U.S. Army Aviation Epidemiology Data Register: Incidence and Age-Specific Rates of Herniated Nucleus among U.S. Army Aviators, 1987-1992. Fort Rucker, AL: U.S. Army Aeromedical Research Laboratory. 95-33. 1995.

[7] Schoenfeld AJ, George AA, Bader JO, Caram PM, Jr. Incidence and Epidemiology of Cervical Radiculopathy in the United States Military: 2000 to 2009. Journal of spinal disorders & techniques. 2012;25:17-22.

[8] Wang MC, Chan L, Maiman DJ, Kreuter W, Deyo RA. Complications and Mortality Associated with Cervical Spine Surgery for Degenerative Disease in the United States. Spine. 2007;32:342-7.

[9] Bailey RW, Badgley CE. Stabilization of the Cervical Spine by Anterior Fusion. The Journal of bone and joint surgery American volume. 1960;42-A:565-94.

[10] Cloward RB. The Anterior Approach for Removal of Ruptured Cervical Disks. Journal of neurosurgery. 1958;15:602-17.

[11] Nesterenko SO, Riley LH, 3rd, Skolasky RL. Anterior Cervical Discectomy and Fusion Versus Cervical Disc Arthroplasty: Current State and Trends in Treatment for Cervical Disc Pathology. Spine. 2012;37:1470-4.

[12] Smith GW, Robinson RA. The Treatment of Certain Cervical-Spine Disorders by Anterior Removal of the Intervertebral Disc and Interbody Fusion. The Journal of bone and joint surgery American volume. 1958;40-A:607-24.

[13] Matsunaga S, Kabayama S, Yamamoto T, Yone K, Sakou T, Nakanishi K. Strain on Intervertebral Discs after Anterior Cervical Decompression and Fusion. Spine. 1999;24:670-5.

[14] Uschold TD, Fusco D, Germain R, Tumialan LM, Chang SW. Cervical and Lumbar Spinal Arthroplasty: Clinical Review. AJNR American journal of neuroradiology. 2012;33:1631-41.

[15] Albert TJ, Eichenbaum MD. Goals of Cervical Disc Replacement. The spine journal : official journal of the North American Spine Society. 2004;4:292S-3S.

[16] Baaj AA, Uribe JS, Vale FL, Preul MC, Crawford NR. History of Cervical Disc Arthroplasty. Neurosurgical focus. 2009;27:E10.

[17] Traynelis VC. Cervical Arthroplasty. Clinical neurosurgery. 2006;53:203-7.

[18] DiAngelo DJ, Foley KT, Morrow BR, Schwab JS, Song J, German JW, et al. In Vitro Biomechanics of Cervical Disc Arthroplasty with the Prodisc-C Total Disc Implant. Neurosurgical focus. 2004;17:E7.

[19] Galbusera F, Bellini CM, Raimondi MT, Fornari M, Assietti R. Cervical Spine Biomechanics Following Implantation of a Disc Prosthesis. Medical engineering & physics. 2008;30:1127-33.

[20] Liu F, Cheng J, Komistek RD, Mahfouz MR, Sharma A. In Vivo Evaluation of Dynamic Characteristics of the Normal, Fused, and Disc Replacement Cervical Spines. Spine. 2007;32:2578-84.

[21] Puttlitz CM, Rousseau MA, Xu Z, Hu S, Tay BK, Lotz JC. Intervertebral Disc Replacement Maintains Cervical Spine Kinetics. Spine. 2004;29:2809-14.

[22] Womack W, Leahy PD, Patel VV, Puttlitz CM. Finite Element Modeling of Kinematic and Load Transmission Alterations Due to Cervical Intervertebral Disc Replacement. Spine. 2011;36:E1126-33.

[23] Boselie TF, Willems PC, van Mameren H, de Bie R, Benzel EC, van Santbrink H. Arthroplasty Versus Fusion in Single-Level Cervical Degenerative Disc Disease. Cochrane database of systematic reviews. 2012;9:CD009173.

[24] Chen J, Fan SW, Wang XW, Yuan W. Motion Analysis of Single-Level Cervical Total Disc Arthroplasty: A Meta-Analysis. Orthopaedic surgery. 2012;4:94-100.

[25] Ding C, Hong Y, Liu H, Shi R, Hu T, Li T. Intermediate Clinical Outcome of Bryan Cervical Disc Replacement for Degenerative Disk Disease and Its Effect on Adjacent Segment Disks. Orthopedics. 2012;35:e909-16.

[26] Fallah A, Akl EA, Ebrahim S, Ibrahim GM, Mansouri A, Foote CJ, et al. Anterior Cervical Discectomy with Arthroplasty Versus Arthrodesis for Single-Level Cervical Spondylosis: A Systematic Review and Meta-Analysis. PloS one. 2012;7:e43407.

[27] McAfee PC, Reah C, Gilder K, Eisermann L, Cunningham B. A Meta-Analysis of Comparative Outcomes Following Cervical Arthroplasty or Anterior Cervical Fusion: Results from 4 Prospective Multicenter Randomized Clinical Trials and up to 1226 Patients. Spine. 2012;37:943-52.

[28] Mummaneni PV, Amin BY, Wu JC, Brodt ED, Dettori JR, Sasso RC. Cervical Artificial Disc Replacement Versus Fusion in the Cervical Spine: A Systematic Review Comparing Long-Term Follow-up Results from Two Fda Trials. Evidence-based spine-care journal. 2012;3:59-66.

[29] Mummaneni PV, Burkus JK, Haid RW, Traynelis VC, Zdeblick TA. Clinical and Radiographic Analysis of Cervical Disc Arthroplasty Compared with Allograft Fusion: A Randomized Controlled Clinical Trial. Journal of neurosurgery Spine. 2007;6:198-209.

[30] Nunley PD, Jawahar A, Kerr EJ, 3rd, Gordon CJ, Cavanaugh DA, Birdsong EM, et al. Factors Affecting the Incidence of Symptomatic Adjacent-Level Disease in Cervical Spine after Total Disc Arthroplasty: 2- to 4-Year Follow-up of 3 Prospective Randomized Trials. Spine. 2012;37:445-51.

[31] Rollinghoff M, Zarghooni K, Hackenberg L, Zeh A, Radetzki F, Delank KS. Quality of Life and Radiological Outcome after Cervical Cage Fusion and Cervical Disc Arthroplasty. Acta orthopaedica Belgica. 2012;78:369-75.

[32] Tharin S, Benzel EC. Cervical Spine Arthroplasty: Fact or Fiction: The Absence of Need for Arthroplasty. Clinical neurosurgery. 2012;59:82-90.

[33] Upadhyaya CD, Wu JC, Trost G, Haid RW, Traynelis VC, Tay B, et al. Analysis of the Three United States Food and Drug Administration Investigational Device Exemption Cervical Arthroplasty Trials. Journal of neurosurgery Spine. 2012;16:216-28.

[34] Yang B, Li H, Zhang T, He X, Xu S. The Incidence of Adjacent Segment Degeneration after Cervical Disc Arthroplasty (Cda): A Meta Analysis of Randomized Controlled Trials. PloS one. 2012;7:e35032.

[35] Yin S, Yu X, Zhou S, Yin Z, Qiu Y. Is Cervical Disc Arthroplasty Superior to Fusion for Treatment of Symptomatic Cervical Disc Disease? A Meta-Analysis. Clinical orthopaedics and related research. 2013;471:1904-19.

[36] Heller JG, Sasso RC, Papadopoulos SM, Anderson PA, Fessler RG, Hacker RJ, et al. Comparison of Bryan Cervical Disc Arthroplasty with Anterior Cervical Decompression and Fusion: Clinical and Radiographic Results of a Randomized, Controlled, Clinical Trial. Spine. 2009;34:101-7.

[37] Park JH, Roh KH, Cho JY, Ra YS, Rhim SC, Noh SW. Comparative Analysis of Cervical Arthroplasty Using Mobi-C(R) and Anterior Cervical Discectomy and Fusion Using the Solis(R) -Cage. Journal of Korean Neurosurgical Society. 2008;44:217-21.

[38] Kang DG, Lehman RA, Tracey RW, Cody JP, Rosner MK, Bevevino AJ. Outcomes Following Cervical Disc Arthroplasty in an Active Duty Military Population. Journal of surgical orthopaedic advances. 2013;22:10-5.

[39] Tumialan LM, Ponton RP, Garvin A, Gluf WM. Arthroplasty in the Military: A Preliminary Experience with Prodisc-C and Prodisc-L. Neurosurgical focus. 2010;28:E18.

[40] Department of the Air Force. Air Force Waiver Guide. Wright-Patterson Air Force Base. 88ABW-2012-3597. 2013.

[41] Department of the Army. Standards of Medical Fitness. Army Regulation 40-501. 2011.

[42] Department of the Navy. U. S. Navy Aeromedical Reference and Waiver Guide. 134 Orthopedic: Intervertebral Disc Disease. Pensacola, FL: Naval Aerospace Medical Institute; 2013.

[43] Bass CR, Salzar R, Ash J, Ziemba A, Lucas S, Peterson R, et al. Dynamic Models for the Assessment of Spinal Injury from Repeated Impact in High Speed Planing Boats. International Research Council on Biomechanics of Injury. The Netherlands. 2007.

[44] Hendriksen IJ, Holewijn M. Degenerative Changes of the Spine of Fighter Pilots of the Royal Netherlands Air Force (RNLAF). Aviation, space, and environmental medicine. 1999;70:1057-63.

[45] Knapp SC. Medical and Physiological Effects of Ejection and Parachuting an Overview. Fort Rucker, AL: US Army Aeromedical Research Laboratory. USAARL Report No. 71-9. 1970.

[46] Petren-Mallmin M, Linder J. Cervical Spine Degeneration in Fighter Pilots and Controls: A 5-Yr Follow-up Study. Aviation, space, and environmental medicine. 2001;72:443-6.

[47] Reaume J. Cervical Total Disc Replacement in a Military Helicopter and General Aviation Pilot. The Federal Air Surgeon's Medical Bulletin. 2012;50:11-2.

[48] Reaume J. You're the Flight Surgeon: Cervical Degenerative Joint Disease and Total Disc Arthroplasty. Aviation, space, and environmental medicine. 2013;84:169-71.

[49] Paskoff GR. Cervical Injury Risk Resulting from Rotary Wing Impact: Assessment of Injury Based Upon Aviator Size, Helmet Mass Properties and Impact Severity. Patuxent River, Maryland. . NAWCADPAX/RTR-2004/86. 2004.

[50] Paskoff GR, Sieveka E. Influence of Added Head Mass Properties on Head/Neck Loads During Standard Helicopter Impact Conditions. Forty Second Annual SAFE Association Symposium. Salt Lake City, Utah. 2004.

[51] Gayzik FS, Moreno DP, Geer CP, Wuertzer SD, Martin RS, Stitzel JD. Development of a Full Body CAD Dataset for Computational Modeling: A Multi-Modality Approach. Annals of biomedical engineering. 2011;39:2568-83.

[52] Hayes AR, Vavalle NA, Moreno DP, Stitzel JD, Gayzik FS. Validation of Simulated Chestband Data in Frontal and Lateral Loading Using a Human Body Finite Element Model. Traffic Injury Prevention. 2013.

[53] Vavalle NA, Jelen BC, Moreno DP, Stitzel JD, Gayzik FS. An Evaluation of Objective Rating Methods for Full-Body Finite Element Model Comparison to PMHS Tests. Traffic Inj Prev. 2013;14 Suppl:S87-94.

[54] Vavalle NA, Moreno DP, Rhyne AC, Stitzel JD, Gayzik FS. Lateral Impact Validation of a Geometrically Accurate Full Body Finite Element Model for Blunt Injury Prediction. Annals of biomedical engineering. 2013;41:497-512.

[55] DeWit JA, Cronin DS. Cervical Spine Segment Finite Element Model for Traumatic Injury Prediction. Journal of the mechanical behavior of biomedical materials. 2012;10:138-50.

[56] Fice JB, Cronin DS. Investigation of Whiplash Injuries in the Upper Cervical Spine Using a Detailed Neck Model. Journal of biomechanics. 2012;45:1098-102.

[57] Fice JB, Cronin DS, Panzer MB. Cervical Spine Model to Predict Capsular Ligament Response in Rear Impact. Annals of biomedical engineering. 2011;39:2152-62.

[58] Mattucci SF, Moulton JA, Chandrashekar N, Cronin DS. Strain Rate Dependent Properties of Younger Human Cervical Spine Ligaments. Journal of the mechanical behavior of biomedical materials. 2012;10:216-26.

[59] Stitzel JD. Global Human Body Models Consortium (GHBMC) Male 50th Percentile (M50) Occupant Model Manual. Virginia Tech – Wake Forest University Center for Injury Biomechanics. GHBMC-FBM-MANUAL-01. 2011.

[60] DIN ISO 5834-2:2007-12. Implants for Surgery: Ultra-High-Molecular-Weight-Polyethylene, Part 2: Moulded Forms (ISO 5834-2:2006). Berlin, Germany2007.

[61] eFunda. Aisi Type 316l. Web. April 8 2013. <http://www.efunda.com/materials/alloys/stainless_steels/show_stainless.cfm?ID=AISI_Type_316L&show_prop=all&Page_Title=AISI%20Type%20316L>.

[62] Hallab NJ, Wimmer M, Jacobs JJ. Material Properties and Wear Analysis. In: Yue JJ, Bertagnoli R, McAfee PC, An HS, editors. Motion Preservation Surgery of the Spine: Advanced Techniques and Controversies. Philadelphia: Saunders; 2008. p. 52-62.

[63] ASM International. Materials and Coatings for Medical Devices - Cardiovascular. 1 ed. Materials Park, OH: ASM International; 2009.

[64] White NA, Moreno DP, Gayzik FS, Stitzel JD. Cross-Sectional Neck Response of a Total Human Body Fe Model During Simulated Frontal and Side Automobile Impacts. Computer methods in biomechanics and biomedical engineering. 2013.

[65] Society of Automotive Engineers. SAE J211/1 - Instrumentation for Impact Test-Part 1-Electronic Instrumentation. 2007.

[66] Eppinger R, Sun E, Bandak F, Haffner M, Khaewpong N, Maltese M, et al. Development of Improved Injury Criteria for the Assessment of Advanced Automobile Restraint Systems - II. NHTSA Docket No. 1999-6407-5. 1999.

[67] Eppinger R, Sun E, Kuppa S, Saul R. Supplement: Development of Improved Injury Criteria for the Assessment of Advanced Automobile Restraint Systems - II. NHTSA Docket No. 2010-03-19. 2000.

[68] Association for the Advancement of Automotive Medicine. Abbreviated Injury Scale © 2005 Update 2008. In: Gennarelli TA, Wodzin E, editors. Barrington, IL. 2008.

[69] Bass CR, Donnellan L, Salzar R, Lucas S, Folk B, Davis M, et al. A New Neck Injury Criterion in Combined Vertical/Frontal Crashes with Head Supported Mass. International Research Council on Biomechanics of Injury. Madrid, Spain. 2006.

[70] Bass CR, Salzar R, Donnellan L, Lucas H. Injury Risk from HSM Loading (HM 2,3,4,5 Series). Charlottesville, VA.: University of Virginia Center for Applied Biomechanics. Report HEADMASS2. 2004.

[71] Gehre C, Gades H, Wernicke P. Objective Rating of Signals Using Test and Simulation Responses. 21st International Technical Conference on the Enhanced Safety of Vehicles. Stuttgart, Germany. 2009.

[72] Gehre C, Stahlschmidt S. Assessment of Dummy Models by Using Objective Rating Methods. 22nd International Technical Conference on the Enhanced Safety of Vehicles. Washington, DC. 2011.

[73] Thunert C. CORA Release 3.6 User's Manual. Germany: GNS mbH; 2012.

[74] White NA, Begeman P, Hardy W, Yang KH, Ono K, Sato F, et al. Investigation of Upper Body and Cervical Spine Kinematics of Post Mortem Human Subjects (PMHS) During Low-Speed, Rear-End Impacts. SAE Technical Paper 2009-01-0387. 2009.

[75] Mertz HJ, Irwin AL, Prasad P. Biomechanical and Scaling Bases for Frontal and Side Impact Injury Assessment Reference Values. Stapp car crash journal. 2003;47:155-88.

[76] Chang UK, Kim DH, Lee MC, Willenberg R, Kim SH, Lim J. Range of Motion Change after Cervical Arthroplasty with Prodisc-C and Prestige Artificial Discs Compared with Anterior Cervical Discectomy and Fusion. Journal of neurosurgery Spine. 2007;7:40-6.

[77] Lee SH, Im YJ, Kim KT, Kim YH, Park WM, Kim K. Comparison of Cervical Spine Biomechanics after Fixed- and Mobile-Core Artificial Disc Replacement: A Finite Element Analysis. Spine. 2011;36:700-8.

[78] Rousseau MA, Bonnet X, Skalli W. Influence of the Geometry of a Ball-and-Socket Intervertebral Prosthesis at the Cervical Spine: A Finite Element Study. Spine. 2008;33:E10-4.

[79] Kowalczyk I, Lazaro BC, Fink M, Rabin D, Duggal N. Analysis of in Vivo Kinematics of 3 Different Cervical Devices: Bryan Disc, Prodisc-C, and Prestige Lp Disc. Journal of neurosurgery Spine. 2011;15:630-5.

[80] Bertagnoli R, Yue JJ, Pfeiffer F, Fenk-Mayer A, Lawrence JP, Kershaw T, et al. Early Results after Prodisc-C Cervical Disc Replacement. Journal of neurosurgery Spine. 2005;2:403-10.

[81] Lee DJ, Winkelstein BA. The Failure Response of the Human Cervical Facet Capsular Ligament During Facet Joint Retraction. Journal of biomechanics. 2012;45:2325-9.

[82] Panjabi MM, Pearson AM, Ito S, Ivancic PC, Gimenez SE, Tominaga Y. Cervical Spine Ligament Injury During Simulated Frontal Impact. Spine. 2004;29:2395-403.

[83] Cavanaugh JM, Lu Y, Chen C, Kallakuri S. Pain Generation in Lumbar and Cervical Facet Joints. The Journal of bone and joint surgery American volume. 2006;88 Suppl 2:63-7.

[84] Lu Y, Chen C, Kallakuri S, Patwardhan A, Cavanaugh JM. Neural Response of Cervical Facet Joint Capsule to Stretch: A Study of Whiplash Pain Mechanism. Stapp car crash journal. 2005;49:49-65.

Chapter 8: Research Summary and Future Work

Research Summary

A human body finite element (FE) model was used to evaluate dynamic neck response during simulated automobile and rotary-wing aircraft impacts (Table 8-1). A novel method to measure cross-sectional forces and moments in the neck during these impacts was developed and implemented. Neck loading was reported in three automobile impact simulations: a frontal impact of a belted driver with airbag deployment, a frontal impact of a belted passenger without airbag deployment, and an unbelted side impact. These loads were compared to existing injury thresholds and used to calculate injury criteria values. Loading contributions from individual anatomical components, including the bones, ligaments, muscles, and soft tissue, were also investigated. Four additional simulations were conducted to evaluate the effects of cervical arthrodesis and cervical arthroplasty at the C5-6 level on neck response during a frontal impact of a belted driver with airbag deployment. While the alterations to the cervical spine did not appreciably affect the cross-section loading at C5 and C6, there was an increase in facet tension in the arthroplasty simulations. This increase was due to the inability of the cervical total disc replacements (CTDRs) to support tension.

An FE simulation environment was then developed to investigate aviator head and neck response during a simulated rotary-wing aircraft impact using both an anthropomorphic test device (ATD) and a human body model. The simulation setup was based on an experimental test previously conducted to assess head-supported mass (HSM) effects using a Hybrid III ATD. The head and neck response of the ATD FE model was successfully validated against the experimental results. Initial positioning of the aviator surrogate was found to affect the magnitude of the head and neck response, but not the timing. A more biofidelic head and neck response was produced with the human body model, including realistic changes in neck curvature. Force and moments were reported for each level of the cervical spine, with the upper and lower neck loading compared to loads measured in the ATD. Additional simulations were conducted with the human body model to investigate the neck response after cervical arthroplasty at C5-6. While the adjacent-level, cross-sectional loading for the C5-6 segment was not appreciably altered by the CTDRs, the interbody range-of-motion (ROM) was increased; subsequently altering both the interbody and cervical facet loading. This increased ROM also increased the facet capsule tension; however, established injury threshold levels were not reached. Overall, cervical arthroplasty at the C5-6 level did not appear to have a deleterious effect on the dynamic neck response.

Table 8-1: Publication plan.

Chapter	Title	Journal
3	Cross-Sectional Neck Response of a Total Human Body FE Model during Simulated Frontal and Side Automobile Impacts	Computer Methods in Biomechanics and Biomedical Engineering (E-Published August 2013)
5	Effects of Cervical Arthrodesis and Arthroplasty on Neck Response during a Simulated Frontal Automobile Collision	The Spine Journal
6	Head and Neck Response of a Finite Element Anthropomorphic Test Device and Human Body Model during a Simulated Rotary-Wing Aircraft Impact	The Journal of Biomechanical Engineering
7	Effects of Cervical Arthroplasty on Neck Response during a Simulated Rotary-Wing Aircraft Impact	TBD

Recommendations for Future Work

This dissertation research has provided insight into the effects of cervical arthrodesis and cervical arthroplasty on neck response during dynamic loading scenarios. Further investigation is required to fully understand the effects of CTDRs on neck response during such a dynamic event. Simulations of additional automobile impacts, including rear-end impacts, should be conducted to evaluate neck response with a CTDR. Additional rotary-wing aircraft impact simulations may be conducted, with variations in sled velocity, seat orientation, and HSM. Tension within neck ligaments, other than the facet capsules, should also be evaluated from these simulations. The effects of muscle activation on neck response, particularly the interbody kinematics at the level of the CTDR, should also be evaluated.

Future experimental endeavors should include kinematic studies of intact cervical spines using a six-degree-of-freedom force-torque controlled industrial robotic arm, and full body or regional post mortem human subject (PMHS) tests with a high-speed, biplane x-ray system. While direct measurement of cross-sectional loading would be difficult to achieve, a variety of different instrumentation techniques can be employed to understand the loading of the neck in a PMHS. These techniques include pressure transducers implanted into the cervical facet capsules and intervertebral discs, and accelerometers mounted to the cervical vertebrae.